Quantum dot and carbon dot polymer nanocomposites for latent fingermark detection

A thesis submitted to the School of Chemical & Physical Sciences, Faculty of Science & Engineering, at The Flinders University of South Australia in fulfilment of the degree of

Doctor of Philosophy

March 2014

Jessirie Dilag

BTech (Forensic & Analytical Chemistry), BSc (Hons)

Supervisors: Professor Amanda V. Ellis,

Co-supervisors: Professor Hilton J. Kobus &

Professor Joseph G. Shapter

Table of Contents

Chapter 6. Application of the CdS QD and C-dot polymer nanocomposites as fingermark developing reagents 207

Declaration

I certify that this thesis does not incorporate without acknowledgment any material previously submitted for a degree or diploma in any university; and that to the best of my knowledge and belief it does not contain any material previously published or written by another person except where due reference is made in the text.

____

Jessirie Dilag on __________

Acknowledgements

The research presented in this thesis has been conducted at Flinders University, Adelaide, South Australia. Furthermore the project was funded by The Department of Justice of South Australia.

I am extremely grateful to my supervisor, Amanda Ellis, and co-supervisors Hilton Kobus and Joe Shapter for their supervision and guidance. In particular I would like to give a special thanks to my primary supervisor, Amanda Ellis for her encouragement, patience, and for believing in me over the last few years during this research. Your positive attitude and strong work ethic towards research in science has moulded me into the confident researcher I am today. I am certain that your wealth of knowledge, constructive criticism, and constant strive for excellence has made the last few years possible, it has been a great pleasure to be your student.

I must thank members of the ever changing Ellis research group, staff and academia at Flinders University, and members of the Flinders Centre for NanoScale Science and Technology, for their help, support, and amity over the past years.

Thanks to Kez, as a colleague, travel buddy and good friend. Jade, my bestie thanks for your mental-moral support and advice. Additional shout outs to Christine (my lunch buddy), Praveen, Luke, Bloky, Ra, Jess, Claire, Tony, Marky, Taryn, and Lee-Ann.

Finally I would like to thank my family in Adelaide and Darwin for their love, support (financially and mentally) and patience, which has always helped me towards achieving my goals. Love you all xo.

Abstract

Over the last decade interest in fluorescent nanoparticles for forensic applications has greatly increased. This thesis describes the synthesis of fluorescent nanoparticles with polymer grafted from their surface for latent fingermark detection. This allows for essential colour contrast for fingermark visualisation and subsequent person identification.

In the first part of the thesis cadmium sulfide (CdS) quantum dots (QDs) were synthesised. These QDs have size tuneable fluorescence, which was investigated using theoretical calculations of band gap energies measured by UV-visible spectrophotometry. Once synthesised a chain transfer agent (CTA) was immobilised onto the QD surface using a Steglich esterification method. Subsequently reversible addition fragmentation chain transfer (RAFT) polymerisation (a controlled polymerisation technique), was used to graft dimethylacrylamide (DMA) from the surface of the QDs *via* the CTA on its surface. This gave a CdS/p(DMA) nanocomposite, which was water soluble. Aqueous solutions of CdS/p(DMA) were then applied as a solution reagent to successfully detect latent fingermarks deposited on non-porous substrates. The fluorescently developed fingermarks were visualised and photographed using a Polilight® (UV = 350 nm).

The RAFT process was versatile in that different monomers could be used, and hence different polymers with suitable physical attributes were synthesised. Random copolymers of DMA with methyl methacrylate (MMA) and styrene (Sty) were then grafted from the CdS QDs to give CdS/p(DMA-*co*-MMA) and CdS/p(DMA-*co*-Sty). This ultimately led to the synthesis of fluorescent powders that could be dusted onto

the latent fingermarks for detection. The powders were found to give better ridge definition than the solution form.

Despite protection of the CdS QDs in the core of the polymers synthesised, there was always a residual concern for the use of the heavy metal, Cd, in the synthesis of these and other conventional QDs. Over the past decade years, research into nanocarbons has grown exponentially, with our interest particularly focused on using fluorescent carbon nanoparticles (C-dots) for this thesis. C-dots, in literature, have been reported as non-toxic, biocompatible, alternatives to conventional QDs. C-dots were synthesised *via* thermal oxidation of activated charcoal (AC) in nitric acid. They were inexpensive to synthesise. Their optical properties were visually comparable to the CdS QDs, and emission intensities were found to be defined by working pH (acidity/basicity). We applied the same polymerisation techniques (RAFT) to synthesise C-dot/polymer nanocomposites to successfully detect latent fingermarks that were deposited on non-porous materials. Visually, these were comparable to the QD/polymer nanocomposites previously synthesised and applied successfully to the detection latent fingermark on non-porous surfaces.

Lastly, the RAFT process was further exploited - by which the active end group (given by the RAFT agent) of the polymer was modified in a straightforward manner. Divinyl sulfone (DVS) modified magnetic beads were attached to CdS and C-dot polymer nanocomposites *via* a one-pot aminolysis/thiol-ene click reaction. This resulted in a magnetic fluorescent CdS QD or C-dot polymer powder that could potentially be used as a type of “Magna Powder” in latent fingermark detection.

Publications

Journal articles

Dilag, J., Kobus. H, Ellis, A.V, CdS/polymer nanocomposites synthesised *via* surface initiated RAFT polymerization for the fluorescent detection of latent fingermarks. *Forensic Science International*, **228**, 105 (2013).

Dilag, J., Kobus. H, Ellis, A.V, Nanotechnology as a new tool for fingermark detection: A review. *Current Nanoscience*, **7**, 153 (2011).

Conference/Symposia proceedings

Dilag, J., Kobus, H., Yu, Y., Gibson, C., Shapter, J.G., Ellis, A.V, Quantum dot and carbon dot polymer nanocomposites for latent fingermark detection, *RACI SA Student Polymer & Bionanotechnology Symposium*, Adelaide, SA, Australia, October 2013.

Dilag, J., Kobus, H., Yu, Y., Gibson, C., Ellis, A.V., Fluorescent carbon dots for latent fingermark detection, *Centre for Nanoscale Science and Technology, 3rd Annual Symposium*, Adelaide, SA, Australia, July 2013.

Dilag, J., Kobus., H., Ellis, A.V., Forensic Nanotechnology, Forensic Nanotechnology: Synthesis and Application of Innovative Materials for Fingermark Detection, *The 21st International Symposium on the Forensic Sciences*, Hobart, TAS, Australia, September 2012.

Dilag, J., Kobus., H., Ellis, A.V., New fluorescent nanocomposites for fingermark detection, *33rd Australasian Polymer Symposium*, Hobart, TAS, Australia, February 2012.

Dilag, J., Kobus., H., Ellis, A.V., Quantum dots as a new tool for latent fingerprint detection, *APMC10/ICONN2012/ACMM22*, Perth, WA, Australia, February 2012.

Dilag, J., Kobus, H., Allan, K.E., D.A., Khodakov Ellis, A.V., Nanotechnology: New materials for fingermark detection & current advances in DNA analysis *Invited*

Speaker at Ecole de Sciences Criminelles, Institut de Police Scientifique, University of Lausanne, Lausanne, Switzerland, July 2011.

Dilag, J., Kobus. H., Ellis, A.V., Quantum Dots Functionalised with Polymers *via* RAFT Polymerisation for the Fluorescent Detection of Latent Fingerprints, *European Polymer Congress*, Granada, Spain. June 2011.

Dilag, J., Kobus. H, Ellis, A.V., Synthesis of CdS/PDMA nanocomposites *via* surface initiated RAFT polymerisation for fingermark detection, *The 32nd Australasian Polymer Symposium*, Coffs Harbour, NSW, Australia, February 2011.

Dilag, J. Kobus, H., Ellis, A.V., Nanotechnology as a new tool for fingerprint detection, *The 20th International Symposium on the Forensic Sciences*, Sydney, NSW, Australia, September 2010.

Dilag, J., Kobus, H., Ellis, A.V., Nanotechnology as a new tool for fingerprint detection, *Australian Research Network for Advanced Materials and the Australian Research Council Network for Nanotechnology (ARNAM/ARCNN) Joint Workshop*, Adelaide, SA, Australia, June 2010.

List of Figures

List of Tables

Lists of abbreviations, symbols and units

Symbol/acronym/unit	Translation/explanation
Ω	Ohms
$\hbar$	The Dirac constant
δ	Chemical shift
%	Per cent
^{13}C NMR	Carbon 13 nuclear magnetic resonance spectroscopy
^{1}H NMR	Proton nuclear magnetic resonance spectroscopy
a.u	Arbitrary units
AC	Activated charcoal/carbon
AF	Autofocus
AIBN	Azobisisobutyronitrile
Al	Aluminium
Ar	Aromatic ring
C	Carbon
C=O	Carbonyl
C_{12}CTA	C_{12} chain transfer agent
Ca	Calcium
$CDCl_3$	Deuterated chloroform (chloroform-d)
$CdCl_2$	Cadmium chloride
C-dot	Carbon dot
CdS	Cadmium sulfide
CdSe	Cadmium selenium
cm^{-1}	Wavenumber
COOH	Carboxylic acid
co	Co-polymer
cps	Counts per second
CTA	Chain transfer agent
Cu	Copper
D_2O	Deuterated water
D-band	Disorder band
DCC	Dicyclocarbodimmide
°C	Degrees Celsius
DHU	Dicyclohexylurea
DMA	*N*-n-dimethylacrylamide
DMAP	4-dimethylaminopyridine
DMF	*N*-*N*-Dimethylformamide
DMSO-d_6	Deuterated dimethylsulfoxide
DTP	2,2'- dithiodipyridine
DVS	Divinyl sulfone
Eg	Band gap energy

eV	Electron volts
FTIR	Fourier transform infra-red
G	Generation
g mol^{-1}	Grams per mole
G-band	Graphite band
h	Hour
H_2SO_4	Sulfuric acid
HNO_3	Nitric acid
HPLC	High performance/pressure liquid chromatography
I	Intensity
Ind-Zn	1-2-indandione/zinc
J	Joule
K	Potassium
Kg	Kilogram
L	Litre
λ	Lambda (wavelength)
M , mol L^{-1}	Moles per litre
MHz	Mega Hertz
min	Minute
mL	Millilitre
MMA	Methyl methacrylate
M_N	Molecular weight number average
M_w	Molecular weight
mW	Mega Watts
MWCNT	Multiwalled carbon nanotubes
N or N_2	Nitrogen
Na	Sodium
Na_2S	Sodium sulfide
$NaBH_4$	Sodium borohydride
NaCl	Sodium chloride
nano	Nanometer
$NaNO_3$	Sodium nitrate
NaOH	Sodium hydroxide
Nd	neodymium
nm	Nanometer
O	Oxygen
OH	Hydroxyl
p	Poly- (e.g., p(DMA) = poly(dimethylacrylamide))
PAGE	Polyacrylamide gel electrophoresis
PAMAM	Polyamidoamine
PDI	Polydispersity index
PEG	Polyethylene glycol
Ph	Phenyl
pH	Power of Hydrogen (per Hydrogen)
π	Pi
PPE	Personal protective equipment

ppm	Parts per million
QD	Quantum dot
QY	Quantum yield
r	Radius
R6G	Rhodamine 6G
RAFT	Reversible addition fragmentation chain transfer
RT	Room temperature
S	Sulfur
s	Second
Si	Silicon
б	Sigma
SIP	Surface initiated polymerisation
sp	Sharp principle orbital
Sty	Styrene
T_d	Degradation temperature
TEM	Transmission electron microscopy
TGA	Thermal gravimetric analysis
UV	Ultra violet
UV-vis	Ultra violet-visible
V	Volts
wt/wt %	Weight per weight per cent
Xe	Xenon
YAG	yttrium aluminium garnet
ZnS	Zinc sulfide

Thesis Guide

Chapter #	**Short description**
1	Introduction: Background information about the significance of latent fingermark detection, and conventional methods of detection, quantum dots (QDs) including a literature review of QDs in latent fingermark detection, carbon dots, reversible addition fragmentation chain transfer (RAFT) polymerisation and RAFT end-group removal/modification.
2	Experimental methods: Details pertaining to the synthesis and characterisation of Cd QD and C-dot polymer nanocomposites and magnetic CdS and C-dot polymer nanocomposites.
3	CdS/polymer nanocomposites: Describes the synthesis and characterisation of the CdS QDs used for the synthesis of CdS/polymers: CdS/p(DMA), CdS/p(DMA-*co*-MMA) and CdS/p(DMA-*co*-Sty) *via* surface initiated RAFT polymerisation.
4	C-dot/polymer nanocomposites: Describes the synthesis and characterisation of the C-dots used for the synthesis of C-dot/polymer: C-dot/p(DMA) *via* surface initiated RAFT polymerisation.
5	RAFT end group modification: The synthesis of magnetic CdS/p(DMA-*co*-MMA) and C-dot/p(DMA-*co*-MMA) – describes the synthesis of these magnetic nanocomposites *via* a one-pot aminolysis/thio-lene click chemistry reaction.
6	Application of CdS QD and C-dot polymer nanocomposites to latent fingermark detection: Describes the preparation and application of the synthesised nanocomposites from Chapters 3, 4, and 5 to latent fingermark detection. This chapter will contain its own introduction and experimental sections describing the preparation of latent fingermarks, the CdS and C-dot polymer nanocomposites as reagents for fingermark detection.
7	Conclusions and future directions: Concluding remarks on the research presented in the thesis, and potential research projects related to the research presented.

Chapter 1. Introduction

1.1 Synopsis

Background information relevant to this thesis will be outlined in this chapter. The significance of fingermark detection in forensic science, conventional methods of detection and fluorescent enhancement will be discussed. This includes the composition of latent fingermarks, and the types of surfaces that fingermarks are found on at crime scenes, which ultimately determine how detection and visualisation will be approached. The optical properties and synthesis of conventional quantum dots (QDs) and carbon dots (C-dots) will be discussed. Particular attention will be drawn toward the potential use of QDs for latent fingermark detection with a literature review. This will be followed by a discussion on the emergence of novel carbon dots, their interesting optical properties and potential for a non-toxic alternative to quantum dots in latent fingermark detection. The synthetic route of surface initiated reversible addition fragmentation chain transfer (RAFT) polymerisation will also be introduced as this was the chosen route used to modify the surface of the nanoparticles (QDs and C-dots) synthesised in this research. In particular, surface modification provides protection of the QDs from toxic leaching, and provides functionality in latent fingermark detection.

1.2 Latent fingermark detection

To date, there have been no two individuals on the planet which have been shown to have identical fingerprints. Fingerprints, or fingermarks, are results of impressions of friction ridge skin from the palm side of fingers [1]. The term fingerprint is usually associated with an identified print, whereas the term fingermark is used with unidentified prints found at a crime scene. The individuality of a fingerprint, determined by carefully studying ridge characteristics (or minutiae), makes fingermarks one of the oldest yet most significant sources of physical evidence that can be obtained from a crime scene [1-3]. These patterns of friction ridge skin are unique to an individual and remain unchanged throughout the individual's life; even identical twins possess different fingermarks [1].

Latent fingermarks are often left behind at a crime scene and are particularly difficult for investigators as they are invisible to the naked eye. As a result it is up to the forensic investigator/scientist to evaluate the crime scene and choose the most appropriate method to visualise and photograph the latent fingermark for analysis and identification [4, 5]. The evaluation process for choosing an appropriate fingermark development method depends on the composition of the latent fingermark and the type of surface on which the latent fingermark has been deposited [3, 4, 6, 7]. This section will discuss the composition of latent fingermarks, surface types, and briefly describe conventional methods of latent fingermark detection, and light sources used for fluorescent detection. A separate introduction describing in detail the process of developing a fingermark, visualisation and photography techniques can be found in Chapter 6.

1.2.1 Composition of latent fingermarks

A latent fingermark is a complex emulsion derived from natural body sweat secretions and environmental contaminants. Furthermore, factors such as age, sex and diet of the donor also influence the chemical composition of the sweat secretions [8-11]. Latent fingermarks are primarily composed of an aqueous emulsion (>98 %) containing a mixture of sweat deposits excreted from three different types of sweat glands, namely the eccrine, apocrine and sebaceous glands, from around the body [1, 3-7, 10].

Table 1.1 outlines the excretion components of these sweat glands and their locations on our bodies [5, 7]. This results in two broad approaches to latent fingermark detection that either targets the water soluble components (usually amino acids) or the water insoluble organic components.

Table 1.1. Location and components of sweat excreted from the eccrine apocrine and sebaceous glands [5, 7].

Sweat gland	Part of body	Components
Eccrine	All over the body, including the palmer side of the hands and soles of feet.	Water, metal ions (Na^+, K^+, Ca^{2+}), chlorides, sulphates, phosphates, ammonia, amino acids, urea, and uric acid.
Apocrine	Groin and armpit areas, associated with hair follicles.	Water, sterols, carbohydrates
Sebaceous	All over the body except the palms and soles of the feet and associated with hair roots.	Glycerides, fatty acids, wax esters, squalene, sterols, and sterol esters.

1.2.2 Surface types: Porous, non-porous, and semi-porous

There are three types of surfaces; porous, non-porous and semi-porous, which influence the type of reagent that can be used to detect latent fingermarks [1, 5]. For a non-porous surface, the fingermark sits on top of the surface and will not be absorbed into the surface [5, 7, 12, 13]. Therefore development techniques using powders are the most appropriate, where the dry powder is attracted to the moist fingermark [12, 13]. Examples of non-porous surfaces include metals and glass. However in the case of a porous surface, such as paper, the reagent used must be absorbed into the surface and specifically interact with components of the latent fingermark [1, 4, 5, 7, 14]. Surfaces can also be classified as semi-porous, for example, polymer bank notes, other polymers such as polythene bags and varnished woods [1, 15]. The next section will detail the conventional methods currently used for detecting latent fingermarks from at or from a crime scene.

1.2.3 Conventional methods of development

In order to develop a latent fingermark from a porous surface the chosen reagent must penetrate the surface and react with a specific component of the deposit (and be inert to the surface) to create a visible product [1, 4, 5, 7, 16]. Ninhydrin is a good example of a reagent used extensively for developing latent fingermarks on porous surfaces [17-19]. The ninhydrin molecule reacts specifically with amino acids to produce a purple coloured complex, known as Ruhemann’s purple, resulting in a purple fingermark [16-18, 20]. Over time there have been a range of analogues of ninhydrin and other amino acid specific reagents that have been developed in an effort to improve on ninhydrin. 5-methoxy ninhydrin was one of the earliest successful analogues and more recently 1,3-indandione has been shown to be very effective and is being used widely in operational work [21]. Although specificity is required for this development method fingermarks absorbed into porous substrates are quite stable over time, which allows for fingermark development in older materials [16-22].

Latent fingermarks left behind on a non-porous surface do not always require a chemical reaction in development but they are fragile as they can be easily obliterated upon physical abrasion. In addition, over time, the aqueous components of the fingermark evaporate leaving behind the greasy, organic components such as the long chain fatty acids and waxy esters [7]. The popular methods of development in these cases is the use of a powder or dusting agent [13], and cyanoacrylate fuming [1, 4, 23]. There are a plethora of powders available to a forensic scientist such as titanium dioxide and aluminium flake powders [3, 24, 25]. Magnetic powders are also a popular choice, and are available in different colours [26-28]. By using an applicator wand, only the powder itself touches and adheres to the latent fingermark (as opposed to the brush and powder) [29]. Excess magnetic powder can also be removed using the same wand applicator [26-28]. Magnetic powders are often used on smoother non-porous surfaces, but have also shown to be successful in developing fingermarks on paper (depending on the age), and from skin on cadavers [30]. Cyanoacrylate fuming, also referred to as SuperGlue® fuming [1] consists of predominantly (98 – 99 %) cyanoacrylate ester (monomers) and when vapourised upon heating the monomers are attracted to the moisture of the fingermark where it polymerises to form a visible white cyanoacrylate polymer [1, 23]. Thus ridge definition is feasible. This method is particularly useful for latent fingermark detection on both non-porous and semi-porous substrates, as the cyanoacrylate polymerised onto the fingermark is stable. A post treatment staining with an organic dye (commonly, Rhodamine 6G (R6G)) is often required to improve visualisation. There have been efforts towards using one-step fluorescent superglue fuming methods, however they were found to affect developing times and the fluorescence was often short-lived [31, 32].

Methods used to develop fingermarks on porous and non-porous surfaces are considered when developing fingermarks on semi-porous substrates [1, 3, 5]. However development may prove difficult due to broad variables such as age, and the ambiguous porosity of the surface [15, 33]. In these cases a more elaborate means of development are required. A common example is vacuum metal deposition (VMD), where under vacuum visually detectable metals such as gold or silver are deposited onto the latent fingermark [33, 34]. Recently, Ma *et al*. [15] reported the use of $NaYF_4$:Er,Yb up-converter particles to detect latent marks on polymer bank notes. Polymer bank notes are often difficult to develop latent fingermarks from due to their multi-coloured patterned surfaces.

1.3 Fluorescent visual enhancement of developed fingermarks

Fluorescence offers high sensitivity, providing contrast between the fluorescent specimen and its background. The introduction of fluorescent detection, or enhancement of fingermarks, was first explored when it was shown that latent fingermarks could be visualised by exposure to light from an argon ion laser [35-39]. The components of a latent fingermark that are considered fluorescent were found to be riboflavin and pyridoxine, in addition to any contaminants that may be present in the sweat deposit [37, 40]. In reality inherent luminescence of fingermarks was found to be not as common as first thought and this led to a range of chemical and physical processes being developed that would create a fluorescent mark either through derivitisation or directly applying a fluorescent material. For example, the post application of the dye rhodamine 6G (R6G) after SuperGlue® fuming [1, 4, 5, 41]. Today, there are now a variety of highly efficient one-step luminescent fingermark development methods available, such as fluorescent styryl dye-integrated cyanoacrylate monomers for fuming fingermarks [32] and 1,2-indanedione/zinc reagents (Ind-Zn) for detection of fingermarks on porous substrates, such as paper [42, 43].

Powerful light sources are a requirement for fluorescent detection of developed fingermarks. The development of the Polilight® was a significant advancement in latent fingermark detection [1, 39]. The Polilight® is portable and offers a wide range of filtered light (often ranging from 335 nm to 665 nm), created by a xenon light source, to excite fluorescent components of fingermarks (and other biological excretions) [1, 39, 44]. Recently, light sources such as "Crime Light" became available with the progress in LED technology [45-47].

The concept of fluorescent enhancement of developed latent fingermarks was the underlying principle behind the research undertaken in this thesis. The next section will introduce the concept of using fluorescent nanoparticles; quantum dots (QDs) and carbon dots (C-dots), in latent fingermark detection. Literature exists in the synthesis and application of QDs in latent fingermark detection and will be reviewed; however, to date the use of C-dots in this application has not yet been reported.

1.4 Quantum dots (QDs)

Photoluminescence detection of latent fingermarks has over the last quarter century brought about a new level of fingermark detection sensitivity, even though conventional methods previously described are still regularly employed in forensic investigations [48, 49]. More recently a new direction in fingermark science has involved modern innovations in nanotechnology. One such innovation is the incorporation of quantum dots (QDs) into fingermark detection. The application of QDs has recently shown great potential in providing visual contrast between fingermarks and substrates [12, 48-58]. This section will introduce QDs, their electronic properties, synthesis and a literature review of their application in fingermark detection.

QDs are semiconducting nanocrystals which possess size dependent band gap energies (E_g) and conveniently lend themselves to a wide range of photoluminescent excitation sources, as they exhibit broad absorption band structure, yet emit a distinct fluorescence [59-64]. Alongside these benefits, QDs are robust and are not as susceptible, as many organic molecules are, to photo-bleaching [60, 65-68]. These characteristics make them a desirable candidate for the fluorescent detection of latent fingermarks.

QDs are nanocrystals composed of the periodic group elements of II-VI, III-V or IV-VI [59, 63, 69]. Examples include cadmium sulfide (CdS) [12, 51, 56], cadmium selenium (CdSe) [50, 58, 70-72], lead sulfide (PbS) [64] and zinc sulfide (ZnS) [73]. They are typically less than 10 nm in diameter and as such have a very high surface to volume ratio which means that during fabrication, care must be taken to protect the surface from defects and agglomeration which ultimately diminishes their fluorescence capacity [59, 61, 63, 68, 71].

1.4.1 Electronic properties of QDs

The intrinsic optical properties (along with electronic properties) of QDs are due to the quantum confinement effect. This phenomenon is better understood by recognising the molecular orbital construction of these semiconductors [59, 61-63]. In bulk semiconductor material, the electronic structure consists of continuous bands of molecular orbitals which ultimately assemble into a conduction and valence band [61, 63]. As the size of the semi-conductor material becomes smaller, its radius decreases to less than the Bohr exciton radius (the distance between the electron and electron hole). In addition, the molecular orbital structure becomes discrete and atom-like resulting in increased band gap energy [61, 62]. The differences in energy levels of the bulk and QD band gap energies ($E_{g(bulk)}$ and $E_{g(QD)}$, respectively) are illustrated in Figure 1.1(a) and (b), respectively.

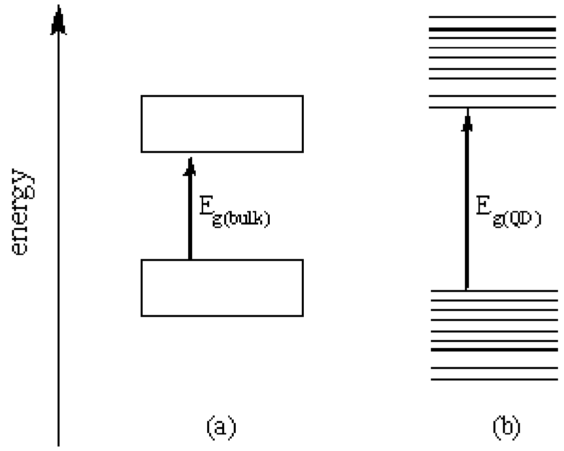

Figure 1.1. Energy level diagram of (a) a bulk semi-conductor with continuous energy bands and (b) a QD with discrete energy levels and larger band gap energy.

1.4.2 Optical properties of QD - absorbance and fluorescence

QDs can absorb energies equal to, or greater than, their $E_{g(QD)}$ and display an emission peak that corresponds to this band. Therefore, QDs are easily excited with high energy radiation such as Ultra-Violet (UV) light, with a broad absorbance, while their emission spectrum (fluorescence emission) is narrow. This relationship is depicted in Figure 1.2. Absorption occurs due to the overlapping of energy levels in the electronic bands, and the narrow emission from the band gap.

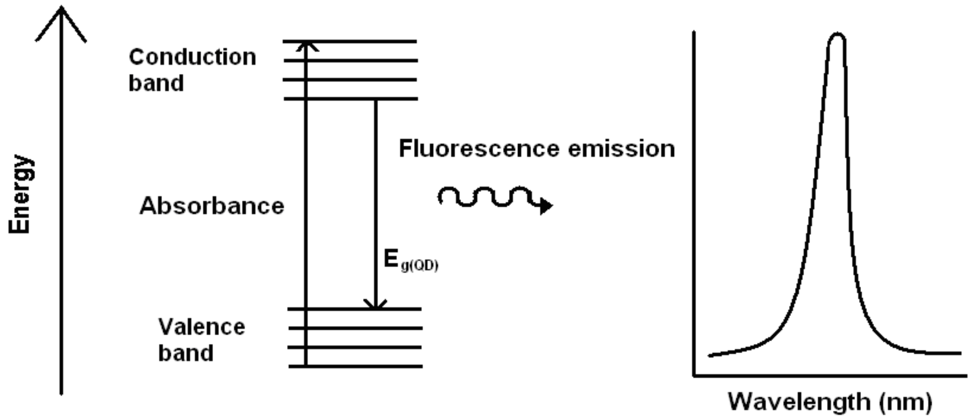

Figure 1.2. Energy level diagram showing a broad absorption and the narrow fluorescence emission characteristic of $E_{g(QD)}$. Image adapted from [74].

The $E_{g(QD)}$ indicates the energy (and hence colour) of the photon emitted. Smaller QDs will possess larger band gap energies and appear blue while larger QDs with lower band gap energies will appear red. For this reason QDs can be size-tuneable in order to provide control over emission colour [63, 68, 75].

UV-vis and fluorescence spectrophotometry are often used to indicate whether QDs have been successfully synthesised, as the wavelength absorbed (absorption onset) or emitted corresponds to the $E_{g(QD)}$. The absorption onset represents the electronic transition from the valence to the conduction band in the QD. Compared to bulk semiconductor material the absorption onset of a QD will be at a lower wavelength. For example, bulk CdS absorbs at 512 nm corresponding to a band gap energy of 2.42 eV – therefore CdS QDs would exhibit an absorption onset at smaller wavelengths than 512 nm as they possess greater band gap energies [63, 75]. The size-tuneability of the QDs can be exploited by observing the changes in the absorption onset of a QD, upon changing the size of the QDs with precursor concentrations, or experimental conditions (e.g., pH and temperature).

1.4.2.1 The hyperbolic band model

The inverse relationship between the $E_{g(QD)}$ and the QD's diameter is expressed through the hyperbolic band model (Equation 1.1) [76]. This equation is used with UV-vis spectrophotometry data to estimate the QD's diameter.

$$E_{g(QD)} = \sqrt{E_{g(Bulk)}^{2} + \frac{2\hbar^{2} E_{g(Bulk)} (\pi / r)^{2}}{m*}}$$

Equation 1.1.

Where:

$E_{g(QD)}$ = Band gap energy of the QD, from the wavelength of the absorption onset.

$E_{g(Bulk)}$ = Band gap energy of the bulk (512 nm, 2.42 eV for CdS) [75]

$\hbar$ = The Dirac Constant (1.054×10^{-34} J.s).

m* = The effective electron mass (0.2 m_{e}, 1.82×10^{-31} kg for CdS) [75]

r = The particle radius in nanometers

As an example, a report by Nedeljkovic *et al*. [75] presented a UV-vis absorption spectrum of an aqueous solution of CdS QDs (Figure 1.3) where the absorption onset was at 439 nm, corresponding to an $E_{g(QD)} = 2.92$ eV. The $E_{g(QD)}$ value when substituted into Equation 1.1 gives a calculated diameter of 5.71 nm for the CdS QDs synthesised.

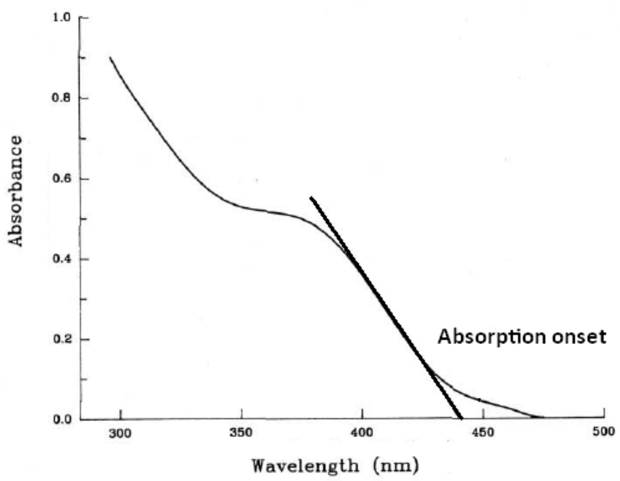

Figure 1.3. UV-vis absorption spectrum of aqueous CdS QDs with an absorption onset of 439 nm [77].

The hyperbolic band model ignores effects such as the coupling of the electronic states to vibrations, the structure of the QD surface, and the coulomb interaction energy and as such makes two main assumptions [63, 76]:

I. Excitation occurs with a charge transfer from the anion to the metal cation with energy equal to the band gap energy of the bulk. That is, from the sulphide ion to the cadmium ion in CdS.

II. It only takes into account relevant bands to calculate the band gap energy which are the highest occupied valence band and the lowest unoccupied conduction band.

This is a simple model, but has been shown to effectively estimate QD size, when compared to TEM imaging measurements [12, 78, 79].

1.4.3 QD synthesis

In order to maintain control over the QD size it is important to understand how QDs are formed during synthesis. QD formation occurs in two steps; nucleation and growth. Upon reaction of QD precursors (i.e., the source of Cd^{2+} and S^{2-} for CdS QDs), nucleation occurs. Further nucleation is prevented through the depletion of these precursors. Nucleation can be reduced or halted by a rapid decrease in temperature from high temperatures [80]. Once nucleation has been terminated, the growth of the QDs will then occur *via* Ostwald ripening. Ostwald ripening describes the diffusion of precursors from smaller nanoparticles to larger ones due to the favourable low surface area energetic conditions of the larger nanoparticles. This implies that small particles are depleted as larger particles grow [80-82].

In QD synthesis the surface of a QD must be protected against possible surface defects which may affect its fluorescent behaviour. Alongside these, the nucleation and growth of the QD can be controlled by monitoring the environment that they are synthesised in; that is the temperature, pH, concentration and solvents [81].

1.4.4 QD surface protection – capping/stabilising agents

The surface area to volume ratio of the QDs is large making the radiative processes that occur on the surface significant [74, 80]. The surface of QDs has atoms which are missing a bond, termed dangling bonds, making the surface highly reactive. Defects such as reconstructions occur to minimise the surface energy [74, 82]. These surface defects give rise to electron traps and an electron hole within the band gap, which can result in non-radiative processes (no fluorescence), or abnormal radiative processes such as QD blinking [83]. Figure 1.4 shows a schematic representation of the electronic structure of a QD with electron and electron hole traps, which disrupts the band gap energy of the QD ($E_{g(QD)}$).

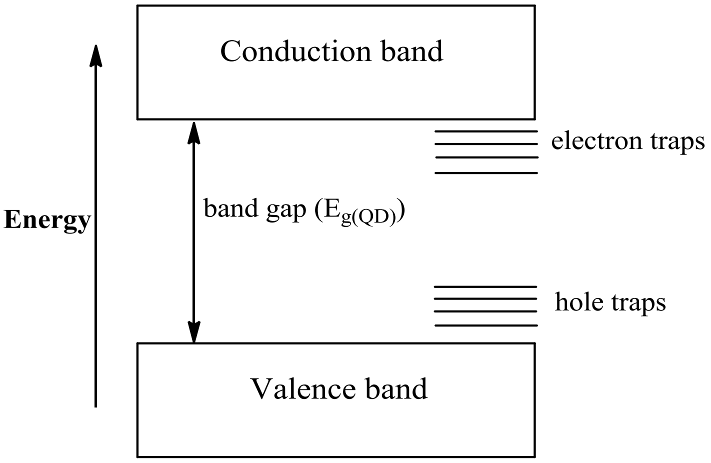

Figure 1.4. Electronic structure of a QD with electron and electron hole traps [74].

In a study by Weller [74] it was revealed that there exists a broad fluorescence emission at higher wavelengths which corresponds to defects on the surface of CdS QDs. Figure 1.5 shows the fluorescence emission spectrum of CdS QDs with surface defects

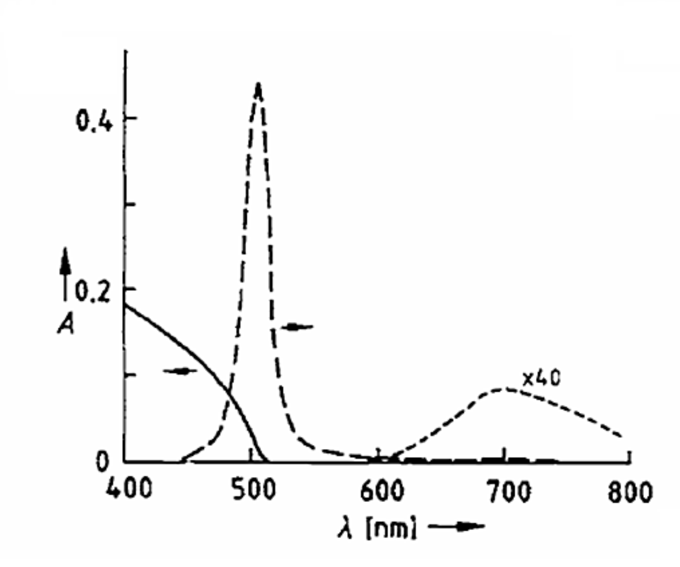

Figure 1.5. Absorption (solid line) and fluorescence (dashed line) spectra of colloidal CdS (20 mM), with the long-wavelength fluorescence magnified 40 times [74].

In order to protect the surface of a QD from these defects they can be synthesised *in-situ* with a stabilising or capping agent [68, 84-86]. Stabilising agents, for example a polymer, generally ensure that QDs do not agglomerate, which results in a highly defected QD or even just bulk semi-conductor material, by providing steric hindrance. This slows down the effects of Ostwald ripening during the growth of the QD and can be controlled by monitoring the concentration of stabilising agent used [12, 84]. Capping agents often referred to as ligands or polymers can effectively reduce the occurrence of surface defects by bonding to the dangling bonds on the surface of the QDs [84]. This is not only dependent on the concentration of the precursors, but also the stability of the interaction between the stabilising agent and the QDs (i.e., if there is a bond, such as an ion-dipole in a complex), and also the size of the stabilising agent [87].

In the selection of a suitable stabilising agent for QDs for use in latent fingermark detection, the agent must protect the QD surface from non-radiative processes, and should also have an affinity (chemical or physical) towards a latent fingermark.

1.4.5 Experimental factors that affect QD size

The extent of QD nucleation and growth will depend on a number of experimental factors including: temperature, pH, concentration of precursors, and the solvents used [81]. The rate of the depletion of the precursors in the nucleation stage will depend on the concentration of the precursors and also temperature [80]. The pH of the reaction can affect the dissociation of the precursors from their salt form – and hence the rate of their depletion during nucleation.

However an abnormal fluorescence emission due to surface defects of QDs may not necessarily be detrimental, but can be exploited in latent fingermark detection. For example, Dilag *et al*. [12] observed a broad emission at higher wavelengths in the fluorescence emission spectrum of synthesised CdS QDs used for latent fingermark detection. This enabled the QDs on the latent fingermarks, to be detected at two wavelengths – resulting in a green or orange fingermark shown in Figure 1.8 (see section 1.5).

The following section is a literature review of the application of QDs to latent fingermark detection.

1.5 QDs in fingermark detection – Literature review

The incorporation of QDs into the detection of latent fingermark detection is a new area of research. Menzel *et al*. [88] were the first to report the use of QDs to detect latent fingermarks. In their work, CdS QDs were synthesised and capped with dioctyl sulfosuccinate (sodium salt) and dispersed in solvents heptane and hexane. Prepared bare latent fingermarks and cyanoacrylate fumed fingermarks, on non-porous surfaces such as aluminium foil and soft drink cans were immersed in the nanocomposite solution. UV illumination was used to excite the CdS/dioctyl sulfosuccinate QDs, and analyse if fingermark development with the nanocomposite was successful. Development of the bare latent fingermarks on the non-porous substrates was unsuccessful as the fingermark deposits were washed away by the nanocomposite solvent. However, cyanoacrylate fumed fingermarks gave a better result and it was observed that the CdS/dioctyl sulfosuccinate QD nanocomposite concentrated itself onto the fumed ridges and required a rinse with the solvent (hexane/heptane). Adherence of the CdS/dioctyl sulfosuccinate QD nanocomposite was achieved but this required the initial pre-treatment of cyanoacrylate fuming and post-rinsing with the solvent.

Menzel *et al*. [88] introduced several QD-fingermark studies involving dendrimers as a capping or stabilising agent for CdS. CdS QDs were synthesised *in-situ* with polyamidoamine (PAMAM) generation 4 dendrimers that were amine terminated. Preliminary studies involved using the CdS/PAMAM nanocomposite on bare latent fingermarks (i.e., not cyanoacrylate fumed) deposited on non-porous aluminium foil substrates. To prevent the fingermark from washing away by the solvent (in this case methanol), the nanocomposite was carefully applied to the fingermark by ‘spotting’ the solution onto the fingermark deposit. After application the substrate was left to dry. Adherence of the nanocomposite to the latent fingermark deposit was achieved, but again, ridge detail was observed only after rinsing with methanol to remove the excess nanocomposite on the substrate.

Spotting (slowly adding drop-wise) to carefully apply the nanocomposite was impractical, so immersion of the aluminium foil substrates bearing the bare sebaceous fingermarks and cyanoacrylate fumed fingermarks were employed. With the potential of bare (unfumed) fingermarks being washed away by the methanol solvent, Menzel *et al*. [88] studied the effects of diluting CdS/PAMAM in ethanol with water. This improved the adherence of the nanocomposite to both the bare sebaceous latent fingermarks and the cyanoacrylate fumed fingermarks. However, the nanocomposite did still adhere to the substrate as well as resulting in low detection and ridge detail. The fingermarks were visualised and photographed under UV illumination.

Menzel *et al*.'s [88] studies with amino terminated dendrimers to stabilise CdS implied that an amide bond would form between the amine (from the dendrimer) and the fatty acids in the lipid composition of the latent fingermark deposits. However the hydroxyl groups present on fatty acids are poor leaving groups, so this reaction was unlikely. Therefore the extent of the interaction (whether chemical or physical) between CdS/PAMAM and the sebaceous fingermark deposit was not clear.

Bouldin worked with Menzel *et al*. [53] to improve the detection of latent fingermarks on aluminium foil with CdS/PAMAM by introducing a pre-treatment with carbodiimide. The bare sebaceous fingermarks on aluminium foil were immersed in a carbodiimide solution which was an aqueous solution of 1-(3-dimethylaminopropyl)-3-ethylcarbodiimide), followed by the CdS/PAMAM (in water and ethanol) solution for development. The carbodiimide pre-treatment resulted in the conversion of the carboxylic acid (from fatty acids in the fingermark deposit) to an ester which reacted more readily with the amine group on the dendrimers containing the CdS QDs, to form the anticipated amide bond.

Jin *et al*. [89] reported an identical study, using synthesised CdS/PAMAM nanocomposites for fingermark detection and proposed that the amine groups on the dendrimer's core and exterior could also interact with the CdS QDs (*via* ion-dipole moments between the cadmium ion and nitrogen during synthesis). The interaction between CdS and the exterior amines would be weaker compared to the poly-dentate core (of amine groups) in the dendrimers. Therefore it was possible for unbound CdS QDs to adhere to the substrate as well as the cyanoacrylate fumed fingermark causing the low ridge detail observed.

Jin *et al*.'s [89] synthesis involved the addition of hydrochloric acid which protonated the exterior amines of the PAMAM dendrimer, while the amines in the core of the dendrimers were able to chelate to the cadmium ions during synthesis. Dendrimers tend to act as nanoreacters, holding the QDs in their cores through ion-dipole interactions. This leaves the terminal amines available to selectively adhere to cyanoacrylate fumed fingermark deposits, which in turn results in improved resolution without the post-rinsing with methanol. This verified that the unbound CdS QDs were responsible for the low ridge detail observed in the study by Menzel *et al*. Figure 1.6 (a), and (b) are photographs of a cyanoacrylate ester-fumed fingermark developed with the CdS/G 4.0 PAMAM nanocomposites (Figure 1.6 (b)), and without (Figure 1.6 (a)).

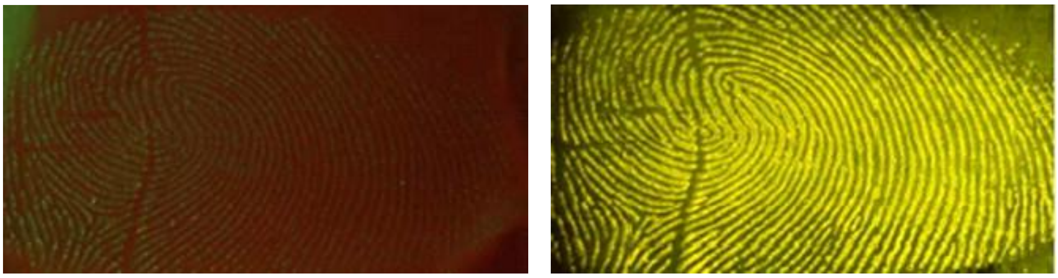

Figure 1.6. Cyanoacrylate ester-fumed fingermark on aluminium foil, (a) without CdS/PAMAM and (b) developed with CdS/G4.0 PAMAM nanocomposite (using a yellow filter) [89].

The unknown encapsulation efficiency of dendrimers and poor water solubility of CdS/dendrimer nanocomposites have greatly hindered further development of these nanomaterials as practical and useful latent fingermark developing agents.

Cheng *et al*. [90] investigated water-soluble CdTe nanoparticles coated with thioglycolic acid of different sizes. The nanoparticles exhibited absorption peaks at 525 nm and 605 nm, corresponding to 3 nm and 8 nm sized nanoparticles, respectively. Fluorescence was observed at 582 nm and 755 nm for each sized nanoparticle.

Fingermark samples were prepared on non-porous surfaces, aluminium foil and glass slides. Small amounts (1 mL aliquots) were gently applied to the surface of the fingermarks. Development times from 30 minutes to up to 24 hours were undertaken followed by rinsing with deionised water. Then the surfaces were left to dry for at least 20 minutes. The interaction between the nanocomposite and the fingermark deposit was suspected as an amidation reaction occurring with the surface carboxylic acid groups on the nanoparticles with amine groups on the biomaterials present in the fingermarks. However, similar to CdS/dendrimer proposed interaction [53, 88], the OH group of the acid is a poor leaving group, so the reaction was unlikely. Physiosorption of the nanoparticle to other organic or inorganic components of the fingermarks was also suggested to have taken place but was not specifically discussed.

A recent study by Sametband *et al*. [91] showed the synthesis of CdSe/ZnS QDs stabilised in octadecaneamine and petroleum ether for latent fingermark development *via* immersion. Fingermark deposits on silicon wafers (non-porous) and paper (porous) were immersed into the QD nanocomposite petroleum ether solution. Under UV illumination, it was observed that the QD nanocomposite preferably adhered to the fingermarks deposited on the silicon wafer. A micrograph of the developed fingermark, under UV illumination is shown in Figure 1.7. However, with the fingermarks deposited on paper, development was unsuccessful due to the porosity of the paper and excess background fluorescence. The authors gave no explanation of the chemical or physical interactions between the QD nanocomposite and the fingermark deposit (or surface).

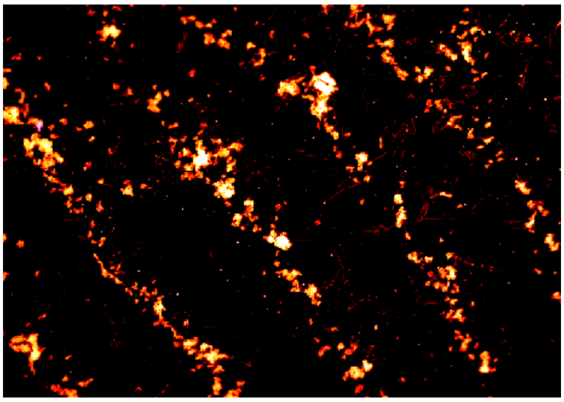

Figure 1.7. Optical micrograph of fingermarks under UV illumination on a silicon wafer developed using the CdSe/ZnS QDs stabilised with octadecaneamine (magnification not specified in literature) [91].

The choice of stabilising agent (octadecaneamine) and the solvent (petroleum ether) may give rise to hydrophobic interactions and therefore preferential adherence. This study is an example of how the developing reagent can be selective but not specific. The CdSe/ZnS QDs stabilised with octadecaneamine are selective toward the fingermark deposit (over the surface) on non-porous substrates, but despite the probably hydrophobic interaction, it was not specific enough toward the fingermark to successfully develop fingermarks absorbed in porous paper [91].

All the QD-nanocomposite developing agents discussed so far were synthesised for use as a suspension/solution. This means that fingermark development relies on immersion and drying times, and sometimes a subsequent rinse with the solvent to remove excess nanocomposite from the substrate. The obliteration of sebaceous latent fingermarks is often blamed on the ‘harshness’ of the solvent, and also the agitation of the liquid solution falling over the deposit (when immersed) gives the potential for the fingermark to be physically washed away. In an effort to prevent agitation and solubilisation of a fingermark with a nanocomposites solution, Dilag *et al.* [12] have used powdered QD-nanocomposites. CdS QDs stabilised in chitosan, a biopolymer, were dispersed in a detergent-surfactant solution of Tergitol which was freeze-dried into a quantum dot surfactant (QDS) powder. QDS powder was then dusted onto sebaceous latent fingermarks deposited on aluminium foil substrates and photographed using the Polilight® with an excitation of 450 nm. These photographs are shown in Figure 1.8. Barrier filters attached to the camera aided in acquiring the optimum emission from the QD-nanocomposite on the fingermark deposit. Adherence mechanisms were based upon the physical adherence of the dry QDS powder to the moist sebaceous latent fingermark.

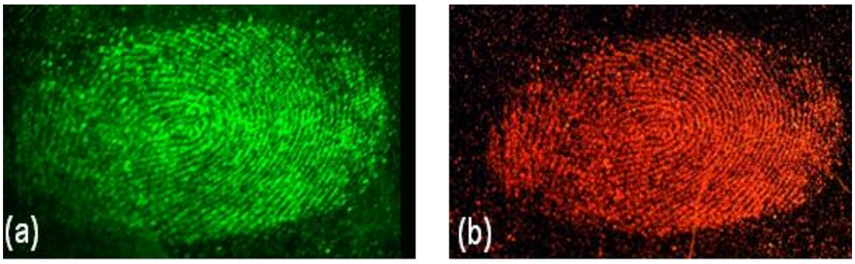

Figure 1.8. Photograph of CdS-chitosan-Tergitol powder developed latent fingermarks with 450 nm and (a) 550 nm band pass barrier filter (b) 565 nm long pass barrier filter [92].

Recently, aqueous solution based nanocomposites of CdSe QDs incorporated into a mesoporous phosphate heterostructure with mercaptopropyl functionalities were synthesised and applied to detect latent fingermarks on a range of non-porous substrates (credit cards, tweezers, and aluminium foil) [50].

1.6 Toxicity – health concerns of QDs

As the use of heavy metals is involved in the composition of conventional QDs, in particular cadmium, concerns toward the safety of these nanoparticles often arise in discussions with their particular application [66, 93, 94]. There are no specific reports that address the health and safety precautions/consequences, of using QDs in fingermark detection in comparison to the safety of current methods of detection. This is understandable as the use of QDs in real life crime scene investigations has not been conventionally implemented. Safety precautions already implemented for current techniques may be transferable to the application of QDs in fingermark detection, and additional personal protective equipment (PPE) may not be necessary.

In this research, two approaches were undertaken using nanoparticles. The first was to ensure the QDs, in this case CdS, were securely capped and encapsulated in a polymer. This was done by using surface initiated polymerisation (SIP) and will be discussed in Sections 1.8 and 1.9. The addition of a polymer coating on the nanoparticle not only protects the QD from leaching [93-95], but it also increases the size of the nanocomposite. This increased size decreases the chance of distribution in the body (*via* the blood stream) as demonstrated for gold nanoparticles in the study by Hillyer *et al*. [96]. When gold nanoparticles of decreasing size from 58, 28, 10 and 4 nm were administered to mice the smallest particle (4 nm) resulted in an increased presence in the kidney, liver, spleen and lungs and even the brain, whereas the larger particles (58 nm) were mostly detected inside the gastrointestinal tract [96].

The second part of this thesis was to eliminate the use of heavy metals. Initially this was done by synthesising ZnS QDs, however, the electronic properties in terms of fluorescence were not appropriate and the ZnS QDs fluoresced weakly in the blue region. Fortunately, the convenient evolution of nano-carbons, brought about the potential use of carbon nanoparticles, called carbon dots (C-dots) as an alternative to QDs with comparative optical properties in terms of quantum yields. C-dots will be described in the following sections.

1.7 Carbon dots (C-dots)

C-dots are a potential non-toxic alternative fluorescent nanomaterials to heavy metal based QDs. Studies have shown that C-dots are biocompatible and ideal for imaging applications [97, 98]. To our knowledge, C-dots have not been used as an alternative to QDs in latent fingermark detection. Their physical structure, how they are synthesised and theories behind their fluorescence mechanisms will be reviewed.

C-dots are simply nanoparticles of carbon. C-dots join fullerenes, nanotubes, nanodiamonds and nanographene and nanographene oxides as a new member to the “nanocarbon family”. C-dots are most similar to nanodiamonds and graphene QDs [99, 100]. To distinguish between these nanocarbons, the carbogenic nanocrystalline structure and surface functionalisation must be considered. Figure 1.9 shows Raman spectra taken of C-dots, multiwall carbon nanotubes (MWCNTs), graphite and microdiamonds, respectively.

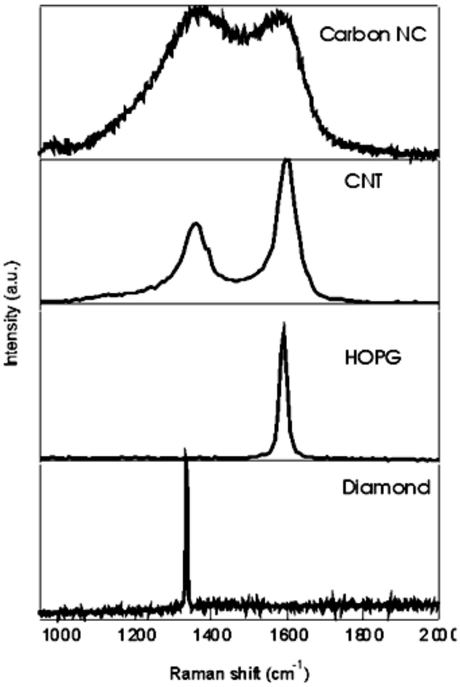

Figure 1.9. Raman spectra of C-dots, MWCNTs, highly ordered pyrolytic graphite (HOPG), and microdiamond powder [101].

Nanodiamonds, typically derived from milling microdiamonds possess an sp^3 hybridised core and are comprised of 98 % carbon with residual hydrogen, oxygen and nitrogen on their surface, alongside very small quantities of graphitic carbon [102, 103]. Fluorescence emission of nanodiamonds arises from point defects, particularly the negatively charged nitrogen vacancy sites, where they absorb strongly at 569 nm and emit near 700 nm, hence fluoresce red [104-106]. Graphene QDs are typically derived from sheets of layered graphene oxide. This creates a system where finite molecular sp^2 clusters sit in an sp^3 matrix resulting in the confinement of the π electrons in graphene oxide which results in a blue fluorescence emission (typically around 400-450 nm) [99, 107-109]. This has been debated by Pan *et al*. [110], where based on their analysis, emission from free zigzag sites with a carbine like triplet ground state (Ϭ- π) has been proposed as a possible explanation for the fluorescence.

C-dots are believed to be more closely related to graphene QDs. Structurally, C-dots, like graphene QDs, have greater sp^2 character, and contain smaller amounts of carbon with higher oxygen content than nanodiamonds. However, their source of fluorescence emission differs from graphene QDs and nanodiamonds. There is developing evidence that fluorescence emission arises from radiative recombination of excitons (electron/hole pairs) located at surface energy traps – as a result of oxidation or surface passivation. Oxidation of the surface leaves the surface of the C-dots decorated with oxygen containing functional groups such as COOH, C-OH and C=O [111-113]. This will be further discussed in Section 1.7.3. The distinct nanocrystalline structure and oxidative functionalised surface derived in C-dots can be explained through how they were synthesised. There are two general approaches, physically or chemically, to synthesising C-dots. The next section will briefly review the experimental process used to synthesise carbon dots using these two approaches. More attention is drawn toward the wet chemical approach as it is the chosen synthetic route in this research for application in latent fingermark detection.

1.7.1 Physical synthetic routes

Although the physical approach was not used in this work, C-dots were first discovered by accident and warrants recognition. Xu *et al*. [114] discovered C-dots during their purification methods when synthesising single-wall carbon nanotubes (SWCNTs). SWCNTs were synthesised *via* an arc discharge method, then oxidising the soot with HNO_3 (3.3 M), followed by extraction using NaOH, resulting in a black suspension. In order to isolate the SWCNTs, the suspension was separated using gel electrophoresis. During this isolation process C-dots were discovered, as they were found to be fluorescent after UV light excitation (366 nm), emitting green, and yellow and orange respective of their electrophoretic elution times.

Recently, laser ablation has been used to synthesise C-dots. Commonly a Nd:YAG laser is used to ablate a chosen carbon target (e.g., graphite particles) [97, 111-113]. Preparation involves hot-pressing a mixture of graphite powder and cement, followed by baking, curing and annealing under an argon flow prior to laser ablation. To functionalise the surface, laser ablation was followed by thermal oxidation under acidic reflux followed by surface passivation with a polymer (commonly polyethylene glycol (PEG) [112]). Hu *et al*. [115] have also developed one step procedures where PEG, or the chosen passivation material, was introduced during laser irradiation. C-dots have also been synthesised *via* electrochemical routes. This was first demonstrated by Zhou *et al*. [116], who similarly to Xu *et al*. [114], discovered C-dots after purification of MWCNTs. C-dots were exfoliated from the MWCNTs after cycling a potential between -2.0 V and +2.0 V at a scan rate of 0.5 V s^{-1}. The C-dots were then recovered by redissolving the solution in water and running the solutions through dialysis membranes to remove electrolyte salts. Chi *et al*. [117] used a graphite rod working electrode with a Pt mesh counter electrode and Ag/AgCl reference electrode immersed in pH 7.0 phosphate buffer cycled between -3.0 V and +3.0 V to produce C-dots. In both cases, oxidation and production of the C-dots were observed as a change in solution colour from colourless to a dark brown suspension [116].

1.7.2 Wet chemical synthetic routes

The wet chemical approach to producing C-dots is much easier, and hence more popular than the previously discussed methods. This approach was used in this research to synthesise C-dots with an oxidised surface. Chemical approaches often involve a thermal oxidation of a chosen carbon source under strongly acidic conditions, followed by purification or isolation of the C-dots. Mao *et al*. [118] were the first to present this approach. Interestingly, soot was collected by placing a piece of aluminium foil or glass plate on top of a burning candle. The soot was then refluxed under acidic conditions (5 M HNO_3), cooled and isolated *via* centrifugation, dialysis and polyacrylamide gel electrophoresis (PAGE) fractionation. Ray and co-workers [119] followed Mao *et al*.'s [118] research by refluxing collected candle soot under acidic conditions (5 M HNO_3) for 12 h. They found that if the carbon soot was refluxed for less than 12 h, this resulted in a smaller C-dot yield. However, refluxing for longer than 12 h gave no appreciable gain in C-dot yield. The C-dots were purified *via* precipitation using acetone and centrifugation [119].

An additional study involved collecting combustion soot from natural gas. Here, Chen and co-workers [120] placed a glass beaker over a flame, sourced by natural gas, and the soot was collected as the carbon source. C-dots were produced as previous studies (reflux under 5 M HNO_3, followed by isolation by centrifugation, and dialysis.). There have been a number of papers published that followed this same procedure of refluxing a carbon source under acidic conditions [98, 100, 113, 117, 119, 121-134] but unique to each study was the carbon source used, in particular food products such as orange juice [98], bread and sugar [135].

A chemical approach that did not involve HNO_3 has been reported by Bourlinos *et al*. [100, 136] where the thermal decomposition of C-dots was achieved by first protonating the amine group of sodium 11-aminoundecanoate with citric acid, followed by heating the compound in air for 2 h at 300 °C.

C-dots have also been synthesised by growing the nanocarbons onto silica sphere supports. Liu *et al*. [128] used surfactant modified silica spheres, which allowed carbon precursor resols (phenol/formaldehyde resins) to polymerise on the surface. The silica was etched away, and the carbon dots were oxidised and surface passivated with PEG.

All the C-dots described were less than 20 nm in diameter and possessed excitation wavelength (λ_{ex}) dependent broadband fluorescence with wavelength emission (λ_{em}) maxima ranging between 400 nm and 580 nm [98, 100, 113, 117, 119, 121-134]. The next section will explain details in the optical properties of C-dots.

1.7.3 Optical properties of carbon dots

This section aims to explain the origins of fluorescence observed for C-dots, taking into account the nanocrystalline structure and surface functionalities, reviewing both bare C-dots and surface passivated C-dots. To further understand the mechanisms for fluorescence, environmental factors such as pH, presence of a cation, and oxidation/reduction that affect fluorescence will also be addressed.

Typical absorbance spectra of C-dots will often show strong absorbance in the UV region with a tail extending out into the visible range of the spectrum. Figure 1.10 shows a UV-vis absorbance spectrum of C-dots synthesised by the thermal decomposition of 2-(2-aminoethoxy)ethanol citrate salt [136].

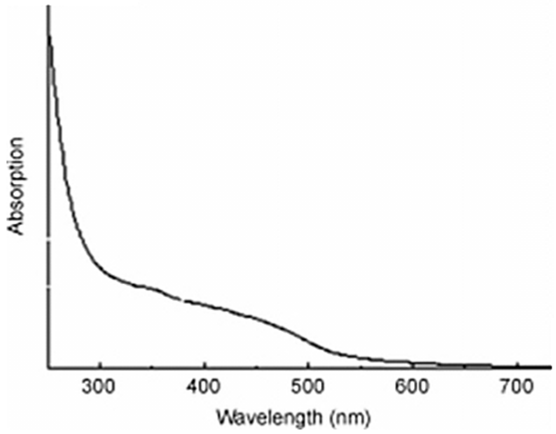

Figure 1.10. A UV spectrum of hydrophilic C-dots made from thermal decomposition of 2-(2-aminoethoxy)ethanol citrate salt. Figure taken from [136].

The strongest absorptions observed at smaller wavelengths (between 250 nm and 350 nm) are often ascribed to the sp^2 hybridised carbons, π-π^* transitions, whereas the weaker absorptions observed at higher wavelengths (between 350 nm and 550 nm) are ascribed to the oxidised surface, n-π^* transitions (e.g., C=O) [111, 129, 136, 137].

A unifying feature of the C-dots fluorescence is an apparent λ_{ex} dependent fluorescence emission wavelength and intensity [111, 116, 118, 129, 136-138]. Figure 1.11 shows an overlayed fluorescence emission spectra of C-dots excited between 290 nm and 390 nm (increasing by 10 nm). As the excitation wavelength is increased from 290 nm to

330 nm the fluorescence intensity increases. The fluorescence intensity decreases, however, as the excitation is further increased to 380 nm [116].

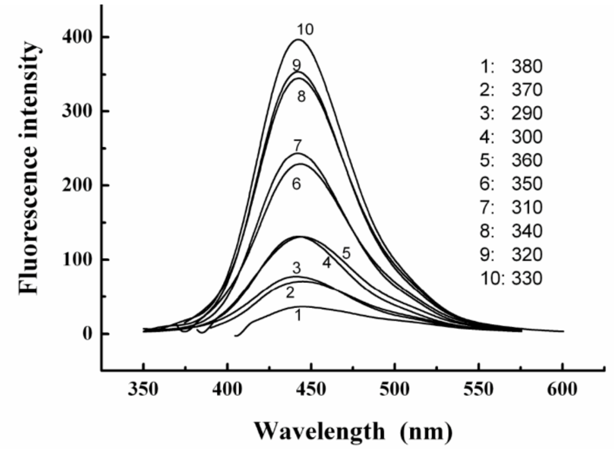

Figure 1.11. Overlayed fluorescence emission spectra of 1.9 nm C-dots at different excitation wavelengths of 290–380 nm. Figure from [116].

This helps supports the hypothesis that the origin of the fluorescence arises from emissive traps on the oxidised or passivated surface of the C-dots. As the λ_{ex} is increased π-π* transitions can no longer occur. Therefore, the n-π* transitions, which are present on the oxidised or passivated surface are the most probable source of fluorescence. This hypothesis has also been challenged by experiments performed by Mao *et al*. [118]. In their work C-dot fractions eluted from PAGE purification were collected and optically analysed to find each fraction containing different sized C-dots that emitted a different colour. Therefore the λ_{ex} dependent fluorescence occurred due to optical selection of differently sized C-dots.

The effect of surface passivation can play an important role in the optical properties of the C-dots, although in some instances is not required. It was found that C-dots synthesised by chemical routes with thermal oxidation under acidic conditions require no further functionalisation for fluorescence to occur [98, 100, 113, 117, 119, 121-

134]. On the other hand, C-dots produced by laser ablation of a carbon source require post-thermal oxidative treatments and/or surface passivation for fluorescence to occur [99, 100].

It was also found that the quantum yield (QY) of C-dots were dependent on what the surface was passivated with (if surface passivation was required for fluorescence to occur). Sun *et al*. [112] were able to achieve high QYs with PEG passivated C-dots when compared to poly(propionylethyleneimine-*co*-ethyleneimine) (PPEI-EI), poly(propionylethyleneimine) (PEI) or poly(acrylic acid) (PAA) surface passivated C-dots. They found that the QY could be tuned by reversibly changing the surface passivation polymer, i.e., PEG can replace PPE-EI on the C-dot surface to increase the QY of the nanocomposites [112]. The QY of C-dots have also been recorded to be as high as 45 % and 50 %, when coated with ZnO or ZnS, respectively [111, 113].

This supports the hypothesis that surface emissive traps, present as either functional group from surface passivation or oxidisation of the C-dot surface, are the origins for fluorescence emission in the visible region after irradiation with UV light.

1.7.3.1 Environmental factors that affect optical properties

Aside from the λ_{ex} and surface passivation, factors such as pH, solvent polarity, temperature and the presence of a cation have been shown to affect or even enhance the fluorescence of C-dots. Many studies have found that the greatest fluorescence intensity was recorded in the acidic pH range, with intensity dramatically decreasing by up to 90 % when the pH was increased. Jia *et al*. [124] hydrothermally synthesised oxidised C-dots using ascorbic acid (AA) and copper acetate. When the pH of the C-dot solution was increased from 4 to 8, upon the addition of NaOH, a linear decrease in fluorescence intensity was observed (λ_{ex} = 365 nm), however no QY was reported. Similar results were reported by Liu *et al*. [128], where they observed a substantial decline in fluorescence intensity by 40-89 % upon reducing the pH from 7 to 14. Zhao *et al*. [138] found that fluorescence intensity decreased when the pH value of the solution was higher or lower than 4.5. Furthermore, they discovered that this was a reversible effect; the fluorescence intensity was recovered by changing the pH back to 4.5.

Contradictory to the decrease in fluorescence intensity when pH is increased (toward basic conditions), there are studies that report that fluorescence can be enhanced upon the addition of bases, such as NaOH and $NaBH_4$, in order to produce C-dots with a reduced surface rather than an oxidised surface. Recently, Lin *et al*. [139] reported a dramatic fluorescence enhancement of oxidised carbon dots through reduction chemistry using $NaBH_4$. C-dots (5 mg) were treated with 1.32 M $NaBH_4$. They reported that the QY of their C-dots could be enhanced by up to 40.5 %. Zheng *et al*. [140] reported a reduction pathway that enhances the fluorescence QY of C-dots from 2 to 24 %. Clearly changing the pH or reduction in functional groups on the surface of the C-dots causes electronic changes to the π-π^* and n-π^* electronic transitions by refilling, or depleting, their valence band [97, 140].

1.7.4 Photo-stability and blinking

Alongside their biocompatibility and low cost, another competing characteristic that C-dots have with respect to conventional inorganic QDs is their photo-stability. This has been validated by various studies where C-dots were excited by UV light over a period of time and the fluorescence intensity was continuously measured. Zhao *et al*. [138] used laser scanning confocal microscopy to show that neither blinking (fluorescence intermittency) nor significant reduction in fluorescence intensity was observed for 6 h of continuous exposure to UV light excitation from a Xe lamp. Another study by Peng *et al*. [130] reported only a 17 % decrease in fluorescence intensity after the C-dots were exposed to 360 nm of light for duration of 19 h.

1.8 Nanoparticle-polymer nanocomposites

It is important to stabilise QDs in a medium with retention of their fluorescent properties. Polymer mediums are often chosen as they are able to sterically hinder QDs from agglomeration, or further growth of QDs *via* Ostwald ripening [141]. In the previous studies discussed, QDs were stabilised in pre-made polymeric mediums such as PAMAM dendrimers [53, 88, 89] and chitosan [92]. This makes the choice of the polymer important as it plays a crucial role in the adherence of the QD-nanocomposite to the latent fingermark deposit. It would be ideal to synthesise a polymer off the surface of a QD in order to control the size of the nanocomposite and the terminal functional groups that determine the adherence mechanisms when it comes to latent fingermark detection [53, 89]. Furthermore, with respect to the toxicity concerns of conventional heavy metal QDs, the presence of a covalent bond between the core nanoparticle and the polymer passivating the surface may prevent leaching. This is of particular concern with Cd based QDs used in this research.

1.8.1 Synthesis of nanoparticle-polymer nanocomposites

In terms of synthesising nanocrystals/nanoparticles with a polymer coating there are two main approaches. The first approach is grafting-to, where the polymer is already synthesised and is attached to the surface of the nanoparticle or encapsulates the nanoparticle. The second approach is the grafting-from approach; here techniques such as surface initiated polymerisation (SIP) are applied. The grafting-from approach, although more complex than grafting-to, allows for a higher density of polymer on the surface of the nanoparticle [142, 143]. This is advantageous for QDs and C-dots in that the nanoparticle will be surface passivated and protected from leaching and also agglomeration, which may diminish their intrinsic optical properties [142-146]. The approach used in this research, involved a recently developed controlled radical polymerisation, called reversible addition fragmentation chain transfer (RAFT) polymerisation with SIP from the CdS QD and C-dot surface. The following sections will briefly describe the RAFT polymerisation process.

1.9 Reversible addition fragmentation chain transfer (RAFT) polymerisation

RAFT polymerisation process is a reversible deactivation radical polymerisation [147-150], and is a controlled radical polymerisation (CRP). With RAFT polymerisation, narrow distributions of molecular weight and polymer chain lengths are achievable and complex architectures such as blocks and stars are possible. Understanding RAFT polymerisation depends highly on the role played by a RAFT chain transfer agent (CTA) [147, 151]. This thesis reports for the first time the use of RAFT polymerisation to graft polymer from the surface of QDs and C-dots for applications in latent fingermark detection.

This section will describe RAFT polymerisation, by first describing the role of a RAFT CTA in conjunction with the mechanism of the RAFT process, polymerisation kinetics, and lastly post-RAFT benefits with CTA-end group removal or functional transformation.

1.9.1 RAFT chain transfer agents (CTAs)

RAFT chain transfer agents (CTAs) are generally thiocarbonylthio (Z-C(=S)S-R) compounds, where the most effective agents are those of: dithioesters, thiocarbonates, xanthates and some aromatic dithiocarbamates [147, 151]. Figure 1.12 illustrates the structural features of a thiocarbonylthio RAFT agent. The effectiveness of a RAFT agent depends on the monomer to be polymerised and also on the R group and Z group. These R and Z groups can be chosen to activate or deactivate the thiocarbonyl (C=S) bond and control the stability of the intermediate radicals [150, 152].

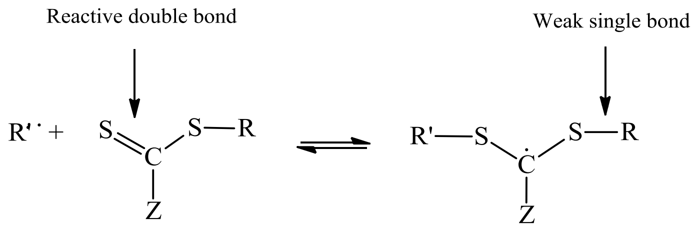

Figure 1.12. Structure of thiocarbonylthio RAFT agent and intermediate form on radical addition (figure adapted from [150]).

During RAFT polymerisation the propagating radical, R'·, will react with the C=S bond of the RAFT agent to form a stable CTA intermediate. The rate of the addition of radicals to the reactive C=S double bond depends highly on the Z group. These rates are higher for Z groups of aryl, or alkyl groups. The R group, labelled where the weak single bond is in Figure 1.12, must be a good leaving group relative to the attacking R'· radical [150]. Therefore, the choice in RAFT agent will be influenced by the monomer to be polymerised [147-150]. The next section will describe in detail the mechanism of the RAFT process.

1.9.2 Mechanism of RAFT polymerisation

The mechanism of RAFT involves an insertion of monomer units into the C-S (R-S weak single bond in Figure 1.12 of a RAFT agent. This mechanism is described step by step in this section where the key feature is a sequence of addition-fragmentation reactions is in equilibrium step IV [150, 152].

I. Initiation occurs as in conventional chain addition or radical polymerisation.

Initiation

$$\text{I (initiator)} + \text{M (monomer)} \longrightarrow P_n^{\cdot}\ \text{(propagating radical)}$$

II. The addition of a propagating radical (P_n•) to the thiocarbonylthio compound (Z-C(=S)S-R) followed by fragmentation of the intermediate radical gives rise to a polymeric thiocarbonyl compound (P_n•) and a new radical (R•).

Chain transfer

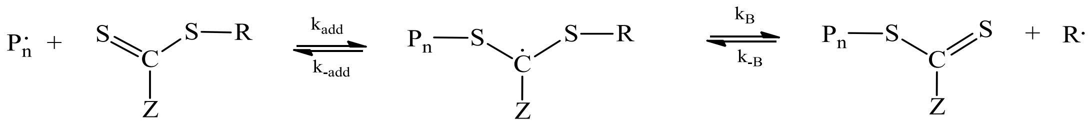

III. The reaction of this radical (R•) with monomers forms a new propagating radical (P_m•).

Reinitiation

$$R^{\cdot} + M \xrightarrow{k_i} R\text{—}M^{\cdot} \xrightarrow{M} \xrightarrow{M} P_m^{\cdot}\ \text{(propagating radical)}$$

IV. Rapid equilibrium between the two propagating radicals (P_m• and P_n•), and the dormant polymeric thiocarbonylthio compound, provides equal probability for all chains to grow, and allows for the production of polymers with narrow polydispersity indices (PDIs).

Chain equilibration

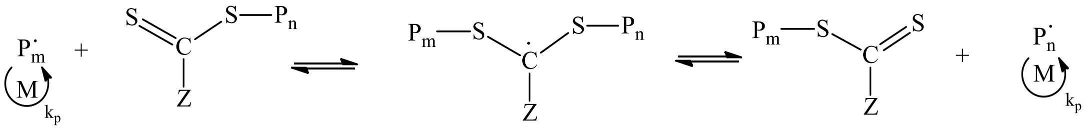

V. Termination occurs as in conventional radical polymerisation through collision of two active sites.

Termination

$$P_n^{\bullet} + P_m^{\bullet} \xrightarrow{k_t} \text{termination}$$

1.9.3 Kinetics of RAFT polymerisation

First order kinetics is often an indication that the polymerisation a living process and can be used as an indicator to the successful occurrence of the RAFT process. Typically, proton nuclear magnetic resonance (^{1}H NMR) spectroscopy and/or gel permeation chromatography (GPC) is used. The RAFT process is monitored, taking into account the decrease in peaks associated with the monomers with respect to the increasing peaks associated with the growing polymer. For example, the C=C-**H** in typical monomers, can be monitored by ^{1}H NMR (chemical shifts between 7 ppm and 5 ppm) as it is consumed to become the polymer back bone (C-C-**H**) (chemical shifts between 2 ppm and 1 ppm).

1.9.4 RAFT end-group removal and functionalisation

RAFT-synthesised polymers retain the chain transfer functionality [153-155]. In some circumstances the removal of the thiocarbonylthio group is desired as they give colour to the polymer synthesised and this may be unwanted. The polymers may also release odour over time due the decomposition of the thiocarbonylthio groups and the evolutions of volatile sulphur containing compounds. Additionally, due to the reactivity of this end-group it may also be desirable to deactivate the polymer to inhibit further reactions [153-156]. The thiocarbonylthio group may also be transformed to achieved a desired functionality such as post-polymerisation processes (construction of block/grafting polymers and other polymeric architectures) [156-158], functional nanoparticles or biopolymer conjugates [159].

There are several processes utilised for end-group removal/functionalisation. These processes include; reaction with nucleophiles or aminolysis [155, 158, 159], thermolysis [160], radical induced elimination [161], and re-initiation of active end-group for post-polymerisation [155]. In most instances where post-functionalisation of the RAFT synthesised polymer is desired, the thiocarbonylthio group is transformed into a thiol group *via* aminolysis. The thiol group can then be subjected to ligand exchange or coupling reactions to a desired functional compound [150, 158, 159, 162-165]. Aminolysis is performed with a straightforward addition of a primary or secondary amine [150, 164]. However, it has been found that the reaction occurs more easily with RAFT-polymers synthesised with dithiocarbonylthio rather than trithiocarbonylthio CTAs. This is due to competing side reactions such as the formation of thiolactones *via* backbiting with certain polymers such as methacrylates and polymeric disulphide compounds *via* interchain disulphide cross-linking which often hinder the synthesis of pristine polymeric thiols in high yields [159, 165]. To avoid these competing reactions, aminolysis can be performed under inert atmospheres and/or in the presence of reducing agents such as phosphites which can break the disulphide links [158, 162, 166]. Recently, Boyer *et al*. [97] reported a versatile one-pot route whereby aminolysis and thiol-ene coupling are achieved simultaneously using dithocarbonylthio and trthiocarbonylthio RAFT-synthesised polymers. RAFT-synthesised polymers of poly-*N*-isopropylacrylamide (p(NIPAAM)) synthesised with trithiocarbonate CTA (3-(benzyl-sulfanylthiocarbonylsulfanyl)-propanoic acid) and poly-*N*-(2-hydroxylpropyl) methacrylamide (p(HPMA)) synthesised with a dithiobenzoate CTA (4-cyanopentaoic acid dithiobenzoate) were both functionalised with methacrylate modified mannose and maleimide-modified biotin, with product yields above 85 %. They reported the thiol-ene coupling click chemistry reaction competed with, and prevented, undesirable disulphide crosslinking side reactions during aminolysis [97].

1.10 Summary

The detection of latent fingermarks at a crime scene, or from forensic evidence, relies on obtaining sufficient visual contrast between the fingermark and the surface that it may be on. Furthermore, the composition of the latent fingermark, taking into account its age and possible contaminants and the surface type (porous, non-porous or semi-porous), play an important role in the choice of fingermark developing reagent. Powder reagents are often the easiest technique used to develop latent fingermarks on non-porous surface whereas chemical reagents are widely used on porous substrates with the requirement of chemically specific adherence mechanisms. Magnetic powders applied with a magnetic wand can be particularly useful, as they eliminate possible obliteration of the fingermark, as it is only the powder that is in contact with the fingermark and not a brush (used with conventional powders). The greatest visual contrast can be obtained *via* fluorescent development of latent fingermarks.

Nanoscience offers the potential use of fluorescent nanocrystals, QDs, which over the past decade has gathered increased interest in forensic applications, including fingermark detection. The toxicity of heavy metal containing QDs, however, limits their use when compared to existing less toxic fluorescent organic dye based fingermarks reagents. Therefore, in the synthesis of QDs it is important that the QDs are secure in their host capping agents to prevent leaching and agglomeration. Grafting polymers from the surface of QDs will ensure that the QDs are secure in the polymer core.

Recent advances in RAFT polymerisation offers experimental control and the ability to graft polymers with similar chain lengths (narrow PDIs). Furthermore it allows for the straightforward post modification of the reactive RAFT CTA end-group which is retained after polymerisation. An alternative to QDs is the use of non-toxic fluorescent carbon nanoparticles, C-dots, which to this day have not been considered in latent fingermark detection. In literature, their QYs appear comparable to their QD competitors. Mechanisms behind their fluorescence come about from their crystalline sp^2 core structure and transitions from their oxidised surface. Much like QDs they require surface protection from agglomeration where polymers can again be utilised.

1.11 References for Chapter 1

1. Saferstein, R., *Criminalistics, an Introduction to Forensic Science*. 8th Edition (International) 2004: Pearson Education.
2. Jiang, X. and Yau, W.-Y. *Fingerprint minutiae matching based on the local and global structures*. in *15th International Conference on Pattern Recognition Proceedings.* . 2000. IEEE.
3. Thomas, G.L., *The physics of fingerprints and their detection.* Journal of Physics. E, Scientific Instruments, 2001. **11** (8): p. 722.
4. Margot, P. and Lennard, C., *Fingerprint Detection Techniques*. Criminalistics 1994: Institut de police scientifique et de criminologie, Université de Lausanne.
5. Champod, C., Lennard, C.J., Margot, P., and Stoilovic, M., *Fingerprints and Other Ridge Skin Impressions*2004: Taylor & Francis.
6. Girod, A., Ramotowski, R., and Weyermann, C., *Composition of fingermark residue: A qualitative and quantitative review.* Forensic Science International, 2012. **223** (1–3): p. 10-24.
7. Knowles, A.M., *Aspects of physicochemical methods for the detection of latent fingerprints.* Journal of physics. E, Scientific instruments, 2001. **11** (8): p. 713.
8. Asano, K.G., Bayne, C.K., Horsman, K.M., and Buchanan, M.V., *Chemical composition of fingerprints for gender determination.* Journal of forensic sciences, 2002. **47** (4): p. 805-807.
9. Benton, M., Chua, M., Gu, F., Rowell, F., and Ma, J., *Environmental nicotine contamination in latent fingermarks from smoker contacts and passive smoking.* Forensic Science International, 2010. **200** (1): p. 28-34.
10. Norman, R.A. and Menendez, R., *Structure and function of aging skin.* Diagnosis of Aging Skin Diseases, 2008: p. 5-10.
11. Spindler, X., Hofstetter, O., McDonagh, A.M., Roux, C., and Lennard, C., *Enhancement of latent fingermarks on non-porous surfaces using anti-l-amino acid antibodies conjugated to gold nanoparticles.* Chemical Communications, 2011. **47** (19).
12. Dilag, J., Kobus, H., and Ellis, A.V., *Cadmium sulfide quantum dot/chitosan nanocomposites for latent fingermark detection.* Forensic Science International, 2009. **187** (1–3): p. 97-102.
13. Sodhi, G.S., *Powder method for detecting latent fingerprints: A review.* Forensic Science International, 2001. **120** (3): p. 172.
14. Almog, J. and Glasner, H., *Ninhydrin thiohemiketals: Basic research towards improved fingermark detection techniques employing nano-technology**.* Journal of Forensic Sciences, 2010. **55** (1): p. 215-220.
15. Ma, R., Bullock, E., Maynard, P., Reedy, B., Shimmon, R., Lennard, C., Roux, C., and McDonagh, A., *Fingermark detection on non-porous and semi-porous surfaces using NaYF: Er, Yb up-converter particles.* Forensic Science International, 2011. **207** (1): p. 145-149.
16. Almog, J. and Glasner, H., *Ninhydrin thiohemiketals: Basic research towards improved fingermark detection techniques employing nano-technology.* Journal of Forensic Sciences, 2010. **55** (1): p. 215-220.
17. Almog, J., Hirshfeld, A., and Klug, J., *Reagents for the chemical development of latent fingerprints: synthesis and properties of some ninhydrin analogues.* Journal of forensic sciences, 1982. **27** (4): p. 912-917.
18. Lennard, C., Margot, P., Stoilovic, M., and Warrener, R., *Synthesis and evaluation of ninhydrin analogues as reagents for the development of latent fingerprints on paper surfaces.* Journal of the Forensic Science Society, 1988. **28** (1): p. 3-23.
19. Odén, S. and Von Hofsten, B., *Detection of fingerprints by the ninhydrin reaction.* Nature, 1954. **173** (4401): p. 449.

20. Yemm, E., Cocking, E., and Ricketts, R., *The determination of amino-acids with ninhydrin.* Analyst, 1955. **80** (948): p. 209-214.
21. Lennard, C., Margot, P., Stoilovic, M., and Warrener, R., *Synthesis of ninhydrin analogues and their application to fingerprint development: preliminary results.* Journal of the Forensic Science Society, 1986. **26** (5): p. 323-328.
22. Hansen, D.B. and Joullié, M.M., *The development of novel ninhydrin analogues.* Chemical Society Reviews, 2005. **34** (5): p. 408-417.
23. Kendall, F.G. and Rehn, B.W., *Rapid method of super glue fuming application for the development of latent fingerprints.* Journal of Forensic Sciences, 1983. **28** (3): p. 777.
24. Molina, O.G., *Fingerprint powder and method of application*, 1979, Rockwell International Corporation.
25. Wade, D., *Development of latent prints with titanium dioxide.* Journal of Forensic Identification, 2002. **52** (5): p. 551-560.
26. James, J.D., Pounds, C.A., and Wilshire, B., *Flake metal powders for revealing latent fingerprints.* Journal of Forensic Sciences, 1991. **36** (5): p. 1368-1375.
27. James, J.D., Pounds, C.A., and Wilshire, B., *Magnetic flake powders for fingerprint development.* Journal of Forensic Sciences, 1993. **38**: p. 391-391.
28. James, J., Pounds, C., and Wilshire, B., *Magnetic flake fingerprint technology.* Journal of Forensic Identification, 1991. **41** (4): p. 237-247.
29. Thonglon, T. and Chaikum, N., *Magnetic fingerprint powder from a mineral indigenous to thailand.* Journal of Forensic Sciences, 2010. **55** (5): p. 1343-1346.
30. Trapecar, M. and Balazic, J., *Fingerprint recovery from human skin surfaces.* Science and Justice, 2007. **47** (3): p. 136-140.
31. Prete, C., Galmiche, L., Quenum-Possy-Berry, F.-G., Allain, C., Thiburce, N., and Colard, T., *Lumicyano™: A new fluorescent cyanoacrylate for a one-step luminescent latent fingermark development.* Forensic Science International, 2013. **233** (1): p. 104-112.
32. Weaver, D.E. and Clary, E.J., *A one-step fluorescent cyanoacrylate fingerprint development technology.* Journal of Forensic Identification, 1993. **43** (5): p. 481.
33. Flynn, J., Stoilovic, M., and Lennard, C., *Detection and enhancement of latent fingerprints on polymer banknotes: A preliminary study.* Journal of Forensic Identification, 1999. **49**: p. 594-612.
34. Jones, N., Stoilovic, M., Lennard, C., and Roux, C., *Vacuum metal deposition: factors affecting normal and reverse development of latent fingerprints on polyethylene substrates.* Forensic Science International, 2001. **115** (1-2): p. 73.
35. Bramble, S., Creer, K., Gui Qiang, W., and Sheard, B., *Ultraviolet luminescence from latent fingerprints.* Forensic Science International, 1993. **59** (1): p. 3-14.
36. Menzel, E.R., *Fingerprint detection with lasers*1999: M. Dekker New York.
37. Dalrymple, B., Duff, J., and Menzel, E. *Inherent fingerprint luminescence-detection by laser*. in *1977 SPIE/SPSE Technical Symposium East*. 1977. International Society for Optics and Photonics.
38. Menzel, E.R., *Pretreatment of latent prints for laser development.* Forensic Science Review, 1989. **1** (1): p. 43-66.
39. Stoilovic, M., *Detection of semen and blood stains using Polilight as a light source.* Forensic Science International, 1991. **51** (2): p. 289-296.
40. Bramble, S.K., Creer, K.E., Gui Qiang, W., and Sheard, B., *Ultraviolet luminescence from latent fingerprints.* Forensic Science International, 1993. **59** (1): p. 3-14.
41. Masters, N.E., *Rhodamine 6G: taming the beast.* Journal of Forensic Identification, 1990. **40** (5): p. 265-270.
42. Jelly, R., Patton, E.L., Lennard, C., and Lewis, S.W., *The detection of latent fingermarks on porous surfaces using amino acid sensitive reagents: A review.* Analytical Chimica Acta, 2009. **652** (1): p. 128-142.

43. Stoilovic, M., Lennard, C., Wallace-Kunkel, C., and Roux, C., *Evaluation of a 1, 2-indanedione formulation containing zinc chloride for improved fingermark detection on paper.* Journal of Forensic Identification, 2007. **57** (1): p. 4.
44. Vandenberg, N. and Oorschot, R.A., *The use of Polilight® in the detection of seminal fluid, saliva, and bloodstains and comparison with conventional chemical-based screening ttests.* Journal of Forensic Sciences, 2006. **51** (2): p. 361-370.
45. Takatsu, M., Shimoda, O., Onishi, K., Onishi, A., and Oguri, N., *Detection of pretreated fingerprint fluorescence using an LED-based excitation system.* Journal of Forensic Sciences, 2008. **53** (4): p. 823-827.
46. Lee, W. and Khoo, B., *Forensic light sources for detection of biological evidences in crime scene investigation: a review.* Malaysian Journal of Forensic Science, 2010. **1**: p. 17-28.
47. Moe, A.E., Marx, S., Banani, N., Liu, M., Marquardt, B., and Wilson, D.M., *Improvements in LED-based fluorescence analysis systems.* Sensors and Actuators B: Chemical, 2005. **111**: p. 230-241.
48. Dilag, J., Kobus, H., and Ellis, A.V., *Nanotechnology as a new tool for fingermark detection: A review.* Current Nanoscience, 2011. **7** (2): p. 153-159.
49. Menzel, E.R., Savoy, S.M., Ulvick, S.J., Cheng, K.H., Murdock, R.H., and Sudduth, M.R., *Photoluminescent semiconductor nanocrystals for fingerprint detection.* Journal of Forensic Sciences, 2000. **45** (3): p. 545.
50. Algarra, M., Jiménez-Jiménez, J., Miranda, M.S., Campos, B.B., Moreno-Tost, R., Rodriguez-Castellón, E., and Esteves da Silva, J.C.G., *Solid luminescent CdSe-thiolated porous phosphate heterostructures. Application in fingermark detection in different surfaces.* Surface and Interface Analysis, 2012. **45** (2): p. 612-618.
51. Algarra, M., Jiménez-Jiménez, J., Moreno-Tost, R., Campos, B.B., and Esteves da Silva, J.C.G., *CdS nanocomposites assembled in porous phosphate heterostructures for fingerprint detection.* Optical Materials, 2011. **33** (6): p. 893-898.
52. Becue, A., Moret, S., Champod, C., and Margot, P., *Use of quantum dots in aqueous solution to detect blood fingermarks on non-porous surfaces.* Forensic Science International, 2009. **191** (1–3): p. 36-41.
53. Bouldin, K.K., Menzel, E.R., Takatsu, M., and Murdock, R.H., *Diimide-enhanced fingerprint detection with photoluminescent CdS/dendrimer nanocomposites.* Journal of Forensic Sciences, 2000. **45** (6): p. 1239-1242.
54. Cheng, K.H. and Fiori, *Exploration of functionalized CdTe nanoparticles for latent fingerprint detection.* Journal of Nanoscience and Nanotechnology, 2008. **8** (4): p. 1989.
55. Feng, G., Jiaxing, H., Jun, Z., Qun, L., Xiufeng, S., Jincheng, Z., Liru, B., Xin, L., and Zhiliang, L., *The synthesis of newly modified CdTe quantum dots and their application for improvement of latent fingerprint detection.* Nanotechnology, 2011. **22** (7).
56. Jin, Y., Luo, Y., Li, G., Li, J., Wang, Y., Yang, R., and Lu, W., *Application of photoluminescent CdS/PAMAM nanocomposites in fingerprint detection.* Forensic Science International, 2008. **179** (1): p. 34-38.
57. Menzel, E.R., Takatsu, M., Murdock, R.H., Bouldin, K., and Cheng, K.H., *Photoluminescent CdS/dendrimer nanocomposites for fingerprint detection.* Journal of Forensic Sciences, 2000. **45** (4): p. 770-773.
58. Wang, Y.F., Yang, R.Q., Wang, Y.J., Shi, Z.X., and Liu, J.J., *Application of CdSe nanoparticle suspension for developing latent fingermarks on the sticky side of adhesives.* Forensic Science International, 2009. **185** (1–3): p. 96-99.
59. Alivisatos, A.P., *Semiconductor clusters, nanocrystals, and quantum dots.* Science, 1996. **271** (5251): p. 933-937.
60. Green, M., *Semiconductor quantum dots as biological imaging agents.* Angewandte Chemie International Edition, 2004. **43** (32): p. 4129.

61. Marin, J.L., Riera, R., and Cruz, S.A., *Confinement of excitons in spherical quantum dots.* Journal of Physics: Condensed matter, 1999. **10** (6): p. 1349.
62. Takagahara, T. and Takeda, K., *Theory of the quantum confinement effect on excitons in quantum dots of indirect-gap materials.* Physical Review. B, Condensed matter, 1992. **46** (23): p. 15578.
63. Wang, Y. and Herron, N., *Nanometer-sized semiconductor clusters: materials synthesis, quantum size effects, and photophysical properties.* The Journal of Physical Chemistry, 1991. **95** (2): p. 525-532.
64. Zeng, Z., Wang, S., and Yang, S., *Synthesis and characterization of PbS nanocrystallites in random copolymer ionomers.* Chemistry of Materials, 1999. **11** (11): p. 3365-3369.
65. Gao, X., Cui, Y., Levenson, R.M., Chung, L.W.K., and Xiaohu Gao1, Y.C., Richard M Levenson3, Leland W K Chung2 & Shuming Nie1, *In vivo cancer targeting and imaging with semiconductor quantum dots.* Nature Biotechnology, 2004. **22** (8): p. 969.
66. Gao, X., Yang, L., Petros, J.A., Marshall, F.F., Simons, J.W., and Nie, S., *In vivo molecular and cellular imaging with quantum dots.* Current Opinion in Biotechnology, 2005. **16** (1): p. 63-72.
67. Kwon, W. and Rhee, S.-W., *Facile synthesis of graphitic carbon quantum dots with size tunability and uniformity using reverse micelles.* Chemical Communications, 2012. **48**: p. 5256-5258.
68. Resch-Genger, U., Grabolle, M., Cavaliere-Jaricot, S., Nitschke, R., and Nann, T., *Quantum dots versus organic dyes as fluorescent labels.* Nature Methods, 2008. **5** (9): p. 763-775.
69. Resch-Genger, U., *Quantum dots versus organic dyes as fluorescent labels.* Nature Methods, 2008. **5** (9): p. 763.
70. Dabbousi, B.O., *Electroluminescence from CdSe quantum dot/polymer composites.* Applied Physics Letters, 1995. **66** (11): p. 1316.
71. Knowles, K.E., Tice, D.B., McArthur, E.A., Solomon, G.C., and Weiss, E.A., *Chemical control of the photoluminescence of CdSe quantum dot−organic complexes with a series of para-substituted aniline ligands.* Journal of the American Chemical Society, 2009. **132** (3): p. 1041-1050.
72. Wang, Y.F., Yang, R.Q., Shi, Z.X., Liu, J.J., Zhao, K., and Wang, Y.J., *The effectiveness of CdSe nanoparticle suspension for developing latent fingermarks.* Journal of Saudi Chemical Society, 2011 (In press).
73. Mahamuni, S., *Thiophenol-capped ZnS quantum dots.* Journal of Applied Physics, 1993. **73** (10): p. 5237.
74. Weller, H., *Colloidal semiconductor Q-particles: chemistry in the transition region between solid state and molecules.* Angewandte Chemie International Edition, 1993. **32** (1): p. 41.
75. Nedelijkovic, J., Patel, R., Kaufman, P., Joyce-Pruden, C., and O'Leary, N., *Synthesis and optical properties of quantum-sized metal sulfide particles in aqueous solution.* Journal of Chemical Education, 1993. **70** (4): p. 342.
76. Wang, Y., Suna, A., Mahler, W., and Kasowski, R., *PbS in polymers. From molecules to bulk solids.* The Journal of Chemical Physics, 1987. **87**: p. 7315.
77. Nedeljkovic, J.M., Patel, R. C., Kaufman, P., Joyce-Pruden, C., and O'Leary, N., *Synthesis and optical properties of quantum-sized metal sulfide particles in aqueous solution.* Chemical Education, 1993. **70** (4): p. 342-345.
78. Singh, V., Singh, R., Thompson, G., Jayaraman, V., Sanagapalli, S., and Rangari, V., *Characteristics of nanocrystalline CdS films fabricated by sonochemical, microwave and solution growth methods for solar cell applications.* Solar Energy Materials and Solar Cells, 2004. **81** (3): p. 293-303.
79. Gorer, S., Albu-Yaron, A., and Hodes, G., *Quantum size effects in chemically deposited, nanocrystalline lead selenide films.* The Journal of Physical Chemistry, 1995. **99** (44): p. 16442-16448.

80. Murray, C., Norris, D.J., and Bawendi, M.G., *Synthesis and characterization of nearly monodisperse CdE (E = S, Se, Te) semiconductor nanocrystallites.* Journal of American Chemical Society, 1993. **115** (19): p. 8706-8715.
81. Vossmeyer, T., Katsikas, L., Giersig, M., Popivic, I.G., Diesner, K., Chemseddine, A., Eychmuller, A., and Weller, H., *CdS nanoclusters - synthesis, characterization, size-dependent oscillator strength, temperature shift of the excitonic-transition energy, and reversible absorbance shift.* Physical Chemistry, 1994. **98** (31): p. 7665-7673.
82. Wang, Y., Suna, A., Mahler, W., and Kasowski, R., *PbS in polymers. From molecules to bulk solids.* Journal of Chemical Physics, 1987. **87** (12): p. 7315-7322.
83. Frantsuzov, P.A. and Marcus, R., *Explanation of quantum dot blinking without long-lived trap hypothesis.* arXiv preprint cond-mat/0505604, 2005.
84. Jorge, P., Martins, M.A., Trindade, T., Santos, J.L., and Farahi, F., *Optical fiber sensing using quantum dots.* Sensors, 2007. **7**: p. 3489-3534.
85. Cao, X., Li, C.M., Bao, H., Bao, Q., and Dong, H., *Fabrication of Strongly Fluorescent Quantum Dot−Polymer Composite in Aqueous Solution.* Chemistry of Materials, 2007. **19** (15): p. 3773-3779.
86. Kairdolf, B.A., Smith, A.M., and Nie, S., *One-pot synthesis, encapsulation, and solubilization of size-tuned quantum dots with amphiphilic multidentate ligands.* Journal of the American Chemical Society, 2008. **130** (39): p. 12866.
87. Kortan, A., Hull, R., Opilar, L., Bawendi, M. G., Steigerwald, M. L., Carroll, P. J., and Brus, L. E., *Nucleation and growth of CdSe on ZnS quantum crystallite seeds, and vice versa, in inverse micelle media.* Journal of American Chemical Society, 1990. **112** (4): p. 1327-1332.
88. Menzel, E.R., Savoy, S. M., Ulvick, S.J., Cheng, K. H., Murdock, R. H., and Suduth, M. R, *Photoluminescent semiconductor nanocrystals for fingerprint detection.* Journal of Forensic Sciences, 2000. **45** (3): p. 545-551.
89. Jin, Y., Luo, Y., Li, G., Li, J., Wang, Y., Yang, R., and Lu, W., *Application of photoluminescent CdS/PAMAM nanocomposites in fingerprint detection.* Forensic Science International, 2008. **179** (1): p. 34-38.
90. Cheng, K.H., Ajimo, J., and Chen, W., *Exploration of functionalized CdTe nanoparticles for latent fingerprint detection.* Nanoscience and Nanotechnology, 2008. **8** (3): p. 1170-1173.
91. Sametband, M., Shweky, I., Banin, U., Mandler, D., and Almog, J. , *Application of nanoparticles for the enhancement of latent fingerprints.* Chemical Communications, 2007 (11): p. 1142 -1144
92. Dilag, J., Kobus, H., and Ellis, A.V., *Cadmium sulfide quantum dot/chitosan nanocomposites for latent fingermark detection.* Forensic Science International, 2009. **187** (1-3): p. 97-102.
93. Derfus, A.M., Chan, W.C., and Bhatia, S.N., *Probing the cytotoxicity of semiconductor quantum dots.* Nano Letters, 2004. **4** (1): p. 11-18.
94. Hardman, R., *A Toxicologic Review of Quantum Dots: Toxicity Depends on Physicochemical and Environmental Factors.* Environ Health Perspect, 2006. **114** (2).
95. Jiang, J., Oberdörster, G., and Biswas, P., *Characterization of size, surface charge, and agglomeration state of nanoparticle dispersions for toxicological studies.* Journal of Nanoparticle Research, 2009. **11** (1): p. 77-89.
96. Hillyer, J.F. and Albrecht, R.M., *Gastrointestinal persorption and tissue distribution of differently sized colloidal gold nanoparticles.* Journal of Pharmaceutical Sciences, 2001. **90** (12): p. 1927-1936.
97. Cao, L., Wang, X., Meziani, M.J., Wang, H., Luo, P.G., Lin, Y., Harruf, B.A., Veca, M., Murray, D., Xie, S.Y., and Sun, Y.P., *Carbon dots for multiphoton bioimaging.* Journal of the American Chemical Society, 2007. **129** (37): p. 11318.

98. Sahu S., Behera, B., Maitib, T.K., and Mohapatra, S., *Simple one-step synthesis of highly luminescent carbon dots from orange juice: Application as excellent bio-imaging agents.* Chemical Communications, 2012.
99. Baker, S.N. and Baker, G.A., *Luminescent Carbon Nanodots: Emergent Nanolights.* Angewandte chemie international edition, 2010. **49** (38): p. 6726-6744.
100. Bourlinos, A.B., Stassinopoulos, A., Anglos, D., Zboril, R., Georgakilas, V., and Giannelis, E.P., *Photoluminescent carbogenic dots.* Chemistry of Materials, 2008. **20** (14): p. 4539-4541.
101. Zhou, J., Booker, C., Li, R., Sun, X., Sham, T.-K., and Ding, Z., *Electrochemistry and electrochemiluminescence study of blue luminescent carbon nanocrystals.* Chemical Physics Letters, 2010. **493** (4): p. 296-298.
102. Yu, S.-J., Kang, M.-W., Chang, H.-C., Chen, K.-M., and Yu, Y.-C., *Bright fluorescent nanodiamonds: no photobleaching and low cytotoxicity.* Journal of the American Chemical Society, 2005. **127** (50): p. 17604-17605.
103. Mohan, N., Tzeng, Y.K., Yang, L., Chen, Y.Y., Hui, Y.Y., Fang, C.Y., and Chang, H.C., *Sub-20-nm fluorescent nanodiamonds as photostable biolabels and fluorescence resonance energy transfer donors.* Advanced Materials, 2010. **22** (7): p. 843-847.
104. Chang, H.-C., Chen, K., and Kwok, S., *Nanodiamond as a possible carrier of extended red emission.* The Astrophysical Journal Letters, 2008. **639** (2): p. L63.
105. Liu, J.-H., Yang, S.-T., Chen, X.-X., and Wang, H., *Fluorescent carbon dots and nanodiamonds for biological Imaging: Preparation, application, pharmacokinetics and toxicity.* Current Drug Metabolism, 2012. **13** (8): p. 1046-1056.
106. Mochalin, V.N. and Gogotsi, Y., *Wet chemistry route to hydrophobic blue fluorescent nanodiamond.* Journal of the American Chemical Society, 2009. **131** (13): p. 4594-4595.
107. Jiaojiao, W., Miao, F., and Hongbing, Z., *Advances in preparation of graphene quantum dots.* Progress in Chemistry, 2013. **25** (01): p. 86-94.
108. Markovic, Z.M., Ristic, B.Z., Arsikin, K.M., Klisic, D.G., Harhaji-Trajkovic, L.M., Todorovic-Markovic, B.M., Kepic, D.P., Kravic-Stevovic, T.K., Jovanovic, S.P., and Milenkovic, M.M., *Graphene quantum dots as autophagy-inducing photodynamic agents.* Biomaterials, 2012 (29): p. 7084-92.
109. Shinde, D.B. and Pillai, V.K., *Electrochemical preparation of luminescent graphene quantum qots from multiwalled carbon nanotubes.* European Journal of Chemistry A, 2012. **18** (39): p. 12522-12528.
110. Pan, D., Zhang, J., Li, Z., and Wu, M., *Hydrothermal route for cutting graphene sheets into blue luminescent graphene quantum dots.* Advanced Materials, 2009. **22** (6): p. 734-738.
111. Sun, Y.P., Wang, X., Lu, F., Cao, L., Meziani, M.J., Luo, P.G., Gu, L., and Veca, L.M., *Doped carbon nanoparticles as a new platform for highly photoluminescent dots.* The Journal of Physical Chemistry C, 2008. **112** (47): p. 18295-18298.
112. Sun, Y.P., Zhou B., Lin Y., Wang W., Fernando K.A., Pathak P., Meziani M. J., Harruff B. A., Wang X., Wang H., Luo P.G., Yang H., Kose M. E., Chen B., Veca L. M., and Y., X.S., *Quantum-sized carbon dots for bright and colorful photoluminescence.* Journal of the American Chemical Society, 2006. **128** (24): p. 7756.
113. Sun, Y.-P., Luo, P.G., Sahu, S., Yang, S.-T., Sonkar, S.K., Wang, J., Wang, H., LeCroy, G.E., and Cao, L., *Carbon quantum dots for optical bioimaging.* Journal of Material Chemistry B, 2013 (1): p. 2116-2127.
114. Xu, X., Ray, R., Gu, Y., Ploehn, H.J., Gearheart, L., Raker, K., and Scrivens, W.A., *Electrophoretic analysis and purification of fluorescent single-walled carbon nanotube fragments.* Journal of the American Chemical Society, 2004. **126** (40): p. 12736-12737.

115. Hu, S.-L., Niu, K.-Y., Sun, J., Yang, J., Zhao, N.-Q., and Du, X.-W., *One-step synthesis of fluorescent carbon nanoparticles by laser irradiation.* Journal of Materials Chemistry, 2009. **19** (4): p. 484-488.
116. Zhao, Q.-L., Zhang, Z.-L., Huang, B.-H., Peng, J., Zhang, M., and Pang, D.-W., *Facile preparation of low cytotoxicity fluorescent carbon nanocrystals by electrooxidation of graphite.* Chemical Communications, 2008. **0** (41): p. 5116-5118.
117. Zheng, L., Chi, Y., Dong, Y., Lin, J., and Wang, B., *Electrochemiluminescence of water-soluble carbon nanocrystals released electrochemically from graphite.* Journal of the American Chemical Society, 2009. **131** (13): p. 4564-4565.
118. Mao, X.-J., Zheng, H.-Z., Long, Y.-J., Du, J., Hao, J.-Y., Wang, L.-L., and Zhou, D.-B., *Study on the fluorescence characteristics of carbon dots.* Spectrochimica Acta Part A: Molecular and Biomolecular Spectroscopy, 2010. **75** (2): p. 553-557.
119. Ray, S.C., Saha, A., Jana, N.R., and Sarkar, R., *Fluorescent carbon nanoparticle: Synthesis, characterization and bio-imaging application.* arXiv preprint arXiv:0909.4622, 2009.
120. Tian, L., Ghosh, D., Chen, W., Pradhan, S., Chang, X., and Chen, S., *Nanosized carbon particles from natural gas soot.* Chemistry of Materials, 2009. **21** (13): p. 2803-2809.
121. Allam, A. and Sarkar, S., *Water soluble fluorescent quantum carbon dots*, 2010, Afreen Allam, Sabyasachi Sarkar: USA.
122. Anilkumar, P., Wang, X., Cao, L., Sahu, S., Liu, J.-H., Wang, P., Korch, K., Tackett II, K.N., Parenzan, A., and Sun, Y.-P., *Toward quantitatively fluorescent carbon-based "quantum" dots.* Nanoscale, 2011. **3** (5): p. 2023-2027.
123. Callan, J.F., Fowley, C.P., McCaughan, B., and Devlin, A., *Highly luminescent biocompatible carbon quantum dots by encapsulation with an amphiphilic polymer.* Chemical Communications, 2012 (48): p. 9361-9363.
124. Guo, Y., Wang, Z., Shao, H., and Jiang, X., *Hydrothermal synthesis of highly fluorescent carbon nanoparticles from sodium citrate and their use for the detection of mercury ions.* Carbon, 2012 (52): p. 583–589.
125. Khanam, A., Tripathi, S., Roy, D., and Nasim, M., *A facile and novel synthetic method for the preparation of hydroxyl capped fluorescent carbon nanoparticles.* Colloids and Surfaces B: Biointerfaces, 2012.
126. Qiao, Z.-A., Wang, Y., Gao, Y., Li, H., Dai, T., Liu, Y., and Huo, Q., *Commercially activated carbon as the source for producing multicolor photoluminescent carbon dots by chemical oxidation.* Chemical Communications, 2010. **46** (46): p. 8812-8814.
127. Liu, H., Ye, T., and Mao, C., *Fluorescent carbon nanoparticles derived from candle soot.* Angewandte Chemie International Edition, 2007. **46** (34): p. 6473-6475.
128. Liu, R., Wu, D., Liu, S., Koynov, K., Knoll, W., and Li, Q., *An aqueous route to multicolor photoluminescent carbon dots using silica spheres as carriers.* Angewandte Chemie International Edition, 2009. **121** (25): p. 4668-4671.
129. Lu, W., Qin, X., Liu, S., Chang, G., Zhang, Y., Luo, Y., Asiri, A.M., Al-Youbi, A.O., and Sun, X., *Economical, green synthesis of fluorescent carbon nanoparticles and their use as probes for sensitive and selective detection of mercury (II) ions.* Analytical Chemistry, 2012. **84** (12): p. 5351-5357.
130. Peng, H. and Travas-Sejdic, J., *Simple aqueous solution route to luminescent carbogenic dots from carbohydrates.* Chemistry of Materials, 2009. **21** (23): p. 5563-5565.
131. Wang, J., Wang, C.F., and Chen, S., *Amphiphilic egg-derived carbon dots: rapid plasma fabrication, pyrolysis process, and multicolor printing patterns.* Angewandte Chemie International Edition, 2012. **124** (37): p. 9431-9435.

132. Wang, Q., Zheng, H., Long, Y., Zhang, L., Gao, M., and Bai, W., *Microwave–hydrothermal synthesis of fluorescent carbon dots from graphite oxide.* Carbon, 2011. **49** (9): p. 3134-3140.
133. Yang, Y., Cui, J., Zheng, M., Hu, C., Tan, S., Xiao, Y., Yang, Q., and Liu, Y., *One-step synthesis of amino-functionalized fluorescent carbon nanoparticles by hydrothermal carbonization of chitosan.* Chemical Communications, 2012. **48** (3): p. 380-382.
134. Zhao, L.-X., Di, F., Wang, D., Guo, L.-H., Yang, Y., Wan, B., and Zhang, H., *Chemiluminescence of carbon dots under strong alkaline solutions: A novel insight into carbon dots optical properties.* Nanoscale, 2013.
135. Palashuddin, S.K., Amit, J., Anumita, P., Ghosh, S.S., and Chattopadhyay, A., *Presence of amorphous carbon nanoparticles in food caramels.* Nature Scientific Reports, 2012. **2**.
136. Bourlinos, A.B., Stassinopoulos, A., Anglos, D., Zboril, R., Karakassides, M., and Giannelis, E.P., *Surface functionalized carbogenic quantum dots.* Small, 2008. **4** (4): p. 455-458.
137. Zhao, Q.-L., Zhang, Z.-L., Huang, B.-H., Peng, J., Zhang, M., and Pang, D.-W., *Facile preparation of low cytotoxicity fluorescent carbon nanocrystals by electrooxidation of graphite.* Chemical Communications, 2008 (41): p. 5116-5118.
138. Zhou, L., Lin, Y., Huang, Z., Ren, J., and Qu, X., *Carbon nanodots as fluorescence probes for rapid, sensitive, and label-free detection of mercury 2+ and biothiols in complex matrices.* Chemical Communications, 2012. **48** (8): p. 1147-1149.
139. Lin, C.A.J., Yang, T.Y., Lee, C.H., Huang, S.H., Sperling, R.A., Zanella, M., Li, J.K., Shen, J.L., Wang, H.H., Yeh, H.I., Parak, W.J., and Chang, W.H., *Synthesis, characterization, and bioconjugation of fluorescent gold nanoclusters toward biological labeling applications.* American Chemical Society Nano, 2009. **3** (2): p. 395-401.
140. Zheng, H., Wang, Q., Long, Y., Zhang, H., Huang, X., and Zhu, R., *Enhancing the luminescence of carbon dots with a reduction pathway.* Chemical Communications, 2011. **47** (38): p. 10650-10652.
141. Tomczak, N., Janczewski, D., Han, M., and Vancso, G.J., *Designer polymer - quantum dot architectures.* Progress in Polymer Sciences, 2009. **34**: p. 393-430.
142. Esteves, A.C.C., Bombalski, L., Trindade, T., Matyjaszewski, K., and Barros-Timmons, A., *Polymer grafting from CdS quantum dots via AGET ATRP in miniemulsion.* Small, 2007. **3** (7): p. 1230-1236.
143. Fogg, D.E., Radzilowski, L.H., Dabbousi, B.O., Schrock, R.R., Thomas, E.L., and Bawendi, M.G., *Fabrication of quantum dot-polymer composites: Semiconductor nanoclusters in dual-function polymer matrices with electron-transporting and cluster-passivating properties.* Macromolecules, 1997. **30** (26): p. 8433-8439.
144. Farmer, S.C. and Patten, T.E., *Photoluminescent polymer/quantum dot composite nanoparticles.* Chemistry of Materials, 2001. **13** (11): p. 3920-3926.
145. Lee, J., Sundar, V.C., Heine, J.R., Bawendi, M.G., and Jensen, K.F., *Full color emission from II–VI semiconductor quantum dot–polymer composites.* Advanced Materials, 2000. **12** (15): p. 1102-1105.
146. Sanchez, C., Julian, B., Belleville, P., and Popall, M., *Applications of hybrid organic-inorganic nanocomposites.* Journal of Materials Chemistry, 2005. **15** (35-36).
147. Moad, G., *The emergence of RAFT polymerization.* Australian Journal of Chemistry, 2006. **59** (10): p. 661-662.
148. Chiefari, J., Chong, Y.K., Ercole, F., Krstina, J., Jeffery, J., Le, T.P.T., Mayadunne, R.T.A., Meijs, G.F., Moad, C.L., Moad, G., Rizzardo, E., and Thang, S.H., *Living free-radical polymerization by reversible addition−fragmentation chain transfer: The RAFT process.* Macromolecules, 1998. **31** (16): p. 5559-5562.

149. Moad, G., Chiefari, J., Chong, Y.K., Krstina, J., Mayadunne, R.T.A., Postma, A., Rizzardo, E., and Thang, S.H., *Living free radical polymerization with reversible addition – fragmentation chain transfer (the life of RAFT).* Polymer International, 2000. **49** (9): p. 993-1001.
150. Moad, G., Chong, Y.K., Postma, A., Rizzardo, E., and Thang, S.H., *Advances in RAFT polymerization: the synthesis of polymers with defined end-groups.* Polymer, 2005. **46** (19): p. 8458-8468.
151. Chiefari, J., Chong, Y.K., Ercole, F., Krstina, J., Jeffery, J., Le, T.P.T., Mayadunne, R.T.A., Meijs, G.F., Moad, C.L., Moad, G., Rizzardo, E., and Thang, S.H., *Living free-radical polymerization by reversible addition-fragmentation chain transfer: The RAFT process.* Macromolecules, 1998. **31** (16): p. 5559-5562.
152. Moad, G., Chong, Y.K., Postma, A., Rizzardo, E., and Thang, S.H., *Advances in RAFT Polymerization: the synthesis of polymers with defined end-groups.* Polymer 2005. **46** (19): p. 8458-8468.
153. Moad, G., Chong, Y., Postma, A., Rizzardo, E., and Thang, S.H., *Advances in RAFT polymerization: the synthesis of polymers with defined end-groups.* Polymer, 2005. **46** (19): p. 8458-8468.
154. Moad, G., Rizzardo, E., and Thang, S.H., *End-functional polymers, thiocarbonylthio group removal/transformation and reversible addition–fragmentation–chain transfer (RAFT) polymerization.* Polymer International, 2011. **60** (1): p. 9-25.
155. Willcock, H. and O'Reilly, R.K., *End group removal and modification of RAFT polymers.* Polymer Chemistry, 2010. **1** (2): p. 149-157.
156. Perrier, S., Takolpuckdee, P., and Mars, C.A., *Reversible addition−fragmentation chain transfer polymerization: End group modification for functionalized polymers and chain transfer dgent recovery.* Macromolecules, 2005. **38** (6): p. 2033-2036.
157. Li, M., De, P., Gondi, S.R., and Sumerlin, B.S., *End group transformations of RAFT-generated polymers with bismaleimides: Functional telechelics and modular block copolymers.* Journal of Polymer Science Part A: Polymer Chemistry, 2008. **46** (15): p. 5093-5100.
158. Qiu, X.-P. and Winnik, F.M., *Facile and efficient one-pot transformation of RAFT polymer end groups via a mild aminolysis/michael addition sequence.* Macromolecular Rapid Communications, 2006. **27** (19): p. 1648-1653.
159. Boyer, C., Granville, A., Davis, T.P., and Bulmus, V., *Modification of RAFT-polymers via thiol-ene reactions: A general route to functional polymers and new architectures.* Journal of Polymer Science Part A: Polymer Chemistry, 2009. **47** (15): p. 3773-3794.
160. Postma, A., Davis, T.P., Moad, G., and O'Shea, M.S., *Thermolysis of RAFT-synthesized polymers. A convenient method for trithiocarbonate group elimination.* Macromolecules, 2005. **38** (13): p. 5371-5374.
161. Chong, Y.K., Moad, G., Rizzardo, E., and Thang, S.H., *Thiocarbonylthio end group removal from RAFT-synthesized polymers by radical-induced reduction.* Macromolecules, 2007. **40** (13): p. 4446-4455.
162. Roth, P.J., Kessler, D., Zentel, R., and Theato, P., *A method for obtaining defined end groups of polymethacrylates prepared by the RAFT process during aminolysis.* Macromolecules, 2008. **41** (22): p. 8316-8319.
163. Shen, W., Qiu, Q., Wang, Y., Miao, M., Li, B., Zhang, T., Cao, A., and An, Z., *Hydrazine as a nucleophile and antioxidant for fast aminolysis of RAFT polymers in air.* Macromolecular Rapid Communications, 2010. **31** (16): p. 1444-1448.
164. Xu, J., He, J., Fan, D., Wang, X., and Yang, Y., *Aminolysis of polymers with thiocarbonylthio termini prepared by RAFT polymerization: The difference between polystyrene and polymethacrylates.* Macromolecules, 2006. **39** (25): p. 8616-8624.

165. Boyer, C., Liu, J., Bulmus, V., and Davis, T.P., *RAFT polymer end-group modification and chain coupling/conjugation via disulfide bonds.* Australian Journal of Chemistry, 2009. **62** (8): p. 830-847.
166. Levere, M.E., Pascual, S., Montembault, V., Soutif, J.C., and Fontaine, L., *Phosphites as alternative coreagents for the one-pot aminolysis/thiol-ene synthesis of maleimide-functionalized RAFT polymers.* Journal of Polymer Science Part A: Polymer Chemistry, 2012. **50** (8): p. 1657-1661.

Chapter 2. Experimental

2.1 Synopsis

Information pertaining to the materials, reagents, experimental procedures and characterisation techniques used in Chapters 3, 4 and 5 of this thesis can be found here. Experimental methods used to synthesise and characterise the CdS QD and C-dot polymer nanocomposites are described here.

Information regarding the preparation and application of these synthesised CdS QD and C-dot polymer nanocomposites to latent fingermark detection will be described in Chapter 6.

2.2 Materials

This section lists all reagents and chemicals used in this research for the synthesis of the CdS QD and C-dot polymer nanocomposites described in this chapter.

2.2.1 Table of chemicals and reagents

Chemical Name	**Supplier/Manufacturer**	**Info.**
Acetone, analytical grade	Ajax Finechem Pty Ltd, Australia	Used as purchased
Acetone, HPLC grade	Merck, Australia	Filtered through 0.45 µm syringe filters prior to use for GPC
Activated Charcoal (Mesh 900)	Sigma Aldrich, Australia	Used as purchased
Aluminium oxide (basic activated)	Sigma Aldrich, Australia	Used as purchased
Azobisisobutyronitrile (AIBN)	Merck, Germany	Recrystallised twice from methanol
Cadmium chloride ($CdCl_2$)	Merck, Germany	Used as purchased
Deuterium oxide (D_2O)	Wilmad –Lab Glass, USA	Used as purchased
Deuterated dimethylsulfoxide (DMSO-d_6)	Wilmad –Lab Glass, USA	Used as purchased
Deuterated chloroform ($CDCl_3$)	Wilmad –Lab Glass, USA	Used as purchased
Diethyl ether (anhydrous)	Chemsupply, Australia	Used as purchased
N*,*N-Dimethylacrylamide (DMA)	Sigma-Aldrich, Australia	Inhibitor removed, by passing through an alumina column prior to immediate use
4-Dimethylaminopyridine (DMAP)	Sigma-Aldrich, Australia	Used as purchased
Dicyclohexylcarbodiimide (DCC)	Sigma-Aldrich, Australia	Used as Purchased
N*,*N-Dimethylformamide (DMF) (99 % anhydrous)	Sigma-Aldrich, Australia	Stored under molecular sieves
Divinyl sulfone (DVS) functionalised magnetic beads	BioClone, USA	Used as purchased
Ethanol	Ajax Finechem Pty Ltd, Australia	Stored in freezer, used cold.

Hexylamine (HA) 99 %	Sigma-Aldrich, Australia	Used as purchased
Magnesium sulphate ($MgSO_4$) (Anhydrous)	Sigma-Aldrich, Australia	Used as purchased
2-Mercaptoethanol	Sigma-Aldrich, Australia	Used as purchased
2-Methyl-2-[(dodecylsulfanylthiocarbonyl)sulfanyl]propanoic acid, min. 97 % (C_{12}CTA)	Strem Chemicals, USA	Used as purchased
Methyl methacrylate (MMA)	Sigma-Aldrich, Australia	Inhibitor removed, by passing through an alumina column prior to immediate use
Methanol	Ajax Finechem Pty Ltd, Australia	Stored in freezer, used cold.
Milli-Q water		Prepared by filtering through resin membrane filters to a resistivity of 18.2 MΩ cm. This water was used for all dilutions and aqueous solutions
Nitric acid (HNO_3) (70 wt/wt %)	Sigma-Aldrich, Australia	Used as purchased
Potassium hydroxide (KOH) (99 %, Pellets)	Sigma-Aldrich, Australia	Used as purchased
Sodium hydroxide (NaOH) (99 %, pellets)	Sigma-Aldrich, Australia	Used as purchased
Sodium sulphide (Nona hydrate Hydrate) ($Na_2S.9H_2O$)	Sigma-Aldrich, Australia	Used as purchased
Styrene (Sty)	Sigma-Aldrich, Australia	Inhibitor removed by passing through an alumina column prior to immediate use.
Tetrahydrofuran (THF) (HPLC grade)	Sigma-Aldrich, Australia	Used for GPC analysis, filtered through a 0.45 µm filter before use
Toluene (anhydrous)	Sigma-Aldrich, Australia	Used as purchased
Triethylamine (TEA) 99 %	Sigma-Aldrich Australia	Used as purchased

2.3 Synthetic procedures

The following is in regards to the synthesis of the QD-polymer and C-dot/polymer nanocomposites:

1. CdS/p(DMA), CdS/p(DMA-*co*-MMA) and CdS/p(DMA-*co*-Sty)
2. C-dots/p(DMA) and C-dots/p(DMA-*co*-MMA)
3. Magnetic C-dots/p(DMA-*co*-MMA) and CdS/p(DMA-*co*-Sty)

2.3.1 Synthesis of CdS/2-mercaptoethanol QDs

The synthesis of CdS/2-mercaptoethanol in DMF has been reported previously, and was chosen for its versatility in post modification as it offers hydroxyl surface moieties [1-3]. $CdCl_2$ (2 mL H_2O, 5 mM) and 2-mercaptoethanol (0.25 mL, 20 mM) in DMF (20 mL) were stirred with a magnetic stir bar in a 50 mL round bottom flask for 20 min at room temperature under nitrogen. $Na_2S.9H_2O$ (2 mL H_2O, 5 mM) was then added drop-wise over a 2 min period to the stirring $CdCl_2$/2-mercaptoethanol solution. This was then left to stir vigorously for 4 h at room temperature under nitrogen. The solution was then dried over anhydrous $MgSO_4$ (2 g) to yield a clear colourless solution of CdS/2-mercaptoethanol in DMF (see Figure 2.1).

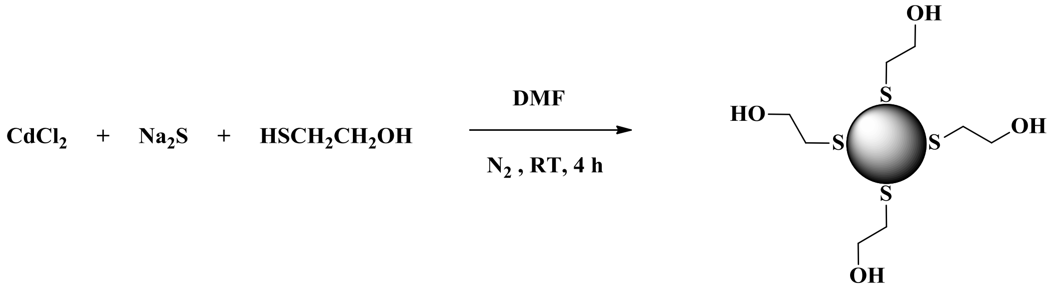

Figure 2.1. Reaction scheme for the synthesis of CdS/2-mercaptoethanol QDs.

2.3.2 Synthesis of CdS/C_{12}CTA QDs

From above, CdS/2-mercaptoethanol in DMF (20 mL), DMAP (5 mg) and C_{12}CTA (10 mg) were added in a 50 mL round bottom flask and stirred with a magnetic stir bar for 80 min at 0 °C under nitrogen. DCC (8 mg in 1 mL DMF) was then added to the solution, drop-wise over a 1 min time period. The solution was then left to stir, under nitrogen at room temperature for 48 h. Any undesirable by-product of the DCC/DMAP coupling reaction (e.g., *N,N'*-dicyclohexylurea, a white precipitate) was removed *via* filtration to yield a clear pale yellow solution of CdS/C_{12}CTA in DMF (see Figure 2.2).

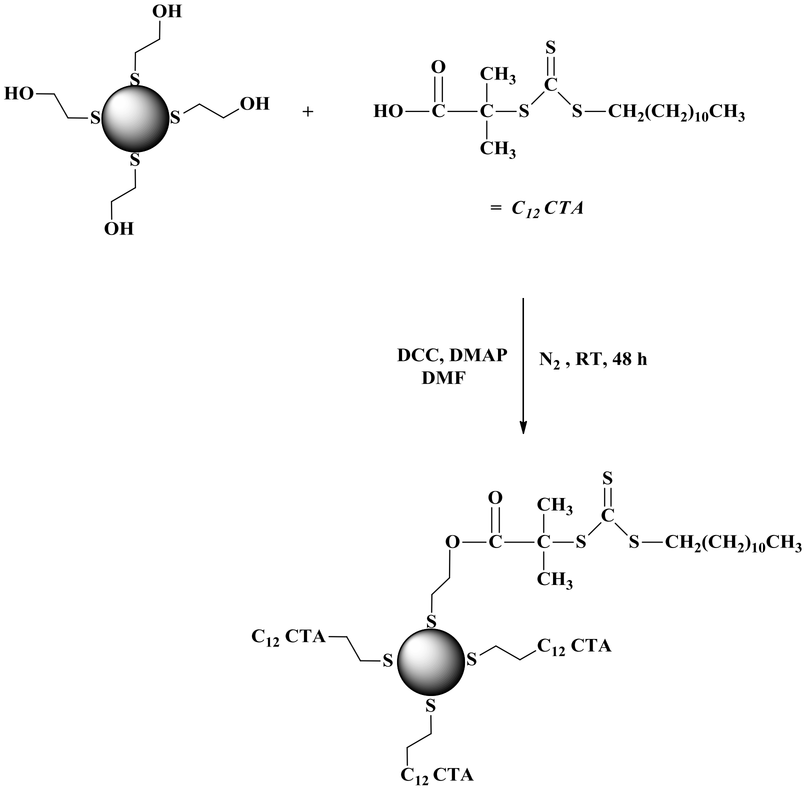

Figure 2.2. Reaction scheme for the immobilisation of C_{12}CTA to CdS/2-mercaptoethanol QDs.

2.3.3 Surface initiated RAFT polymerisation

Prior to surface initiated RAFT polymerisation the monomers (DMA, Sty and MMA) were purified to remove any inhibitors by passing each monomer through a basic alumina column. The radical initiator, AIBN, was purified by recrystallisation with methanol. Synthesis of the following homopolymers and copolymers was chosen due to the adhesive properties of DMA and the MMA and Sty monomers ability to aid in the fabrication of a powder [4, 5]. The monomers chosen were also compatible with the chemical properties of the RAFT agent. The polymerisation reactions using CdS QDs are shown in Figure 2.1, and described in the following.

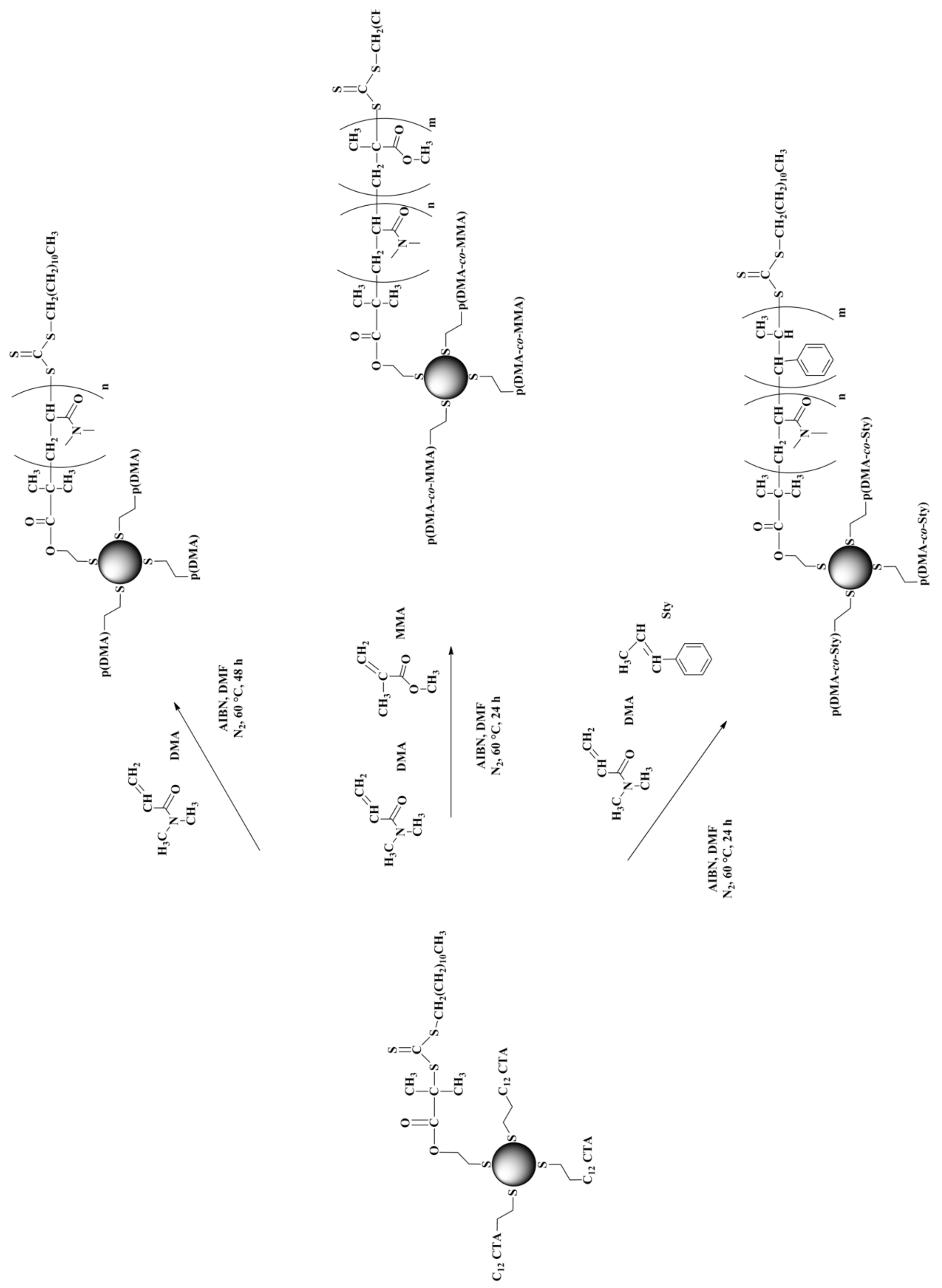

Figure 2.3. Reaction scheme for RAFT polymerisation of DMA, MMA and Sty monomers from CdS/C_{12}CTA QDs.

2.3.3.1 Synthesis of CdS/p(DMA)

DMA (2 mL), AIBN (3 mg) and CdS/C_{12}CTA in DMF (5 mL) were placed into a 20 mL glass vessel with a magnetic stir bar and sealed (with a rubber septum and copper wire). This solution was degassed under nitrogen *via* syringe for 10 min before placing in a 60 °C heating block for 48 h. After polymerisation, the solution was allowed to cool to room temperature before purifying *via* precipitation into excess diethyl ether (50 mL). This yielded a clear gel-like material of CdS/p(DMA) which was soluble in water.

^{1}H NMR ($CDCl_3$) δ (ppm) 0.98-1.20 (C-CH_3), 1.62 (CH_2), 2.12 (OC-CH), 2.71 (N-CH_3) and 3.21 (S-CH_2) [6].

2.3.3.2 Synthesis of CdS/p(DMA-*co*-MMA)

DMA (1 mL), MMA (1 mL), AIBN (3 mg), and CdS/C_{12}CTA in DMF (5 mL) were placed into a 20 mL glass vessel with a magnetic stir bar and sealed (with a rubber septum and copper wire). This solution was then degassed under nitrogen *via* syringe for 10 min before placing in a 60 °C heating block for 48 h. The polymerised solution was allowed to cool to room temperature before purifying *via* precipitation in excess cold methanol (100 mL). This yielded a white powder of CdS/p(DMA-*co*-MMA).

^{1}H NMR ($CDCl_3$) δ (ppm) 0.92-1.41 (C-CH_3), 1.63 (CH_2), 2.19 (OC-CH), 2.71 (N-CH_3), 3.70 (O-CH_3) and 3.26 (S-CH_2) [6].

2.3.3.3 Synthesis of CdS/p(DMA-*co*-Sty)

DMA (1 mL), Sty (1 mL), AIBN (3 mg) and CdS/C_{12}CTA in DMF (5 mL) were placed into a 20 mL glass vessel with a magnetic stir bar and sealed with a rubber septum and copper wire. This solution was then degassed under nitrogen *via* syringe for 10 min

before placing in a 60 °C heating block for 48 h. After polymerisation the solution was allowed to cool to room temperature before purifying *via* precipitation in excess cold methanol (100 mL). This yielded a white powder of CdS/p(DMA-*co*-Sty).
^{1}H NMR ($CDCl_3$) δ (ppm) 0.98-1.45 ($C-CH_3$), 1.66 (CH_2), 2.24 (OC-CH), 2.86 ($N-CH_3$), 3.31 ($S-CH_2$) and 7.11 (Ph-H) [6].

For comparative studies pristine (p(DMA), p(DMA-*co*-MMA) and p(DMA-*co*-Sty)) were also synthesised using only the C_{12}CTA.

2.3.4 C-dot synthesis

The method for the synthesis of C-dots was based on procedures reported in the literature, which were based upon the thermal oxidation of a carbon source *via* reflux in concentrated HNO_3 [7-14]. A literature review on the synthesis of C-dots is described in the introduction of the thesis in Chapter 1 Section 1.7. For synthesis activated charcoal (1 g) and nitric acid (100 mL, 4 M) were stirred with a magnetic stir bar in a 200 mL round bottom flask under reflux for 24 h. The solution was filtered by gravity using filter paper (100 mm, 20-25 μm Whatman© paper), to remove any unreacted activated carbon. The acidic aqueous solution of C-dots was neutralised using NaOH (4 M).

The salt by-products ($NaNO_3$) were recrystallised (*via* water evaporation and cooling the solution) and removed from the neutral aqueous C-dot solution by gravity filtration using filter paper (100 mm, 20-25 μm Whatman© paper). DMF (50 mL) was added to the aqueous C-dots solution and the solution gently heated to remove water *via* evaporation. After cooling, the solution was further dried using $MgSO_4$ (c.a. 2 g). This resulted in C-dots dispersed in DMF.

2.3.5 Synthesis of the C-dot/polymer nanocomposites

The synthesis of C-dot/p(DMA) and C-dot/p(DMA-*co*-MMA) was carried out similarly to that previously discussed for CdS QD nanocomposites in Section 2.3.3 of this chapter. Briefly, the C_{12}CTA was immobilised to the surface of C-dots and surface initiated RAFT polymerisation of the appropriate monomers from the modified surface was performed. The following details the specific synthetic route used.

2.3.5.1 Synthesis of C-dot/C_{12}CTA

DMAP (10 mg), C_{12}CTA (20 mg) and C-dots in DMF (50 mL), were stirred with a magnetic stir bar in a 100 mL round bottom flask for 80 min at 0 °C under nitrogen. DCC (20 mg in 5 mL DMF) was then added to the solution, drop-wise over a 2 min time period. The solution was then left to stir, under nitrogen at room temperature for 48 h. Any undesirable by-product of the DCC/DMAP coupling reaction (e.g., *N*,*N'*-dicyclohexylurea, a white precipitate) was removed *via* gravity filtration using filter paper (100 mm, 20-25 µm Whatman© paper).

2.3.5.2 Synthesis of C-dot/p(DMA)

DMA (5 mL), AIBN (10 mg) and C-dots/C_{12}CTA in DMF (50 mL) were placed into a 100 mL glass vessel with a magnetic stir bar and sealed (with a rubber septum and copper wire). This solution was then degassed under nitrogen *via* syringe for 1 h before placing in a silicon oil bath with a stable temperature set at 60 °C, for 48 h. The polymerised solution was allowed to cool to room temperature before purifying *via* precipitation in excess cold diethyl ether (400 mL) to give C-dots/p(DMA).

^{1}H NMR ($CDCl_3$) δ (ppm) 0.98-1.20 (C-CH_3), 1.62 (CH_2), 2.12 (OC-CH), 2.71 (N-CH_3), 3.21 (S-CH_2) and 10.23 (C-COOH) [6].

2.3.5.3 Synthesis of C-dot/p(DMA-*co*-MMA)

DMA (2 mL), Sty (2 mL) AIBN (8 mg) and C-dots/C_{12}CTA in DMF (50 mL) were placed into a 100 mL glass vessel with a magnetic stir bar and sealed (with a rubber septum and copper wire). This solution was then degassed under nitrogen *via* syringe for 1 h before placing in a silicon oil bath with a stable temperature set at 60 °C, for 48 h. The polymerised solution was allowed to cool to room temperature before purifying *via* precipitation in excess cold diethyl ether (400 mL) to give C-dots/p(DMA-*co*-MMA).

^{1}H NMR ($CDCl_3$) δ (ppm) 0.90-1.45 ($C-CH_3$), 1.63 (CH_2), 2.22 (OC-CH), 2.73 ($N-CH_3$), 3.78 ($O-CH_3$) and 3.33 ($S-CH_2$) and 10.45(C-COOH) [6].

2.3.6 Synthesis of magnetic C-dot/p(DMA-*co*-MMA) and CdS/p(DMA-*co*-MMA) nanocomposite

A one-pot aminolysis/thiol-ene click reaction was performed to modify the RAFT group in the p(DMA-*co*-MMA) grafted from the CdS and C-dot surface, with a magnetic bead functionalised with divinyl sulfone (DVS). The DVS-magnetic beads were purchased from BioClone Inc. (CA, USA). The reaction was based on methods established by Boyer and co-workers [15]. This section will detail the experimental procedures for this reaction.

2.3.6.1 One-pot aminolysis/thiol-ene click chemistry of C-dot/p(DMA-*co*-MMA) and CdS//p(DMA-*co*-MMA) to DVS-activated magnetic particles.

C-dot/p(DMA-*co*-MMA) or CdS/p(DMA-*co*-MMA) (0.25 g), previously described in Section 2.3.5.2 and 2.3.5.3 of this chapter respectively, and DVS-activated magnetic beads (0.005 g) were dissolved in DMF (5 mL) and placed into a 20 mL vessel and sealed with a rubber septum. The solution was degassed for 30 min. Hexylamine (1 M, 1 mL) and triethylamine (1 M, 1 mL) in DMF (5 mL) was placed into a separate 20 mL vessel, sealed with a rubber septum, and degassed under nitrogen for 30 min. The hexylamine/triethylamine (HA/TEA) solution was added to the C-dot/p(DMA-*co*-MMA)/DVS-magnetic bead solution *via* syringe, and the solution was placed on a hot plate set at 50 °C for 30 min. The reaction scheme is shown in Figure 2.4.

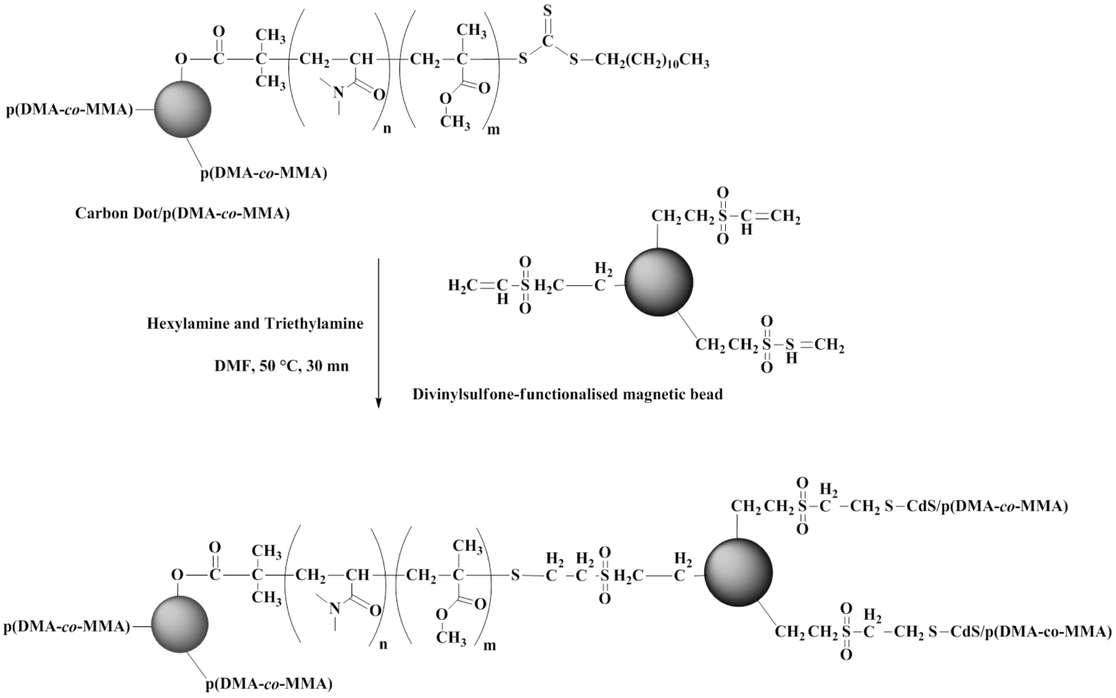

Figure 2.4. One pot aminolysis/thiol-ene click reaction of C-dot and CdS/p(DMA-*co*-MMA) to DVS-magnetic beads.

2.3.6.1.1 Purification of magnetic C-dot/p(DMA-*co*-MMA) and C-dot//p(DMA-*co*-MMA)

After the reaction had proceeded (Section 2.3.6.1) the solution was then left to cool to room temperature. The DMF was removed *via* evaporation with the aid of N_2 gas flowing above the solution at room temperature. The dried nanocomposite was then suspended in acetone (5 mL). Centrifugation of this 5 mL suspension (using a Clements Orbital 325 centrifuge at 1000 rpm for 10 min) allowed for the unreacted DVS magnetic beads to settle into an insoluble precipitate at the bottom of the centrifuge tube. The supernatant was collected and added drop-wise to stirring cold diethyl ether (200 mL), upon which the magnetic nanocomposite precipitated out. Precipitation into excess cold diethyl ether (200 mL) was performed twice to produce magnetic C-dot/p(DMA-*co*-MMA) and C-dot//p(DMA-*co*-MMA nanocomposite powders.

2.3.7 Ultra-Violet (UV) – visible (vis) spectrophotometry

UV-vis spectrophotometry is a technique used to measure a molecule’s absorption of UV light. In organic chemistry it can recognise the presence of a conjugated system π-π* transitions, and n-π* transitions. In inorganic chemistry d-d orbital transitions between metal ions and ligands and band gap energies of UV-excitable semiconductors can be measured [16]. In this work UV-vis spectrophotometry was used to determine the band gap energy of the CdS QDs in order to estimate the QDs’ diameter using the hyperbolic band model. This technique was also utilised for monitoring the synthesis of C-dots from thermal oxidation of AC, and to investigate their optical properties with respect to surface oxidation. In literature it is known that π-π* transitions are observed with respect to the carbonaceous nature of the carbon dots at shorter wavelengths (280 nm to 350 nm). However, the n-π* transitions are observed at longer wavelengths (350 nm to 450 nm) when the surface is oxidised with hydroxyl (R-OH) and carboxylic acid groups (R-COOH) [17, 18].

2.3.7.1 UV-vis spectrophotometry sample preparation and data acquisition

All samples were diluted by a factor of 1/25 in the appropriate solvents (DMF for polymers and QD-polymer nanocomposites and Milli-Q water for C-dot products). UV-vis data were recorded using a Varian 50 Scan Spectrophotometer installed with Win UV Scan Application (Cary Varian). A quartz cuvette (6Q) with a 10 mm path length was used. Absorbance spectra of the samples were recorded from 600 nm to 230 nm, with baseline correction using the appropriate solvent. The scan rate was 300 nm min^{-1} at 0.5 nm intervals with an average read time of 0.1 s.

2.3.7.2 Estimation of CdS QD diameter using the hyperbolic band model

The absorption onset of the CdS QDs is representative of the band gap energy of the semiconducting nanocrystal and hence can be used in the hyperbolic band model to estimate the QD diameter [19, 20]. In order to determine the absorption onset the second derivative of the absorbance spectra was plotted. From here, the peak maxima were determined which accurately represented the absorption onset [21]. This absorption onset wavelength was then inserted into the hyperbolic band model equation. A detailed procedure of this calculation is outlined in Chapter 3 Section 3.1.2, where an example calculation of the CdS QD size is shown.

2.4 Characterisation techniques

This section will describe the instrumentation used to characterise CdS/polymer and C-dot/polymer nanocomposites. Each section will provide an introduction to the technique, and specifies which samples were used in analysis. Sample preparation, data acquisition, and analysis and calculations (where appropriate) will also be described.

2.4.1 Fluorescence spectrophotometry

Fluorescence spectrophotometry was used in conjunction with UV-vis spectrophotometry. When QDs are exposed to UV light they emit photons, with respect to their band gap energy in the visible region, and this is measured using this technique. The full width half maximum (FWHM), shape and peak position give an indication of the QD's size, presence of potential surface defects, and/or interactions of the surface capping agent with the solvent chosen [3]. For example, emissions that are broad can be attributed to trap defect sites localised at QD surfaces [22, 23]. This technique was used to measure the fluorescence emission profiles, intensities and quantum yields (QY) of the CdS QDs and C-dots, before and after surface modification.

2.4.1.1 Sample preparation and instrumentation

All samples were diluted by a factor of 1/25 in the appropriate solvents (DMF for polymers and nanocomposites and Milli-Q water for C-dots). Fluorescence emission spectra were recorded using a Varian Cary Eclipse Fluorescence Spectrophotometer. A glass cuvette (10G) with a 10 mm path length was used. Fluorescence emission data were recorded between 900 nm and 500 nm with an emission and excitation slit width of 5 nm. An average of 100 scans was recorded at a scan rate of 120 nm min^{-1}, a data interval of 1 nm (average time 0.5 s), and with the PMT voltage set to 800 V.

2.4.1.2 Quantum yield (QY) determination

The quantum yield (QY) is a quantitative measure of how effective the QD or C-dot reemits energy or light (radiatively) that has been absorbed [22, 24]. Rhodamine 6G (R6G) was used as the reference dye for QY measurements. This was done by comparing integrated fluorescence emissions of the sample (CdS QDs or C-dots) against that of a fluorescent dye of similar absorbance. The QY can be expressed as a number between 0 and 1 or as a percentage and is calculated by multiplying the QY of the dye (QY_{R6G}) by the ratio of integrated fluorescence (Int. Fluorescence) of the sample to the dye, in this case Rhodamine 6G (R6G). This is shown in Equation 2.1 [16].

$$QY_{sample} = QY_{dye} \text{ x } \frac{Int.Fluorescence_{sample}}{Int.Fluorescence_{dye}}$$

Equation 2.1

Standards of increasing concentration of R6G, CdS QDs, and C-dots were prepared separately. The absorbance of each standard was determined using UV-vis spectrophotometry, using the same data acquisition settings mentioned previously in Section 2.3.7.1 of this chapter. The integrated fluorescence intensity was calculated after measuring the fluorescence emission with an excitation of 375 nm. Fluorescence emission data was recorded between 400 nm and 800 nm. An average of 5 scans was recorded for each standard at acquisition settings, as previously used in Section 2.4.1.1

of this chapter. A calibration plot of integrated fluorescence versus absorbance was constructed for R6G and is shown in Figure 2.5.

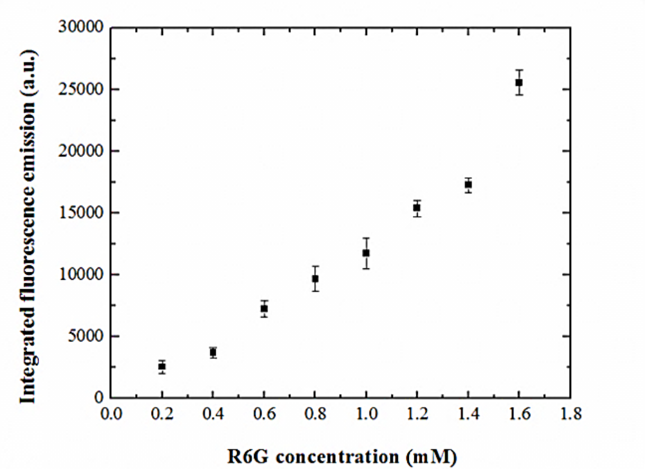

Figure 2.5. Calibration curve for the integrated fluorescence versus measured absorbance of the dye R6G (y = 1958 x, R^2 = 0.97383).

2.4.2 Dynamic light scattering (DLS) for C-dot size determination

Particle size analysis by dynamic light scattering was performed with a High Performance Particle Sizer HPPS-HPP5001 (Malvern Instruments Ltd.) Immediately after synthesis, aqueous C-dot solutions (1/4 dilution) were analysed at room temperature (25 °C), where a volume distribution was measured with a water dispersant refractive index and viscosity set to 1.5900 and 0.8872 cP, respectively. A count rate of 65 cps and a run duration of 10 s was used.

2.4.3 Transmission electron microscopy (TEM) for CdS QD size determination

TEM is a useful instrument to image materials below 100 nm, and to determine QD size and size distribution [25]. This technique was used to image and ultimately determine the size (diameter) of the CdS QDs only. TEM measurements of CdS QD diameter were compared to the calculated results from UV-vis spectrophotometry and hyperbolic band model studies.

2.4.3.1 Sample preparation and instrumentation

A drop of the diluted sample used in UV-vis spectrophotometry (see section 2.3.7.1, i.e., a 1/25 dilution in water of the CdS/2-mercaptoethanol or the C-dots) was dispersed on a carbon coated copper grid and allowed to dry overnight at room temperature. TEM images were taken at 200,000 x magnification with a JEOL 1200 EX TEM fitted with a MegaView 3 digital imaging camera.

2.4.4 X-ray photoelectron spectroscopy (XPS) analysis of C-dots

XPS is a surface sensitive analytical tool, which is used for elemental analysis. XPS has been used in C-dot analysis to determine the surface chemistry and hence oxidation (increased of ratio of elemental oxygen to carbon) of C-dots when compared to its carbon precursor or carbon source [9, 26-28].

XPS analysis was performed only on C-dots and its precursor, AC. Samples were prepared in dry powder-form. Survey analysis were performed on the C-dots and AC samples, and high resolution scans of the carbon and oxygen peaks were performed on a Leybold LHS-10 XPS spectrometer equipped with a monochromatic Al Kα source (1486.6 eV). The X-ray source was operated at 13 kV, 20 mA. Data were recorded in the VAMAS format and processed using the CasaXPS software package. Data manipulation in CasaXPS involved smoothing (standard grade quadratic, smoothing width = 9) and background subtractions (Shirley background) before the data were exported into Origin Pro 7.5.

2.4.5 Raman spectroscopy analysis of C-dots

Raman spectroscopy is a useful tool for investigating the carbon species (sp^2 or sp^3) of a carbonaceous compound. It has been used extensively in carbon based nanostructures research (i.e., nanotubes, fullerenes, nanodiamonds and graphene research). In particular, peak positions and shape of the disorder (D) and graphite (G) bands which lie around 1360 cm^1 and 1560 cm^{-1}, respectively, were investigated [29, 30].

Raman spectroscopic analysis was only performed on dry samples (c.a 0.05 g) of the C-dots and its precursor; AC, mounted on a glass microscope slide. Raman spectra were collected with a WiTEC alpha300R Microscope in Confocal imaging Raman mode using a 40x (Numerical Aperture 0.6) and 532 nm (E_{laser} = 2.33 eV) laser operating at constant power for each spectra collected. Laser power was kept below the maximum of 60 mW to avoid sample burning. Raman data were collected by the WiTEC Control software and analysed in the WiTEC Project software, with the surface perpendicular to the excitation source. Standalone spectra were collected using integration times of 10 s for 3 accumulations.

2.4.6 Nuclear magnetic resonance (NMR) spectroscopy

NMR spectroscopy is an important technique for chemical structural determination It measures the absorption of energy by a molecule when placed in a magnetic field [4]. Both proton NMR (^1H NMR) and 13 carbon solution NMR (^{13}C NMR) spectroscopies were used in this research. ^1H NMR spectroscopy was primarily used in this work to characterise/identify the RAFT polymers grafted from the CdS QD and C-dot surface; p(DMA), p(DMA-*co*-MMA) and p(DMA-*co*-Sty). It was also used to perform kinetic studies to monitor the controlled radical polymerisation and validating the RAFT process [31]. ^{13}C solution NMR spectroscopy was used to characterise the purified C-dots only, where the R-C-OH and R-C-COOH moieties and carbon type (sp^2 or sp^3) were investigated, similar to studies performed by Liu *et al* [10].

2.4.6.1 Sample preparation and instrumentation for ^1H NMR spectral analysis of RAFT polymers

Solution ^1H NMR data of all samples were recorded on a 600 MHz Bruker Advance NMR Spectrometer. Solid (5 - 10 mg) and liquid samples were dissolved in either $CDCl_3$ or DMSO-d_6 (1:10 ratio of sample to deuterated solvent) and placed in an NMR tube (5 mm, Wilmad). Chemical shifts (δ) were recorded in ppm and referenced to the solvent peak (7.26 ppm for $CDCl_3$ and 2.50 ppm for DMSO-d_6). All data (16 scans) were acquired using TopSpin NMR Software (Bruker), and the Free Induction Decay (FID) signals (text files) were imported into MestRec NMR Software (Mestrelab). Data manipulation and analysis such as Fourier transform and peak integration were performed. The transformed data were exported into Origin Pro 7.5 for data presentation.

2.4.6.2 Data acquisition and analysis for kinetic studies

A solution of CdS/C_{12}CTA and C-dots/C_{12}CTA, with their appropriate monomers (DMA, Sty and/or MMA), AIBN initiator, and internal standard of toluene (5 mL) in DMF solvent (up to 30 mL) were prepared. This polymerisation solution was evenly divided into 10 samples (in 20 mL reaction vessels, and stir bar, sealed with a rubber septum and copper wire). The 10 samples corresponded to reaction times (t, in hours), 0, 1, 2, 4, 8, 12, 18, 24, and 48, and were degassed under nitrogen (using a syringe with an outlet syringe) for at least 10 min each. Reactions were initiated, by placing the sample in a heating block. At the appropriate times, the sample was removed from the heating block, and rapidly cooled (in an ice bath), to stop further initiation and polymerisation. ^{1}H NMR spectroscopy measurements were taken immediately after quenching the polymerisation reaction in the ice bath, by accurately preparing a 1:10 solution of the polymerisation solution in DMSO-d_6. The data (16 scans) were collected using Bruker software fitted to the NMR spectrometer and integrations against the internal standard (toluene) after importing FID data into the MestRec program/software.

2.4.6.3 Sample preparation and instrumentation for ^{13}C NMR spectral analysis of purified C-dots

Solution ^{13}C NMR data of all C-dot samples were recorded on a 600 MHz Bruker Advance NMR Spectrometer. Liquid samples of C-dots in H_2O were dissolved in D_2O (1:1 ratio) and syringed into an NMR tube (5 mm, Wilmad). Chemical shifts (δ) were recorded in ppm. All data were acquired using TopSpin NMR Software (Bruker). Averages of 4000 scans were taken with the sample in spin mode. FID signals (text files) were imported into MestRec NMR Software (Mestrelab). Data manipulation and analysis such as Fourier transform and peak integration were performed. The transformed data were exported into Origin Pro 7.5 for data presentation. There were no reference peaks for D_2O as there was no carbon present.

2.4.7 Fourier transform infrared (FTIR) spectroscopy

FTIR spectroscopy was used to identify functional groups present in the products. It is a technique that relies on the vibration of bonds at characteristic frequencies specific to a certain functional group, and is particularly useful in polymer chemistry [32]. It is a complimentary technique with other spectroscopic methods and is therefore useful for structural determination of unknown compounds [33]. In this work, FTIR spectroscopy was used to confirm immobilisation of C_{12}CTA to the CdS or C-dot surface and characterise the polymers (p(DMA), p(DMA-*co*-MMA), p(DMA-*co*-Sty)), and C-dot surface. It was also a useful tool to monitor the thiol-ene click reaction between C-dots/p(DMA-*co*-MMA) and CdS/p(DMA-*co*-MMA) with DVS-magnetic beads.

2.4.7.1 Sample preparation and instrumentation

FTIR samples were prepared by either thin film on NaCl windows or preparation of a KBr disc. In order to make thin films, the polymer sample was dissolved in a minimal amount of acetone. NaCl windows were first cleaned with ethanol and dried before the polymer/acetone solution was pipetted onto the window, enough to cover, and allowed to dry. The pipetting process was repeated up to a further 3 times.

KBr discs were prepared by grinding the solid product with oven dried KBr in a 1:10 ratio of the polymer sample to KBr in weight, and compression (up to 10 tonne) into discs using a Pye Unicam KBr Press connected to a Welch self-cleaning dry vacuum system (model 2025, Southern Cross Scientific).

Samples were analysed on a Thermo Electron FTIR spectrometer (Nicolet Avatar 370 PTGS Model) installed with EZ OMNIC software, in % transmittance mode. A background scan (256 scans) of the empty chamber was taken before each sample was scanned. The samples were recorded (256 scans) with a resolution of 4 cm^{-1}, and a data spacing of 1.929 cm^{-1}.

2.4.8 Gel permeation chromatography (GPC)

GPC is based on high performance liquid chromatography (HPLC), which has been tailored for polymer characterisation. Separation is based on size exclusion chromatography (SEC). GPC was used in this work to determine the weight average molecular weight (M_w), number average molecular weight (M_n), in order to calculate the polydispersity index (PDI) of the synthesised polymers from Equation 2.2 [32, 34].

$$PDI = \frac{M_w}{M_n}$$

Equation 2.2

The PDI gives a measure of the distribution of molecular weight in a polymer sample. A value of 1.00 means a completely uniform distribution of molecular weights indicating that all polymer chains within the sample are approximately the same length. A PDI of one signifies a controlled reaction. As the PDI increases above one, the reaction is said to be less controlled and the polymer chain lengths vary in the sample [32, 34].

2.4.8.1 Sample preparation and instrumentation

Polymer samples for GPC were prepared in THF (HPLC grade) to a concentration of ~1 mg mL^{-1} and filtered through Whatman 0.45 μm syringe filters prior to injection. All samples were stored in the fridge at 4 ^{o}C when not in use. All samples were analysed using a Shimadzu HPLC with a Varian PolarGel™ Organic GPC column

(300 mm length, 7.5 mm internal diameter), using a 3.0 mL min^{-1} flow rate, and a refractive index detector. EasiVial Polystyrene (PS) standards were used to prepare a molecular weight calibration curve before each run. The Mw, elution time (in min) and PDI of the PS standards are shown in Table 2., followed by the standard calibration curve of Log Mw versus Time (min) and is shown in Figure 2.6.

Table 2. Molecular weight and PDI of PS standards used to construct a calibration curve for GPC analysis.

Time (min)	**PS Mw (g mol^{-1})**	**PDI**
8.62	467 400	1.03
10.18	79 250	1.07
12.02	5 720	1.09
13.70	690	1.09

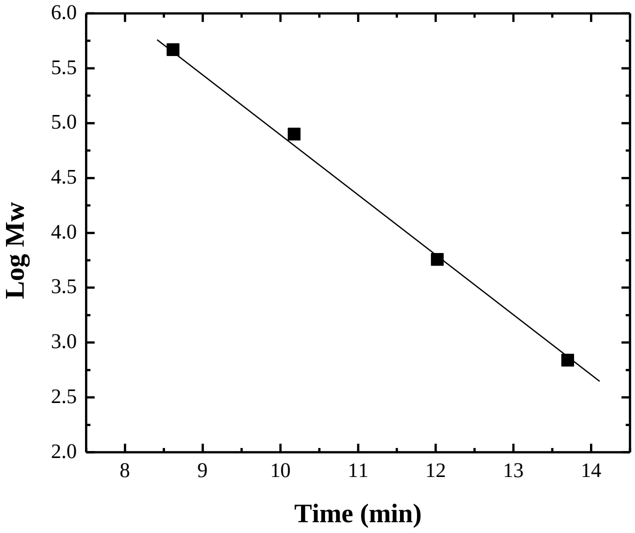

Figure 2.6. GPC calibration curve of PS standards.

2.4.9 Thermogravimetric analysis (TGA)

TGA is a method which measures changes in chemical and physical properties of polymers as a function of increasing temperature through mass loss. This technique was used to confirm the immobilisation of the C_{12}CTA to the CdS QDs and the C-dots, and also to calculate the degradation temperatures of the polymers grafted from the

CdS QD and C-dot surfaces. It was also useful for determining the grafting densities [35-37] of the polymers from the CdS QD or C-dot core. The grafting densities were calculated using Equation 2.3,

$$Grafting\ density\ (\mu mol\ m^{-2}) = \frac{W_a \text{ x } Mw \text{ x } Av}{SA} \text{ x } 10^6$$

Equation 2.3

Where W_a is the polymer weight loss (between 300 °C and 500 °C), Mw is the polymer molecular weight (determined by GPC), Av is Avogadro's number and SA is the calculated surface area of the CdS QD or C-dot (assuming spherical). The SA of CdS was calculated from the diameter measured from the TEM measurements and the SA of the C-dots was calculated from their diameter measured using DLS. In addition, TGA was used to monitor the thiol-ene click reaction between the DVS-magnetic bead with the CdS/p(DMA-*co*-MMA) and C-dot/p(DMA-*co*-MMA) nanocomposites.

2.4.9.1 Sample preparation and instrumentation

TGA was performed using a Thermal Advantage (TA) Hi-Res modulated TGA 2950 Thermogravimetric Analyser (with TA Universal Analysis software). Prior to analysis, each sample was dried under nitrogen for 24 h. Samples (5 mg) were then placed in a platinum pan with a disposable aluminium insert. A nitrogen flow rate of 50 mL min^{-1}, with a temperature range of 30 – 600 °C, at a 10 °C min^{-1} ramp rate.

The data collected and analysed, described in this chapter, will be discussed in the following Chapters 3, 4 and 5.

2.5 References for Chapter 2

1. Chen, L., Zhu, J., Li, Q., Chen, S., and Wang, Y., *Controllable synthesis of functionalized CdS nanocrystals and CdS/PMMA nanocomposite hybrids.* European Polymer Journal, 2007. **43** (11): p. 4593-4601.
2. Majumder, M., Karan, S., and Mallik, B., *Study of steady state and time resolved photoluminescence of thiol capped CdS nanocrystalline powders dispersed in N, N-dimethylformamide.* Journal of Luminescence, 2011. **131** (12): p. 2792-2802.
3. Resch, U., Eychmüller, A., Haase, M., and Weller, H., *Absorption and fluorescence behavior of redispersible cadmium sulfide colloids in various organic solvents.* Langmuir, 1992. **8** (9): p. 2215-2218.
4. Inagaki, H. and Myamoto, T., *Preparation of block copolymers of A-B-A type and its behaviour in dilute solution.* Macromolecular Chemistry and Physics, 1965. **87** (1): p. 166.
5. Meier, L.P., Shelden, R.A., Caseri, W.R., and Suter, U.W., *Polymerization of styrene with initiator ionically bound to high surface area mica: grafting via an unexpected mechanism.* Macromolecules, 1994. **27** (6): p. 1637.
6. Tian, L., Ghosh, D., Chen, W., Pradhan, S., Chang, X., and Chen, S., *Nanosized carbon particles from natural gas soot.* Chemistry of Materials, 2009. **21** (13): p. 2803-2809.
7. Guo, Y., Wang, Z., Shao, H., and Jiang, X., *Hydrothermal synthesis of highly fluorescent carbon nanoparticles from sodium citrate and their use for the detection of mercury ions.* Carbon, 2012 (52): p. 583–589.
8. Hu, S.-L., Niu, K.-Y., Sun, J., Yang, J., Zhao, N.-Q., and Du, X.-W., *One-step synthesis of fluorescent carbon nanoparticles by laser irradiation.* Journal of Materials Chemistry, 2009. **19** (4): p. 484-488.
9. Qiao, Z.-A., Wang, Y., Gao, Y., Li, H., Dai, T., Liu, Y., and Huo, Q., *Commercially activated carbon as the source for producing multicolor photoluminescent carbon dots by chemical oxidation.* Chemical Communications, 2010. **46** (46): p. 8812-8814.
10. Liu, H., Ye, T., and Mao, C., *Fluorescent carbon nanoparticles derived from candle soot.* Angewandte Chemie International Edition, 2007. **46** (34): p. 6473-6475.
11. Liu, R., Wu, D., Liu, S., Koynov, K., Knoll, W., and Li, Q., *An aqueous route to multicolor photoluminescent carbon dots using silica spheres as carriers.* Angewandte Chemie International Edition, 2009. **121** (25): p. 4668-4671.
12. Lu, W., Qin, X., Liu, S., Chang, G., Zhang, Y., Luo, Y., Asiri, A.M., Al-Youbi, A.O., and Sun, X., *Economical, green synthesis of fluorescent carbon nanoparticles and their use as probes for sensitive and selective detection of mercury (II) ions.* Analytical Chemistry, 2012. **84** (12): p. 5351-5357.
13. Wang, F., Pang, S., Wang, L., Li, Q., Kreiter, M., and Liu, C.-y., *One-step synthesis of highly luminescent carbon dots in noncoordinating solvents.* Chemistry of Materials, 2010. **22** (16): p. 4528-4530.
14. Wohlgemuth, S., White, R., and Titirici, M., *Fluorescent carbon nanoparticles from hydrothermal carbon.* Carbon, 2010. **1** (1): p. 1-4.
15. Boyer, C., Granville, A., Davis, T.P., and Bulmus, V., *Modification of RAFT-polymers via thiol-ene reactions: A general route to functional polymers and new architectures.* Journal of Polymer Science Part A: Polymer Chemistry, 2009. **47** (15): p. 3773-3794.
16. Anderson, R.J., Bendell, D.J., Groundwater, P.W., and Chemistry, R.S.o., *Organic Spectroscopic Analysis*2004: Royal Society of Chemistry.
17. Galande, C., Mohite, A.D., Naumov, A.V., Gao, W., Ci, L., Ajayan, A., Gao, H., Srivastava, A., Weisman, R.B., and Ajayan, P.M., *Quasi-molecular fluorescence from graphene oxide.* Scientific Reports, 2011. **1**.

18. Rance, G.A., Marsh, D.H., Nicholas, R.J., and Khlobystov, A.N., *UV–vis absorption spectroscopy of carbon nanotubes: Relationship between the π-electron plasmon and nanotube diameter.* Chemical Physics Letters, 2010. **493** (1): p. 19-23.
19. Wang, Y. and Herron, N., *Nanometer-sized semiconductor clusters: materials synthesis, quantum size effects, and photophysical properties.* The Journal of Physical Chemistry, 1991. **95** (2): p. 525-532.
20. Wang, Y., Suna, A., Mahler, W., and Kasowski, R., *PbS in polymers. From molecules to bulk solids.* The Journal of Chemical Physics, 1987. **87**: p. 7315.
21. Nedelijkovic, J., Patel, R., Kaufman, P., Joyce-Pruden, C., and O'Leary, N., *Synthesis and optical properties of quantum-sized metal sulfide particles in aqueous solution.* Journal of Chemical Education, 1993. **70** (4): p. 342.
22. Alivisatos, A.P., *Semiconductor clusters, nanocrystals, and quantum dots.* Science, 1996. **271** (5251): p. 933-937.
23. Yusuf, H., Kim, W.-G., Lee, D.H., Guo, Y., and Moffitt, M.G., *Size control of mesoscale aqueous assemblies of quantum dots and block copolymers.* Langmuir, 2007. **23** (2): p. 868-878.
24. Frantsuzov, P.A. and Marcus, R., *Explanation of quantum dot blinking without long-lived trap hypothesis.* arXiv preprint cond-mat/0505604, 2005.
25. Gattás-Asfura, K.M. and Leblanc, R.M., *Peptide-coated CdS quantum dots for the optical detection of copper (II) and silver (I).* Chemical Communications, 2003 (21): p. 2684-2685.
26. Li, X., Wang, H., Shimizu, Y., Pyatenko, A., Kawaguchi, K., and Koshizaki, N., *Preparation of carbon quantum dots with tunable photoluminescence by rapid laser passivation in ordinary organic solvents.* Chemical Communications, 2011. **47** (3): p. 932-934.
27. Sun, Y.P., Zhou B., Lin Y., Wang W., Fernando K.A., Pathak P., Meziani M. J., Harruff B. A., Wang X., Wang H., Luo P.G., Yang H., Kose M. E., Chen B., Veca L. M., and Y., X.S., *Quantum-sized carbon dots for bright and colorful photoluminescence.* Journal of the American Chemical Society, 2006. **128** (24): p. 7756.
28. Zheng, H., Wang, Q., Long, Y., Zhang, H., Huang, X., and Zhu, R., *Enhancing the luminescence of carbon dots with a reduction pathway.* Chemical Communications, 2011. **47** (38): p. 10650-10652.
29. Ferrari, A. and Robertson, J., *Interpretation of Raman spectra of disordered and amorphous carbon.* Physical Review B, 2000. **61** (20): p. 14095.
30. Escribano, R., Sloan, J.J., Siddique, N., Sze, N., and Dudev, T., *Raman spectroscopy of carbon-containing particles.* Vibrational Spectroscopy, 2001. **26** (2): p. 179-186.
31. McLeary, J.B., Calitz, F.M., McKenzie, J.M., Tonge, M.P., Sanderson, R.D., and Klumperman, B., *Beyond Inhibition: A 1H NMR Investigation of the early kinetics of RAFT-mediated polymerization with the same initiating and leaving groups.* Macromolecules, 2004. **37** (7): p. 2383-2394.
32. Painter, C.P. and M, C.M., *Fundementals of Polymer Sciences* 2nd. An Introductory Text1997: CRC press. 119.
33. Scheirs, J., *Compositional and Failure Analysis of Polymers: A Practical Approach*2000: Wiley.
34. Holding, S.R. and Meehan, E., *Molecular Weight Characterisation of Synthetic Polymers*1995: Rapra Technology Limited.
35. Ranjan, R. and Brittain, W.J., *Tandem RAFT polymerization and click chemistry: An efficient approach to surface modification.* Macromolecular Rapid Communications, 2007. **28** (21): p. 2084-2089.
36. Bartholome, C., Beyou, E., Bourgeat-Lami, E., Chaumont, P., and Zydowicz, N., *Nitroxide-mediated polymerizations from silica nanoparticle surfaces:"graft*

from" polymerization of styrene using a triethoxysilyl-terminated alkoxyamine initiator. Macromolecules, 2003. **36** (21): p. 7946-7952.

37. Moraes, J., Ohno, K., Gody, G., Maschmeyer, T., and Perrier, S., *The synthesis of well-defined poly (vinylbenzyl chloride)-grafted nanoparticles via RAFT polymerization.* Beilstein Journal of Organic Chemistry, 2013. **9** (1): p. 1226-1234.

Chapter 3. CdS/polymer nanocomposites

3.1 Synopsis

This chapter describes the synthesis and characterisation of CdS/polymer nanocomposites in a chronological manner. First the synthesis of CdS QDs capped with 2-mercaptoethanol is described, followed by the immobilisation of the RAFT agent, C_{12}*CTA, to the functionalised CdS QDs via DCC/DMAP coupling (Steglich esterification). The last section describes the synthesis of the final nanocomposites; CdS/p(DMA), CdS/*p(DMA-*co*-MMA), *and CdS/*p(DMA-*co*-Sty), *respectively via surface initiated RAFT polymerisation. These CdS/polymer nanocomposites were used in latent fingermark detection, described in Chapter 6.*

3.2 Synthesis of CdS/2-mercaptoethanol

For the synthesis of CdS QDs capped with 2-mercaptoethanol, millimolar concentrations of Na_2S (in DMF) were added drop-wise to a vigorously stirring solution of millimolar concentrations of $CdCl_2$ and 2-mercaptoethanol in DMF solvent under a N_2 atmosphere (at room temperature). This is shown in Figure 3.1.

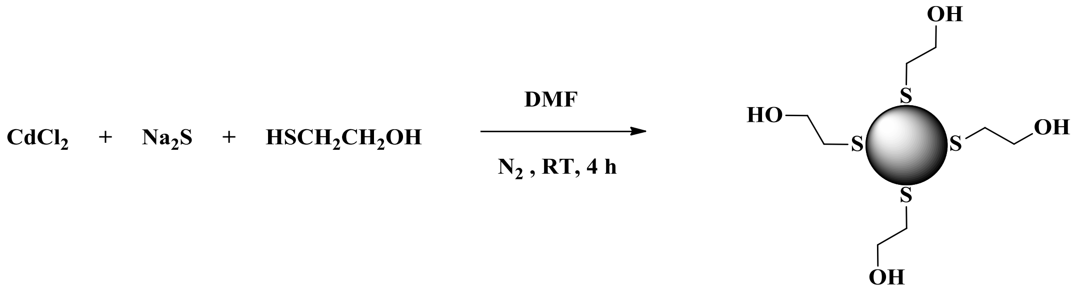

Figure 3.1. Synthesis of CdS/2-mercaptoethanol.

During the addition of Na_2S (in DMF) to a solution of $CdCl_2$ and 2-mercaptoethanol in DMF, the solution changed from a clear colourless liquid to an opaque light grey solution in natural lighting. At the end of the reaction time (4 h) the solution appeared clear colourless again. This indicated the nucleation and growth and dispersion of the CdS/2-mercaptoethanol QDs. To visually monitor the reaction and the formation of the CdS QDs, a UV-torch (450 nm ± 25 nm) was shone on the reaction in a dark room. Once the reaction had reached completion the solution fluoresced green at a consistent intensity (visually).

Unsuccessful synthesis of CdS/2-mercaptoethanol (and hence synthesis of bulk CdS) was observed when the solution did not fluoresce after excitation with the UV torch. These validations were supported by UV-vis spectrophotometry investigations in the next section.

It should also be noted that reactions performed without one of the precursors, $CdCl_2$, Na_2S or 2-mercaptoethanol, resulted in a non-fluorescent clear colourless solution (for example, a stirring solution of $CdCl_2$ with 2-mercaptoethanol and without Na_2S did not fluoresce).

3.2.1 Absorbance (CdS bulk vs. CdS QDs) – the quantum confinement effect

This section will describe investigations using UV-vis spectrophotometry to observe the quantum confinement effect, and hence support the successful synthesis of CdS QDs capped with 2-mercaptoethanol. It is known in literature that the absorbance of bulk semiconductor CdS occurs at 512 nm (2.42 eV) as a broad onset (shoulder profile) [1-3], in comparison to CdS QDs which absorb at shorter wavelengths with a sharp absorbance onset. UV-vis absorbance is a technique used to witness the quantum confinement effect spectrally. In addition, the quantum confinement effect expressed as the observed absorption onset of the QD is proportional to the band gap energy, and hence size of the QDs synthesised [4-8].

Bulk CdS was synthesised with the same experimental conditions as the CdS/2-mercaptoethanol, but without the capping agent, 2-mercaptoethoanol. This was carried out to prove the role of 2-mercaptoethanol as a capping agent for the protection of the CdS QDs surface and to prevent agglomeration. The absorbance spectrum of bulk CdS and CdS/2-mercaptoethanol synthesised is shown in Figure 3.2 (a) and (b), respectively.

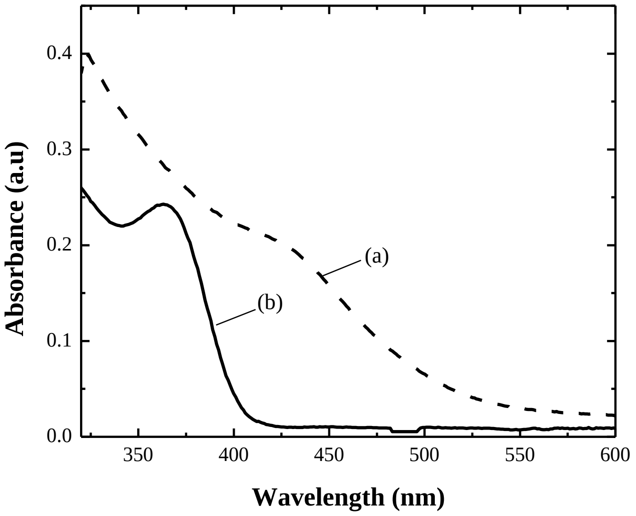

Figure 3.2. Absorbance spectra of (a) bulk CdS and (b) CdS/2-mercaptoethanol QDs.

Figure 3.2 (a) shows that the absorbance of bulk CdS synthesised had a broad absorbance onset at approximately 512 nm, in agreement with literature [9-11]. However, the absorbance onset observed for CdS/2-mercaptoethanol QDs in Figure 3.2 (b) was sharp and observed at shorter wavelengths than 377 nm. This confirmed that the CdS/2-mercaptoethanol QDs were successfully synthesised. Furthermore, this showed that the 2-mercaptoethanol on the surface of the CdS QDs plays a role in preventing agglomeration during synthesis.

The absorbance profile of both bulk CdS and CdS QDs is attributed to the energy absorbed between the HOMO of the valence band and the LUMO of the conduction band of the semiconductor. In bulk CdS the atomic orbitals overlap to form molecular orbitals and ultimately bands, hence the term valence band and conduction band. However, as the number of atoms required to form CdS nanocrystals is reduced quantum confinement is observed [11]. The atomic/molecular orbitals shared between Cd and S are discrete, and the band gap becomes larger than the bulk and the Bohr radius [9-11]. When the size of the nanocrystal is further reduced the band gap further increases, hence the size-dependent optical properties intrinsic to QDs are observed [3, 8, 11-14].

This phenomenon of the quantum confinement effect was further explored with an investigation of the effects of precursor concentration on size (and hence optical properties of CdS/2-mercaptoethanol). This is discussed in the following section.

3.2.1.1 UV-vis spectrophotometry and the hyperbolic band model

The absorbance spectra of CdS/2-mercaptoethanol synthesised using an equal ratio of $CdCl_2$:Na_2S, was recorded and shown in Figure 3.3 (I). In order to accurately determine the absorption onset, where the onset slope is at an absolute maximum, the first derivative was calculated and plotted, shown in Figure 3.3 (II).

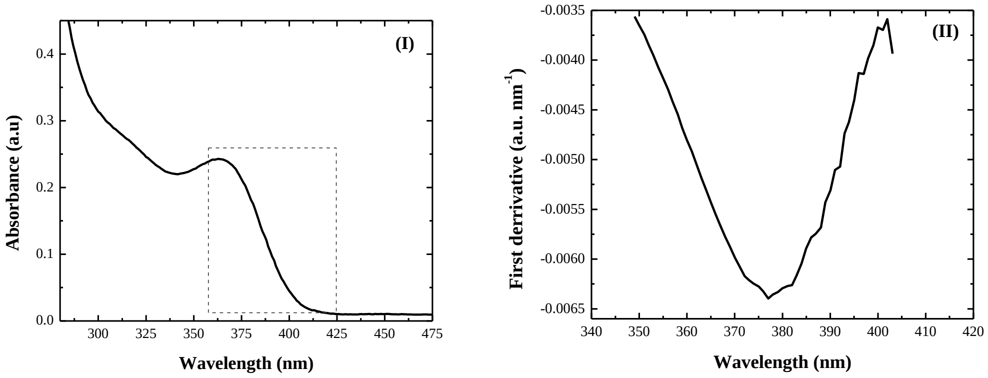

Figure 3.3. Absorbance spectra of (I) CdS/2-mercaptoethanol QDs synthesised using equal ratio of precursors $CdCl_2$: Na_2S and (II) first derivative of spectra (I).

The area in which the first derivative was calculated was between 350 nm and 400 nm, see dashed box in Figure 3.3 (I). The first derivative, or slope, calculated in this case was negative (Figure 3.3 (II)). The negative maximum at 377 nm was recorded as the absorbance onset and corresponds to an E_g of 3.29 eV which is larger than the bulk literature value of 2.42 eV. This increased E_g implies that quantum confinement has occurred and that CdS QDs were synthesised. Using the hyperbolic band model (see Chapter 2, Equation 1.1) this E_g (3.29 eV) was then used to estimate the CdS QD size of 3.78 nm.

3.2.2 Precursor concentration effects

In order to monitor the effect of Ostwald ripening during QD synthesis, precursor concentrations (i.e., $CdCl_2$: Na_2S) where tested. This section will discuss the study performed where by the $CdCl_2$:Na_2S concentration was varied, ultimately resulting in different sized QDs (as calculated previously, in Section 3.2.1.1, using UV-vis spectrophotometry and the hyperbolic band model). Figure 3.4 shows the UV-vis spectra recorded of CdS/2-mercaptoethanol synthesised using increasing ratios of $CdCl_2$:Na_2S from 1:2, 1:1 and 2:1, respectively.

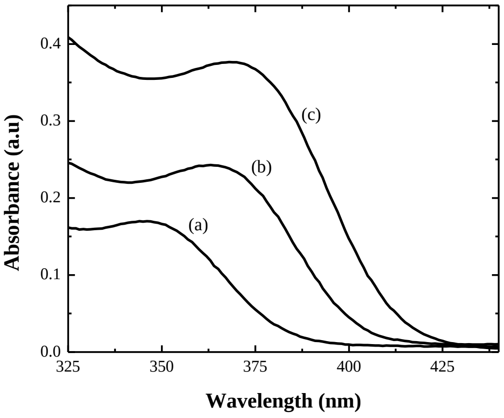

Figure 3.4. Overlayed UV-vis spectra of CdS/2-mercaptoethanol QDs with varied $CdCl_2$:Na_2S concentrations of (a) 1:2, (b) 1:1 and (c) 2:1.

As the concentration ratio of $CdCl_2$:Na_2S increased the absorbance (a.u) increases (Figure 3.4) which is due to Beers law, where absorbance is directly proportional to the concentration [15]. The wavelength at which CdS/2-mercaptoethanol QDs absorbed at (absorption onset) also increased from shorter wavelengths to longer wavelengths as the concentration of $CdCl_2$:Na_2S increased. Therefore the size of the CdS QDs synthesised also increased. The values for the wavelength absorption onset, band gap energy (E_g) and estimated diameter (in nm), calculated as previously detailed in Section 3.2.1.1, are summarised in Table 3.1.

Table 3.1. Values for absorption onset, Eg (eV) and estimated diameter (nm) of CdS QDs synthesised calculated from Figure 3.4.

$CdCl_2$:Na_2S concentration	Absorption onset wavelength (nm)	E_g (eV)	Estimated diameter (nm)
1:2	377	3.29	3.78
1:1	390	3.18	4.08
2:1	411	3.02	4.65

As the ratio of $CdCl_2$:Na_2S was increased, the absorbance onset wavelength decreased. This corresponded to an increase in E_g, and hence diameter, of CdS QDs capped with 2-mercaptoethanol. This was due to the mechanisms of nucleation and growth of the CdS nanocrystals [3, 4, 13, 16, 17]. Nucleation is limited at smaller concentrations of Na_2S and with Ostwald ripening, subsequent growth through diffusion of the precursors from the surrounding environment to the surface of growth will only continue until the concentration reduces to the equilibrium concentration [3, 13]. Note: the CdS QDs (4.65 nm) synthesised using $CdCl_2$:Na_2S at a ratio of 2:1 were used for the remainder of this thesis.

3.2.3 Size determination *via* TEM imaging

As mentioned earlier, the absorbance onset can be directly related to the band gap energy, and hence size (diameter) of QDs. This section will detail how the CdS QDs diameter were estimated using UV-vis spectrophotometry (4.65 nm) and calculations *via* the hyperbolic band model (4.65 nm), and compare these values to the average sizes determined by TEM imaging. Figure 3.5 shows a TEM image of CdS/2-mercaptoethanol QDs on a carbon coated copper grid, taken with at a 200 000 x magnification.

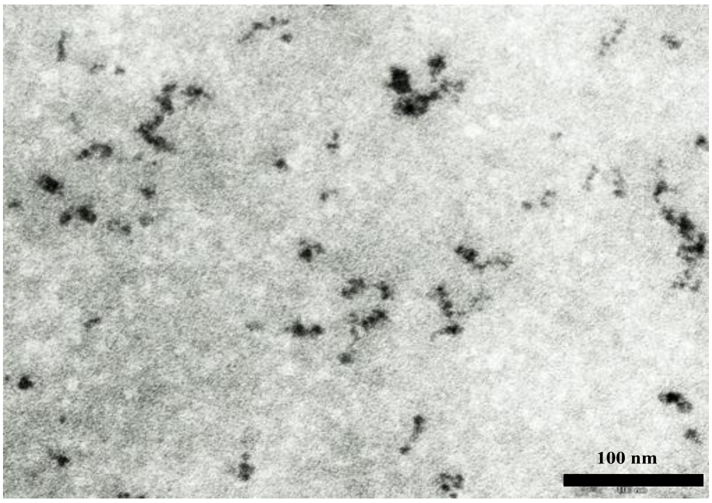

Figure 3.5. TEM image of CdS/2-mercaptoethanol QDs at 200 000 x magnification.

Figure 3.5 shows that the CdS/2-mercaptoethanol QDs appear agglomerated. A size (diameter in nm) distribution histogram is shown in Figure 3.6. Agglomeration of the nanocrystals can be attributed to a number of conditions including the solvent evaporation dynamics and the wetting behaviour of the solvent on the TEM grid, if the particles are electrostatically or sterically stabilised, and the diffusion of the particles through the solvent during the drying process, and sample concentration. In this case the residual DMF solvent used for CdS QD synthesis would dissolve the coatings on the TEM grids under the electron beam. From Figure 3.6, the CdS/2-mercaptoethanol QD diameter was measured to be 4.8 nm ± 1.6 nm from the TEM image (Figure 3.5). A t-test test was conducted and it was found that with 95 % confidence, there was no significant difference between the diameter measured by TEM (4.8 nm ± 1.6 nm) and calculated using the hyperbolic model with UV-vis absorbance spectroscopy (4.65 nm).

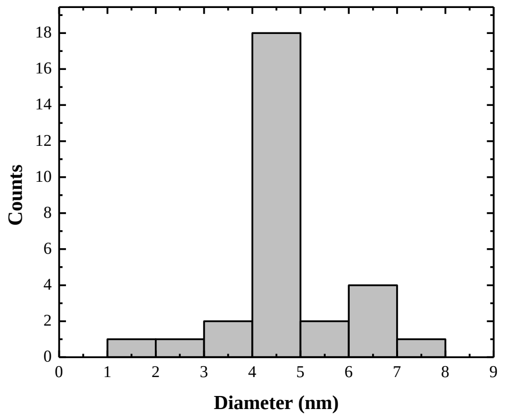

Figure 3.6. Histogram of CdS/2-mercaptoethanol QD diameter measured from TEM imaging (n = 30).

3.2.4 Fluorescence spectra of CdS/2-mercaptoethanol QDs

An excitation wavelength of 350 nm was chosen for fluorescence spectrophotometry measurements based on the absorbance profile of CdS/2-mercaptoethanol QDs, shown in Section 3.2.1, Figure 3.3 (a). In addition, 350 nm is a light setting on the Polilight® instrument which is used to photograph latent fingermarks developed by the fluorescent nanocomposites and discussed later in Chapter 6. Figure 3.7 illustrates the fluorescence emission profile of CdS/2-mercaptoethanol QDs in DMF (using a 25-fold dilution) at an excitation wavelength of 350 nm.

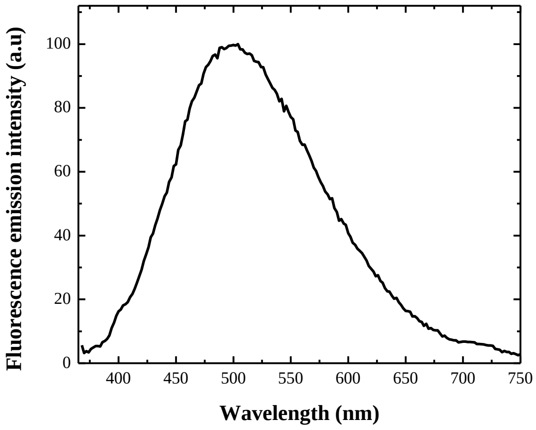

Figure 3.7. Fluorescence emission spectrum of CdS/2-mercaptoethanol QDs in DMF using an excitation wavelength of 350 nm (averaged 50 scans).

QDs are known to possess narrow emission profiles, with FWHMs of typically less than 50 nm, which indicates a narrow size distribution and good crystal quality [4, 7, 18-21], however, this was not observed for CdS/2-mercaptoethanol QDs in DMF in Figure 3.7. The fluorescence emission was broad with a FWHM of 146 nm and a peak maximum of 501 ± 6 nm (n = 10, with 100 averaged scans).

The sharp UV absorbance profile (see Section 3.2.1.1, Figure 3.3), and TEM images for size determination (see Section 3.2.3, Figure 3.5 of this chapter) suggested that the broad fluorescence was not a direct result of a large size distribution. In fact, broad fluorescence emission can be attributed to events on the surface of the QDs, such as surface defects/traps and their interactions with the solvent and capping agent present [4, 7, 9, 14, 16, 21-23].

It has been shown that fluorescence bands depend on the hydrogen bonding ability of the solvent, dielectric constant of both the capping agent and the solvent used [9, 22]. In the case of this thesis DMF was used. DMF is an aprotic solvent with a dielectric constant of 40. The stabilisation of Cd^{2+} ions in DMF has been studied in literature [14, 24, 25]. It was proposed that the C=O from DMF coordinates with Cd^{2+} ions to give Cd^{2+} ---C--- O. Therefore it may be likely that this coordination complex may then compete with the 2-mercaptoethanol capping agent during the synthesis of CdS, after addition of Na_2S. These processes occurring during nucleation and growth of the CdS/2-mercaptoethanol QDs would then contribute to defects on the QD surface [9, 14, 18, 22].

3.3 Synthesis of CdS/C_{12}CTA QDs

This section describes the synthesis of CdS/C_{12}CTA QDs, and characterisation of the successful immobilisation of C_{12}CTA onto the CdS/2-mercaptoethanol QD surface. This immobilisation involved the use of DCC/DMAP in a Steglich esterification, as shown in Figure 3.8.

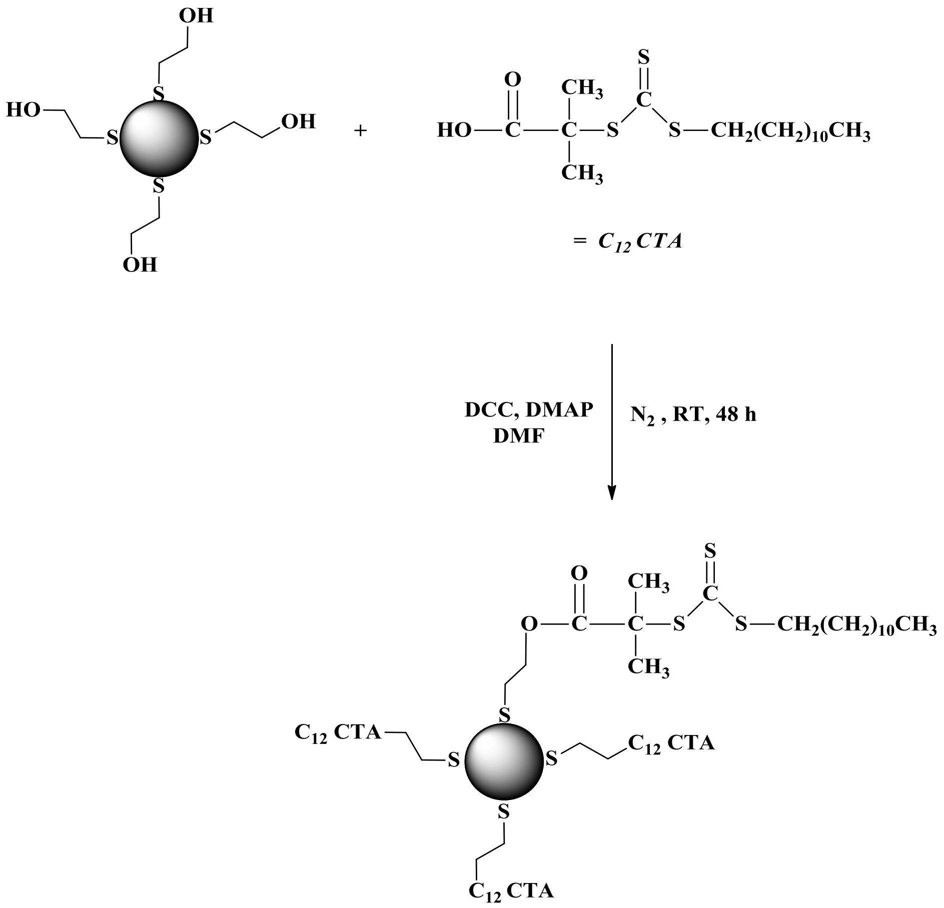

Figure 3.8. Reaction scheme for immobilisation of C_{12}CTA to CdS/2-mercaptoethanol QDs to give CdS/C_{12}CTA QDs.

This is a crucial step in the overall synthesis of CdS/polymer nanocomposites. The immobilised C_{12}CTA aids with additional QD core protection and steric bulk to prevent aggregation, and is also essential for the surface initiated RAFT polymerisation process to be employed.

Indications that the CdS/C_{12}CTA QDs were successfully synthesised was observed visually in the laboratory and are discussed in the next section in conjunction with the mechanism of the Steglich esterification process.

The sections following this will discuss their characterisation by ^{1}H NMR spectroscopy, TGA, and FTIR spectroscopic analysis, respectively.

3.3.1 Steglich esterification - Mechanism

The Steglich esterification is a mild esterification technique performed at or below room temperatures and often favoured for use with sensitive carboxylic acids and/or alcohols [26]. This technique was chosen as the CdS QDs, though capped with 2-mercaptoethanol, may be susceptible to destruction under high temperatures used in conventional esterification. Figure 3.9 shows the mechanism for the Steglich reaction between CdS/2 mercaptoethanol QDs and C_{12}CTA using DCC/DMAP coupling. Figure 3.10 shows the role of DMAP as a catalyst for the reaction.

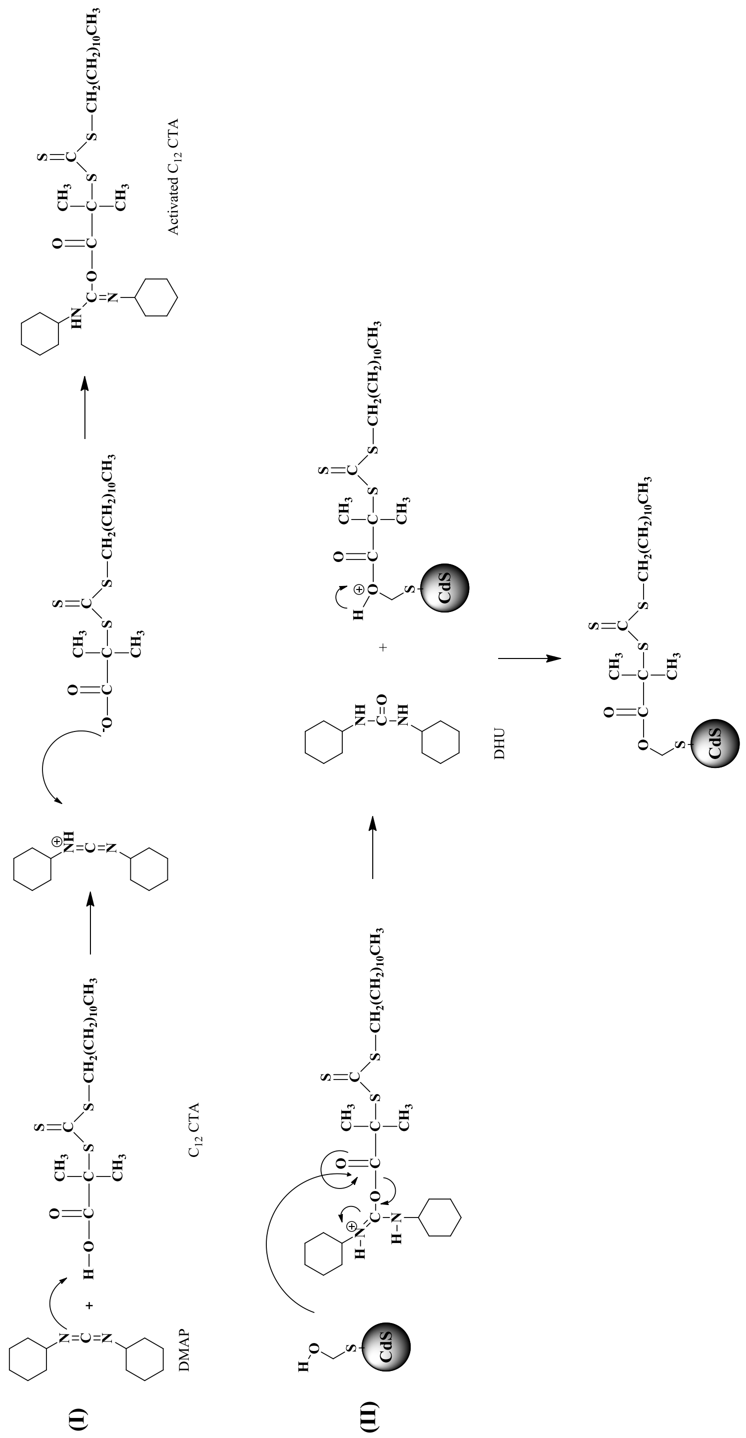

Figure 3.9. Mechanism for the DCC coupling reaction between CdS/2-mercaptoethanol QDs and C_{12}CTA (I) Initial activation of C_{12}CTA with DCC and (II) esterification between the activated C_{12}CTA and CdS/2-mercaptoethanol.

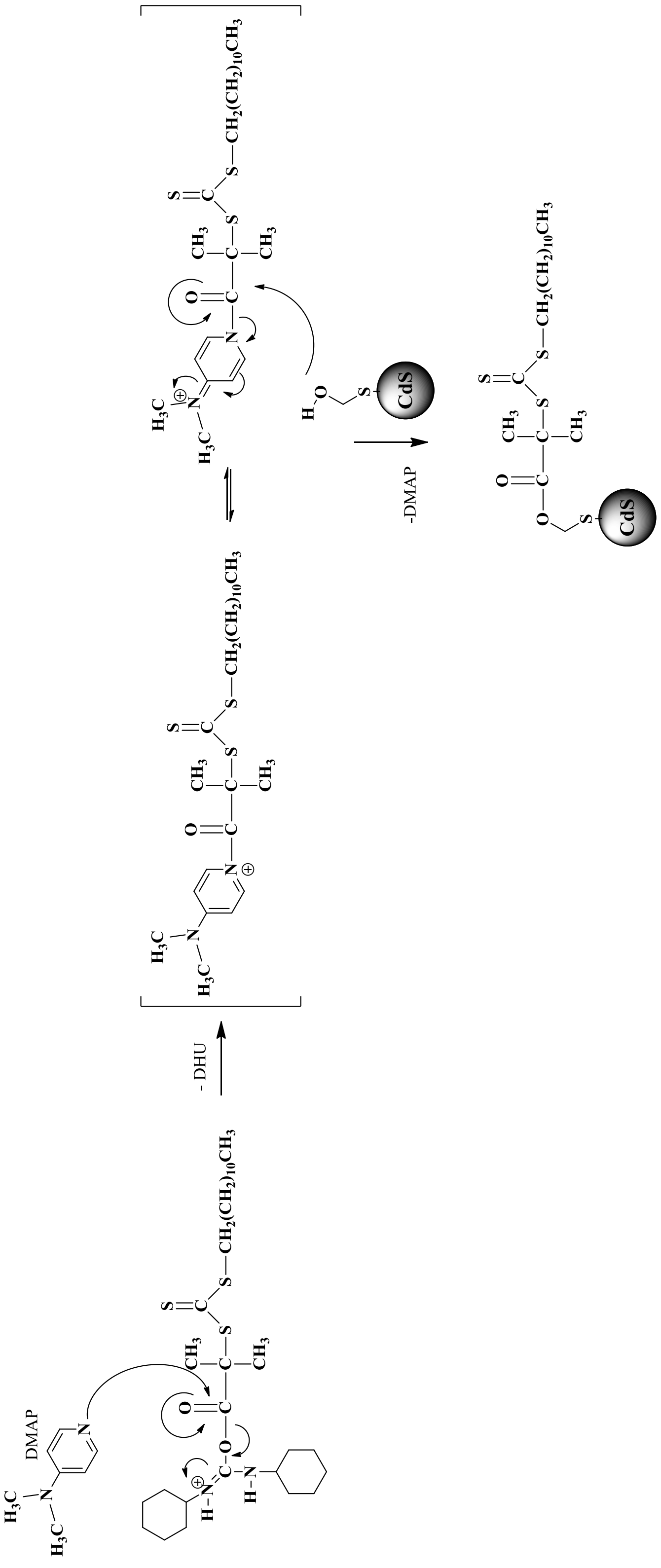

Figure 3.10. Mechanism for the role of DMAP in accelerating the esterification from Figure 3.9.

The product was a slightly opaque yellow solution, consisting of CdS/C_{12}CTA QDs and dicyclohexylurea (DHU) in DMF. The opaqueness was a result of the secondary product, DHU, produced during Steglich esterification (see Figure 3.9). DHU is a result of the water uptake by DCC during esterification [26, 27].

If the solution stayed clear and yellow after 48 h, and did not turn opaque then DHU was not produced and esterification was unsuccessful. If the solution turned completely opaque, non-translucent and white; the by-product (*N*-acyl urea) was favoured [26, 27]. DMAP aids in reducing the production of this by-product, and accelerates the esterification (shown in Figure 3.10) [26, 27].

3.3.2 Thermal and spectral analysis of CdS/2-mercaptoethanol QDs versus CdS/C_{12}CTA QDs

To analyse the CdS/C_{12}CTA QDs, the product was isolated by drying 5 mL samples of the bulk solution under nitrogen for at least 48 h to evaporate off the DMF solvent. This section will discuss the spectral analysis performed on the isolated CdS/C_{12}CTA QDs using FTIR and TGA, respectively and provide evidence of successful Steglich esterification, and hence immobilisation of C_{12}CTA onto the CdS/2-mercaptoethanol QD surface.

3.3.2.1 Fourier transform infra-red (FTIR) spectral analysis

FTIR was employed to structurally differentiate between CdS/2-mercaptoethanol QDs and CdS/C_{12}CTA QDs after the Steglich esterification. Figure 3.11 shows the overlayed FTIR spectra of (a) CdS/2-mercaptoethanol QDs and (b) CdS/C_{12}CTA QDs.

Despite extensive sample drying under N_2 to evaporate the DMF, both spectra show amide vibrations/stretches at 1680 cm^{-1}, attributed to residual DMF in the samples.

The spectrum of the CdS/2-mercaptoethanol QDs (Figure 3.11 (a)) shows a strong OH stretch at 3300 cm^{-1} corresponding to the OH in 2-mercaptoethanol, and any residual water in the sample. C-O stretches occurring in the 1000 cm^{-1} to 1300 cm^{-1} were also attributed to the OH in 2-mercaptoethanol. This shows that there are free OH groups where by C_{12}CTA can be immobilised to. C-H stretching vibrations were observed at 3000 cm^{-1} and 2800 cm^{-1} and CH_2 bending vibrations at 1430 cm^{-1}, corresponding to the CH_2 groups present in 2-mercaptoethanol [28]. C-S stretching at 570-710 cm^{-1} was not observed as it is known to be a weak vibration [29].

The free OH groups from the 2-meraptoethanol on the surface were used to form an ester link with carboxyl terminated C_{12}CTA *via* Steglich esterification to give CdS/C_{12}CTA QDs (FTIR spectra shown in Figure 3.11 (b)).

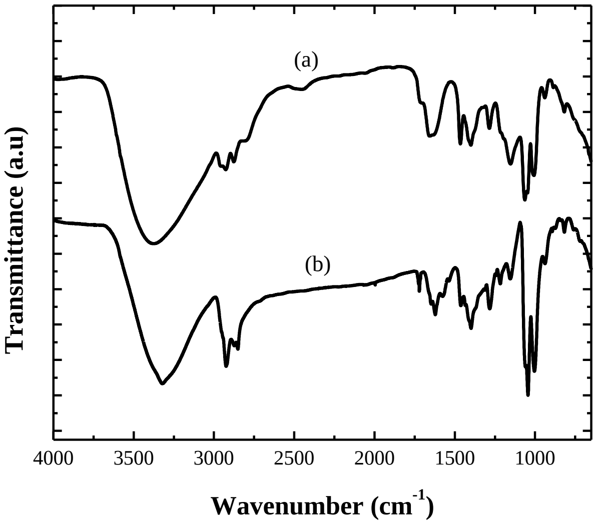

Figure 3.11. Stacked FTIR spectra of (a) CdS/2-mercaptoethanol QDs and (b) CdS/C_{12}CTA QDs.

The spectrum of CdS/C_{12}CTA QDs (Figure 3.11 (b)) also shows a peak at 3300 cm^{-1} which was attributed to either one of, or a mixture of, unreacted OH groups (from the CdS/2-mercaptoethanol QDs or free C_{12}CTA), and/or residual water in the sample. The C-H stretching vibrations at 3000 cm^{-1} and 2800 cm^{-1} and CH_2 bending at 1430 cm^{-1} appear stronger for CdS/C_{12}CTA QDs due to the longer CH_2 chain in the immobilised C_{12}CTA. C=S peaks are observed between 1275 cm^{-1} and 1030 cm^{-1} and coincide with C-O peaks that correspond to the new ester bond formed. Due to this overlap in vibrations they could not be used conclusively to show evidence of successful immobilisation of the C_{12}CTA onto the CdS/2-mercaptoethanol QD surface. However, there is a significant C=O stretch at 1720 cm^{-1} that appears after the esterification reaction which is at a lower frequency than that of the original C_{12}CTA carboxylic acid C=O stretch at 1780 cm^{-1}. This provides strong evidence of the formation of an ester bond and hence immobilisation of the C_{12}CTA [28].

3.3.2.2 Thermogravimetric analysis (TGA)

The thermal degradation, or decomposition temperatures (T_d), and TGA curve profiles of CdS/2-mercaptoethanol QDs and CdS/C_{12}CTA QDs were compared. Figure 3.12 shows the TGA thermograms for (a) CdS/2-mercaptoethanol QDs and (b) CdS/C_{12}CTA QDs.

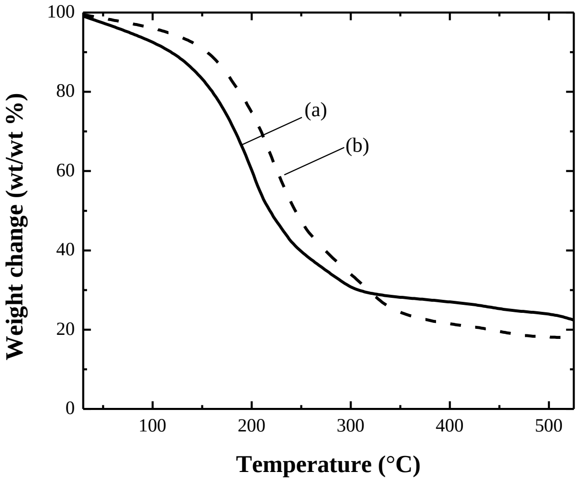

Figure 3.12. TGA thermograms for (a) CdS/2-mercaptoethanol QDs (solid line) and (b) CdS/C_{12}CTA QDs.

Table 3.2. Calculated values of residue, T_d as a range and weight loss after T_d, from the TGA thermograms of CTA (a) CdS/p(DMA) and (b) CdS/p(DMA-*co*-MMA).

	Residue (wt/wt %) after T_d	Td (°C) range	T_d calculated (°C)	Max. weight loss at T_d (wt/wt %)
(a)	21.8	200-350	221.1	56.9
(b)	18.7	230-370	232.6	65.7

Physically adsorbed water and residual DMF solvent was accounted for in the weight loss between 100 °C and 200 °C. The TGA thermogram for CdS/2-mercaptoethanol QDs ((Figure 3.12 (a)) has its maximum weight loss (56 wt/wt %) between 200 °C and 350 °C. After immobilisation of the C_{12}CTA onto CdS/2-mercaptoethanol QD surface *via* Steglich esterification, the TGA thermogram recorded (Figure 3.12 (b)) a larger weight loss of 65 wt/wt % at higher temperatures between 230 °C and 370 °C. The slightly higher weight loss accounts for the larger C_{12}CTA molecule on the CdS QD surface (with respect to 2-mercaptoethanol). The wt/wt % calculated for the CdS/C_{12}CTA QDs (18.7 wt/wt %) was less than that calculated for the CdS/2-mercaptoethanol QDs (21.8 wt/wt %). The difference between these two residue wt/wt % (3.1 wt/wt %) correlates to a degradation of the larger molecule C_{12}CTA immobilised to the surface as opposed to the smaller 2-mercaptoethanol molecules. This indicates that immobilisation of C_{12}CTA onto CdS/2-mercaptoethanol QD surface *via* the Steglich reaction was successful.

3.3.3 Optical properties of CdS/2-mercaptoethanol QDs versus CdS/C_{12}CTA QDs

It is important to monitor the fluorescence emission of the CdS QDs throughout the surface functionalisation. This was done by visually using a UV-torch alongside measuring the emission intensity using a fluorescence spectrophotometer at an excitation of 350 nm. Under UV-light illumination (UV torch) the solution that contained CdS/C_{12}CTA QDs fluoresced green and appeared to have not have lost fluorescence integrity with respect to the CdS/2-mercaptoethanol QDs prior to esterification. Figure 3.13 shows the fluorescence emission spectra of the CdS/2-mercaptoethanol QDs (Figure 3.13 (a), dashed line) compared to the CdS/C_{12}CTA QDs (Figure 3.13 (b), solid line).

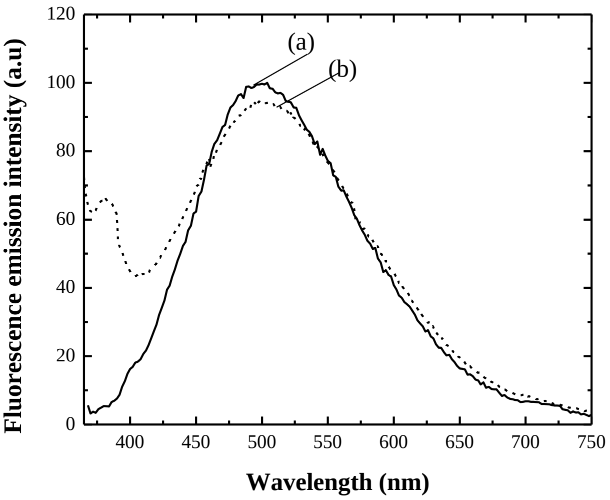

Figure 3.13. Overlayed fluorescence spectra of (a) CdS/2-mercaptoethanol QDs and (b) CdS/C_{12}CTA QDs.

The starting material CdS/2-mercaptoethanol QDs shows a strong emission maximum at 499 nm (Figure 3.13 (a)) which was unchanged after DCC coupling with the carboxylated C_{12}CTA to form the CdS/C_{12}CTA QDs (Figure 3.13 (b)). There was however an additional emission peak in the CdS/C_{12}CTA QD spectrum at 388 nm, attributed to the presence of C_{12}CTA and confirming attachment to the CdS QD. This observation will also be important for the RAFT polymerisation of monomers from the CdS/C_{12}CTA QD surface, discussed later in this chapter. It was important that this peak remains after surface initiated RAFT polymerisation indicating that the CTA still resides at the end of the polymer chains and is therefore available for post-derivitisation after the polymerisation. Later in this thesis, Chapter 5, the CTA end group of the various nanocomposites will be used to attach magnetic Fe_2O_3 nanoparticles to the CdS/C_{12}CTA produced earlier.

To this end, importantly, there were no significant changes in fluorescence emission intensities, or peak maxima, after immobilisation of the C_{12}CTA onto CdS/2-mercaptoethanol QD surface (Figure 3.13). This was accredited to the mild conditions used for the Steglich esterification performed. Hence surface initiated RAFT polymerisation was then performed.

This subsequent SIP step is discussed in the following sections. First the synthesis of CdS/p(DMA) will be discussed, including information about experimental design and polymerisation monitoring of the DMA using ^{1}H NMR and FTIR analysis. This will then lead into of the characterisation of synthesised CdS/p(DMA-*co*-MMA) and CdS/p(DMA-*co*-Sty) nanocomposites (Chapter 2 Section 2.3.3). The last sections of this chapter will focus on comparing the three nanocomposites in terms of kinetic studies, TGA, and optical properties (characterisation *via* UV-vis and fluorescence spectrophotometry).

3.4 Synthesis of CdS/p(DMA) *via* surface initiated RAFT polymerisation from CdS/C_{12}CTA QDs

RAFT polymerisation is capable of controlling the grafting polymerisation of a wide choice of monomers thus creating a polymer with low PDI [30-33]. Its experimental conditions are often versatile, using similar conditions to that of conventional free-radical polymerisation. However the difference lies in the use of a RAFT agent, or CTA, to provide an intermediate step in radical formation, and hence control. The CTA end group is retained after polymerisation allowing for straightforward modification of the polymer with either re-initiation for polymerisation of a different monomer (i.e., to form a block co-polymer), or with a functional molecule/substrate [33-35].

This section describes the surface initiated RAFT polymerisation of DMA from the CdS/C_{12}CTA QD surface to give a CdS/p(DMA) nanocomposite. Figure 3.14 shows the general synthesis of CdS/p(DMA) *via* surface initiated RAFT polymerisation.

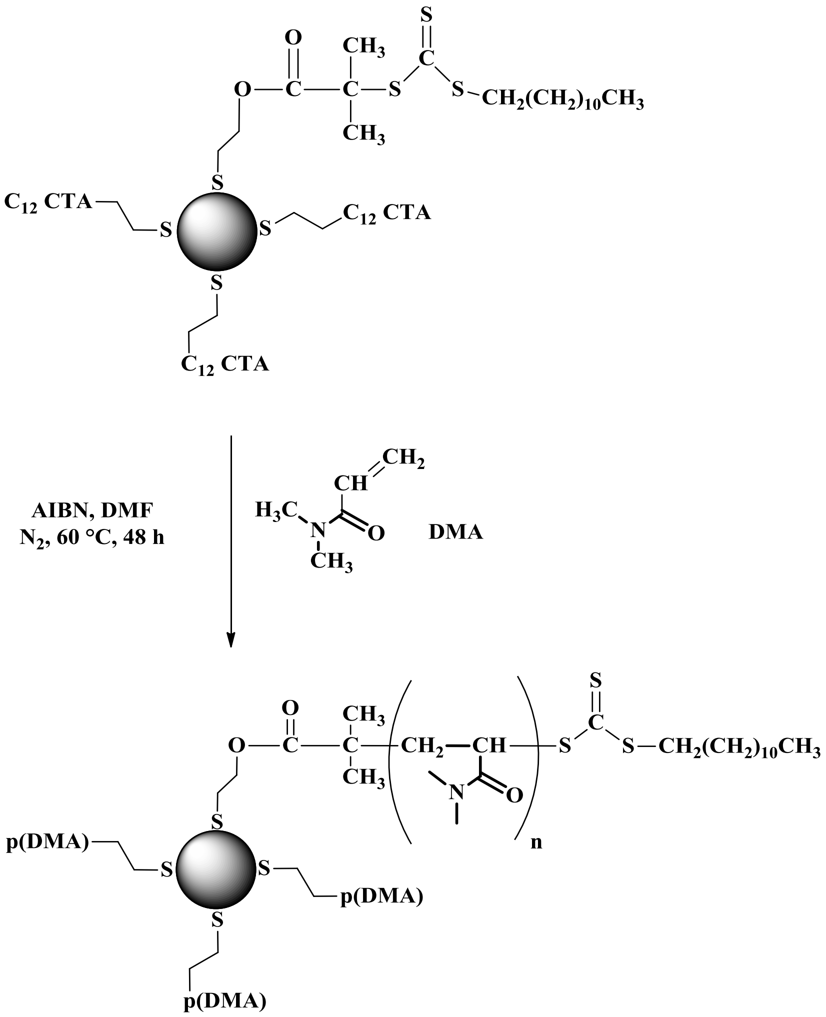

Figure 3.14. Scheme for the synthesis of CdS/p(DMA) nanocomposite *via* surface initiated RAFT polymerisation of DMA from CdS/C_{12}CTA QDs.

Polymerisation was carried out at 60 °C, for 48 h. A temperature of 60 °C was chosen for the stable initiation of AIBN. As the DMA was grafted from the CdS/C_{12}CTA QDs the solution viscosity visually increased. After polymerisation was complete (at a reaction time of t=48 h) the polymer nanocomposite was purified *via* precipitation into excess cold diethyl ether to give a clear, sticky, water soluble CdS/p(DMA) nanocomposite gel that had a slight yellow tinge. This yellow tinge was from the C_{12}CTA end-groups, and the presence of the sulfur moieties in the thiocarbonylthio active site. Thiocarbonylthio CTAs are known to transcribe its yellow colour to the resultant RAFT polymer, whereas dithioesters are often red or orange [36-38].

Upon illumination with a UV-torch the CdS/p(DMA) nanocomposite fluoresced green. Full characterisation using UV-vis and fluorescence spectrophotometry will be discussed in Section 3.8 later in this chapter.

3.4.1 Experimental design of the RAFT polymerisation of DMA from CdS/C_{12}CTA QDs

Background information on RAFT polymerisation, including a schematic of the mechanism for the reversible chain transfer is discussed in Chapter 1, Section 1.9. Here, this section will briefly discuss the experimental design behind the RAFT process used to synthesise the CdS/p(DMA) nanocomposites.

As described by Moad and co-workers [31-33], the key idea is that in RAFT polymerisation, the deactivation-activation equilibria of chain transfer reactions, and radicals are neither formed nor destroyed in these steps. This is evident through the kinetics of a RAFT polymerisation (discussed in section 3.7 later in this chapter). Although similar to conventional radical polymerisation, the rate should be half order with respect to the initiator but independent of the RAFT agent as radical-radical termination, molecular weight, chain length does not affect the polymerisation [39-41]. The experimental design for the synthesis of CdS/p(DMA) was therefore based on conventional free radical polymerisation reactions with careful consideration of initiator (AIBN) concentration with respect to the quantity of the CdS/C_{12}CTA QDs which influences the rate of radical generation.

The next section will outline the differences observed when RAFT polymerisation was used in comparison to conventional radical polymerisation, for the polymerisation of

DMA. Also discussed is the optimisation of ratios of RAFT agent (C_{12}CTA) to initiator (AIBN).

3.4.1.1.1 Conventional free radical polymerisation versus RAFT polymerisation of DMA

An investigation on the effects of concentration of AIBN and C_{12}CTA concentration on the molecular weight and PDI of p(DMA) synthesised *via* RAFT was performed. Different ratios of AIBN to C_{12}CTA were used to determine the optimum ratio of CTA to AIBN for use to synthesise the desired polymer.

Polymerisation reactions were performed at 60 °C in DMF for 48 h. Table 3.3 summarises the data collected using GPC and ^{1}H NMR spectroscopy, showing the M_n and PDI of the p(DMA) synthesised *via* conventional free radical polymerisation, RAFT polymerisation using the C_{12}CTA only and RAFT polymerisation using the CdS/C_{12}CTA QDs (where the polymer was cleaved from the CdS QDs using H_2SO_4 before analysis in the GPC column). All were carried out at various AIBN:CTA ratios (a) 1:2, (b) 1:3 and (c) 1:5.

Table 3.3. M_n, Conversion and PDI determined by GPC and ^1H NMR spectroscopy of synthesised by conventional polymerisation and RAFT polymerisation.

		M_n (g.mol^{-1})	**Conversion (%)**	**PDI**
Conventional free radical	(a)	2 354	> 99	1.35
	(b)	8 156	> 99	1.36
	(c)	11 006	> 99	1.38
RAFT polymerisation using C_{12}CTA	(a)	10 065	92	1.21
	(b)	11 654	94	1.11
	(c)	13 236	> 99	1.09
RAFT polymerisation using CdS/C_{12}CTA QDs	(a)	8 886	97	1.18
	(b)	9 054	92	1.12
	(c)	11 041	95	1.06

Conversion of monomer was high in all cases. This was due to the high reactivity of DMA to form radicals upon initiation with AIBN. In the conventional free radical polymerisation of DMA there was a drastic decrease in the M_n and increase in the PDI. This is due to the constant formation of radicals and radical-radical terminations of polymer chains [42]. As the amount of AIBN radical initiator increased, the number of propagating chains increases which leads to smaller polymeric chains and uncontrolled chain lengths. In the case of RAFT polymerisation of DMA with C_{12}CTA, or with C_{12}CTA immobilised onto the CdS QD surface smaller, PDIs were calculated. When conditions (a), (b), and (c) are compared to that of the conventional radical polymerisation, there are smaller decreases in M_w. This decrease in M_w was due to the controlled conditions given by the presence of the C_{12}CTA. As a RAFT agent it mediates polymerisation *via* a reversible chain-transfer process [30-33].

The M_n in general was below 15,000 hence small PDIs were expected (Table 3.1). However, upon critical comparison of these two polymerisation techniques it can be seen that the PDIs recorded for conventional free radical were greater at 1.3 whereas for the RAFT polymerisations were equal to or smaller than 1.1. This is a common advantageous feature of RAFT polymerisations where the control of the radical species with the introduction of a RAFT agent produces polymers with small PDIs [30-33]. This investigation was an initial indication that RAFT polymerisation was successful. It was also important to conduct kinetic studies on the consumption of monomers during RAFT polymerisation [30-33, 40, 41, 43]. This is described later in Section 3.7 of this chapter.

Condition (c), where a ratio of 1:5 AIBN : C_{12}CTA was chosen for the synthesis of the CdS/p(DMA) nanocomposites. These conditions were also used in the synthesis of CdS/p(DMA-*co*-MMA) and CdS/p(DMA-*co*-MMA) powders, described in Section 3.5.

The following section will describe how the RAFT polymerisation of DMA from CdS/C_{12}CTA QDs was monitored using spectral analysis, ^{1}H NMR and FTIR, respectively.

3.4.2 Monitoring the RAFT polymerisation of DMA from CdS/C_{12}CTA QDs using ^{1}H NMR and FTIR spectroscopies

RAFT polymerisation of DMA from CdS/C_{12}CTA QDs was monitored spectrally using ^{1}H NMR and FTIR spectroscopies. Using ^{1}H NMR the disappearance of peaks attributed to the protons on the vinyl groups of the DMA monomer (between 6 ppm and 8 ppm) can be monitored. In addition, the appearance of broad peaks attributed to CH_2-CH_2 of the growing p(DMA) (between 1 ppm and 3 ppm) indicated successful polymerisation. Similarly, for FTIR analysis peaks associated with the C=C vinyl group stretching of the monomer at 700 cm^{-1} diminishes and the C-H stretching of the polymers at approximately 2900 cm^{-1} increases as polymerisation progresses.

The surface initiated RAFT polymerisation of DMA from the CdS/C_{12}CTA QDs was monitored using ^{1}H NMR and FTIR spectroscopies, comparing reaction times of t = 0 h to t = 48 h (when polymerisation had reached maximum monomer conversion). Characterisation of the final purified CdS/p(DMA) after precipitation into excess diethyl ether is also shown. The ^{1}H NMR spectra of CdS/p(DMA) at t = 0 h, CdS/p(DMA) (t=48 h) with a toluene internal standard, and isolated/purified CdS/p(DMA) are respectively shown in Figure 3.15 (a) to (c).

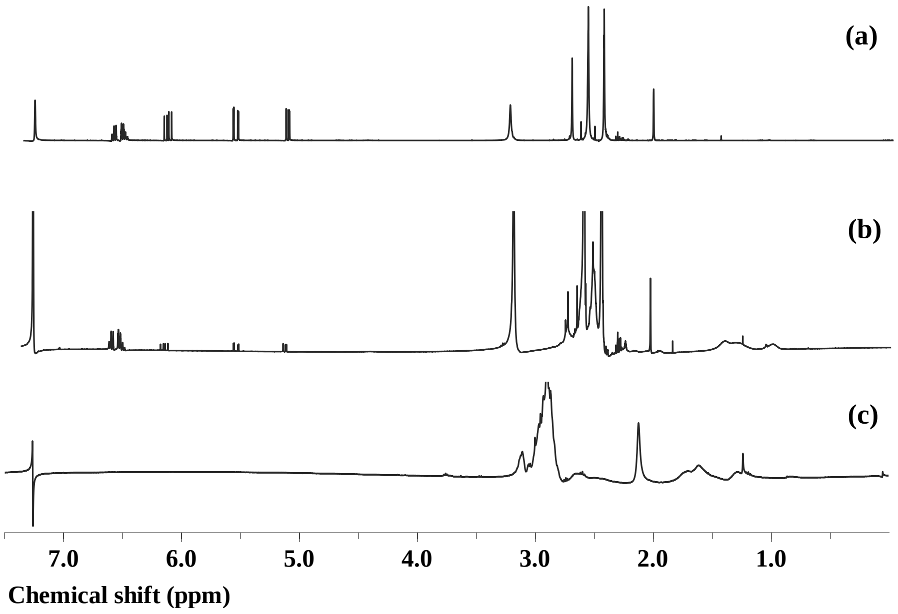

Figure 3.15. Overlayed ^{1}H NMR spectra of CdS/p(DMA) at (a) t = 0 h, (b) t = 48 h and (c) isolated CdS/p(DMA) upon precipitation in excess diethyl ether. Solvent: $CDCl_3$.

It is clear that the peaks associated with the protons on $\mathbf{H_2}$C=C**H-**, in the regions between 7 ppm and 5 ppm and about 3 ppm have diminished considerably from t = 0 h reaction time (Figure 3.15 (a)) to t = 48 h (Figure 3.15 (b)). This showed that the DMA monomer has been consumed during polymerisation. The difference in integration values of these vinyl peaks were used to calculate monomer % conversion, shown in Section 3.4.1.1.1 of this chapter. The ^{1}H NMR spectra of CdS/p(DMA) at t = 48 h reaction time, and purified CdS/p(DMA) (Figure 3.15 (b) and (c)) also showed the consumption of the DMA monomers by peaks associated with protons on $\mathbf{H_2}$C-C-**H** polymer backbone apparent between 2 ppm and 1 ppm [42]. These peaks were also broad which is characteristic of polymers [42].

Figure 3.16 shows stacked FTIR spectra of CdS/p(DMA) at t = 0 and after purification into excess diethyl ether.

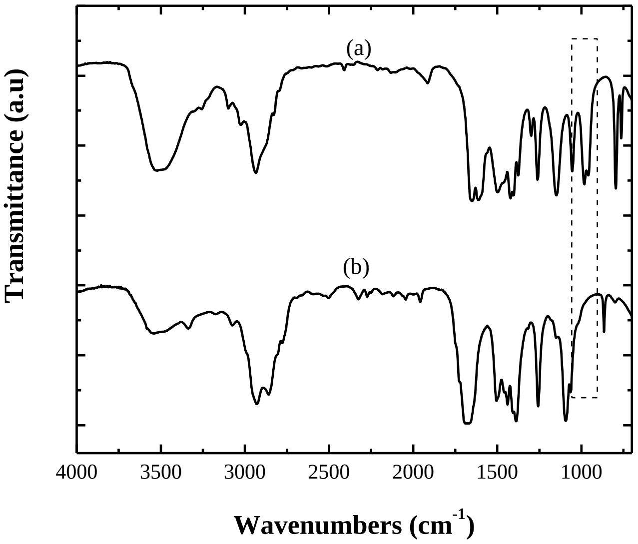

Figure 3.16. FTIR spectra of CdS/p(DMA) at (a) t = 0 h and(b) purified CdS/p(DMA).

From the FTIR spectra in Figure 3.16 (a) versus (b) it is evident that the vinyl monomer peaks in the 990-910 cm^{-1} region (shown in the dashed box) diminished, and that the C-H stretching from the polymer appeared at 3000 cm^{-1} and 2800 cm^{-1} became more apparent (indicative of the polymer chain). Methyl peaks at 1380 cm^{-1} and amide C=O peaks at 1680 cm^{-1} were attributed to DMA, however, the presence of residual DMF solvent would also contribute to these peaks. It was difficult to achieve conclusive results on the presence of the C=S peaks associated with the C_{12}CTA typically observed between 1275 cm^{-1} and 1030 cm^{-1}, as they were obscured by the C-O peaks present from the DMF, and DMA monomer or repeating units. There are weak peaks however around the 750 cm^{-1} region which correspond to the C-S stretching in the C_{12}CTA [44].

3.5 Synthesis of CdS/p(DMA-*co*-MMA) and CdS/p(DMA-*co*-Sty) powders

This section will describe the surface initiated RAFT polymerisation of DMA with MMA and Sty (independently) from CdS/C_{12}CTA QDs to give CdS/p(DMA-*co*-MMA) and CdS/p(DMA-*co*-Sty). Note, these polymers are random co-polymers p(DMA-*co*-MMA) and p(DMA-*co*-Sty), grafted from the CdS surface. Figure 3.17 (a) and (b) shows the general scheme for the synthesis of CdS/p(DMA-*co*-MMA) and CdS/p(DMA-*co*-Sty), respectively, *via* surface initiated RAFT polymerisation using CdS/C_{12}CTA QDs and the appropriate monomers.

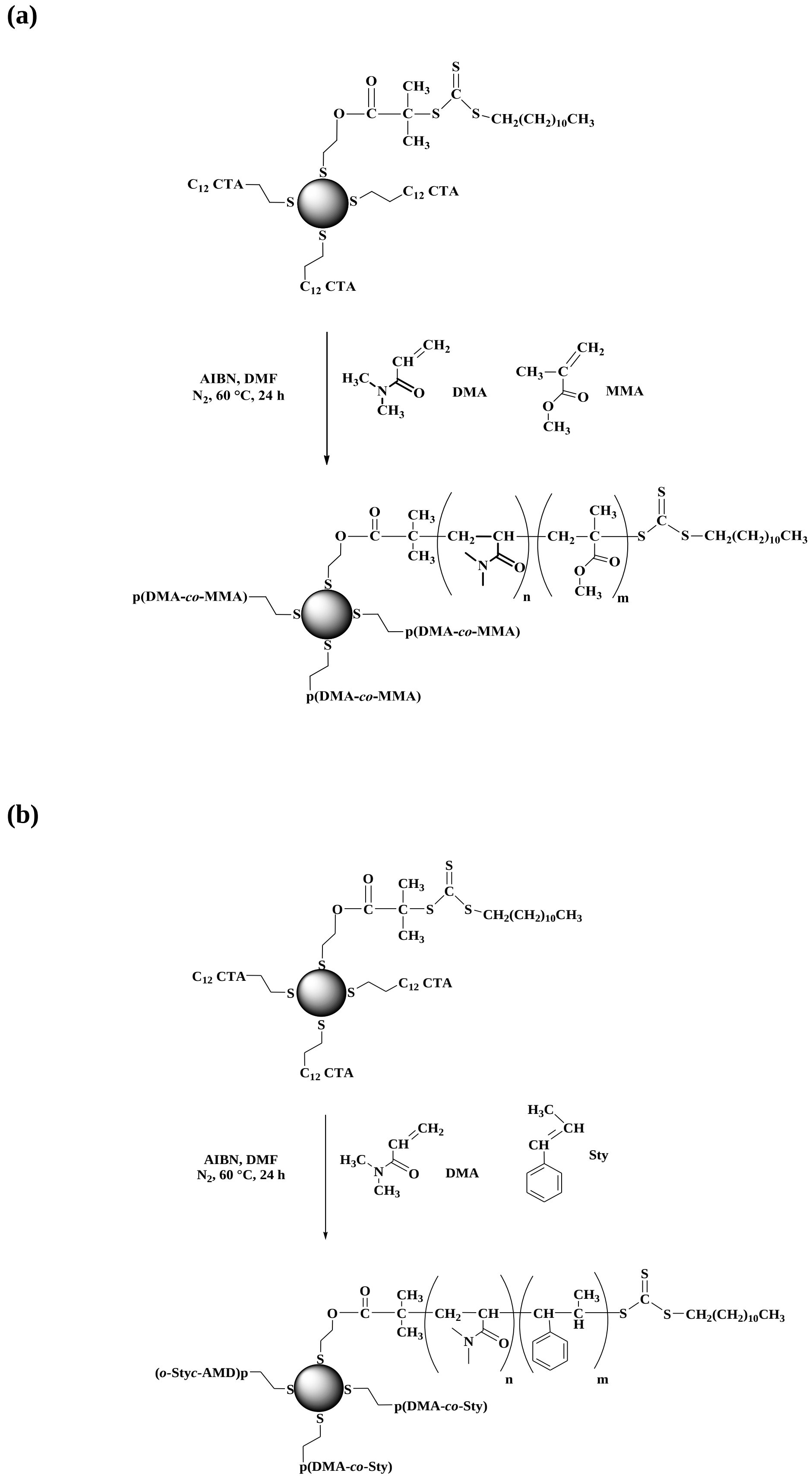

Figure 3.17. Scheme for the synthesis of (a) CdS/p(DMA-*co*-MMA) and (b) CdS/p(DMA-*co*-Sty) *via* initiated RAFT polymerisation of DMA, MMA and Sty from CdS/C$_{12}$CTA QDs.

The synthesis of CdS/p(DMA-*co*-MMA) and CdS/p(DMA-*co*-Sty) were based on the experimental design established earlier in this chapter (Section 3.4.1, for CdS/p(DMA) nanocomposites). A 1:1 ratio of each monomer (i.e., DMA:MMA and DMA:Sty) and a 1:5 ratio of AIBN initiator to CdS/C_{12}CTA QDs was used. Polymerisation was carried out at 60 °C for 24 h (not 48 h as for the p(DMA)). A shorter polymerisation time (t = 24 h) was required for the copolymerisation in comparison to the homopolymerisation of DMA because over 95 % conversion of the monomers (DMA, MMA and Sty) were observed after 24 h which was attributed to the differences in monomer reactivity. This will be discussed further in the polymer characterisation Section 3.6.

As the polymerisation progressed the solution viscosity visually increased as the monomers were randomly grafted from the CdS/C_{12}CTA QD surface. After polymerisation was complete (at a reaction time of t = 24 h) purification *via* precipitation into excess cold methanol yielded a fine powder with a yellow tinge, for both the CdS/p(DMA-*co*-MMA) and CdS/p(DMA-*co*-Sty) nanocomposites. Similar to the CdS/p(DMA) this yellow tinge was attributed to the C_{12}CTA end-groups and the presence of the sulfur moieties in the active site. Upon illumination with a UV-torch the CdS/p(DMA-*co*-MMA) and CdS/p(DMA-*co*-Sty)) nanocomposite powders fluoresced green. The optical properties of these CdS/polymer nanocomposites are discussed in Section 3.8 of this chapter.

3.6 Characterisation of the RAFT polymers in the CdS/polymer nanocomposites

Similar to the previous sections, describing the synthesis and characterisation of CdS/p(DMA), the synthesis of CdS/p(DMA-*co*-MMA) and CdS/p(DMA-*co*-Sty) nanocomposites was monitored using FTIR, ^{1}H NMR and GPC analysis. This section discusses the results obtained using these techniques.

3.6.1 Monitoring the RAFT co-polymerisation of DMA with MMA and Sty, from CdS/C_{12}CTA QD surfaces using ^{1}H NMR spectroscopy and GPC

^{1}H NMR spectra of the monomers, DMA, MMA and Sty, AIBN initiator, CdS/C_{12}CTA QDs, and CdS/p(DMA-*co*-MMA) and CdS/p(DMA-*co*-Sty) nanocomposites were recorded in $CDCl_{3.}$This section will describe the ^{1}H NMR spectra recorded for a reaction time of t = 0 h, t = 24 h, and purified after precipitation into cold excess methanol. The ^{1}H NMR of the purified samples, CdS/p(DMA-*co*-MMA) and CdS/p(DMA-*co*-Sty) can be seen in Chapter 8 Section 8.1 Appendix A.

3.6.1.1 ^{1}H NMR analysis of CdS/p(DMA-*co*-MMA)

In all ^{1}H NMR spectra, the characteristic peak associated with the C_{12}CTA, S-$CH_{2,}$ was present at 3.2 ppm. It is clear that the peaks associated with the protons on $\mathbf{H_2}C=C\mathbf{H}$**-**, in the regions between 6.5 ppm and 5 ppm have diminished considerably when the ^{1}H NMR spectrum of CdS/p(DMA-*co*-MMA) at t = 0 h reaction time is compared to the ^{1}H NMR spectrum at t = 24. This shows that the DMA and MMA monomers were consumed during RAFT polymerisation. The integration values of these alkene peaks were used to calculate monomer % conversion (82 %), shown in Section 0 of this chapter. The ^{1}H NMR spectra of CdS/p(DMA-*co*-MMA) at t = 24 h reaction time and purified CdS/p(DMA-*co*-MMA) also show the consumption of the DMA and MMA monomers by the presence of broad peaks for $\mathbf{H_2}$C-C-**H** (of the growing polymer chain), apparent between 2 ppm and 1 ppm [42]. The peak observed at 3.78 ppm is from the O-C$\mathbf{H_3}$ moiety of the methacrylate. Finally the peak at 2.71 ppm correlates to the N-$\mathbf{CH_3}$ of dimethylacrylamide.

3.6.1.2 ^{1}H NMR analysis of CdS/p(DMA-*co*-Sty)

In all ^{1}H NMR spectra, the characteristic peak associated with the C_{12}CTA, S-$CH_{2,}$ was present at 3.2 ppm. It is clear that the peaks associated with the protons on $\mathbf{H_2}$C=C**H**-, in the regions between 7 ppm and 5 ppm have diminished considerably when the ^{1}H NMR spectrum of CdS/p(DMA-*co*-Sty) at t = 0 h reaction time is compared to the ^{1}H NMR spectrum at t = 48 h. This shows that the DMA and Sty monomers were consumed during RAFT polymerisation. The integration values of these alkene peaks were used to calculate monomer % conversion (91 %) stated in Section 0 of this chapter. The ^{1}H NMR spectra of CdS/p(DMA-*co*-Sty) at t = 48 h reaction time and purified CdS/p(DMA-*co*-Sty) also show the consumption of the DMA and Sty monomers by the presence of broad peaks for $\mathbf{H_2}$C-C-**H** (of the growing polymer chain) apparent between 2 ppm and 1 ppm [42]. The peak observed 7.11 ppm is from the Ph-**H** moiety of the styrene and the peak at 2.71 ppm correlates to the N-$\mathbf{CH_3}$ of dimethylacrylamide.

GPC analysis of CdS/polymer nanocomposites

RAFT polymerisation was validated by ^{1}H NMR and GPC analysis. Table 3.4 shows the PDIs, molecular weight number average (M_n), monomer ratios in the final random co-polymers (DMA:MMA/Sty) and monomer conversions (%) for each CdS/polymer nanocomposite, as determined by ^{1}H NMR and GPC measurements.

Table 3.4. Monomer ratio consumed in polymerisation monomer conversion, M_n and PDI values calculated for polymers grafted from CdS QDs; p(DMA), p(DMA-*co*-MMA) and p(DMA-*co*-Sty), respectively.

CdS/polymer	Monomer ratios	Conversion (%)	M_n (g.mol^{-1})	PDI
p(DMA)	N/A	95	10 098	1.06
p(DMA-*co*-MMA)	6.3:2.7	82	18 756	1.21
p(DMA-*co*-Sty	5.3:4.7	91	26 987	1.19

All nanocomposites exhibited low PDIs (between 1.06 and 1.21) characteristic of RAFT polymerisations, and a clear indication of a controlled (or reversible-deactivation radical) polymerisation [31, 45, 46]. Further, all nanocomposites show low M_n values typical of a “grafting-from” approach. These low M_n values are a direct result of steric hindrance from the growing polymer chains reducing the probability of subsequent monomer attachment. It does however allow for a higher grafting density [47] ensuring that the core QDs are well protected. Importantly, polymers with a low M_n have several advantages in the work presented here; firstly, the nanocomposite retains a high degree of optical transparency so that maximum fluorescence can be observed [47], secondly smaller nanocomposite particle sizes resulted from the low M_n which is ideal for deposition onto fingermark ridges.

The final CdS/p(DMA-*co*-MMA) and CdS/p(DMA-*co*-Sty) nanocomposites showed a DMA:MMA and DMA:Sty ratio of 0.63:0.27 and 0.53:0.47, respectively, as determined by ^{1}H NMR spectroscopy (Table 1). This agreed with the compatibility of the $C_{12}CTA$ which, in the presence of AIBN, has been shown to polymerise acrylamides and styrene monomers more readily than methacrylate based monomers [45, 48]. This was also expressed in the higher monomer conversions for the acrylamide and styrene monomers than the methacrylate monomer, namely 95 % for the CdS/p(DMA), 91 % for the CdS/p(DMA-*co*-Sty) and 82 % for the CdS/p(DMA-*co*-MMA).

3.7 Kinetic studies for the RAFT polymerisation of DMA, MMA and Sty from the CdS/C_{12}CTA QDs

The kinetics of the RAFT polymerisation of MMA monomer with the CdS/C_{12}CTA QDs was determined using multiple timed reactions. A bulk reaction was first prepared from purified DMA monomer, CdS/C_{12}CTA QDs and AIBN in DMF (made up to 30 mL). Then 3 mL aliquots of the bulk reaction were reacted separately for a chosen time period (t = 0, 1, 4, 8, 12, 18, 24 and 48 h for DMA and t = 0, 1, 4, 8. 24 and 48 h for DMA, Sty and MMA copolymers). Removal from heat and exposure to air quenched the polymerisation process, from which 1 mL of sample was extracted for immediate ^{1}H NMR analysis (using DMSO-d_6). Figure 3.18 shows the kinetic plots for p(DMA) (Figure 3.18, ■), p(DMA-*co*-MMA) (Figure 3.18, □) and p(DMA-*co*-Sty) (Figure 3.18, ○) grafted from the CdS/C_{12}CTA QD surface *via* the RAFT process. The slowest rate was observed for the p(DMA) at k = 0.010 min^{-1} (Figure 3.18, ■) followed by p(DMA-*co*-MMA) at 0.038 min^{-1} (Figure 3.18, □) then p(DMA-*co*-Sty) at 0.047 min^{-1} (Figure 3.18, ○). For copolymerisation the faster rates are attributed to the non-specific order of monomer addition in grafting random copolymers, and again reactivity of the CTA with the MMA and Sty monomers compared to DMA [32, 34, 49].

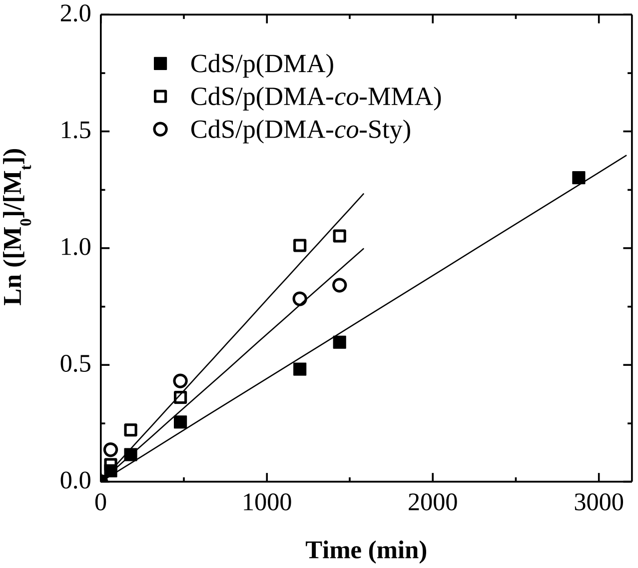

Figure 3.18. Kinetic plots of Ln$[M_0]/[M]_t$ versus time, for (■) p(DMA), (□) p(DMA-*co*-MMA) and (○) p(DMA-*co*-Sty) grafted from CdS/C_{12}CTA QDs.

3.7.1 TGA studies of CdS/polymer nanocomposites versus RAFT polymers without CdS QDs

This section will discuss the TGA performed on the CdS/polymer nanocomposites by comparing the degradation temperature (T_d) ranges, weight losses (wt/wt %) and residues (wt/wt %) to that of the RAFT polymers analogously synthesised using the C_{12}CTA without the CdS QDs (i.e., p(DMA), p(DMA-*co*-MMA) and p(DMA-*co*-Sty). TGA thermograms were recorded between 40 °C and 550 °C under N_2 at a ramp rate of 10 °C/min for all samples. Figure 3.19 shows the TGA thermograms of (i) samples (a) – (c), and (ii) samples (d) to (f). Table 3.5 shows the values of the residues, T_d ranges, and weight losses after the T_d for all samples.

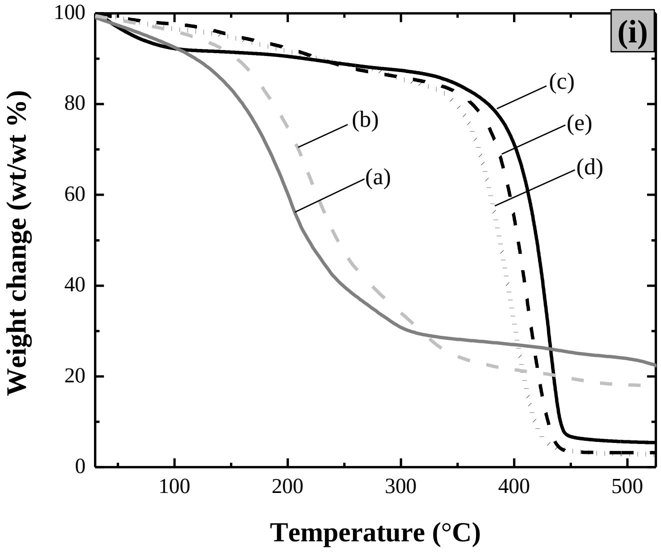

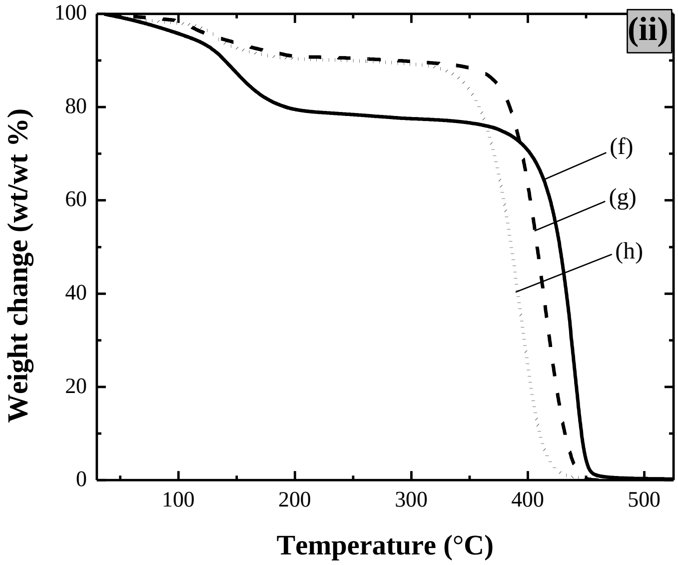

Figure 3.19. TGA thermograms of (i): (a) CdS/2-mercaptoethanol (b) CdS/C_{12}CTA (c) CdS/p(DMA) (d_ CdS/p(DMA-*co*-MMA) and (e) CdS/p(DMA-*co*-Sty); and (ii): (f) p(DMA), (g) p(DMA-*co*-MMA) and (h) p(DMA-*co*-Sty).

Table 3.5. Calculated values of residue, T_d as a range and weight loss after T_d, from the TGA thermograms of CTA (a) CdS/p(DMA), (b) CdS/p(DMA-*co*-MMA) and (c) CdS/p(DMA-*co*-Sty), and RAFT polymers without CdS QDs; (d) p(DMA), (e) p(DMA-*co*-MMA) and (f) p(DMA-*co*-Sty).

	Residue (wt/wt %) after T_d	**T_d (°C) range**	**T_d calculated (°C)**	**Weight loss at T_d (wt/wt %)**
(a)	5.4	347 – 451	434.3	79.5
(b)	3.6	328 – 433	397.2	81.4
(c)	3.2	333 – 449	414.7	81.0
(d)	> 0.1	335 – 448	439.6	78.3
(e)	> 0.1	289 – 428	349.8	91.0
(f)	> 0.1	326 – 446	393.2	90.6

Weight loss was observed between 100 °C and 200 °C in all samples and attributed to residual DMF in the final nanocomposite products. The residue wt/wt % for the RAFT polymers synthesised without CdS QDs (samples (d) to (f)), were > 0.1 wt/wt % after T_d. This was expected as the samples only contained polymer. The CdS/polymers, samples (a) to (d) however, had calculated residue wt/wt % of 5.4, 3.6, and 3.2 respectively. The residue wt/wt % represents the amount of CdS QDs in the nanocomposite, as it is inorganic and not thermally degraded. The residue wt/wt % recorded for sample (a) (CdS/p(DMA) was approximately double that of samples (b) and (c), CdS/p(DMA-*co*-MMA) and CdS/p(DMA-*co*-Sty, respectively). This relationship is inversely correlated to the M_n of the polymer on the CdS QDs. In Section 0 of this chapter, it was shown that the M_n of p(DMA) grafted from CdS was 10 098 $g.mol^{-1}$ which is at least halve the values of M_n for the p(DMA-*co*-MMA) and p(DMA-*co*-Sty) grafted from CdS at 19 756 $g.mol^{-1}$ and 26 987 $g.mol^{-1}$, respectively. The larger the polymer (M_n) the smaller the CdS content with respect to the polymer (residue wt/wt %).

It was also noted from Figure 3.19 and Table 3.5, that the T_d (range and values) were at higher temperatures for the CdS/polymer nanocomposites (samples (a) to (c)) than for that of the RAFT polymers synthesised without CdS QDs (samples (d) to (f)). This indicates that grafting from the CdS QDs *via* surface initiated polymerisation of the monomers DMA, MMA and Sty from CdS/C_{12}CTA QDs was successful. The higher T_d correlates to the additional covalent bond between the polymer and the CdS QDs that requires additional energy (heat) for degradation.

3.8 Optical properties of the CdS/polymer nanocomposites

This section will describe the optical properties of the CdS/polymer nanocomposites, with respect to the initial optical properties of the CdS/C_{12}CTA QDs prior to surface initiated RAFT polymerisation. UV-vis absorbance and fluorescence spectrophotometry were used.

3.8.1 UV-vis absorbance spectra of CdS/polymer nanocomposites

UV-vis absorbance spectra were recorded of the CdS/polymer nanocomposites between 300 nm and 600 nm, using DMF as the solvent and baseline. Figure 3.20 shows the UV-vis absorbance spectra of CdS/p(DMA), CdS/p(DMA-*co*-MMA) and CdS/p(DMA-*co*-Sty) nanocomposites in DMF, respectively.

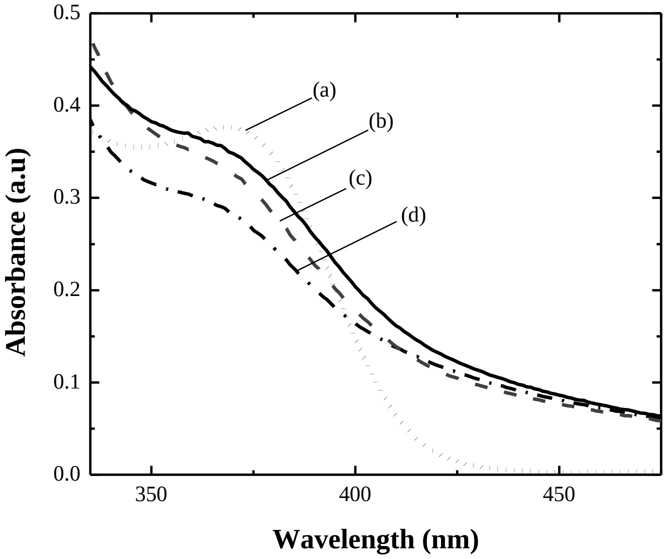

Figure 3.20. UV-vis absorbance spectra of (a) CdS/C$_{12}$CTA QDs, (b) CdS/p(DMA), (c) CdS/p(DMA-*co*-MMA) and (d) CdS/p(DMA-*co*-Sty) in DMF, at an excitation of 350 nm.

In all cases the absorbance peak maximum remained at 370 nm. However, the absorbance onset is red-shifted and broader for the nanocomposites. The smallest red-shift was observed for CdS/p(DMA) (434 nm, 2.74 eV) followed by CdS/p(DMA-*co*-MMA) (437 nm, 2.80 eV) then CdS/p(DMA-*co*-Sty) (440 nm, 2.86 eV).

3.8.2 Fluorescence emission spectra of CdS/polymer nanocomposites

Fluorescence emission spectra were taken of the CdS/polymer nanocomposites in DMF, with an excitation wavelength of 350 nm. A 350 nm excitation was used as this was an appropriate wavelength for excitation with respect to the absorbance spectra (Section 3.8.1), and also was used as the excitation wavelength setting on the Polilight® when visualising and photographing the CdS/polymers applied to latent fingermark deposits, discussed in Chapter 6. Figure 3.21 (a) to (d) shows the fluorescence emission spectra of the CdS/C$_{12}$CTA QDs, CdS/p(DMA), CdS/p(DMA-

co-MMA) and CdS/p(DMA-*co*-Sty) nanocomposites in DMF, respectively, with an excitation wavelength of 350 nm. Table 3.6 shows the maximum fluorescence, fluorescence intensity and FWHM measured from Figure 3.21.

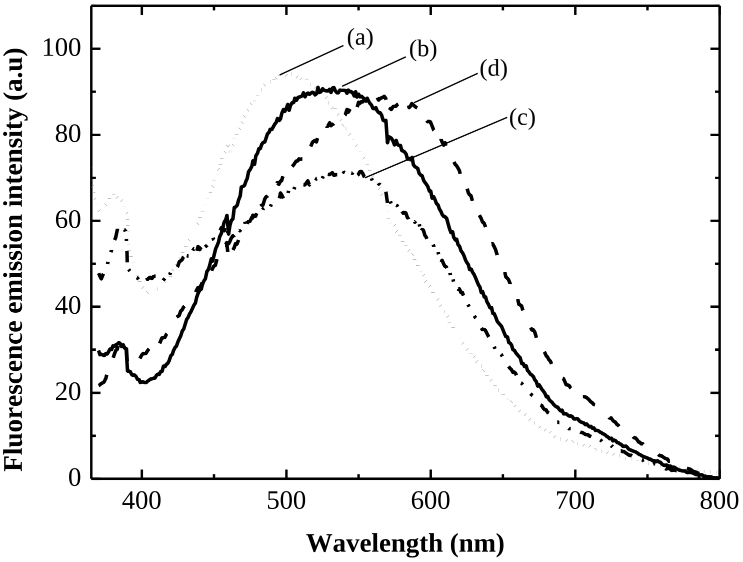

Figure 3.21. Fluorescence emission spectra of (a) CdS/C$_{12}$CTA QDs, (b) CdS/p(DMA), (c) CdS/p(DMA-*co*-MMA) and (d) CdS/p(DMA-*co*-Sty) in DMF, at an excitation of 350 nm.

Table 3.6. Maximum fluorescence, fluorescence intensity and FWHM recorded for (a) CdS/C$_{12}$CTA QDs, (b) CdS/p(DMA), (c) CdS/p(DMA-*co*-MMA) and (d) CdS/p(DMA-*co*-Sty) in DMF, at an excitation of 350 nm.

	Maximum fluorescence wavelength (nm)	**Maximum fluorescence emission intensity (a.u)**	**FWHM (nm)**
(a)	499.1	93.8	141.6
(b)	533.6	90.1	143.1
(c)	548.2	88.7	147.2
(d)	577.2	70.3	~ 250

All spectra show a broad fluorescence emission originating from the recombination of surface electron/hole pairs and their interaction with the DMF solvent [9, 22]. After surface initiated RAFT polymerisation the emission peaks are red-shifted from 499 nm to 533.6 nm ($\Delta E_g = 0.027$ eV), 548.2 nm ($\Delta E_g = 0.040$ eV), and 577.2 nm ($\Delta E_g = 0.063$ eV) for CdS/p(DMA) (Figure 3.21 (b), CdS/p(DMA-*co*-MMA) (Figure 3.21 (c)) and CdS/p(DMA-*co*-Sty) (Figure 3.21 (d)), respectively. The largest red-shift ($\Delta E_g = 0.063$ eV) was observed for the CdS/p(DMA-*co*-Sty) a result of the stronger electron-withdrawing group of the styrene monomers in conjunction with RAFT active site (trithiocarbonyl) on the copolymer. Interestingly, the emission intensity of the CdS/p(DMA-*co*-MMA) nanocomposite is quenched in comparison to the other nanocomposites which suggested that there may be a higher grafting density of this copolymer on the CdS QD surface. Despite slight changes in the optical properties of the CdS after surface initiated RAFT polymerisation, the nanocomposites were still visually adequate for fingermark detection and their optical properties remained stable for many months (photostability graph shown in Chapter 8 Section 8.2 Appendix B) due to the polymer protecting the CdS QDs.

Furthermore, the broad fluorescence (FWHM greater than 50 nm) observed from these CdS QDs gives flexibility to select the colour of fluorescence through the use of filters. This is extremely useful at crime scenes where fingermarks may be left behind on different coloured surfaces. Hence having the option to choose a colour of fluorescence to achieve optimum visualisation is highly desirable.

3.8.2.1 Quantum yield (QY) of the CdS/polymer nanocomposites

The QY of the final nanocomposites, CdS/p(DMA), CdS/p(DMA-*co*-MMA) and CdS/p(DMA-*co*-Sty) were measured against R6G (95 % QY). The QY values are summarised in Table 3.7.

Table 3.7. Calculated QY for CdS/polymer nanocomposites.

CdS/polymer nanocomposite	QY (%)
CdS/C_{12}CTA QDs	34 ± 2
CdS/p(DMA)	32 ± 4
CdS/p(DMA-*co*-MMA)	20 ± 3
CdS/p(DMA-*co*-Sty)	23 ± 3

Literature values for the QY of CdS QDs against R6G generally ranges between 15 % and 40 % [11, 50-52], n = 6. The QY measured for the CdS QDs here, are within this range and are adequate for visualising developed latent fingermarks, later shown in Chapter 6 of this thesis.

3.9 Conclusion

Fluorescent CdS QDs were successfully synthesised with 2-mercaptoethanol as a capping agent. It was found that the diameter of the CdS QDs depended highly on the ratio of the precursors, $CdCl_2$ and Na_2S, used during fabrication. This was characterised using the QDs UV absorbance and the hyperbolic band model. The hydroxyl groups present on the surface of the CdS QDs due to the immobilised 2-mercaptoethanol during synthesis were subjected to a Steglich esterification reaction with carboxyl terminated C_{12}CTA. Subsequently surface initiated RAFT polymerisation of the monomers DMA, MMA and Sty resulted in the synthesis of CdS/polymer nanocomposites namely; CdS/p(DMA), CdS/p(DMA-*co*-MMA) and CdS/p(DMA-*co*-Sty). The CdS/polymer nanocomposites were characterised by ^{1}H NMR, FTIR and TGA. RAFT polymerisation was demonstrated *via* first order kinetics using the consumption of the monomers over time, and low PDIs (less than 1.2). All three CdS/polymer nanocomposites were found to retain their fluorescent properties attributed to the CdS QD core, with QYs up to 32 % (against R6G dye). The retention of their optical properties was crucial for their application toward latent fingermark detection, described later in Chapter 6.

3.10 References for Chapter 3

1. Chuu, D.-S. and Dai, C.-M., *Quantum size effects in CdS thin films.* Physical Review B, 1992. **45** (20): p. 11805.
2. Ozaki, M., Peebles, D., Weinberger, B., Heeger, A., and MacDiarmid, A., *Semiconductor properties of polyacetylene p(CH) x: n-CdS heterojunctions.* Journal of Applied Physics, 1980. **51** (8): p. 4252-4256.
3. Ramsden, J.J., *Nucleation and growth of small CdS aggregates by chemical reaction.* Surface Science, 1985. **156**: p. 1027-1039.
4. Alivisatos, A.P., *Semiconductor clusters, nanocrystals, and quantum dots.* Science, 1996. **271** (5251): p. 933-937.
5. Leutwyler, W.K., Bürgi, S.L., and Burgl, H., *Semiconductor clusters, nanocrystals, and quantum dots.* Science, 1996. **271**: p. 933.
6. Marin, J.L., Riera, R., and Cruz, S.A., *Confinement of excitons in spherical quantum dots.* Journal of Physics: Condensed matter, 1999. **10** (6): p. 1349.
7. Wang, Y. and Herron, N., *Nanometer-sized semiconductor clusters: materials synthesis, quantum size effects, and photophysical properties.* The Journal of Physical Chemistry, 1991. **95** (2): p. 525-532.
8. Takagahara, T. and Takeda, K., *Theory of the quantum confinement effect on excitons in quantum dots of indirect-gap materials.* Physical review B, 1992. **46** (23): p. 15578.
9. Kulkarni, S., Ethiraj, A., Kharrazi, S., Deobagkar, D., and Deobagkar, D., *Synthesis and spectral properties of DNA capped CdS nanoparticles in aqueous and non-aqueous media.* Biosensors and Bioelectronics, 2005. **21** (1): p. 95-102.
10. Hu, J., Bando, Y., Zhan, J., Liao, M., Golberg, D., Yuan, X., and Sekiguchi, T., *Single-crystalline nanotubes of IIB-VI semiconductors.* Applied Physics Letters, 2005. **87** (11): p. 113107-113107-3.
11. Maleki, M., Ghamsari, M.S., Mirdamadi, S., and Ghasemzadeh, R., *A facile route for preparation of CdS nanoparticles.* Semiconductor Physics Quantum Electronics and Optoelectronics, 2007. **10**: p. 30-32.
12. Majumder, M., Karan, S., and Mallik, B., *Study of steady state and time resolved photoluminescence of thiol capped CdS nanocrystalline powders dispersed in N, N-dimethylformamide.* Journal of Luminescence, 2011. **131** (12): p. 2792-2802.
13. Pan, D., Ji, X., An, L., and Lu, Y., *Observation of nucleation and growth of CdS nanocrystals in a two-phase system.* Chemistry of Materials, 2008. **20** (11): p. 3560-3566.
14. Resch, U., Eychmüller, A., Haase, M., and Weller, H., *Absorption and fluorescence behavior of redispersible cadmium sulfide colloids in various organic solvents.* Langmuir, 1992. **8** (9): p. 2215-2218.
15. Leatherdale, C., Woo, W.-K., Mikulec, F., and Bawendi, M., *On the absorption cross section of CdSe nanocrystal quantum dots.* The Journal of Physical Chemistry B, 2002. **106** (31): p. 7619-7622.
16. Nedelijkovic, J., Patel, R., Kaufman, P., Joyce-Pruden, C., and O'Leary, N., *Synthesis and optical properties of quantum-sized metal sulfide particles in aqueous solution.* Journal of Chemical Education, 1993. **70** (4): p. 342.
17. Zeng, Z., Wang, S., and Yang, S., *Synthesis and characterization of PbS nanocrystallites in random copolymer ionomers.* Chemistry of Materials, 1999. **11** (11): p. 3365-3369.
18. He, R., Qian, X.-f., Yin, J., Xi, H.-a., Bian, L.-j., and Zhu, Z.-k., *Formation of monodispersed PVP-capped ZnS and CdS nanocrystals under microwave irradiation.* Colloids and Surfaces A: Physicochemical and Engineering Aspects, 2003. **220** (1–3): p. 151-157.
19. Frantsuzov, P.A. and Marcus, R., *Explanation of quantum dot blinking without long-lived trap hypothesis.* arXiv preprint cond-mat/0505604, 2005.

20. Knowles, K.E., Tice, D.B., McArthur, E.A., Solomon, G.C., and Weiss, E.A., *Chemical control of the photoluminescence of CdSe quantum dot−organic complexes with a series of para-substituted aniline ligands.* Journal of the American Chemical Society, 2009. **132** (3): p. 1041-1050.
21. Resch-Genger, U., *Quantum dots versus organic dyes as fluorescent labels.* Nature Methods, 2008. **5** (9): p. 763.
22. Yeh, S.-W., Wu, T.-L., Wei, K.-H., Sun, Y.-S., and Liang, K.S., *Effect of incorporated CdS nanoparticles on the crystallinity and morphology of poly(styrene-b-ethylene oxide) diblock copolymers.* Journal of Polymer Science Part B: Polymer Physics, 2005. **43** (10): p. 1220-1229.
23. Yusuf, H., Kim, W.-G., Lee, D.H., Guo, Y., and Moffitt, M.G., *Size control of mesoscale aqueous assemblies of quantum dots and block copolymers.* Langmuir, 2007. **23** (2): p. 868-878.
24. Li, X., Wang, H., Shimizu, Y., Pyatenko, A., Kawaguchi, K., and Koshizaki, N., *Preparation of carbon quantum dots with tunable photoluminescence by rapid laser passivation in ordinary organic solvents.* Chemical Communications, 2011. **47** (3): p. 932-934.
25. Wang, F., Pang, S., Wang, L., Li, Q., Kreiter, M., and Liu, C., *One-step synthesis of highly luminescent carbon dots in noncoordinating solvents.* Chemistry of Materials, 2010. **22** (16): p. 4528-4530.
26. Neises, B. and Steglich, W., *Simple method for the esterification of carboxylic acids.* Angewandte Chemie International Edition 1978. **17** (7): p. 522-524.
27. Boden, E.P. and Keck, G.E., *Proton-transfer steps in Steglich esterification: a very practical new method for macrolactonization.* The Journal of Organic Chemistry, 1985. **50** (13): p. 2394-2395.
28. Coates, J., *Interpretation of infrared spectra, a practical approach.* Encyclopedia of Analytical Chemistry, 2000.
29. Rao, C.N.R., Venkataraghavan, R., and Kasturi, T.R., *Contribution to the infrared spectra of organosulphur compounds.* Canadian Journal of Chemistry, 1964. **42** (1): p. 36-42.
30. Chiefari, J., Chong, Y.K., Ercole, F., Krstina, J., Jeffery, J., Le, T.P.T., Mayadunne, R.T.A., Meijs, G.F., Moad, C.L., Moad, G., Rizzardo, E., and Thang, S.H., *Living free-radical polymerization by reversible addition−fragmentation chain transfer: The RAFT process.* Macromolecules, 1998. **31** (16): p. 5559-5562.
31. Moad, G., *The emergence of RAFT polymerization.* Australian Journal of Chemistry, 2006. **59** (10): p. 661-662.
32. Moad, G., Chiefari, J., Chong, Y.K., Krstina, J., Mayadunne, R.T.A., Postma, A., Rizzardo, E., and Thang, S.H., *Living free radical polymerization with reversible addition – fragmentation chain transfer (the life of RAFT).* Polymer International, 2000. **49** (9): p. 993-1001.
33. Moad, G., Chong, Y.K., Postma, A., Rizzardo, E., and Thang, S.H., *Advances in RAFT polymerization: the synthesis of polymers with defined end-groups.* Polymer, 2005. **46** (19): p. 8458-8468.
34. Chong, B.Y.K., Le, T.P.T., Moad, G., Rizzardo, E., and Thang, S.H., *A more versatile route to block copolymers and other polymers of complex architecture by living radical polymerization: the RAFT process.* Macromolecules, 1999. **32** (6): p. 2071.
35. Perrier, S., Takolpuckdee, P., and Mars, C.A., *Reversible addition−fragmentation chain transfer polymerization: End group modification for functionalized polymers and chain transfer dgent recovery.* Macromolecules, 2005. **38** (6): p. 2033-2036.
36. Willcock, H. and O'Reilly, R.K., *End group removal and modification of RAFT polymers.* Polymer Chemistry, 2010. **1** (2): p. 149-157.

37. Xu, J., He, J., Fan, D., Tang, W., and Yang, Y., *Thermal decomposition of dithioesters and Its effect on RAFT polymerization.* Macromolecules, 2006. **39** (11): p. 3753-3759.
38. Skey, J. and O'Reilly, R.K., *Facile one pot synthesis of a range of reversible addition–fragmentation chain transfer (RAFT) agents.* Chemical Communications, 2008 (35): p. 4183-4185.
39. Barner-Kowollik, C., Buback, M., Charleux, B., Coote, M.L., Drache, M., Fukuda, T., Goto, A., Klumperman, B., Lowe, A.B., Mcleary, J.B., Moad, G., Monteiro, M.J., Sanderson, R.D., Tonge, M.P., and Vana, P., *Mechanism and kinetics of dithiobenzoate-mediated RAFT polymerization. The current situation.* Journal of Polymer Science Part A: Polymer Chemistry, 2006. **44** (20): p. 5809.
40. McLeary, J.B., Calitz, F.M., McKenzie, J.M., Tonge, M.P., Sanderson, R.D., and Klumperman, B., *Beyond Inhibition: A 1H NMR Investigation of the early kinetics of RAFT-mediated polymerization with the same initiating and leaving groups.* Macromolecules, 2004. **37** (7): p. 2383-2394.
41. Thomas, D.B., *Kinetics and molecular weight control of the polymerization of acrylamide via RAFT.* Macromolecules, 2004. **37** (24): p. 8941.
42. Painter, C.P. and M, C.M., *Fundementals of Polymer Sciences* 2nd. An Introductory Text1997: CRC press. 119.
43. Goto, A., *Mechanism and kinetics of RAFT-based living radical polymerizations of styrene and methyl methacrylate.* Macromolecules, 2001. **34** (3): p. 402.
44. Ellzy, M.W., Jensen, J.O., and Kay, J.G., *Vibrational frequencies and structural determinations of di-vinyl sulfone.* Spectrochimica Acta Part A: Molecular and Biomolecular Spectroscopy, 2003. **59** (4): p. 867-881.
45. Chiefari, J., Chong, Y.K., Ercole, F., Krstina, J., Jeffery, J., Le, T.P.T., Mayadunne, R.T.A., Meijs, G.F., Moad, C.L., Moad, G., Rizzardo, E., and Thang, S.H., *Living free-radical polymerization by reversible addition-fragmentation chain transfer: The RAFT process.* Macromolecules, 1998. **31** (16): p. 5559-5562.
46. Moad, G., Chong, Y., Postma, A., Rizzardo, E., and Thang, S.H., *Advances in RAFT polymerization: the synthesis of polymers with defined end-groups.* Polymer, 2005. **46** (19): p. 8458-8468.
47. Feng, M., Chen, Y., Gu, L., He, N., Bai, J., Lin, Y., and Zhan, H., *CdS nanoparticles chemically modified PAN functional materials: Preparation and nonlinear optical properties.* European Polymer Journal, 2009. **45** (4): p. 1058-1064.
48. Meier, L.P., Shelden, R.A., Caseri, W.R., and Suter, U.W., *Polymerization of styrene with initiator ionically bound to high surface area mica: grafting via an unexpected mechanism.* Macromolecules, 1994. **27** (6): p. 1637.
49. Inagaki, H. and Myamoto, T., *Preparation of block copolymers of A-B-A type and its behaviour in dilute solution.* Macromolecular Chemistry and Physics, 1965. **87** (1): p. 166.
50. Ghosh, S., Bhattacharya, S., and Saha, A., *Probing of ascorbic acid by CdS/dendrimer nanocomposites: a spectroscopic investigation.* Analytical and bioanalytical chemistry, 2010. **397** (4): p. 1573-1582.
51. Kalasad, M., Rabinal, M., and Mulimani, B., *Facile synthesis of bioconjugated fluorescent CdS nanoparticles of tunable light emission.* Journal of Physics D: Applied Physics, 2010. **43** (30): p. 305301.
52. Mao, J., Yao, J.-N., Wang, L.-N., and Liu, W.-S., *Easily prepared high-quantum-yield CdS quantum dots in water using hyperbranched polyethylenimine as modifier.* Journal of Colloid and Interface Science, 2008. **319** (1): p. 353-356.

Chapter 4. C-dot/polymer nanocomposites

4.1 Synopsis

This chapter describes the synthesis and characterisation of fluorescent carbon dot (C-dot)/polymer nanocomposites. First described is the synthesis of C-dots derived from the thermal oxidation of activated charcoal (AC). The C-dots were characterised via Raman, ^{13}C *NMR, FTIR, XPS and UV-vis spectroscopies to reveal their chemical structure, which aids in understanding the origins of their fluorescence.*

Similarly to CdS/polymer nanocomposites, described in Chapter 3, a C_{12}*CTA was immobilised onto the oxidised surface of the C-dots via DCC/DMAP coupling (Steglich esterification). Lastly, this chapter describes the surface initiated RAFT polymerisation of DMA from the C-dot surface. The application and performance of the C-dots/p(DMA) nanocomposites fabricated, as a fingermark reagent compared to CdS/polymer nanocomposites, is described in Chapter 6.*

4.2 Thermal oxidation of activated charcoal (AC)

C-dots were synthesised by refluxing activated charcoal (AC) in 4 M HNO_3 for 24 h. This process is called thermal oxidation. The chemical structure of AC can be described as a disorganised form of graphite or polymeric aromatic rings [16]. Figure 4.1 shows the synthetic route for the thermal oxidation of AC to produce fluorescent C-dots and for experimental details see Chapter 2, Section 2.3.1.

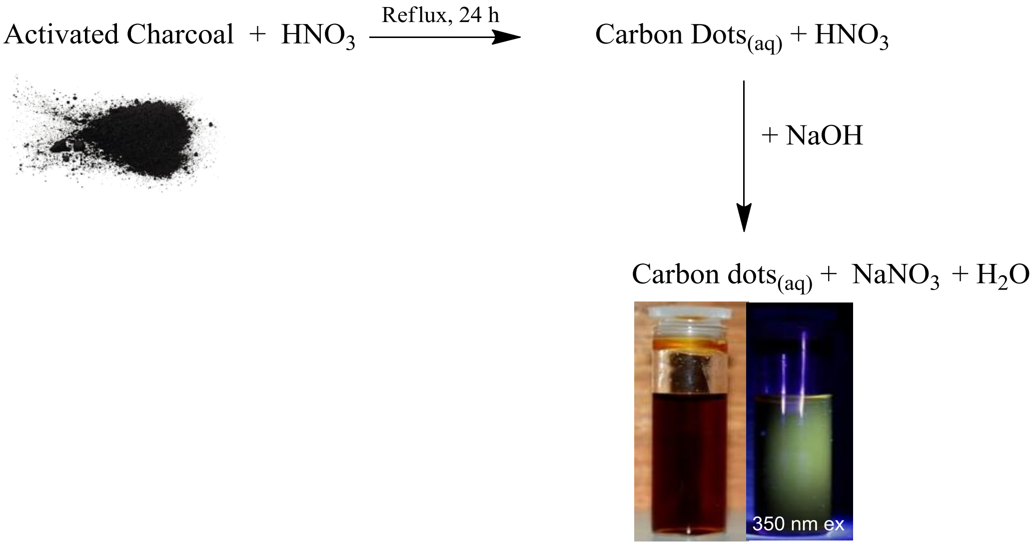

Figure 4.1. Synthesis of C-dots *via* thermal oxidation of AC.

Thermal oxidation of AC (black non-water soluble powder) yielded a clear dark brown aqueous solution of homogenously dispersed C-dots that fluoresced green under UV illumination (350 nm excitation), shown in Figure 4.1. These visual observations were the first indication that the AC had been ‘cut’ into nanoparticles with an oxidised surface – permitting C-dots to be dispersed in water [1-3]. “Cutting” *via* thermal oxidation using a strong acid, as done here with 4 M HNO_3, was considered analogous to the popular methods used in carbon nanotube technology, and is one of the prevalent bottom-up approaches toward synthesising C-dots [1, 4-10].

4.3 Physical and chemical properties of pristine C-dots

This section discusses the characterisation of synthesised pristine C-dots *via* thermal oxidation. Raman spectroscopy was used to determine the crystalline nature and degree of sp^2 hybridisation and hence graphitic or diamond-like structure of these carbon nanoparticles. ^{13}C NMR spectroscopy was used to show the degree of sp^2 hybridisation and type of surface oxidisation, which was later verified using FTIR spectroscopy. Finally, the average size of the C-dots was determined using dynamic light scattering (DLS) techniques.

4.3.1 Raman spectroscopy

Figure 4.2 (a) to (d) shows overlayed Raman spectra of AC, C-dots, pure $NaNO_3$ salt and $NaNO_3$ salt extracted after purification of C-dots, respectively.

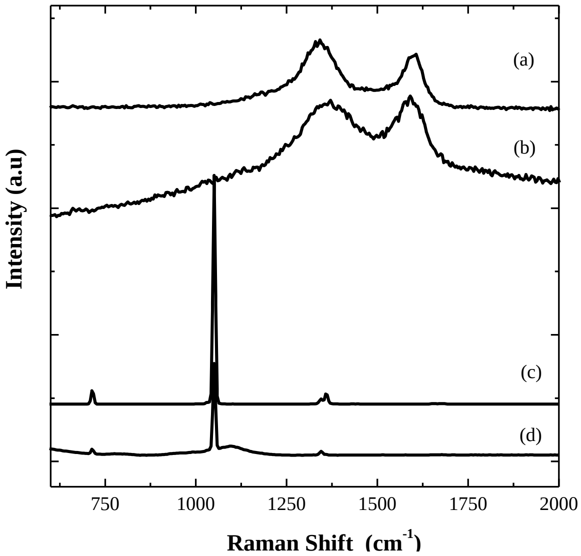

Figure 4.2. Stacked Raman spectra of (a) AC, (b) C-dots, (c) pure KNO_3 and (d) KNO_3 salt removed from C-dot product.

In the Raman spectra of AC (Figure 4.2 (a)) and the C-dots (Figure 4.2 (b)) the D-band relating to the edge defects was observed at 1320 cm^{-1} while the G-band relating to the in-plane vibration of sp^2 carbon was observed at 1590 cm^{-1} [11]. The ratio of intensities (I_D/I_G) of these characteristic bands was used to correlate the structural properties of the carbon. The I_D/I_G calculated for AC was 1.16 and is higher than that for the C-dots at 1.01. This indicates that the structure of the C-dots is more nano-crystalline, as the vibrations of sp^2 carbon (G-band) are larger. In addition, a larger background in the Raman spectrum of the C-dots (Figure 4.2 (b)) was observed, demonstrating some fluorescence emission by the nanoparticles under the Raman laser excitation (532 nm) [12, 13]. This was not observed in the Raman spectra of the starting material, AC nor the $NaNO_3$ salt removed (Figure 4.2 (a) and (d), respectively) indicating that the C-dots are the only fluorescent product of the thermal oxidation process.

The Raman spectra of the $NaNO_3$ extracted from the neutralised C-dot solution matched the spectra for pure $NaNO_3$ salt ((Figure 4.2 (c) and (d), respectively). Peaks associated with the NO_3^- ions were observed at 713 cm^{-1}, 1050 cm^{-1} and 1360 cm^{1}. These wavenumbers correlate to vibrational modes of the NO_3^- ions in-plane bending, symmetric and asymmetric stretching, respectively [14, 15].

The peaks observed for $NaNO_{3,}$ both pure and extracted, were not present in the Raman spectrum of the C-dots (Figure 4.2 (b)). This suggested that the $NaNO_3$ salt by-product was removed after neutralisation producing uncontaminated clean C-dots (purified C-dots). This was later tested in Section 4.3.4 of this Chapter, which describes how XPS contradicts this result showing residual $NaNO_3$ salt by-product present in the purified C-dot samples.

4.3.2 ^{13}C NMR spectroscopy of C-dots in D_2O

The ^{13}C NMR spectrum of the purified C-dots suspended in D_2O is shown in Figure 4.3. The ^{13}C NMR spectrum of AC was not taken as it was insoluble in all solvents (water and organic).

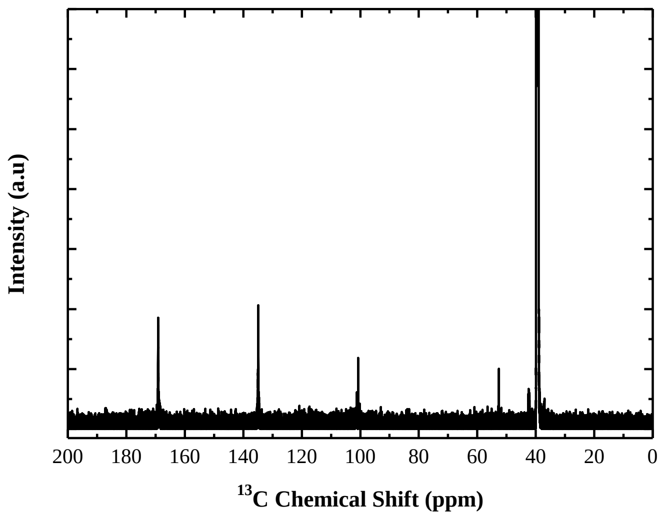

Figure 4.3. ^{13}**C NMR spectrum of C-dots in** D_2O**.**

The chemical shifts observed between 150 ppm and 120 ppm correlate to alkenes, while the signals in the range of 200 ppm to 170 ppm correspond to carboxylic acids (Figure 1.3). There is a small signal at 101 ppm which can be attributed to carbons within an aromatic ring (Ar). Signals observed between 50 and 20 ppm can be assigned to a number of functional groups, including carbons attached to an aromatic ring (Ar-R-C), carbonyl groups, alkanes and unconjugated alkenes. The peak at 51 ppm can be attributed to hydroxyl functionalised carbon. This demonstrates that the C-dots consist of highly functionalised aromatic carbons which are functionalised with carbonyl, hydroxyl and carboxylic acid groups. Similar ^{13}C NMR signals has been previously observed by Tian and co-workers [16]. Evidence for this structure is also observed in the following sections on FTIR spectroscopy and XPS analysis.

4.3.3 FTIR spectroscopy of AC versus C-dots

Figure 4.4 shows the FTIR spectra comparing (a) AC and (b) purified C-dots. Both spectra show C-H stretching vibrations (2 bands between 3000 cm^{-1} and 2800 cm^{-1}) and CH_2 bending vibrations (1450 cm^{-1} and between 900 cm^{-1} and 730 cm^{-1}) corresponding to the CH_2 chains in both the AC and C-dots. However, CH_3 bending at 1380 cm^{-1} is only observed in the spectrum of AC.

In the FTIR spectrum of the purified C-dots (Figure 4.4 (b)), a stronger OH stretching vibration was observed in the region of 3500 cm^{-1} to 3200 cm^{-1} and attributed to OH groups bound to the C-dot surface, such as phenol groups (Ph-OH), C-OH and COOH groups.

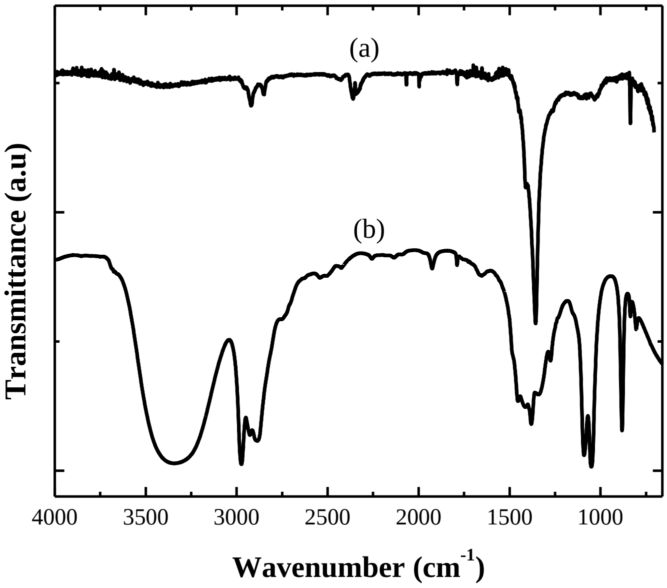

Figure 4.4. Stacked FTIR spectra of (a) AC and (b) purified C-dots.

C-O stretching vibrations were observed between 1320 cm^{-1} and 100 cm^{-1} and a weak signal corresponding to C=O was observed at 1720 cm^{-1}. The presence of sp^2 carbons was shown as a strong C=C-H bending vibration between 1000 cm^{-1} and 650 cm^{-1}, alongside stretching and bending vibrations attributed to sp^3 carbons (alkyl chains) between 2900 cm^{-1} and 3000 cm^{-1}. This indicates that the C-dots have a mixture of sp^2 and sp^3 carbon types with Ph-OH, C-OH and COOH functionalities.

4.3.4 XPS analysis of AC versus C-dots

Figure 1.5 (a) and (b) shows the XPS survey scans taken of AC and C-dots, respectively. The peak positions, peak area (%), full width half maximum (FWHM), and relative atomic concentrations (At %) are outlined in Table 4.1.

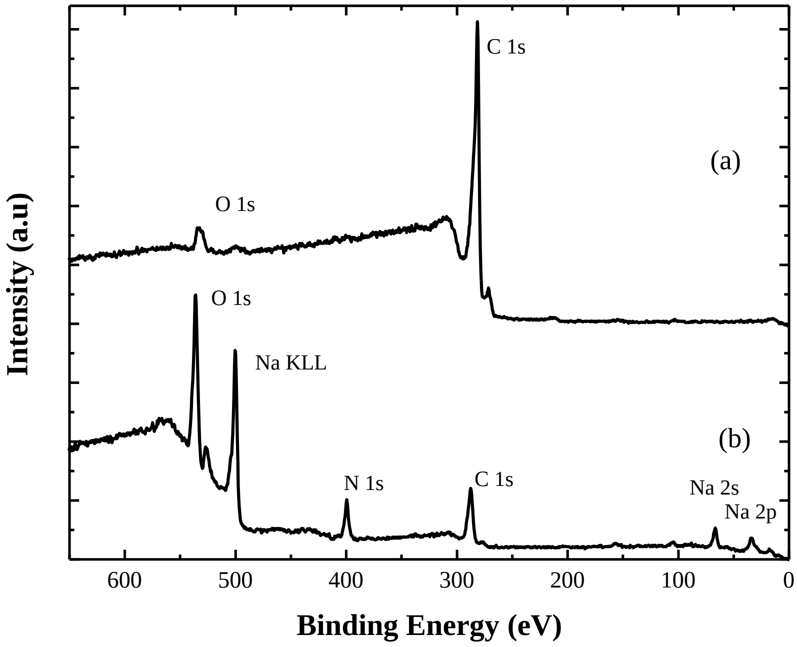

Figure 4.5. Stacked XPS survey scans of (a) AC and (b) purified C-dots.

Table 4.1. Peak position, peak area (%), FWHM and At % values calculated from the XPS analysis of (a) AC and (b) C-dots (Figure 4.4 (a) and (b)).

	Sample	Peak Position (eV)			Peak area (cps.eV)	FWHM (eV)	At %
(a)	AC	O	1s	532.5	1.3	7.1	3.7
		C	1s	281.5	11.6	4.1	96.3
(b)	C-dots	O	1s	532.5	2.4	3.8	28.7
		C	1s	287.5	4.1	5.0	21.6
		N	1s	399.1	1.4	3.0	7.3
		Na	KLL	507.5	7.2	3.7	37.9
			2s	63.2	0.64	3.6	3.2
			2p	31.8	0.24	4.0	1.3

From Table 4.1 it can be deduced that the oxygen content (w.r.t carbon) increased dramatically when the AC (O content of 3.7 % w.r.t C) was transformed into C-dots (O content of approximately 56 % w.r.t. C).

The Na and N peaks were attributed to the $NaNO_3$ salt and therefore contribution to the O peaks would have also come from the NO_3. This is contradictory to observations in the Raman spectral analysis (see Section 4.3.1 of this chapter), where it was indicated that the C-dot samples contained no $NaNO_3$. This suggests that XPS was more sensitive than Raman spectroscopy, as it showed that the $NaNO_3$ salt by-product was not completely removed during purification. The lack of $NaNO_3$ observed in the Raman spectra of the purified C-dots (Figure 4.2 (b) in Section 4.3.1 of this chapter) was also attributed to the high fluorescence background recorded, which may have masked the signals correlating to the $NaNO_3$ salt by product (Figure 4.2 (c) in Section 4.3.1 of this chapter).

4.3.5 C-dot nanoparticle size determined by dynamic light scattering (DLS)

The size of the C-dots produced after thermal oxidation of AC (100 mesh particle size or 150 µm) in HNO_3 was measured using DLS. Figure 4.6 shows the size distribution measurements collated from DLS size determination.

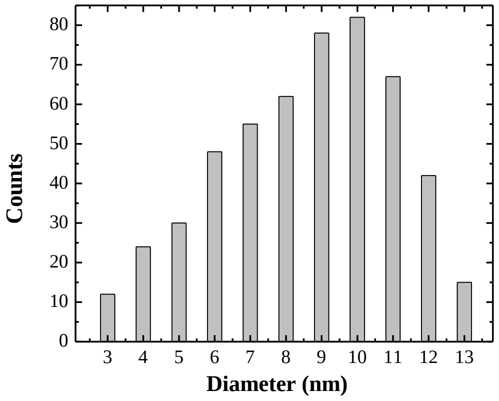

Figure 4.6. Size distribution histogram of C-dots determined by DLS (counts = volume (%)).

The C-dot diameters showed a size distribution of between 3 nm and 13 nm (Figure 4.6) with an average diameter of 8.7 nm ± 0.5 nm. This measured diameter agrees with reports of C-dot diameters ranging between 3 nm and 10 nm synthesised both by physical and wet chemistry [1-3, 8, 17-28].

4.4 Proposed structure of C-dots

By combining the Raman, ^{13}C NMR, FTIR and XPS analysis there is clear evidence that the surface of the C-dots is oxidised with hydroxyl (C-OH), and carboxyl (C-COOH) and various other oxidative moieties. Further, from the DLS data the average size of the C-dots is around 8.7 nm. Therefore, Figure 4.7 shows the proposed structure of the C-dots based on this data where the C-dots can be described as nanoparticles of aromatic carbon core (sp^2 carbon), with an oxidised surface containing alkyl chains, C-OH and C-COOH moieties.

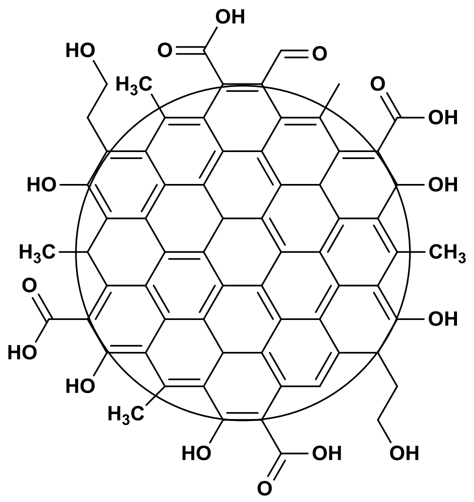

Figure 4.7. Proposed chemical structure of C-dots with an oxidised surface.

This structure then allowed for surface modification with a RAFT chain transfer agent. By utilising the C-OH groups, Steglich esterification of the C_{12}CTA to the surface was possible, followed by surface initiated RAFT polymerisation. The synthesis of C-dot/polymer nanocomposites is discussed later in this chapter, in Section 4.6. Experimental procedures established for the synthesis of CdS/polymer nanocomposites in Chapter 3 were again used here.

4.5 C-dot optical properties

In order to apply C-dots to fingermark detection/visualisation it is imperative that the fluorescence properties of the material be studied. This section will show the characterisation of the C-dot optical properties using UV-vis and fluorescence spectrophotometry. It will also show how factors such as pH and excitation wavelength affect the C-dots fluorescence emission properties, giving rise to a proposed mechanism as to where the C-dots fluorescence originates.

4.5.1 UV-vis absorbance of C-dots

Initially, UV-vis spectrophotometry was used to monitor the successful synthesis and purification of the C-dots derived from the thermal oxidation of AC (reaction scheme described in Section 4.2, Figure 4.1 of this chapter). Figure 4.8 shows the absorbance spectra for (a) HNO_3, (b) the salt by-product, $NaNO_3$ and (c) the NaOH used to neutralise the thermally oxidised C-dots.

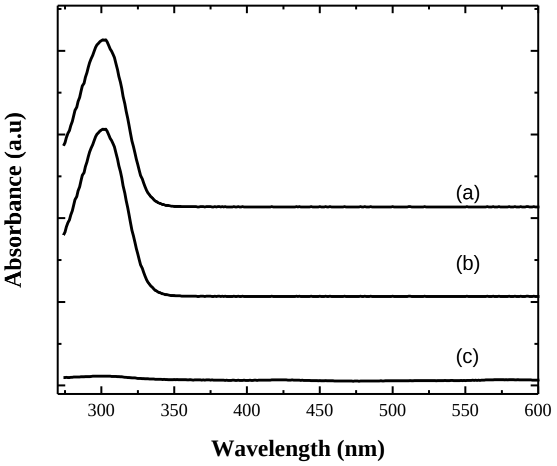

Figure 4.8. Stacked UV-vis absorbance spectra of (a) HNO_3, (b) $NaNO_3$ salt extracted and (c) NaOH. All solutions were prepared in Milli-Q water, with Milli-Q water baselines.

HNO_3 and $NaNO_3$ (Figure 4.8 (a) and (b), respectively) gave a maximum absorbance at 300 nm, which corresponds to the nitrate anion (NO_3^-). This absorbance is a result of transitions between non-bonding orbitals and δ anti-bonding orbitals between nitrogen and oxygen [29]. NaOH (Figure 4.8 (c)) did not absorb in the UV, which was expected as the solution was transparent and chemically does not have any UV-active transitions between Na^+ and OH^- ions or within the hydroxide molecule.

Figure 4.9 shows the UV-vis absorbance spectra of C-dots (a) un-neutralised, (b) after neutralisation with NaOH and (c) after purification *via* the removal of $NaNO_3$ salt by-product.

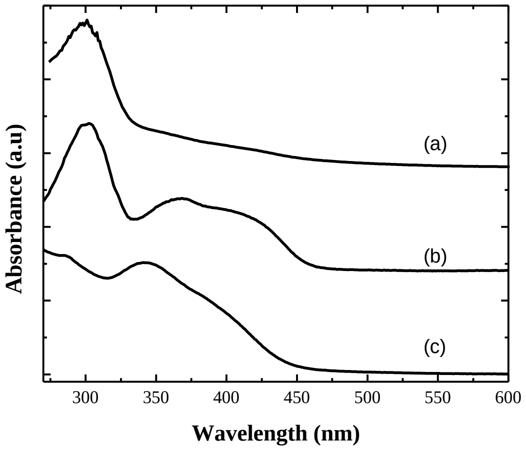

Figure 4.9. Stacked UV-vis absorbance spectra of (a) unneutralised C-dots, (b) neutralised C-dots and (c) purified carbon dots. Solutions were prepared in Milli-Q water, with Milli-Q water baselines.

The UV-vis absorbance profile of unneutralised C-dots (Figure 4.9 (a)) shows the NO_3^- ion peak at 300 nm [14] as a result of the presence of HNO_3 in the solution and a small shoulder is observed between 450 nm to 350 nm, attributed to the C-dot [18, 30]. Previous studies have shown that C-dots have an absorbance shoulder attributed to the n-π* transitions, and hence C=O or C-O bonds, and absorbencies at shorter wavelengths attributed to π-π* transitions in aromatic C=C bonds [18, 30].

After the C-dots have been neutralised by NaOH, the absorbance profile shown in Figure 4.9 (b), still shows the NO_3^- ion peak at 300 nm due to the formation of the $NaNO_3$ salt by-product. The shoulder attributed to the C-dots, however, has a greater distinctive absorbance with an onset 475 nm. After the $NaNO_3$ salt by-product was removed to give purified C-dots (Figure 4.9 (c)), the NO_3^- ion peak at 300 nm is diminished and the shoulder associated with the C-dots is further distinguished. This was also used as an indication that the carbon dots were successfully neutralised, and the majority of the C-dots were indeed isolated.

4.5.2 Fluorescence of C-dots

Fluorescence spectra were taken of the starting materials, by-products and C-dots. Figure 4.10 (a) to (f) shows the overlayed fluorescence emission spectra (excitation wavelength at 350 nm) of HNO_3, $NaNO_3$ salt by-product, NaOH, unneutralised C-dots, neutralised C-dots, and purified C-dots, respectively.

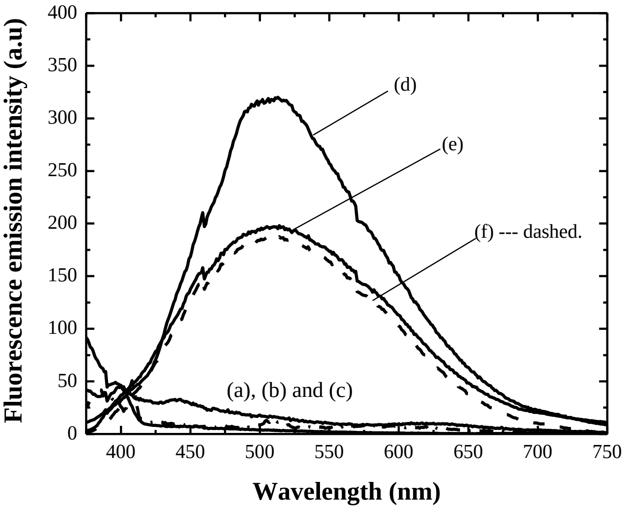

Figure 4.10. Overlayed fluorescence emission spectra of (a) HNO_3, (b) $NaNO_3$, (c) NaOH, (d) unneutralised C-dots, (e) neutralised C-dots and (f) purified C-dots (dashed line). Solutions were prepared in Milli-Q water with an excitation of 350 nm.

The HNO_3, $NaNO_3$ salt by-product and NaOH fluorescence spectra (Figure 4.10 (a)-(c)) did not show significant fluorescence emission when excited at 350 nm. The unneutralised, neutralised and purified C-dot products did, however, showed broad fluorescence in the visible range between 400 nm and 700 nm, with a peak maxima at about 508 nm. The fluorescence emission intensities and FWHM for the unneutralised C-dots, neutralised C-dots and purified C-dots (Figure 4.10 (d)-(f), respectively) are shown in Table 4.2.

Table 4.2. The maximum fluorescence emission intensity and FWHM determined from the fluorescence emission spectra (Figure 4.10) of (d) unneutralised C-dots (e) neutralised C-dots and (f) purified C-dots.

		Maximum fluorescence emission intensity (a.u)	**FWHM (nm)**
(d)	Unneutralised	320.7	151.7
(e)	Neutralised C-dots	198.1	180.2
(f)	Purified C-dots	186.0	167.9

There was a significant decrease in the fluorescence intensity from 122.6 a.u to 134.7 au (c.a. 12.1 a.u) after neutralisation and purification of the C-dots. This suggested that there may have been changes in the surface chemistry when the pH changed from acidic (pH = 1) to neutral (pH = 7). Therefore, the effect of the pH on the fluorescence intensity of the C-dots was investigated and discussed in the following sections.

4.5.3 Excitation wavelength

One unifying optical characteristic of C-dots is their excitation wavelength dependence on the emission wavelength and/or intensity. Figure 4.11 shows the overlayed fluorescence spectra of purified C-dots (in Milli-Q water) excited at 350 nm, 375 nm, 400 nm, 425 nm, 450 mm, and 475 nm. Table 4.3 summarises the fluorescence maxima and peak intensities measured from Figure 4.11.

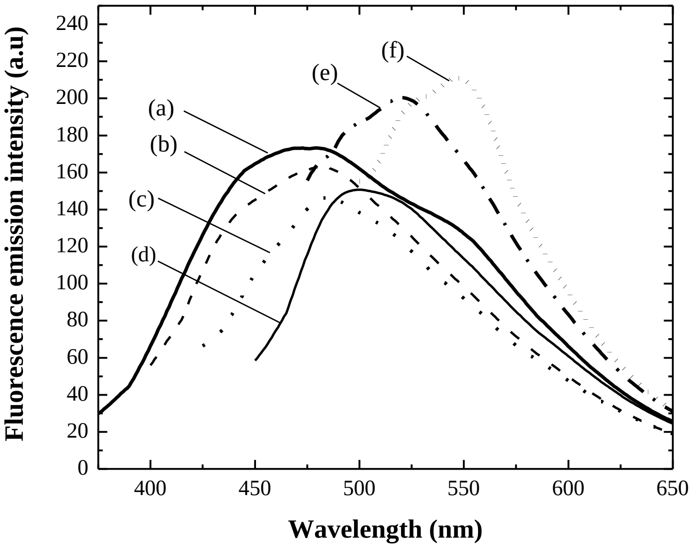

Figure 4.11. Fluorescence spectra of C-dots (in Milli-Q water) excited at (a) 350 nm, (b) 375nm (c) 400 nm, (d) 425 mm, (e) 450 nm and (f) 475 nm.

Table 4.3. Fluorescence peak maxima and intensity measured for purified C-dots excited at 350 nm, 400 nm, 425 nm, and 450 nm.

	Excitation wavelength (nm)	**Fluorescence peak maxima (nm)**	**Fluorescence intensity (a.u)**
(a)	**350**	471.4	173.1
(b)	**375**	475.1	160.7
(c)	**400**	486.2	148.0
(d)	**425**	499.8	151.2
(e)	**450**	519.2	206.2
(f)	**475**	546.4	216.3

As the excitation wavelength is increased from 350 nm to 400 nm, the fluorescence intensity decreased, but then increased as the excitation wavelength shifted from 400 nm through to 475 nm. Overall a red-shift in the fluorescence emission is observed as the excitation wavelength is increased from 350 nm to 475 nm. For conventional QDs, a red-shift indicates different sized nanocrystals due to the quantum confinement effect [31-35]. However, this theory does not apply to C-dots. In this case, the red-shift is caused by the influence of the surface as its primary mechanism for fluorescence rather than quantum confinement [36]. Therefore as the excitation wavelength was increased above 400 nm the surface was preferentially excited over the C-dots core and hence an increase in fluorescence intensity was observed. In literature it has been proposed that the intensity can be controlled by surface chemistry; in particular the protonation and deprotonation of carboxyl groups on the surface [36, 37]. The following section will describe how the pH affects the fluorescence intensity, giving further insight into the fluorescence mechanisms occurring on the C-dot surface.

4.5.4 pH reversible fluorescence properties of C-dots

The effect of pH on the C-dots fluorescence was investigated where the fluorescence intensity was measured when the pH was consecutively increased from 1 to 14, and decreased from 14 to 1 (equivalent to 1 cycle) three times (i.e., 3 cycles). Changes to the pH were made by the addition of HNO_3 or NaOH to the purified C-dot solution. The fluorescence intensity at each pH in each cycle was calculated relative to the fluorescence intensity measured at pH 1 of cycle 1. These measurements are depicted in Figure 4.12. It should be noted that there were no significant changes in the peak position.

As the pH of the C-dot solution was increased from 1 to 14, there was a dramatic decrease in fluorescence intensity. Then as the pH was decreased back from 14 to 1 the fluorescence intensity returned to almost 100 % of the original value. After 3 cycles of increasing and decreasing the pH, the overall fluorescence intensity of C-dots (excited at 350 nm) from the initial value decreased by less than 10 %.

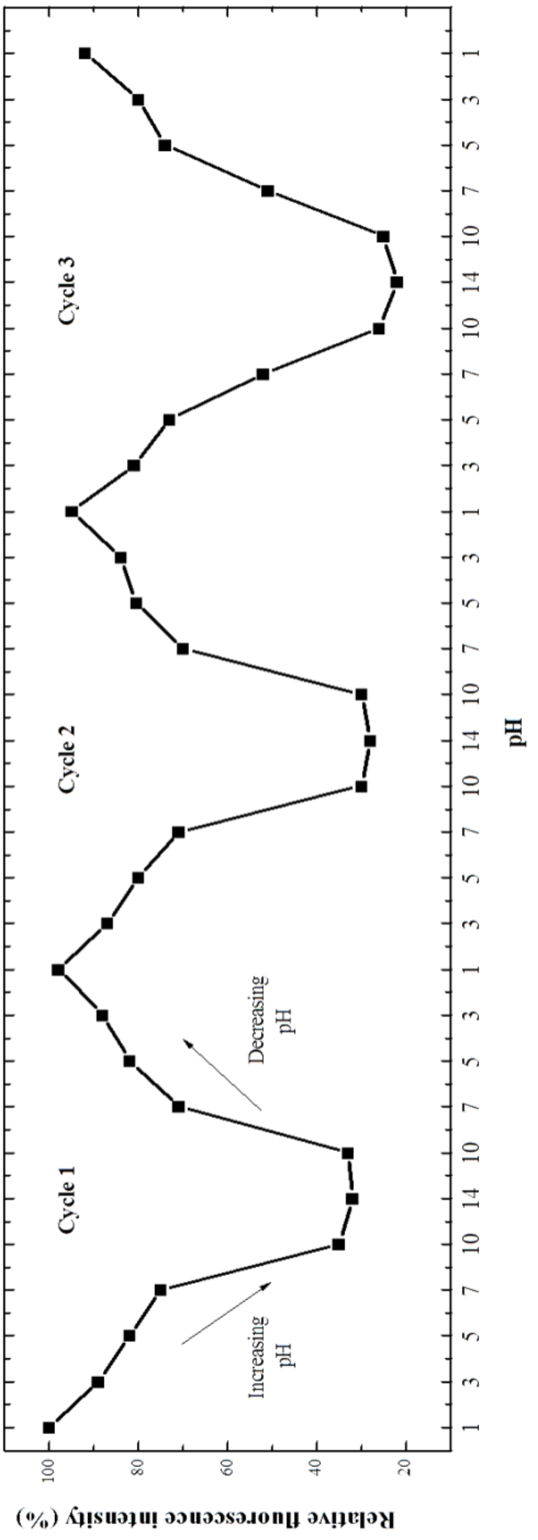

Figure 4.12. Relative fluorescence intensity of the purified C-dots over 3 cycles of consecutively increasing and decreasing pH. pH range of 1 to 14. Excited at 350 nm.

These observations were analogous to studies reported by Galande *et al*. [37], where they observed similar dramatic decreases in fluorescence of aqueous graphene oxide as the pH was increased from 7.6 to 12.7. The explanation of this pH dependent fluorescence can be related to the graphene oxide sheet structure or in our case the C-dot structure (see Section 4.4). Galande *et al*. [37] explained that the fluorescence is dominated by the presence of quasi-molecular fluorophores that consist of isolated carboxylic acid groups with nearby sp^2 carbons (i.e., the carbons in the C-dot core). Under acidic conditions the carboxylic acid groups are protonated therefore the emission is associated with the excited state protonation of $(C\text{-}COO^-)^*$ to $(C\text{-}COOH)^*$ (protonated form) transition. Under basic conditions the carboxylic acid groups are deprotonated so the emission is associated with the electronically excited (C-COOH) to $(C\text{-}COO^-)^*$ (deprotonated form) transition. To this end the emission from the excited states generated under acidic conditions are generally greater than those observed under basic conditions [20]. Therefore the fact that changes in emission with pH were observed in this work would indicate that there are significant amounts of carboxyl groups on the C-dot surfaces making it ideal for further modification chemistries.

4.6 Synthesis of C-dot/p(DMA) nanocomposites

The presence of hydroxyl groups was previously confirmed in Section 4.3 of this chapter (proposed structure shown in Figure 4.7, Section 4.4), where signals attributed to C-OH were observed using FTIR, ^{13}C NMR and XPS. Analogous to CdS/polymer nanocomposites (see Chapter 3) DCC/DMAP coupling was performed between hydroxyl groups on the C-dot surface and carboxyl groups of the C_{12}CTA. This was then followed by surface initiated RAFT polymerisation of DMA from the modified C-dot surface. The reaction scheme for this two-step process is shown in Figure 4.13.

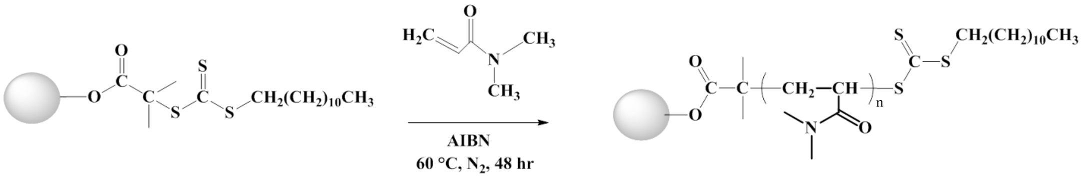

Figure 4.13. Reaction scheme C-dot surface modification and grafting of DMA from C-dot surface using SI RAFT polymerisation.

Surface modification was verified using FTIR spectroscopy, TGA and ^{1}H NMR spectroscopy. Kinetic data and GPC polymer properties proved successful RAFT polymerisation. These are discussed in the following sections.

4.6.1 FTIR spectroscopy of the purified C-dots versus C-dot/C_{12}CTA and C-dot/p(DMA) nanocomposite

Figure 4.14 shows the FTIR spectra of (a) purified C-dots, (b) C-dot/C_{12}CTA and (c) C-dot/p(DMA) nanocomposite.

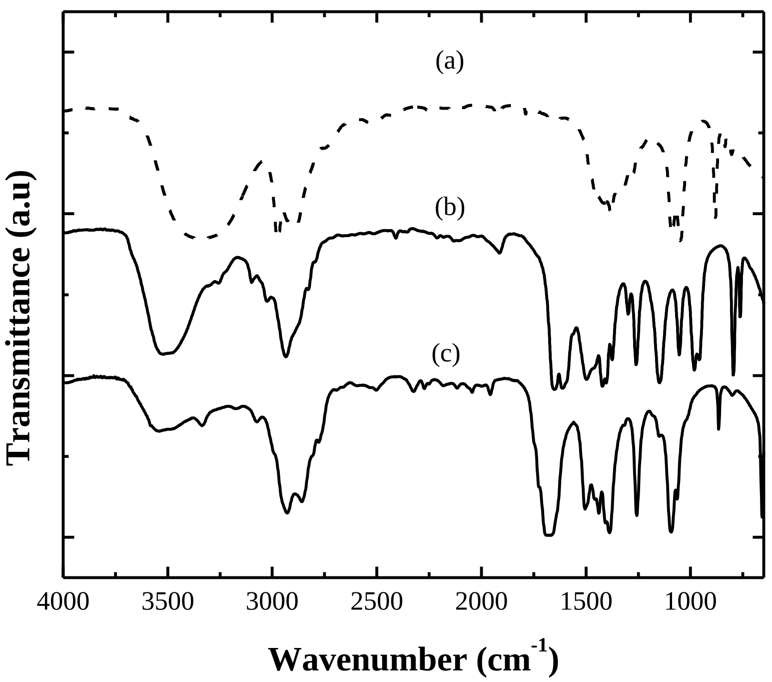

Figure 4.14. FTIR spectra of (a) purified C-dots (dashed line), (b) C-dot/C$_{12}$CTA and (c) C-dot/p(DMA) nanocomposite.

The FTIR spectrum of the oxidised C-dot surface (purified C-dots) has been shown and described previously (Section 4.3.3, Figure 4.4 (b)), but is depicted here for comparison against the C-dot/C$_{12}$CTA and C-dot/p(DMA) nanocomposite in Figure 4.14 (a), (b) and (c), respectively. Vibrations observed between 3600 cm^{-1} and 3400 cm^{1} were correlated to -OH stretching including stretches due to phenol (Ph-OH) groups from Ph-OH or Ph-R-C-OH C-OH on the C-dot surface (Figure 1.16 (a)). Similar peaks were observed in the C-dot/C$_{12}$CTA spectrum (Figure 4.14 (b)).

When the purified C-dots are reacted with the C$_{12}$CTA, the resulting C-dot/C$_{12}$CTA shows prominent double peaks at 1735 cm^{-1} and 1750 cm^{-1} attributed to the ester link formed after Steglich esterification. This was indicative that the surface immobilisation of the CTA was successful.

After polymerisation of the C-dot/C_{12}CTA with DMA the resulting C-dot/p(DMA) nanocomposite FTIR spectrum is shown in Figure 4.14 (c). The confirmation that p(DMA) was successfully grafted-from the C-dot surface is shown by an increased intensity in the C-H stretching vibrations at 3000 cm^{-1} and 2800 cm^{-1}, new C-O stretching vibrations between 1000 cm^{-1} and 1300 cm^{-1}, and acrylamide (C=O) vibrations between 1690 and 1630 cm^{-1}. Peaks observed at 1380 cm^{-1} were correlated to CH_3 bending in dimethylacrylamide.

4.6.2 TGA analysis of the C-dot/p(DMA) nanocomposites

Figure 4.15 (a)-(e) shows the overlayed thermograms for AC, purified C-dots, $NaNO_3$ salt by-product, C-dot/C_{12}CTA and C-dot/p(DMA) nanocomposite, respectively. The AC, C-dots and the $NaNO_3$ salt by-product did not thermally degrade after heating to 600 °C, shown as no change in mass loss with temperature. Physically adsorbed water and residual DMF was accounted for in the mass loss between 100 °C and 180 °C.

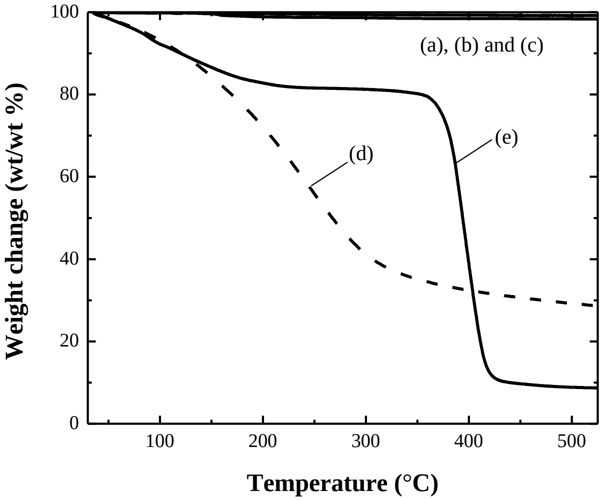

Figure 4.15. TGA thermograms for (a) AC, (b) purified C-dots, (c) $NaNO_3$ salt by-product, (d) C-dot/C_{12}CTA and (e) C-dot/p(DMA) nanocomposite. Under N_2 at a 10 °C min^{-1} ramp rate.

The TGA thermograms of the C-dot/C_{12}CTA (Figure 4.15 (d)) shows a maximum weight change (54 wt/wt %) between 180 °C and 320 °C. This corresponds to the thermal degradation of the C_{12}CTA from the C-dot surface thus leaving a residue of 25 wt/wt % (after heating to 500 °C), which is the C-dot content of the nanocomposite. The TGA thermogram of the C-dot/p(DMA) (Figure 4.15 (e)) shows a maximum mass loss (72.5 wt/wt %) at higher temperatures between 375 °C and 430 °C, with a residue of 9.8 wt/wt %. This corresponds to the degradation of the RAFT p(DMA) polymer from the C-dot surface.

4.6.3 GPC analysis of the C-dot/p(DMA) nanocomposites

GPC analysis revealed that the p(DMA) had a M_n of 13 521 g mol^{-1} and a PDI of 1.13. Given that the diameter of the C-dots was 8.7 nm (previously measured *via* DLS in Section 4.3.5 of this chapter) and assuming that the C-dots are spherical in shape the surface area of the C-dots was calculated to be 237.6 nm^2. Therefore the grafting density of the p(DMA) on the C-dot surface was estimated to be 0.249 µmol nm^{-2} .

4.6.4 ^{1}H NMR spectroscopy of the C-dot/p(DMA) nanocomposites

^{1}H NMR chemical shifts and correlations are detailed in the experimental synthesis of C-dot/p(DMA) nanocomposites in Chapter 2, Section 2.3.7. Analogous to the synthesis of CdS/p(DMA) nanocomposites in Chapter 3 ^{1}H NMR spectroscopy was used to monitor the polymerisation of DMA from the C-dot/C_{12}CTA *via* the RAFT process. Initially ^{1}H NMR spectra were taken of the C-dot/p(DMA) nanocomposite at reaction times of t = 0 h and t = 48 h, shown in Figure 4.16 (a) and (b), respectively. A zoomed in plot of C-dot/p(DMA) nanocomposite at t= 48 h, is shown in Figure 4.17. Data was normalised to the most intense peak in the region of 0 - 7 ppm (excluding the solvent regions).

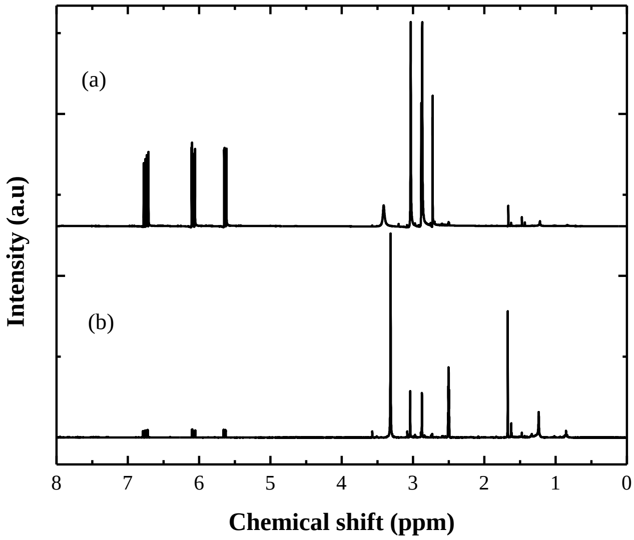

Figure 4.16. ^{1}H NMR spectra of C-dot/p(DMA) nanocomposite at reaction times (a) t = 0 h and (b) t = 48 h. Solvent used was DMSO-d_6.

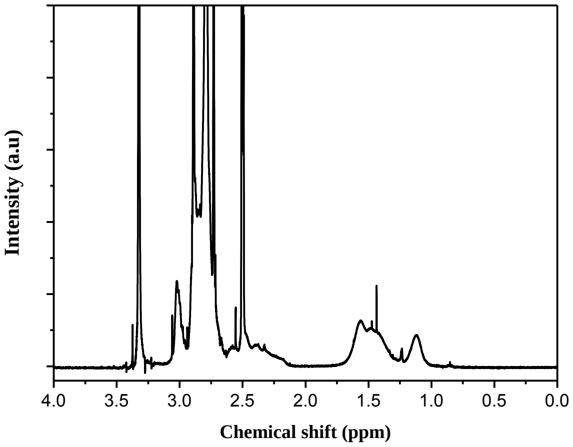

Figure 4.17. ^{1}H NMR spectra of C-dot/p(DMA) nanocomposite at t = 48, between 4 ppm and 0 ppm. Solvent used was DMSO-d_6.

The peaks associated with vinyl groups (H-C=C in unreacted DMA), present for the DMA monomer between 7 ppm and 5 ppm, were monitored with respect to the intensity of the peaks associated with ethylene groups in p(DMA) between 2 ppm and

1 ppm. At t = 0 h (Figure 4.17 (a)) the peaks associated with unreacted DMA have a higher relative intensity with respect to the polymer peaks at between 2 ppm and 1 ppm. At t = 48 h (Figure 4.17 (b)) the intensity of the peaks associated with the monomer between 7 ppm and 5 ppm have declined dramatically and the peaks associated with polymer alkane chain (1.6 ppm and 1.2 ppm, respectively) have increased in intensity. The peaks associated with the polymer between 2 ppm and 1 ppm was also broader, shown in Figure 4.17. This indicated that the monomer (DMA) had been converted into p(DMA). A 94 % conversion was calculated using the integration of the DMA H-C=C peaks between 7 ppm and 5 ppm with respect to the solvent peak (DMSO-d_6 at 2.49 ppm) at t = 48 relative to the integration at t = 0.

This was further investigated in the following section (Section 4.6.5); where the calculated integration of the monomer peaks was used to investigate the kinetics of the RAFT process.

4.6.5 Kinetic plots of the C-dot/p(DMA) nanocomposite formation

^{1}H NMR spectroscopy was used to investigate the kinetic control of the surface initiated RAFT polymerisations. Multiple pot reactions were conducted for assigned times (t = 0, 1, 4, 8, 12, 24 and 48 h). ^{1}H NMR spectra were then collected and peaks were integrated to determine the concentration of the monomer verses the polymer present at time t. Figure 4.18 shows the kinetic plot of DMA monomer grafted-from the C-dot/C_{12}CTA *via* the RAFT process.

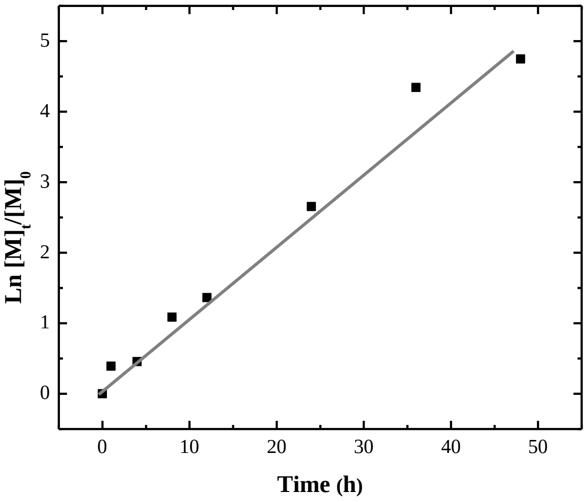

Figure 4.18. Kinetic plot for the polymerisation of DMA from C-dot/C$_{12}$CTA *via* RAFT polymerisation.

Similar to CdS/p(DMA) (which can be seen in Section 3.7 of Chapter 2) the kinetic plot shows a linear trend (R^2= 0.9792) and follows first order kinetics. Linearity indicates a stead state where the rate of initiation = the rate of termination, resulting in a constant radical concentration. That is the monomer, DMA, is being consumed at a constant rate and is dependent on its initial concentration. This was evidence that polymerisation of DMA was a living polymerisation, and is an indication of the RAFT process.

4.6.6 Optical properties of the C-dot/p(DMA) nanocomposites

Fundamental to any successful latent fingermark detection reagent is the ability to be able to produce contrast against the surface that the fingermark is deposited on. This section shows how the optical properties of the C-dots were not negatively affected by surface modification or RAFT polymerisation of DMA from its modified surface.

Samples of (a) C-dots, (b) C-dots/C$_{12}$CTA and (c) C-dots/p(DMA) dissolved in DMF were used. Analysis of these samples *via* UV-vis absorbance and fluorescence spectrophotometry will be discussed respectively. Figure 4.19 (a) to (c) shows the UV-vis absorbance spectra for C-dots, C-dots/C$_{12}$CTA, and C-dots/p(DMA) nanocomposite in DMF.

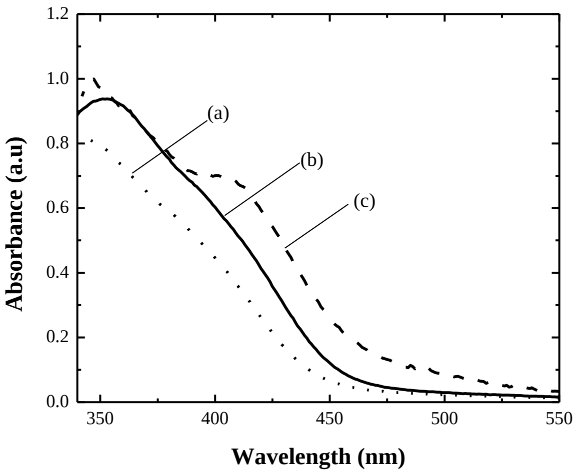

Figure 4.19. Overlayed UV-vis absorbance spectra of (a) C-dots, (b) C-dots/C$_{12}$CTA and (c) C-dots/p(DMA).

A red-shift in the absorbance shoulder of the C-dots/C$_{12}$CTA at 422 nm (Figure 4.19 (b)) when compared to the bare C-dots at 409 nm (Figure 4.19 (a)) was observed. This was attributed to the attachment of the C$_{12}$CTA to the C-dot surface, changing the surface properties of the C-dot. After RAFT polymerisation of DMA from the C-dot/C$_{12}$CTA a shoulder appeared between 400 nm and 450 nm. This suggested that the radicals present during RAFT polymerisation attacked the C=C groups of the C-dot core further changing the surface properties and hence absorbance spectra profile. Figure 4.20 shows the fluorescence emission spectra of (a) C-dots (b) C-dot/C$_{12}$CTA and (c) C-dot/p(DMA) followed by Table 4.4 summarising the fluorescence emission peak maxima, intensity and measured FWHM.

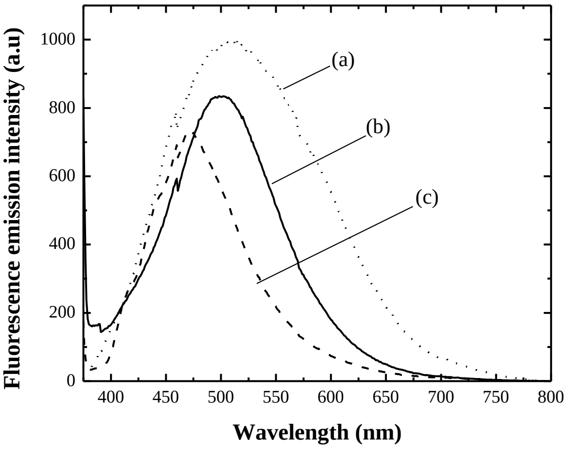

Figure 4.20. Overlayed fluorescence emission spectra of (a) C-dots, (b) C-dot/C$_{12}$CTA and (c) C-dot/p(DMA) nanocomposite.

Table 4.4. Maximum fluorescence wavelength, fluorescence intensity and FWHM recorded from the fluorescence emission spectra of (a) C-dots, (b) C-dot/C$_{12}$CTA and (c) C-dot/p(DMA) nanocomposite. Data normalised to the C-dot fluorescence spectrum (Figure 4.20 (a)).

	Maximum fluorescence wavelength (nm)	**Maximum fluorescence emission intensity (a.u)**	**FWHM (nm)**
(a)	508.6	1000	167.9
(b)	500.2	834	104.7
(c)	473.3	725	94.3

The emission spectrum of the C-dots (Figure 4.20 (a)) shows a broad emission band (FWHM = 167.9 nm). This band is narrowed after surface modification with the C$_{12}$CTA (FWHM = 104.7 nm, Figure 4.20 (b)) and even further narrowed after RAFT polymerisation with DMA (FWHM = 94.3 nm, Figure 4.20 (c)). This narrowing can be attributed to the alteration of the initial C-dot surface. As the surface is functionalised with C$_{12}$CTA, and further with grafting of p(DMA), the quasi-molecular fluorophores on the surface that arise from the carboxylic acid groups [37] are masked. The QY of C-dot/p(DMA) nanocomposite was measured to be 24.1 %, which is lower than CdS/p(DMA) nanocomposites previously described, however, the fluorescence intensity of the C-dots/p(DMA) was still visually suitable for the detection of latent fingermarks, described in Chapter 6.

4.7 Conclusions

C-dots were synthesised via hydrothermal routes and characterised using Raman, FTIR, ^{13}C NMR and XP spectroscopies. These studies revealed that the C-dots have an aromatic carbon core (sp^2 carbon) with an oxidised surface containing with C-OH and COOH moieties. These oxidised surface moieties contributed to the optical properties of the C-dots. The carboxylic acid groups on the surface were influenced by changes in pH. Their fluorescence intensity was greater in acidic conditions when the carboxyl groups were protonated and dramatically decreased in intensity when deprotonated (high pH). Furthermore, the effect of pH on the fluorescence intensity of the C-dots was found to be reversible.

The versatility of RAFT polymerisation on the C-dots was exploited using the same experimental design that was employed on the CdS QDs in Chapter 3. Polymer characterisation gave similar outcomes, however the effects of surface functionalisation on the optical properties of the C-dots differed as their fluorescence mechanisms differed. The C-dots fluorescence was attributed to the surface functionality, in particular free carboxyl groups on the surface, whereas CdS relied on electronic transitions in the band gap of the QD core. Therefore as the surface of C-dots were progressively functionalised with first the C_{12}CTA and finally grafted p(DMA) polymer, the fluorescence was quenched only slightly. This fluorescence quenching, however, was not visually significant, and was still suitable for the application in latent fingermark detection, seen later in Chapter 6.

4.8 References for Chapter 4

1. Allam, A. and Sarkar, S., *Water soluble fluorescent quantum carbon dots*, 2010, Afreen Allam, Sabyasachi Sarkar: USA.
2. Qiao, Z.-A., Wang, Y., Gao, Y., Li, H., Dai, T., Liu, Y., and Huo, Q., *Commercially activated carbon as the source for producing multicolor photoluminescent carbon dots by chemical oxidation.* Chemical Communications, 2010. **46** (46): p. 8812-8814.
3. Li, H., He, X., Liu, Y., Huang, H., Lian, S., Lee, S.-T., and Kang, Z., *One-step ultrasonic synthesis of water-soluble carbon nanoparticles with excellent photoluminescent properties.* Carbon, 2011. **49** (2): p. 605-609.
4. Guo, Y., Wang, Z., Shao, H., and Jiang, X., *Hydrothermal synthesis of highly fluorescent carbon nanoparticles from sodium citrate and their use for the detection of mercury ions.* Carbon, 2012 (52): p. 583–589.
5. Pan, D., Zhang, J., Li, Z., and Wu, M., *Hydrothermal route for cutting graphene sheets into blue luminescent graphene quantum dots.* Advanced Materials, 2009. **22** (6): p. 734-738.
6. Wang, Q., Zheng, H., Long, Y., Zhang, L., Gao, M., and Bai, W., *Microwave–hydrothermal synthesis of fluorescent carbon dots from graphite oxide.* Carbon, 2011. **49** (9): p. 3134-3140.
7. Yang, Y., Cui, J., Zheng, M., Hu, C., Tan, S., Xiao, Y., Yang, Q., and Liu, Y., *One-step synthesis of amino-functionalized fluorescent carbon nanoparticles by hydrothermal carbonization of chitosan.* Chemical Communications, 2012. **48** (3): p. 380-382.
8. Liu, R., Wu, D., Liu, S., Koynov, K., Knoll, W., and Li, Q., *An aqueous route to multicolor photoluminescent carbon dots using silica spheres as carriers.* Angewandte Chemie International Edition, 2009. **121** (25): p. 4668-4671.
9. Sahu S., Behera, B., Maitib, T.K., and Mohapatra, S., *Simple one-step synthesis of highly luminescent carbon dots from orange juice: Application as excellent bio-imaging agents.* Chemical Communications, 2012.
10. Wang, F., Pang, S., Wang, L., Li, Q., Kreiter, M., and Liu, C., *One-step synthesis of highly luminescent carbon dots in noncoordinating solvents.* Chemistry of Materials, 2010. **22** (16): p. 4528-4530.
11. Ferrari, A. and Robertson, J., *Interpretation of Raman spectra of disordered and amorphous carbon.* Physical Review B, 2000. **61** (20): p. 14095.
12. Chandra, S., Pathan, S.H., Mitra, S., Modha, B.H., Goswami, A., and Pramanik, P., *Tuning of photoluminescence on different surface functionalized carbon quantum dots.* RSC Advances, 2012. **2** (9): p. 3602-3606.
13. Escribano, R., Sloan, J.J., Siddique, N., Sze, N., and Dudev, T., *Raman spectroscopy of carbon-containing particles.* Vibrational Spectroscopy, 2001. **26** (2): p. 179-186.
14. Krishnan, K.S. and Guha, A.C., *The absorption spectra of nitrates and nitrities in relation to their photo-dissociation.* Proceedings of the Indian Academy of Sciences - Section A, 1934. **1** (4): p. 242-249.
15. Zangmeister, C.D. and Pemberton, J.E., *Raman spectroscopy of the reaction of sodium chloride with nitric acid: Sodium nitrate growth and effect of water exposure.* The Journal of Physical Chemistry A, 2001. **105** (15): p. 3788-3795.
16. Tian, L., Ghosh, D., Chen, W., Pradhan, S., Chang, X., and Chen, S., *Nanosized carbon particles from natural gas soot.* Chemistry of Materials, 2009. **21** (13): p. 2803-2809.
17. Anilkumar, P., Wang, X., Cao, L., Sahu, S., Liu, J.-H., Wang, P., Korch, K., Tackett II, K.N., Parenzan, A., and Sun, Y.-P., *Toward quantitatively fluorescent carbon-based "quantum" dots.* Nanoscale, 2011. **3** (5): p. 2023-2027.

18. Bourlinos, A.B., Stassinopoulos, A., Anglos, D., Zboril, R., Georgakilas, V., and Giannelis, E.P., *Photoluminescent carbogenic dots.* Chemistry of Materials, 2008. **20** (14): p. 4539-4541.
19. Cao, L., Wang, X., Meziani, M.J., Wang, H., Luo, P.G., Lin, Y., Harruf, B.A., Veca, M., Murray, D., Xie, S.Y., and Sun, Y.P., *Carbon dots for multiphoton bioimaging.* Journal of the American Chemical Society, 2007. **129** (37): p. 11318.
20. Hu, S.-L., Niu, K.-Y., Sun, J., Yang, J., Zhao, N.-Q., and Du, X.-W., *One-step synthesis of fluorescent carbon nanoparticles by laser irradiation.* Journal of Materials Chemistry, 2009. **19** (4): p. 484-488.
21. Kwon, W. and Rhee, S.-W., *Facile synthesis of graphitic carbon quantum dots with size tunability and uniformity using reverse micelles.* Chemical Communications, 2012. **48**: p. 5256-5258.
22. Liu, H., Ye, T., and Mao, C., *Fluorescent carbon nanoparticles derived from candle soot.* Angewandte Chemie International Edition, 2007. **46** (34): p. 6473-6475.
23. Mao, X.-J., Zheng, H.-Z., Long, Y.-J., Du, J., Hao, J.-Y., Wang, L.-L., and Zhou, D.-B., *Study on the fluorescence characteristics of carbon dots.* Spectrochimica Acta Part A: Molecular and Biomolecular Spectroscopy, 2010. **75** (2): p. 553-557.
24. Ray, S.C., Saha, A., Jana, N.R., and Sarkar, R., *Fluorescent carbon nanoparticle: Synthesis, characterization and bio-imaging application.* arXiv preprint arXiv:0909.4622, 2009.
25. Palashuddin, S.K., Amit, J., Anumita, P., Ghosh, S.S., and Chattopadhyay, A., *Presence of amorphous carbon nanoparticles in food caramels.* Nature Scientific Reports, 2012. **2**.
26. Sun, Y.P., Wang, X., Lu, F., Cao, L., Meziani, M.J., Luo, P.G., Gu, L., and Veca, L.M., *Doped carbon nanoparticles as a new platform for highly photoluminescent dots.* The Journal of Physical Chemistry C, 2008. **112** (47): p. 18295-18298.
27. Sun, Y.P., Zhou B., Lin Y., Wang W., Fernando K.A., Pathak P., Meziani M. J., Harruff B. A., Wang X., Wang H., Luo P.G., Yang H., Kose M. E., Chen B., Veca L. M., and Y., X.S., *Quantum-sized carbon dots for bright and colorful photoluminescence.* Journal of the American Chemical Society, 2006. **128** (24): p. 7756.
28. Sun, Y.-P., Luo, P.G., Sahu, S., Yang, S.-T., Sonkar, S.K., Wang, J., Wang, H., LeCroy, G.E., and Cao, L., *Carbon quantum dots for optical bioimaging.* Journal of Material Chemistry B, 2013 (1): p. 2116-2127.
29. Butorac, V., Simeon, V., and Tomišić, V., *Effect of temperature on UV spectra of concentrated NaNO3 aqueous solutions.* Croatica Chemica Acta, 2007. **80** (3-4): p. 533-539.
30. Baker, S.N. and Baker, G.A., *Luminescent Carbon Nanodots: Emergent Nanolights.* Angewandte chemie international edition, 2010. **49** (38): p. 6726-6744.
31. Alivisatos, A.P., *Semiconductor clusters, nanocrystals, and quantum dots.* Science, 1996. **271** (5251): p. 933-937.
32. Kairdolf, B.A., Smith, A.M., and Nie, S., *One-pot synthesis, encapsulation, and solubilization of size-tuned quantum dots with amphiphilic multidentate ligands.* Journal of the American Chemical Society, 2008. **130** (39): p. 12866.
33. Knowles, K.E., Tice, D.B., McArthur, E.A., Solomon, G.C., and Weiss, E.A., *Chemical control of the photoluminescence of CdSe quantum dot−organic complexes with a series of para-substituted aniline ligands.* Journal of the American Chemical Society, 2009. **132** (3): p. 1041-1050.
34. Resch-Genger, U., Grabolle, M., Cavaliere-Jaricot, S., Nitschke, R., and Nann, T., *Quantum dots versus organic dyes as fluorescent labels.* Nature Methods, 2008. **5** (9): p. 763-775.

35. Takagahara, T. and Takeda, K., *Theory of the quantum confinement effect on excitons in quantum dots of indirect-gap materials.* Physical Review. B, Condensed matter, 1992. **46** (23): p. 15578.
36. Zhu, B., Sun, S., Wang, Y., Deng, S., Qian, G., Wang, M., and Hu, A., *Preparation of carbon nanodots from single chain polymeric nanoparticles and theoretical investigation of the photoluminescence mechanism.* Journal of Materials Chemistry C, 2013. **1** (3): p. 580-586.
37. Galande, C., Mohite, A.D., Naumov, A.V., Gao, W., Ci, L., Ajayan, A., Gao, H., Srivastava, A., Weisman, R.B., and Ajayan, P.M., *Quasi-molecular fluorescence from graphene oxide.* Scientific Reports, 2011. **1**.

Chapter 5. RAFT end-group post modification: Synthesis of magnetic nanocomposite powders

5.1 Synopsis

This chapter describes the RAFT end-group post modification of CdS /p(DMA-co-MMA) and C-dot/p(DMA-co-MMA). The RAFT end-group post-modification was performed via a one-pot aminolysis/thio-lene click reaction between CdS/p(DMA-co-MMA) or C-dot/p(DMA-co-MMA) with divinyl-sulfone (DVS) activated magnetic beads. The powders produced were then investigated as fluorescent/magnetic powders for latent fingermark detection. The application of these magnetic nanocomposites to latent fingermark detection is shown in Chapter 6.

5.2 One-pot aminolysis/click reaction

A one-pot aminolysis/click procedure was devised for the synthesis of magnetic CdS/p(DMA-*co*-MMA)* and C-dot/p(DMA-*co*-MMA)* powders. Note, the magnetic nanocomposites are denoted with an asterisk (*) when referred to in the text. The experimental method (details in Chapter 2) was derived from previous work established by Boyer and co-workers [1]. The synthesis of the non-magnetic precursor CdS/p(DMA-*co*-MMA) was previously described in Chapter 3, Section 3.5, and the non-magnetic precursor C-dot/p(DMA-*co*-MMA) was synthesised identically replacing the CdS QD with C-dots (isolated in DMF). Figure 5.1 shows the scheme for the synthetic route used for the synthesis of magnetic CdS/p(DMA-*co*-MMA)* and C-dot/p(DMA-*co*-MMA)* powders, where the sphere in the scheme represents either CdS QDs or C-dots and the oval represents the divinyl sulfone (DVS) magnetic beads iron microparticle. Note, this figure is not to scale as the CdS QDs and C-dots were less than 10 nm in diameter, whereas the DVS-magnetic beads were purchased as 1 µm in diameter

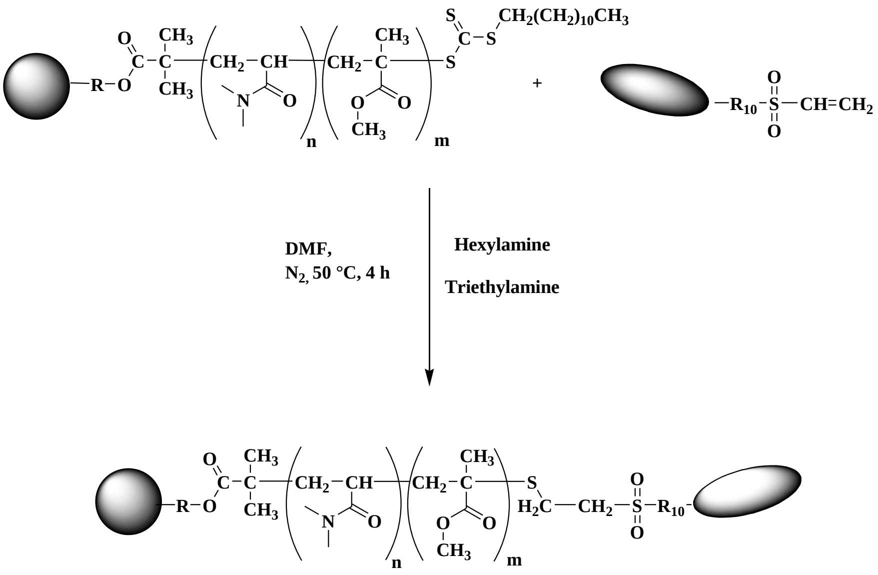

Figure 5.1. Synthesis of magnetic CdS/p(DMA-*co*-MMA)* and C-dot/p(DMA-*co*-MMA)* nanocomposites *via* a one-pot aminolysis/thiol-ene click reaction. The sphere in the scheme represents either CdS QDs or C-dots and the oval represents the iron microparticle (not to scale).

Initial attempts at this reaction were performed at room temperature (not 50 °C) as per work established by Boyer and co-workers [1] which were visually unsuccessful. Precipitation of the final product resulted in a polymeric product with the DVS-magnetic beads sitting at the bottom of the solution (separate to the polymer). The method was modified by introducing heat (up to 50 °C) to accelerate the reaction. There were no noticeable colour changes from the start (reaction time, t = 0 h) to the end of the reaction (reaction time, t = 4 h), and the solution remained milky brown due to the dispersion of the DVS-magnetic beads. Precipitation of both nanocomposites (magnetic CdS/p(DMA-*co*-MMA)* and C-dot/p(DMA-*co*-MMA)*) into excess cold diethyl ether yielded a brown gum-type product. This product was re-dissolved into acetone and centrifuged to separate the desired magnetic nanocomposites (supernatant) from unreacted excess DVS-magnetic beads (precipitate settled at the bottom of the centrifuge tube). The supernatant which contained the desired magnetic nanocomposites was re-precipitated into excess cold diethyl ether to give beige coloured magnetic CdS /p(DMA-*co*-MMA)* and C-dot/p(DMA-*co*-MMA)* nanocomposites powders. Experimental details can be found in Chapter 2 Section 2.3.6.1.

Triethylamine (TEA) and hexylamine (HA) were the reagents used for the simultaneous aminolysis and the thiol-ene click reaction. These two reagents are commonly used in literature for catalysis of the aminolysis and thio-lene reactions interchangeably [1-12]. Therefore TEA and HA were used interchangeably for the simultaneous aminolysis and thiol-ene click reaction in this one-pot reaction. This specific procedure was chosen due to the trithiocarbonyl nature of the RAFT end-group on the CdS/p(DMA-*co*-MMA) and C-dot/p(DMA-*co*-MMA) nanocomposites. The RAFT end-group given by the tri-thiocarbonyl C_{12}CTA is highlighted in Figure 5.2.

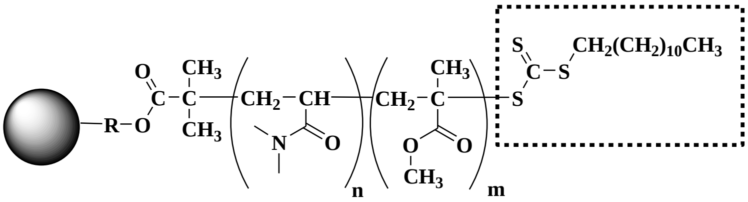

Figure 5.2. Chemical structure of CdS/p(DMA-*co*-MMA) or C-dot/p(DMA-*co*-MMA) with the RAFT end-group highlighted in the dotted box.

This particular RAFT agent, C_{12}CTA, was used due to its purchase availability at the current time of research, and importantly its compatibility with the types of monomers desired for polymerisation. The issue, however, was its nature as a tri-thiocarbonyl CTA. Tri-thiocarbonyl CTAs are susceptible to interchain disulfide linking during aminolysis as there are two possible thiol compounds produced and are susceptible to form interchange disulfide bonds with each other during aminolysis, hence a range of products can be synthesised (uncontrollably) [1, 3, 5, 6, 13-15]. Figure 5.3 shows the possible products in this reaction including the undesirable products as a result of disulfide links.

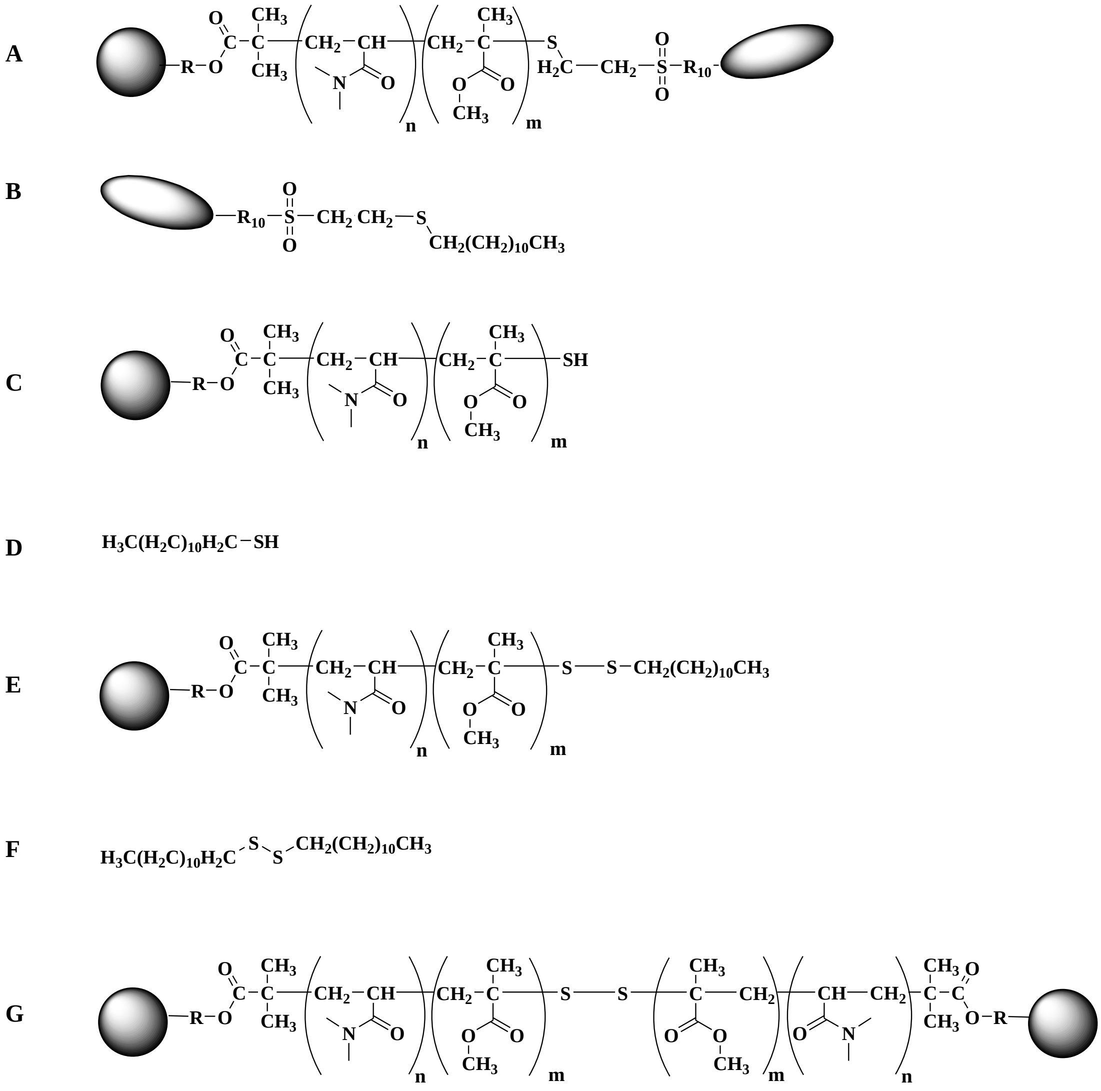

Figure 5.3. Structures of possible side products of simultaneous aminolysis/thiol-ene click reaction and aminolysis only as a result of using trithiocarbonate C_{12}CTA used in this research.

If aminolysis were to be performed without the simultaneous thiol-ene click reaction (i.e., without the addition of the "ene" reagent; DVS-magnetic beads at the start of the reaction) the desired products would be the thiol terminated RAFT products, C and D in Figure 5.3. However, due to the reactivity of thiols (-SH groups), it has been established extensively in literature, that they would be susceptible to disulfide linking, producing the undesired products of E, F and G in Figure 5.3. Efforts have been made to break these disulfide bonds (S-S) such as the addition of 2,2'-dithiopyridine (DTP) [3, 5]. The DTP forms a stable pyridyl disulfide group that could be displaced by the free thiol bearing molecules [3, 5]. It is often desirable for a thiol product to be isolated, as coupling reactions (such as the thiol-ene click reaction) are a popular method for attaching biomolecules to RAFT polymers.

The reaction used in this thesis minimises interchain disulfide linking by performing aminolysis simultaneously with thiol-ene click reactions. Here the DVS-magnetic beads (containing the C=C for the thiol-ene click reaction) are introduced at the start of the aminolysis process. This means the thiol-ene click reaction competes with interchain disulfide linking as the thiols are being produced (upon addition of the primary or secondary amines), producing the desired product A and side product B (Figure 5.3). The side product B is unavoidable due to the trithio feature of the C_{12}CTA. Through precipitation of product A (the magnetic CdS/p(DMA-*co*-MMA)* and C-dot/p(DMA-*co*-MMA)*) into excess cold diethyl ether it is likely that product B was removed (soluble in precipitation solvent).

5.3 Characterisation of the magnetic nanocomposites

This section describes how the magnetic CdS/p(DMA-*co*-MMA)* and C-dot/p(DMA-*co*-MMA)* nanocomposites powders were characterised *via* FTIR spectroscopy and TGA. Fluorescence and UV-vis spectrophotometry were used to characterise the optical properties of the magnetic nanocomposites. Clearly, ^{1}H NMR spectroscopy would have been the most desirable way of monitoring the synthesis of these nanocomposites, however, due to their magnetic behaviour this technique was not applicable.

5.3.1 FTIR analysis of magnetic CdS/p(DMA-*co*-MMA)* and C-dot/p(DMA-*co*-MMA)* nanocomposites

FTIR analysis can be used to monitor the thiol-ene click reaction by observing the elimination of C=C stretching in the 1600 cm^{-1} region =C-H stretching (between 3100 cm^{-1} and 300 cm^{-1}) and bending (800 cm^{-1} region) attributed to the "ene" molecule [16]. Furthermore, a peak at 750 cm^{-1} associated with the new S-C bond should become apparent [17] after the click reaction has taken place. FTIR spectra were collected for samples of (a) DVS-magnetic beads, (b) magnetic p(DMA-*co*-MMA)* and (c) magnetic C-dot/p(DMA-*co*-MMA)* (see, Figure 5.4).

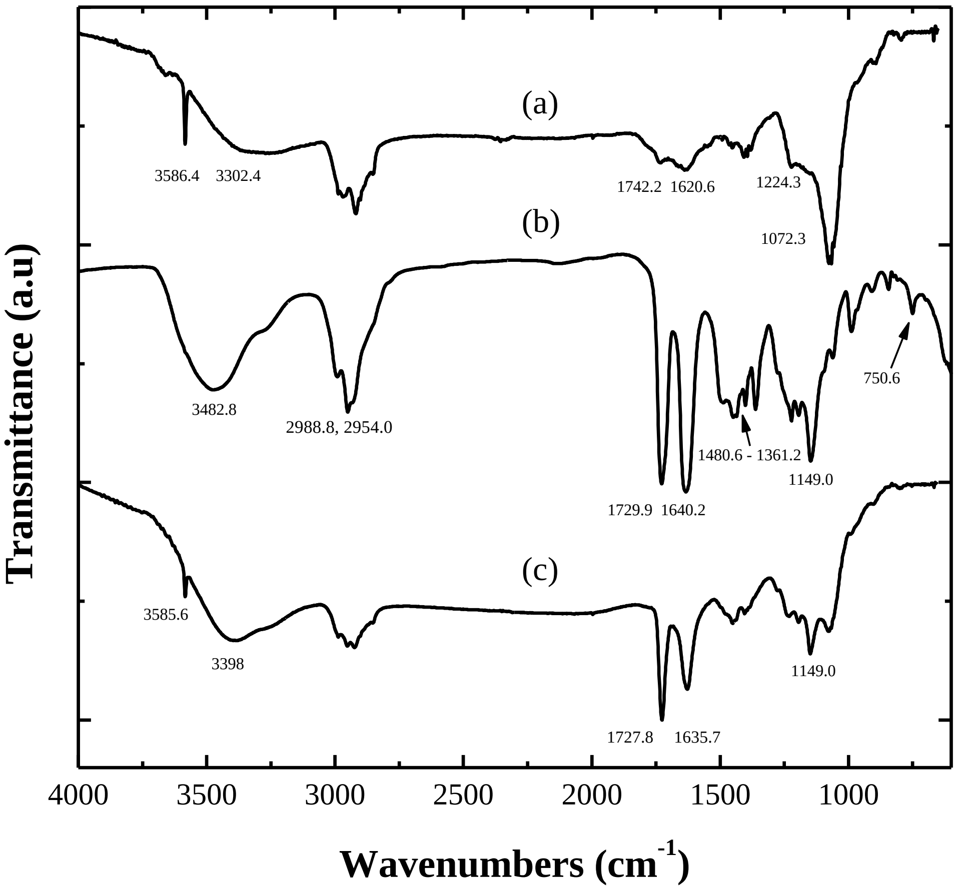

Figure 5.4. FTIR spectra of (a) DVS-magnetic beads, (b) magnetic p(DMA-*co*-MMA)* and (c) magnetic C-dot/p(DMA-*co*-MMA)* nanocomposites.

In the FTIR spectra of the DVS-magnetic beads (Figure 5.4 (a)), S-OH stretching was observed at 3500 cm^{-1} region, and C-H stretching in the 3000 cm^{-1} region respectively [18]. These observations were attributed to how the DVS-magnetic beads were manufactured. In this case the iron oxide particles were silica coated, and the DVS grafted to the surface had a long hydrocarbon chain (10 carbons). Strong vibrational peaks at 1230 cm^{-1} and 1073 cm^{-1} in the DVS-magnetic beads are attributed to the sulfone (S=O) stretching [17] and to S-O stretching in the silica coating [18]. However, weak vibrational peaks at 1640 cm^{-1} can be attributed to C=C stretching or the absorbed water and the Si-OH of the DVS-magnetic beads [18]. The C=C-H stretching (between 3100 cm^{-1} and 3000 cm^{-1}) and bending (between 650 cm^{-1} and 1000 cm^{-1}) modes [16] should have been observed but were not. The strong vibrational peak associated with S-C stretching in the 750 cm^{-1} region for C-S of the sulfone, observed in literature (in the liquid phase) [17], was also not observed. As the C=C stretching vibration is directly adjacent to the sulfone group this may have affected this vibration.

The FTIR spectra of the magnetic CdS/p(DMA-*co*-MMA)* and C-dot/p(DMA-*co*-MMA)* nanocomposites (Figure 5.4 (b and c)) both showed that the C-H stretching is still present due to the long chain DVS on the magnetic bead, and the polymer backbone of p(DMA-*co*-MMA). Strong peaks observed at 1725 cm^{-1} to C=O stretching of the ester in the methacrylate moiety on the back bone and of 1640 cm^{-1} were attributed to C=O stretching of the amide acrylamide moieties of the polymer [16]. This made it difficult to conclude whether the peaks associated with the C=C in 1600 cm^{-1} region had diminished due to the thiol-ene click reaction. Peaks observed in the 1400 cm^{-1} region and 1100 cm^{-1} region of the two magnetic nanocomposites (Figure 5.4 (b and c) correspond to the methyl groups (C-H rock and bend) and C-O stretches of the methacrylate and acrylamide moieties of the grafted polymer.

In the region between 1000 cm^{-1} to 600 cm^{-1} for the magnetic nanocomposites (Figure 5.4 (b and c)), peaks were only observed in the FTIR spectrum of CdS/p(DMA-*co*-MMA)* ((Figure 5.4 (b)). Attention was drawn towards the peak at 750 cm^{-1}, which correlates to C-S stretching. This was an indication of the new C-S peak formed during thiol-ene click reaction.

FTIR spectral analysis showed that the aminolysis/thiol-ene click reaction was successful between the DVS-magnetic beads and CdS/p(DMA-*co*-MMA) with to the prominent C-S vibration present at 750 cm^{-1} in the FTIR analysis of the magnetic CdS/p(DMA-*co*-MMA)*. However, this peak was not observed for the C-dot/p(DMA-*co*-MMA)* nanocomposites hence suggested that the aminolysis/thiol-ene click reaction for this case was not successful. The peaks attributed to the elimination of the alkene group (in the 1600 cm^{-1}, 3000 cm^{-1} and 800 cm^{-1}) were too ambiguous, or not present, in either spectra of the precursor DVS-magnetic beads and the magnetic nanocomposites to suggest whether the reaction was successful/unsuccessful. A plethora of interactions in relation to the C-dot/polymer nanocomposites were envisaged such as the DVS-magnetic beads potentially reacting with the other surface moieties or edges states (from the graphitic core) available on the C-dot. Further investigation is required to understand the exact interactions occurring during the one-pot aminolysis/thiol-ene reaction and was beyond the scope of this thesis.

5.3.2 TGA of the DVS-magnetic beads versus magnetic CdS/p(DMA-*co*-MMA)* and C-dot/p(DMA-*co*-MMA)*

Figure 5.5 shows the TGA thermograms for (a) DVS-magnetic beads, (b) CdS/p(DMA-*co*-MMA), (c) C-dot/p(DMA-*co*-MMA), (d) magnetic p(DMA-*co*-MMA)* and (e) magnetic C-dot/p(DMA-*co*-MMA)*. Table 5.1 following this figure summarises the values for the residue obtained after heating each sample to 500 °C, as well as the T_d and maximum weight loss of each sample determined by their TGA thermograms.

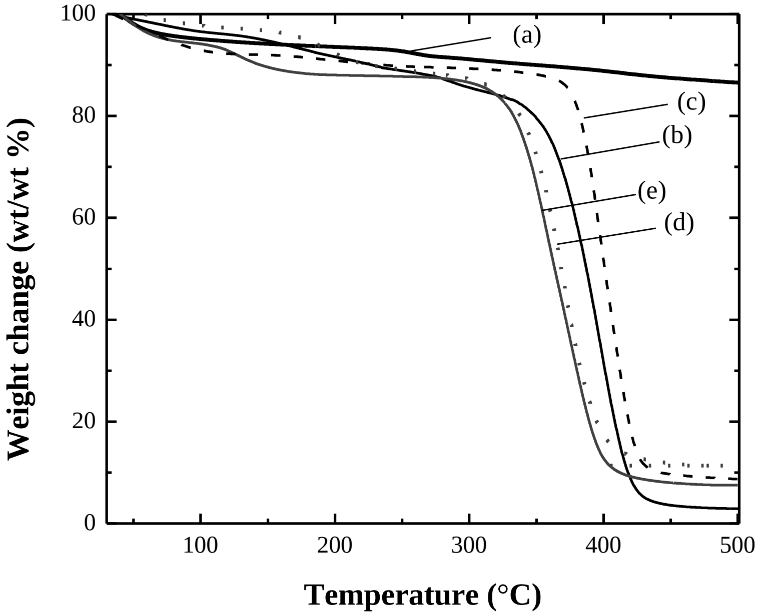

Figure 5.5. Overlayed TGA thermograms of (a) DVS-magnetic beads, (b) CdS/p(DMA-*co*-MMA), (c) C-dot/p(DMA-*co*-MMA), (d) magnetic CdS/p(DMA-*co*-MMA)* and (e) magnetic C-dot/p(DMA-*co*-MMA)*.

Table 5.1. Values for wt/wt % residue after heating to 500 °C, T_d as a range, T_d and wt/wt % maximum weight loss after T_d.

	Residue (wt/wt %)	T_d range (°C)	T_d (°C)	Maximum weight loss after T_d (wt/wt %)
(a)	85.1	200 - 290	257.5	2.0
		387 - 425	415.3	6.4
(b)	3.6	252 - 441	387.2	81.4
(c)	9.3	317 - 457	369.5	79.4
(d)	8.2	270 - 425	400.2	79.3
(e)	13.5	145-274	195.9	7.9
		297 - 426	371.1	77.9

Weight loss observed in all TGA (Figure 5.5) up to 200 °C was attributed to water loss, or residual DMF solvent in the magnetic nanocomposite sample. The TGA curve for DVS-magnetic beads (Figure 5.5 (a)) shows two thermal degradation steps upon heating to 500 °C. As these DVS-magnetic beads were purchased it is suggested that the first weight loss (2.0 wt/wt %) observed at a T_d of 257.5 °C is attributed to the degradation of the vinyl sulfone grafted from the magnetic bead, and the second weight loss (6.4 wt/wt %) at T_d of 415.3 °C is attributed to the silica coating on the iron oxide nanoparticles [19].

To confirm the successful incorporation of the DVS-magnetic beads to the CdS and C-dot nanocomposites, the T_d and residue wt/wt % of the magnetic nanocomposites were compared to their appropriate non-magnetic nanocomposites precursor (included in in Figure 5.5 and Table 5.1, and previously described in Chapter 3, Section 3.3.2 and Chapter 4, Section 4.6.2, respectively). The residue wt/wt % of magnetic CdS/p(DMA-*co*-MMA)* (8.2 wt/wt %) was greater than the non-magnetic CdS/p(DMA-*co*-MMA) (3.6 %), a difference of 4.6 wt/wt %. Similarly, the residue wt/wt % of the magnetic C-dot/p(DMA-*co*-MMA)* (13.5 wt/wt %) was greater than its precursor non-magnetic C-dot/p(DMA-*co*-MMA) (9.3 wt/wt %), by a difference of 4.2 wt/wt %. The differences in residue wt/wt % of the magnetic CdS/p(DMA-*co*-MMA)* (4.6 wt/wt%) and C-dot/p(DMA-*co*-MMA)* (4.2 wt/wt %) with respect to their non-magnetic precursors were similar and attributed to the magnetic bead content in the final nanocomposites produced. This was expected as the experimental design (i.e., the concentration of DVS-magnetic beads used) was identical.

The T_d of magnetic CdS/p(DMA-*co*-MMA)* (at 400.2 °C) was greater than the non-magnetic CdS/p(DMA-*co*-MMA) (at 387.2 °C), a difference of 13 °C. This increase in T_d indicated that click reaction between thiolated CdS/p(DMA-*co*-MMA) and the DVS-magnetic beads was successful. The T_d of magnetic C-dot/p(DMA-*co*-MMA)* (at 371.1 °C) was only slightly greater than its precursor non-magnetic C-dot/p(DMA-*co*-MMA) (at 369.5 °C), a difference of only 1.6 °C. The difference in temperature calculated for the C-dot/polymer nanocomposites was smaller than the ramp temperature (10 °C min^{-1}). Therefore, it was subjective as to conclude whether the DVS-magnetic beads were in fact “clicked” onto the C-dot/p(DMA-*co*-MMA) nanocomposite. These results suggest that the aminolysis/click reaction was successful for synthesis of the CdS/p(DMA-*co*-MMA)* nanocomposites and not C-dot/p(DMA-*co*-MMA)* nanocomposites. This agreed with the FTIR spectroscopy analysis previously discussed and is further investigated in Section 5.3.4, where fluorescence spectrophotometry data shows similar conclusions.

5.3.3 UV-vis absorbance of the DVS-magnetic beads versus magnetic CdS/p(DMA-*co*-MMA)* and C-dot/p(DMA-*co*-MMA)*

Figure 5.6 shows the UV-vis absorbance spectra of (a) DVS-magnetic beads, (b) CdS/p(DMA-*co*-MMA), (c) C-dot/p(DMA-*co*-MMA), (d) magnetic CdS/p(DMA-*co*-MMA)* and (e) C-dot/p(DMA-*co*-MMA)* dissolved in DMF (pure DMF was used as the baseline). The red shifts in absorbance wavelength were measured at absorbance = 0.5 a.u represented as the light grey dotted line in Figure 5.6 and these values are summarised in Table 5.2.

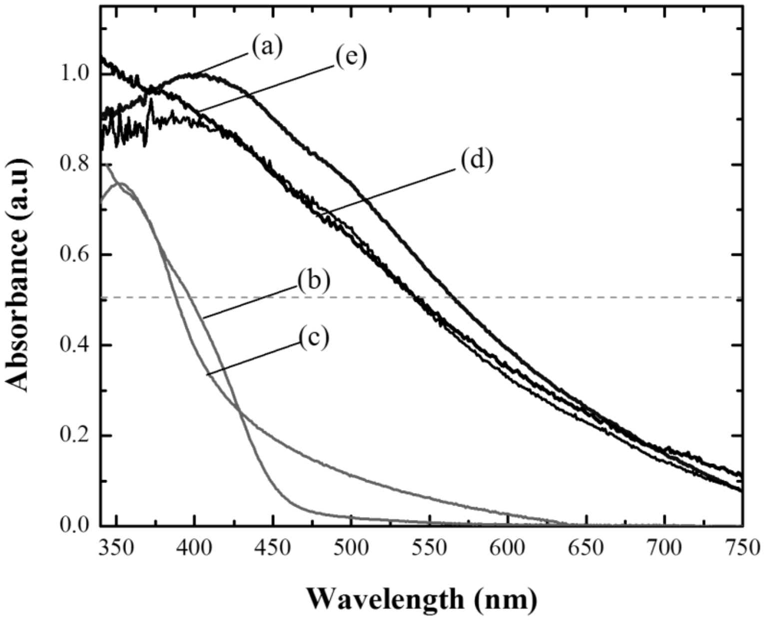

Figure 5.6. Overlayed UV-vis absorbance spectra of (a) DVS-magnetic beads, (b) CdS/p(DMA-*co*-MMA), (c) C-dot/p(DMA-*co*-MMA), (d) magnetic CdS/p(DMA-*co*-MMA)* and (e) magnetic C-dot/p(DMA-*co*-MMA)*.

Table 5.2. Measured absorbance wavelength at absorbance = 0.5 a.u for samples (a) DVS-magnetic beads, (b) CdS/p(DMA-*co*-MMA), (c) C-dot/p(DMA-*co*-MMA), (d) magnetic CdS/p(DMA-*co*-MMA)* and (e) magnetic C-dot/p(DMA-*co*-MMA)*.

	Absorbance wavelength at 0.5 a.u (nm)
(a)	567.1
(b)	396.5
(c)	388.7
(d)	539.1
(e)	543.5

The DVS magnetic beads (Figure 5.6 (a)) had a broad absorbance at long wavelengths (567.1 nm). This was expected as it appears as a milky brown solution. The reaction between the DVS-magnetic beads and non-magnetic CdS/p(DMA-*co*-MMA) and C-dot/p(DMA-*co*-MMA) precursors (Figure 5.6 (b) and (c)), consequently causes the the absorbance spectra of the magnetic products, CdS/p(DMA-*co*-MMA)* and magnetic C-dot/p(DMA-*co*-MMA)* (Figure 5.6 (d) and (e)) to broaden by 142.6 au and 154.8 a.u, respectively). This indicated that the optical properties of the DVS magnetic beads will have a masking effect on the optical properties of the CdS QDs and C-dots in the polymer nanocomposite.

5.3.4 Fluorescence spectra of DVS-magnetic beads versus magnetic CdS/p(DMA-*co*-MMA)* and C-dot/p(DMA-*co*-MMA)*

Ideally, these magnetic nanocomposites will retain their fluorescence properties for their application to latent fingermark detection. Figure 5.7 shows the fluorescence emission spectra excited at 350 nm of (a) DVS-magnetic beads, (b) CdS/p(DMA-*co*-MMA), (c) C-dot/p(DMA-*co*-MMA) before the aminolysis/thiol-ene click reaction and the final products (d) magnetic CdS/p(DMA-*co*-MMA)* and (e) magnetic C-dot/p(DMA-*co*-MMA)*. Table 5.3 summarises the fluorescence properties, fluorescence maxima and intensities, FWHM and calculated QY (against R6G) of the magnetic CdS/p(DMA-*co*-MMA)* and C-dot/p(DMA-*co*-MMA)* nanocomposites compared to the non-magnetic CdS/p(DMA-*co*-MMA) and C-dot/p(DMA-*co*-MMA) nanocomposites.

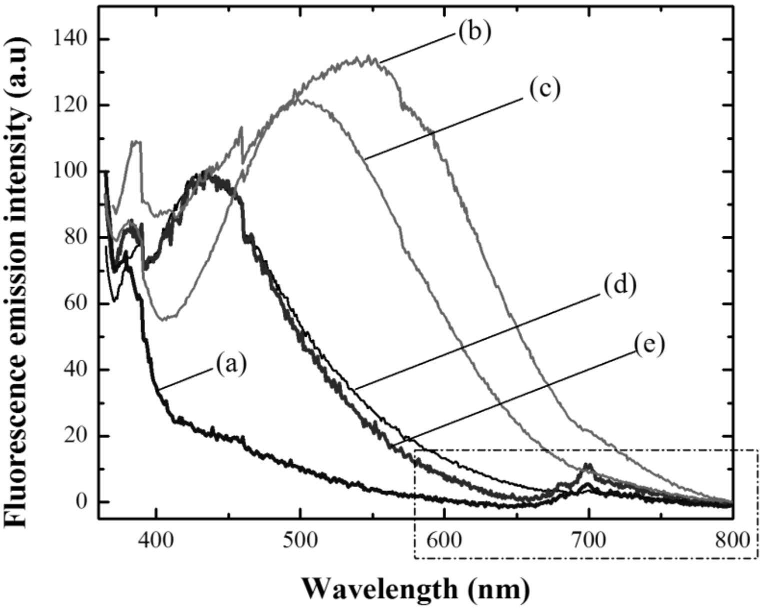

Figure 5.7. Overlayed fluorescence emission spectra of (a) DVS-magnetic beads, (b) CdS/p(DMA-*co*-MMA), (c) C-dot/p(DMA-*co*-MMA), (d) magnetic CdS/p(DMA-*co*-MMA)* and (e) magnetic C-dot/p(DMA-*co*-MMA)*, in DMF, excited at 350 nm.

Table 5.3. Fluorescence maxima, intensity, FWHM and QY % of (a) DVS-magnetic beads, (b) CdS/p(DMA-*co*-MMA), (c) C-dot/p(DMA-*co*-MMA), (d) magnetic CdS/p(DMA-*co*-MMA)* and (e) magnetic C-dot/p(DMA-*co*-MMA)*.

	Fluorescence peak maxima (nm)	**Fluorescence intensity (a.u)**	**FWHM (nm)**	**QY (%)**
(a)	N/A	N/A	N/A	N/A
(b)	543.8	133	233	23.7
(c)	503.3	121	173	12.6
(d)	435	101	N/A	11.4
(e)	441.6	97	N/A	6.3

The fluorescence emission profile of the DVS-magnetic beads (Figure 5.7 (a)) shows a sharp peak at 380 nm and a low intensity peak at 700 nm. It is suggested that these peaks are attributed to both the sulfone group (O=S=O) and alkene (C=C) group, respectively. The peak at 380 nm, however, coincides with the emission peak due to the C_{12}CTA, shown in Figure 5.7 (b), and (c) and therefore could not be defined for the fluorescence emission spectra of magnetic nanocomposites, shown in Figure 5.7 (d) and (e).

The fluorescence emission spectra of the magnetic nanocomposites CdS/p(DMA-*co*-MMA)* and C-dot/p(DMA-*co*-MMA)*, Figure 5.7 (d) and (e), were compared to its precursor non-magnetic CdS/p(DMA-*co*-MMA) and C-do/p(DMA-*co*-MMA), Figure 5.7 (b) and (c). The fluorescence intensity of the precursor non-magnetic CdS/p(DMA-*co*-MMA) and C-dot/p(DMA-*co*-MMA) (Figure 5.7 (b) and (c)) after the aminolysis/thiol-ene click reaction decreased by 32 a.u. and 30 a.u, respectively (Figure 5.7 (d) and (e)). A blue-shift of approximately 100 nm was also observed when comparing the nanocomposites both before (Figure 5.7 (b) and (c)) and after the aminolysis/thiol-ene reaction (Figure 5.7 (d) and (e)). This blue-shift was attributed to the magnetic beads masking a majority of the fluorescent emissions from the CdS and C-dot/p(DMA-*co*-MMA) nanocomposites. A comparison between the measured FWHM (Table 5.3) was not made, as they could not be measured for the magnetic nanocomposites (Figure 5.7 (d) and (e)). However, the QY's were calculated (against R6G dye) and are shown in Table 5.3. As expected due to the reduction in fluorescence intensity of the magnetic CdS/p(DMA-*co*-MMA)* and C-dot/p(DMA-*co*-MMA)* nanocomposites compared to the non-magnetic CdS/p(DMA-*co*-MMA) and C-dot/p(DMA-*co*-MMA) the QY was reduced by a half (calculated to 48.3 % and 55.2 %, respectively).

Figure 5.8 (a) to (c) shows the fluorescence emission spectra magnified to focus on the region between 600 nm and 800 nm for samples of DVS-magnetic beads, CdS/p(DMA-*co*-MMA)* and C-dot/p(DMA-*co*-MMA)*, respectively.

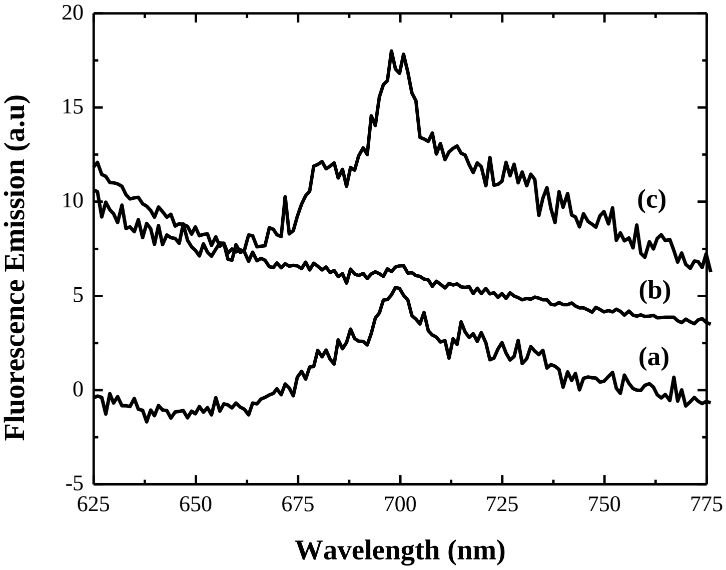

Figure 5.8. Stacked fluorescence emission spectra of (a) DVS-magnetic beads, (b) CdS/p(DMA-*co*-MMA)* and (c) C-dot/p(DMA-*co*-MMA)* using an excitation of 350 nm.

The peak at 700 nm from the DVS-magnetic beads (Figure 5.8 (a)) was more prominent in the fluorescence emission spectrum of the magnetic C-dot/p(DMA-*co*-MMA)* and less prominent in the spectrum of the magnetic CdS/p(DMA-*co*-MMA)*. It was suggested that the peak at 700 nm may be attributed to excitations between the sulfone group and alkene in the DVS-magnetic bead, and the peak at 380 nm was correlated to the transitions involving the sulfur, as this was a similar wavelength to which the C_{12}CTA (also containing sulfur) emitted at.

These results further indicated that the aminolysis/thiol-ene click reaction presented in this research was more successful with the CdS/p(DMA-*co*-MMA) nanocomposites over the C-dot/p(DMA-*co*-MMA) nanocomposites. Only the CdS/p(DMA-*co*-MMA)* will be considered for latent fingermark detection. Further validation of the method is required in order to better understand the mechanism of the reaction occurring with the C-dot/p(DMA-*co*-MMA) nanocomposites

5.4 Visual observations: Photographs of the magnetic CdS/p(DMA-*co*-MMA)* nanocomposites

The magnetisation of the purchased DVS-magnetic beads was stated as ~40 EMU.g^{-1}. It was desirable to measure the magnetism before and after the aminolysis/thiol-ene reaction, however, instruments were not available to the institution. Visual means of testing magnetism were used by using a magnetic rod (stir bar retriever). This is also comparable to the typical magnetism observed in a magnetic wand used in forensic fingerprinting. Shown in Figure 5.9 are photographs of magnetic CdS/p(DMA-*co*-MMA)* attracted to, and adhering to, a magnetic rod under (a) white light and (b) UV (350nm) illumination in a dark room.

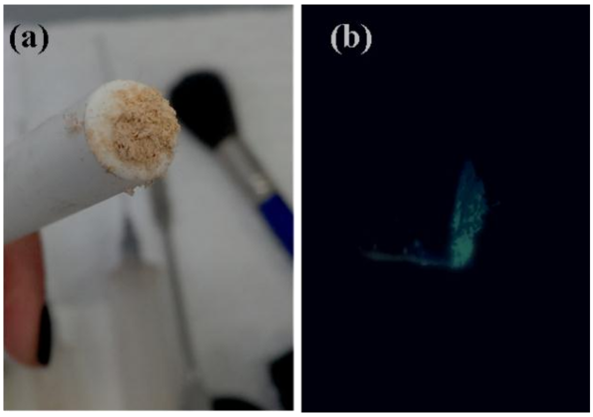

Figure 5.9. Photographs of magnetic CdS/p(DMA-*co*-MMA)* on a magnetic rod under (a) white light and (b) UV illumination in a dark room (shutter speed = 30 s).

It can be seen in Figure 5.9 that the magnetic CdS/p(DMA-*co*-MMA)* was both magnetic and fluorescent (green-blue). The fluorescence intensity was visually poor which was expected due to its reduced intensity fluorescence emission spectra and low QY, discussed in Section 5.3.4 of this chapter. Nonetheless it clearly indicates that these nanocomposites have multi-functionality as a potential fingerprinting agent. The non-magnetic CdS/p(DMA-*co*-MMA) nanocomposite powders showed no magnetic properties as expected.

5.5 Conclusions

Using a one-pot aminolysis/thiol-ene click reaction between CdS/p(DMA-*co*-MMA) and C-dot/p(DMA-*co*-MMA) with DVS-magnetic beads, magnetic nanocomposites powders were synthesised. The simultaneous aminolysis and thiol-ene click reaction minimised the occurrence of undesirable products as a result of interchain disulfide linking. FTIR spectral analysis, TGA, and fluorescence spectrophotometry collectively suggested that the aminolysis/thiol-ene click reaction was more successful with magnetic CdS/p(DMA-*co*-MMA)* than the C-dot/p(DMA-*co*-MMA). The optical properties measured by UV-vis and fluorescence spectrophotometry show that, in solution (DMF solvent), the nanocomposites optical properties were masked by the milky brown nature of the attached magnetic beads. Photographs of magnetic CdS/p(DMA-*co*-MMA adhering to a magnetic rod, however, showed that their magnetism was retained. In addition, photographs taken under UV illumination in a dark room revealed their visually acceptable fluorescence in its dry powdered form. The application of these magnetic CdS/p(DMA-*co*-MMA)* only will be discussed in Chapter 6.

5.6 References for Chapter 5

1. Boyer, C., Granville, A., Davis, T.P., and Bulmus, V., *Modification of RAF-polymers via thiol-ene reactions: A general route to functional polymers and new architectures.* Journal of Polymer Science Part A: Polymer Chemistry, 2009. **47** (15): p. 3773-3794.
2. Roth, P.J., Kessler, D., Zentel, R., and Theato, P., *A method for obtaining defined end groups of polymethacrylates prepared by the RAFT process during aminolysis.* Macromolecules, 2008. **41** (22): p. 8316-8319.
3. Xu, J., He, J., Fan, D., Wang, X., and Yang, Y., *Aminolysis of polymers with thiocarbonylthio termini prepared by RAFT polymerization: The difference between polystyrene and polymethacrylates.* Macromolecules, 2006. **39** (25): p. 8616-8624.
4. Li, M., De, P., Gondi, S.R., and Sumerlin, B.S., *End group transformations of RAFT-generated polymers with bismaleimides: Functional telechelics and modular block copolymers.* Journal of Polymer Science Part A: Polymer Chemistry, 2008. **46** (15): p. 5093-5100.
5. Willcock, H. and O'Reilly, R.K., *End group removal and modification of RAFT polymers.* Polymer Chemistry, 2010. **1** (2): p. 149-157.
6. Boyer, C. and Davis, T.P., *One-pot synthesis and biofunctionalization of glycopolymers via RAFT polymerization and thiol–ene reactions.* Chemical Communications, 2009. **45** (40): p. 6029-6031.
7. Bigg, D.C.H. and Lesimple, P., *Triethylamine/aluminum chloride promoted aminolysis of lactones: a useful method for the preparation of ω-hydroxyalkanamides.* Synthesis, 1992. **1992** (03): p. 277-278.
8. Evans, D.J., Kanagasooriam, A., Williams, A., and Pryce, R., *Aminolysis of phenyl esters by microgel and dendrimer molecules possessing primary amines.* Journal of Molecular Catalysis, 1993. **85** (1): p. 21-32.
9. Hoyle, C.E. and Bowman, C.N., *Thiol–ene click chemistry.* Angewandte Chemie International Edition, 2010. **49** (9): p. 1540-1573.
10. Lowe, A.B., *Thiol-ene "click" reactions and recent applications in polymer and materials synthesis.* Polymer Chemistry, 2010. **1** (1): p. 17-36.
11. Campos, L.M., Killops, K.L., Sakai, R., Paulusse, J.M., Damiron, D., Drockenmuller, E., Messmore, B.W., and Hawker, C.J., *Development of Thermal and Photochemical Strategies for Thiol− Ene Click Polymer Functionalization.* Macromolecules, 2008. **41** (19): p. 7063-7070.
12. Xi, W., Wang, C., Kloxin, C.J., and Bowman, C.N., *Nitrogen-centered nucleophile catalyzed thiol-vinylsulfone addition, another thiol-ene "click" reaction.* American Chemical Scociety Macro Letters, 2012. **1** (7): p. 811-814.
13. Liu, J., Bulmus, V., Barner-Kowollik, C., Stenzel, M.H., and Davis, T.P., *Direct synthesis of pyridyl disulfide-terminated polymers by RAFT polymerization.* Macromolecular Rapid Communications, 2007. **28** (3): p. 305-314.
14. Shen, W., Qiu, Q., Wang, Y., Miao, M., Li, B., Zhang, T., Cao, A., and An, Z., *Hydrazine as a nucleophile and antioxidant for fast aminolysis of RAFT polymers in air.* Macromolecular Rapid Communications, 2010. **31** (16): p. 1444-1448.
15. Chong, Y.K., Moad, G., Rizzardo, E., and Thang, S.H., *Thiocarbonylthio end group removal from RAFT-synthesized polymers by radical-induced reduction.* Macromolecules, 2007. **40** (13): p. 4446-4455.
16. Cramer, N.B. and Bowman, C.N., *Kinetics of thiol–ene and thiol–acrylate photopolymerizations with real-time fourier transform infrared.* Journal of Polymer Science Part A: Polymer Chemistry, 2001. **39** (19): p. 3311-3319.
17. Ellzy, M.W., Jensen, J.O., and Kay, J.G., *Vibrational frequencies and structural determinations of di-vinyl sulfone.* Spectrochimica Acta Part A: Molecular and Biomolecular Spectroscopy, 2003. **59** (4): p. 867-881.

18. Wang, S., Zhang, Z., Liu, B., and Li, J., *Silica coated magnetic iron oxide nanoparticles supported phosphotungstic acid: a novel environmentally friendly catalyst for the synthesis of 5-ethoxymethylfurfural from 5-hydroxymethylfurfural and fructose.* Catalysis Science and Technology, 2013. **3** (8): p. 2104-2112.
19. Wang, G. and Harrison, A., *Preparation of iron particles coated with silica.* Journal of Colloid and Interface Science, 1999. **217** (1): p. 203-207.

Chapter 6. Application of the CdS QD and C-dot polymer nanocomposites as fingermark developing reagents

6.1 Synopsis

This chapter describes the preparation and application of the CdS QD and C-dot polymer nanocomposites (discussed in Chapters 3, 4 and 5) to latent fingermark detection. Background information relevant to this chapter will be provided. The preparation of the CdS QD and C-dot polymer nanocomposites as fingermark developing reagents, the latent fingermark deposits and techniques required for visualisation and photography of the developed fingermarks will be described. The performance of the CdS QD and C-dot polymer nanocomposites as fingermark developing reagents will be discussed and compared to each other.

6.2 Introduction and background information

An introduction to fingermarks and conventional methods of detection was described in the introduction to the thesis in Chapter 1. Here, methods utilised in this thesis are described.

A fingermark identified on an object at a crime scene is often the only proof that there was contact between the person and that particular object. It is important to keep in mind that a fingermark (once matched and identified) is never proof of a person's accountability. It is the forensic examiner's role to prove and present their identification to the courts where it is the judge or jury who are responsible for deciding the guilt or innocence of the identified person [1-3].

There are several approaches towards fingermark detection at a crime scene and these will generally involve the application of a sequence of complementary techniques that are chosen according to the circumstances [2, 4]. Often the first step in visualising latent fingermarks is *via* optical detection using the naked eye or a forensic light source. Alongside the type of surface the fingermark has been deposited (discussed in Chapter 1, Section 1.2.2), the types of reagents chosen for subsequent development will also depend on whether the evidence in question is fixed or transportable. In general, solution based developing reagents (e.g., Ninhydrin and cyanoacrylate fumigation) are preferably used on transportable evidence collected and delivered to a forensic laboratory, whereas powder dusting agents are the preferred methods for latent fingermark detection on-site with fixed objects [2]. These conventional methods were described in Chapter 1.

6.2.1 Forensic light source – The Polilight®

As mentioned, optical detection is the first step in visualising latent fingermarks on a surface (in the laboratory or at the crime scene). The most frequently used device in Australia for visualising and detecting fingermarks and other bodily excretions such as blood and semen, with or without fluorescent enhancement, is the Polilight® Forensic Light Source (PFLS) [2, 5-7]. The Polilight® is comprised of a Xenon lamp under high pressure where its emission spectrum (shown in Figure 6.1) is flat from approximately 250 nm to 700 nm [6].

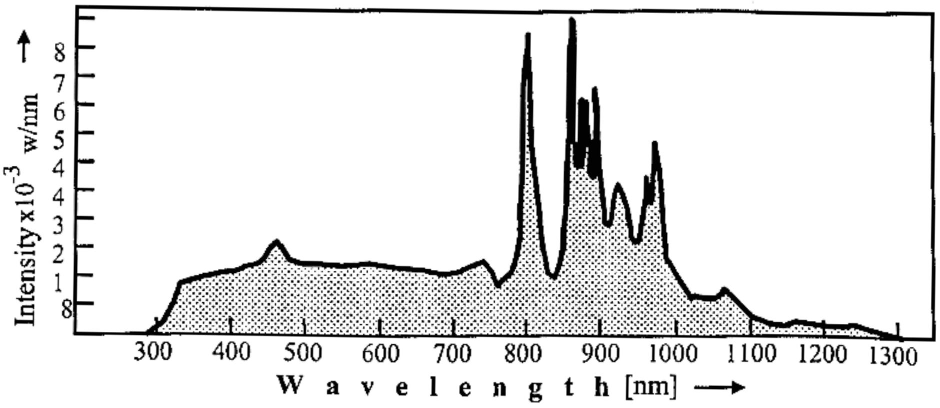

Figure 6.1. The emission spectrum of a high pressure xenon arc lamp used in the Polilight®. Image scanned from Australian Federal Police workshop booklet [6].

Interference filters integrated in the Polilight® systems allow the selection of wavelengths from the UV through to the red in the visible spectrum, shown in Table 6.1. The intensity of light and the colour filters at each band (except the ultraviolet) can be tuned [6].

Table 6.1. Band characteristics of a typical Polilight® (model PL10 used in this thesis, table adapted from [6]).

Band	Central wavelength (nm)	Half bandwidth (nm)
Ultraviolet	360	60
Violet	415	40
Blue I	440	40
Blue II	450	80-100
Blue III	490	40
Blue-Green	505	40
Green I	530	40
Green II	555	30
Orange	590	40
Red I	620	40
Red II	650	40
White	380 – 650	

6.2.2 Visualisation and photography

Visualising and photographing developed fluorescent fingermark a deposit using the Polilight® is aided by the use of barrier filters attached to a camera. These filters effectively screen for the fluorescent emission and screen out the reflected incident light or other competing light. There are two types of filters often used in optical observations in latent fingermark detection and photography; barrier band pass filters and long pass filters. Barrier band pass filters are selective to a specific wavelength range while rejecting the rest outside that range. For example, a green band pass filter will be selective for wavelengths 565 ± 40 nm. Long pass barrier filters are selective to longer wavelengths while rejecting the shorter ones. For example, an orange long pass barrier filter will be selective for wavelengths from 550 nm onwards, while rejecting wavelengths smaller than 550 nm [2, 6, 7].

In this thesis fingermarks developed by the non-magnetic CdS QD and C-dot polymer nanocomposites will be photographed using a green filter (555 ± 24 nm) and a red filter (640 ± 40 nm). This is because the emission spectra of the CdS QDs and C-dots under UV excitation are broad and range between 400 nm and 700 nm (Chapter 3, Section 3.8 and Chapter 4, Section 4.5 , respectively). On the other hand fingermarks developed using the magnetic CdS/polymer nanocomposites will be captured using a blue filter (450 ± 80 nm) as its fluorescence emission maximum was centred at approximately 480 nm (Chapter 5, Section 5.3.4).

6.2.3 Ridge patterns of a fingerprint: Classification and minutiae

Ridge patterns are what makes a fingermark unique to an individual and the identification of these are required for person identification [1, 2]. The amount of ridge characteristics present in a latent fingermark will depend on a number of factors such as its age (how long the fingermark has been sitting on that surface), the pressure applied when the fingermark was deposited, the amount of contaminants, environmental factors, and the age, gender and ethnicity of the fingermark donor [2-4, 8, 9]. Once the latent fingermark is developed and photographed, the examiner then analyses the ridge characteristics by means of their classification and identification of minutiae. Fingermarks can be classified based on their general shape or pattern of the ridges. There are three main classifications: arch, loop and whorl, shown in Figure 6.2

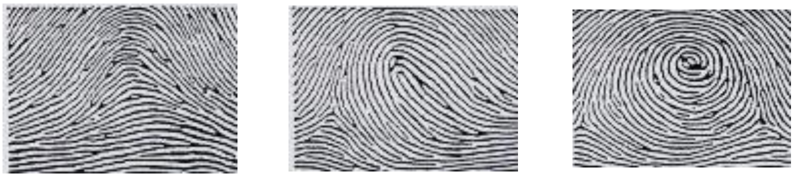

(a) ARCH **(b) LOOP** **(b) WHORL**

Figure 6.2. Main classification patterns (a) arch, (b) loop and (c) whorl (image was taken from the Australian police website http://www.australianpolice.com.au/dactyloscopy/fingerprint-pattern-classification/. visited 2012).

Variations of these patterns such as tented arch, central pocket loop, right loops, left loops, lateral pocket loop, twinned loop and accidental (a mixture of an arch and loop and whorl) are also possible [1, 2, 4]. The minutiae or ridge characteristics that can be identified are annotated in Figure 6.3. After these ridge characteristics have been identified, the fingermark can be matched to the victim or suspect. All fingermarks are now stored electronically, and the first step is the application of the matching algorithm that compares relative positions of minutiae and gives a proved list of the best batches. The fingerprint examiner then further examines the match to confirm identity [1, 10].

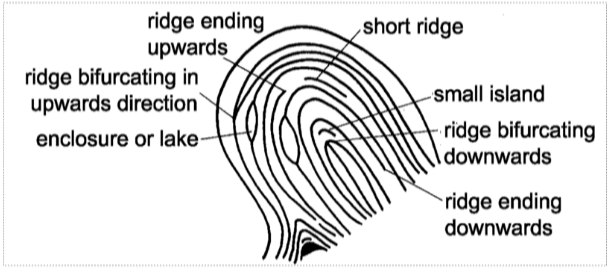

Figure 6.3. Fingermark annotated with the different types of minutiae that can be identified [4].

In this thesis, the ability to visually recognise these fingermark patterns was used to judge the performance of the reagent applied, keeping in mind that the amount of fingermark deposited would also depend on the factors (age, pressure, and contaminants) mentioned earlier in this section.

6.3 Preparation of the CdS QD and C-dot polymer nanocomposites as fingermark reagents for latent fingermark detection

This section will describe the preparation of latent fingermark specimens and the preparation and application of the CdS QD and C-dot polymer nanocomposites.

6.3.1 Table of materials and reagents

Material/Reagent	Origin	Info
Aluminium foil	Black and Gold, Australia	Used as purchased
CdS/p(DMA)	Chapter 3	Redissolved in Milli-Q water (1 g/L)
CdS/p(DMA-*co*-MMA)	Chapter 3	
CdS/p(DMA-*co*-Sty)	Chapter 3	
C-dot/p(DMA)	Chapter 4	Redissolved in Milli-Q water (1 g/L)
C-dot/p(DMA-*co*-MMA)	Chapter 4	
CdS/p(DMA-*co*-MMA)*	Chapter 5	
Milli-Q water (18.2 Ω)		
Glass microscope slides	Livingstone, Australia	Used as purchased.
Fingermark brush	Optitech 8 squirrel hair brush	

6.4 Preparation of latent fingermarks

A female donor, aged 26 was used for the latent fingermark deposits. Sweat was produced by rubbing fingertips on the forehead and back of the neck before subsequently placing hands in gloves for 3-5 min. This was to ensure that the sweat was a mixture of excretions from the different sweat glands (eccrine, apocrine and sebaceous glands) present around the human body. Fingermarks were immediately deposited onto the chosen substrate (aluminium foil or glass microscope slide). Fingermarks developed immediately were and termed as “fresh” and other fingermarks were aged for two weeks and referred to as “aged” fingermarks.

6.4.1 Surface substrates: Aluminium foil and glass microscope slides

Aluminium foil was chosen as a representative for metal substrates on which fingermarks may be found at a crime scene. In addition, aluminium foil is extensively used in clan laboratories during the synthesis of illegal drugs [11, 12].

Glass surfaces are also often encountered at a crime scene. Common examples include windows, drinking glasses, and beer and wine bottles. Glass microscope slide were used as glass representative substrate in this thesis.

6.5 Preparation of the CdS QD and C-dot polymer nanocomposite fingermark reagents

This section will describe the preparation of the fingermark reagents: CdS/p(DMA), CdS/p(DMA-*co*-MMA), CdS/p(DMA-*co*-Sty), C-dot/p(DMA), C-dot/p(DMA-*co*-MMA) and magnetic CdS/p(DMA-*co*-MMA)* nanocomposites. The CdS QDs and C-dots grafted with p(DMA) were water soluble nanocomposites, hence were used in an aqueous solution reagent whereby substrates bearing the latent fingermark were immersed. CdS QD and C-dot polymer nanocomposites with grafted copolymers p(DMA-*co*-MMA) and p(DMA-*co*-Sty) from their surface were powders, and used as dusting agents. Details pertaining to their preparation are summarised in Table 6.2.

Table 6.2. Preparation and application of the CdS QD and C-dot polymer nanocomposite fingermark reagents.

Fingermark reagent	Preparation	Fingermark development
CdS/p(DMA) **C-dot/p(DMA)**	~1 g was dissolved in 100 mL of Milli-Q water.	Substrate bearing the latent fingermark was immersed in aqueous solution for at least 5 s, with fingermark facing down. This was followed by 3 x 100 mL washes with Milli-Q water. Substrate was then dried at room temperature for at least 3 h before photographing.
CdS/p(DMA-*co*-MMA) **CdS/p(DMA-*co*-Sty)** **C-dot/p(DMA-*co*-MMA)** **Magnetic CdS/p(DMA-*co*-MMA)***	Powder used as is.	Using the Optitech squirrel hair brush, powder was gently dusted over the fingermark deposit on the chosen substrate. The brush was also used to gently remove excess powder.

Typically a magnetic wand is used with a magnetic powder to detect latent fingermarks [13-15]; however, the amount of magnetic CdS/p(DMA-*co*-MMA)* powder produced was insufficient for use. Latent fingermarks developed with the magnetic CdS/p(DMA-*co*-MMA)* powders were performed using a brush.

6.6 Visualisation and photography of the developed latent fingermarks

The developed latent fingermarks were visualised using a PL10 Polilight® (Rofin, Australia – donated by the South Australian Police (SAPOL)) using the UV light (350 nm) setting. Photographs were taken (as raw files) in a dark room using a Nikon D3100 Digital Single Lens Reflex (DSLR) camera with an 18-55 mm or 58 mm lens (auto focus (AF) Nikkor) with shutter speed of 30 s and aperture set to *f*/2.8. The experimental setup is shown in an annotated diagram below (Figure 6.4)

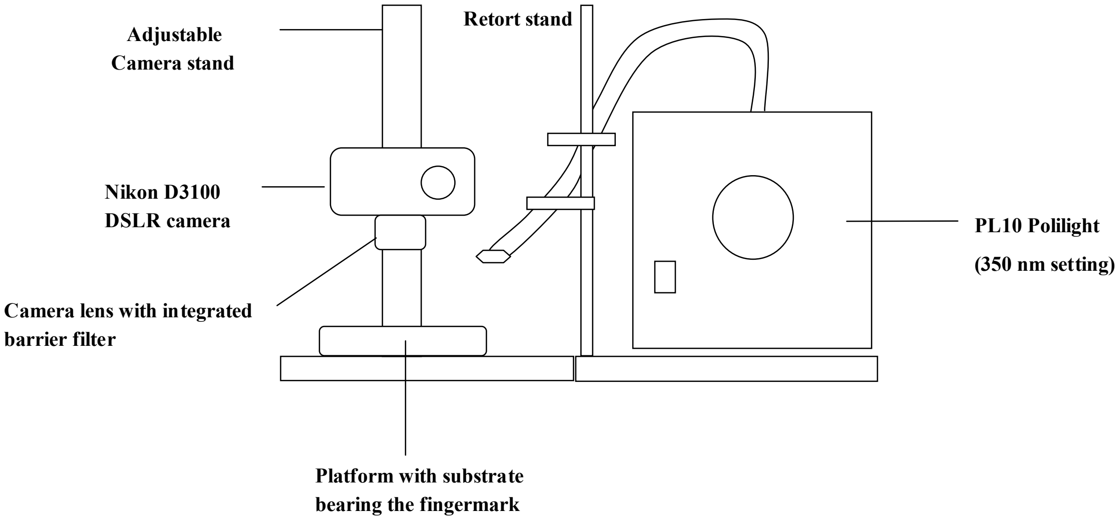

Figure 6.4. Camera and Polilight® setup for latent fingermark visualisation and photography.

6.7 Photographs of the latent fingermarks developed by the CdS QD and C-dot polymer nanocomposites

This section will present the photographs of the latent fingermarks developed by the CdS QD and C-dot polymer nanocomposites. First displayed are the photographs of the latent fingermarks developed on aluminium foil followed by fingermarks on glass microscope slides. The latent fingermarks developed by the magnetic CdS/p(DMA-*co*-MMA)* nanocomposite powders will be displayed separately. The visibility of the latent fingermark in terms of intensity and identifiable ridge characteristics will be discussed and a table summarising the performance of each nanocomposite *via* a score card can be found in Section 6.8.1 of this chapter.

6.7.1 Fingermark development on aluminium foil substrates

Figure 6.5 shows latent fingermarks developed on aluminium foil by the CdS QD and C-dot polymer nanocomposites and photographed under UV light (350 nm setting on the Polilight®). Rows in Figure 6.5 (a-d) correspond to fingermark development using (a) aqueous CdS/p(DMA) solution, (b) CdS/p(DMA-*co*-MMA) powder, (c) CdS/p(DMA-*co*-Sty) powder, (d) C-dot/p(DMA) solution and (e) C-dot/p(DMA-*co*-MMA) powder. The photographs are also arranged into columns corresponding to capture modes (left to right) with no filter, a green filter (555 ± 24 nm) and a red filter (640 ± 40 nm). The developed fingermarks in each column are shown in pairs where fingermarks on the left fingermarks were developed “fresh” (within 2 hours of latent fingermark deposition onto the substrate) and fingermarks on the right were “aged” (2 weeks after latent fingermark deposition onto the substrate).

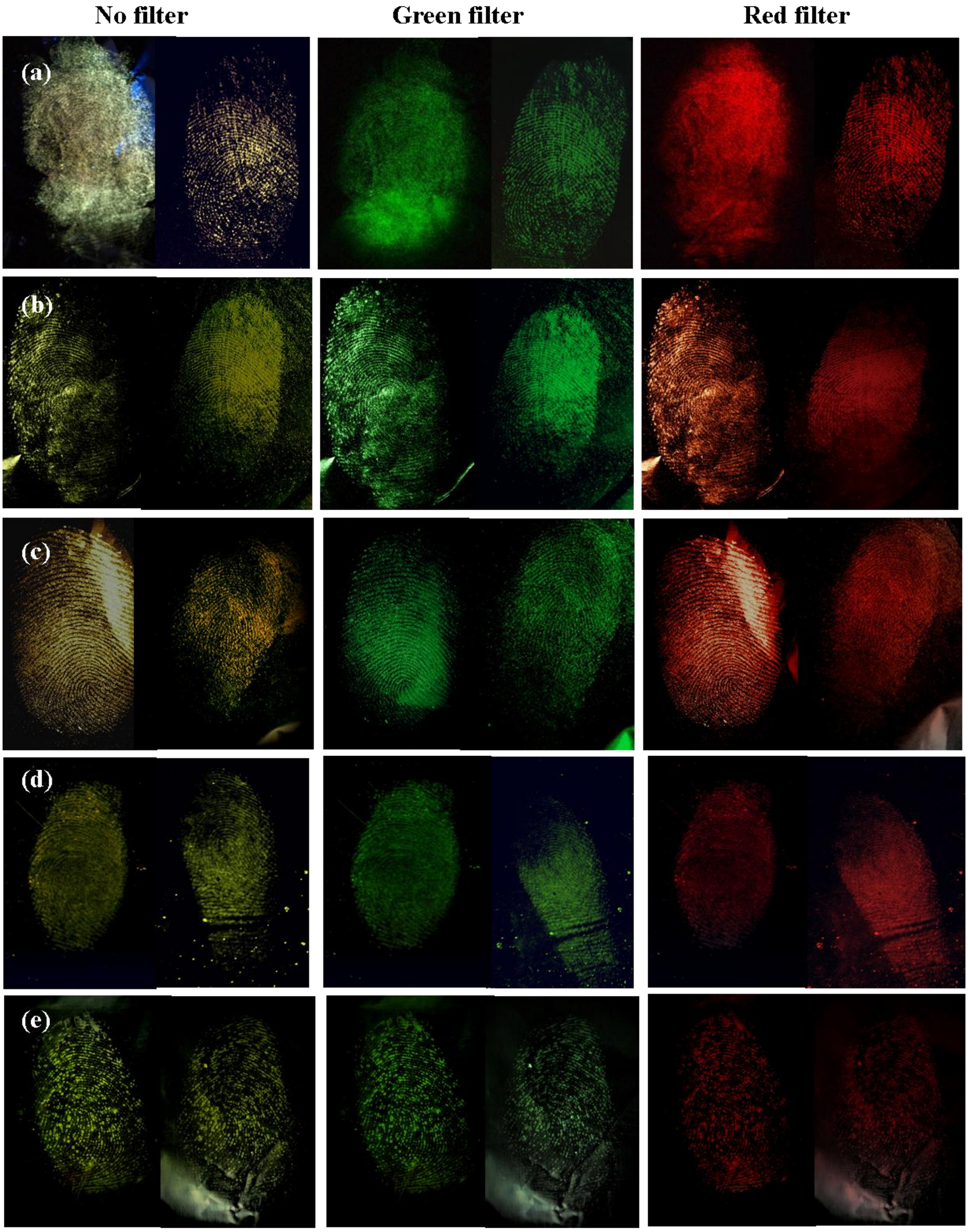

Figure 6.5. Latent fingermarks on aluminium foil developed by row (a) CdS/p(DMA) solution reagent, (b) CdS/p(DMA-*co*-MMA) powder, (c) CdS/p(DMA-*co*-Sty) powder, (d) C-dot/p(DMA) solution reagent and (e) C-dot/p(DMA-*co*-MMA) powder. Photographs were taken under UV illumination (350 nm) using no filter, a green filter (555 ± 24 nm) and a red filter (640 ± 40 nm) as annotated. Left fingermark: fresh latent fingermarks, right fingermark: aged fingermarks.

In Figure 6.5 (a) the CdS/p(DMA) solution reagent showed preferential adherence to the latent fingermark over the aluminium foil substrate. Photographs taken with no filter showed that the CdS/p(DMA) nanocomposite (dried on the latent fingermark) appeared yellow-orange under UV-illumination. This agreed with its fluorescence emission spectra (fluorescence maximum at 533.6 nm, see Chapter 3, Section 3.8.2 for spectrum). The photographs captured with a green filter (555 ± 24 nm) and a red filter (640 ± 40 nm) show the developed latent fingermark has good contrast in these respective colours. Minimal ridge definition was identified in the fresh latent fingermarks developed (the fingermark on the left of each pair), as the solution appeared to have solubilised and disrupted the latent fingermark deposit. In the aged fingermark developed by the CdS/p(DMA) solution reagent (the fingermark on the right of each pair), less disruption of the ridges was observed. There were, however, areas where the fingermark could have potentially been washed away (at the top and bottom), or degraded over the 2 week aging time. Ridge characteristics can be observed and identified in the aged fingermark developed by the CdS/p(DMA) solution reagent. This fingermark was classified as a loop, or a right loop.

Fingermarks developed by the CdS/p(DMA-*co*-MMA) powders are shown in Figure 6.5, row (b). Preferential adherence of the powder to the latent fingermark over the aluminium foil substrate was observed. Under UV illumination the developed fingermark appears orange in colour using no filters and so red and green fluorescence could be successfully extracted using the appropriate filters. This agreed with the CdS/p(DMA-*co*-MMA) fluorescence emission spectra (fluorescence maximum at 548.2 nm, see Chapter 3, Section 3.8.2 for spectrum). A similar amount of ridge definition was achieved in both the fresh and aged fingermarks; however, parts of the fingermark were incomplete – possibly attributed to degradation and evaporation of unstable constituents such as water over 2 weeks. The classification of both fingermarks were identified to follow a loop pattern, and minutiae were identifiable.

Fingermarks developed by the CdS/p(DMA-*co*-Sty) powders are shown in Figure 6.5, row (c). Similar results were observed to that of the CdS/p(DMA-*co*-MMA) powders (Figure 6.5, row (b)). Preferential adherence of the powder to the latent fingermark over the aluminium foil substrate was observed. Under UV illumination, the developed fingermark appeared a green-yellow colour using no filters and so red and green fluorescence could be successfully extracted using the appropriate filters. This agreed with the fluorescence emission spectra (fluorescence maximum at 572.2 nm, see Chapter 3, Section 3.8.2 for spectrum). Different fingermarks were identified for the fresh (fingermark on the left) and the aged (fingermark on the right). The fresh fingermark patterns were classified as a loop whereas the aged fingermark appeared to follow a whorl pattern.

In Figure 6.5 (d), the C-dot/p(DMA) solution reagent showed preferential adherence to the latent fingermark over the aluminium foil substrate. Photographs taken with no filter showed that the C-dot/p(DMA) nanocomposite (dried on the latent fingermark) appeared lime green under UV-illumination which agreed with its fluorescence emission spectra (fluorescence emission maximum at 473.3 nm, described in Chapter 4, Section 4.6.6). The photographs captured with the green and red filter showed that the latent fingermark developed had good contrast in these respective colours. The optical intensity of these fingermarks was less when compared to the fingermarks developed by the CdS/p(DMA) solution reagent (Figure 6.5 (a)). This was expected as the QY of the C-dots measured (QY = 24.1 %) was less than the CdS QDs (QY = 32 % for CdS/p(DMA)).

With the freshly developed latent fingermarks (fingermarks on the right of Figure 1.5) the solution appeared to have disrupted and/or solubilised the latent fingermark near the centre of the deposit. This made it difficult to identify ridge patterns. Ridges on the outer edge, however, appear distinguishable. In the aged fingermark developed by CdS/p(DMA) solution reagent (the fingermark on the right of each pair), less solution agitation was observed. Ridge characteristics can be observed and identified and the classification of this aged fingermark as a loop pattern was distinguishable.

Fingermarks developed by the C-dot/p(DMA-*co*-MMA) powders are shown in Figure 6.5, row (e). Preferential adherence of the powder to the latent fingermark over the aluminium foil substrate was observed. Under UV illumination, the developed fingermark appears lime green in colour using no filters, and the red and green fluorescence were successfully extracted using the appropriate filters. The optical intensity of these fingermarks was less when compared to the fingermarks developed by the CdS/p(DMA) solution reagent (Figure 6.5 (b)) due to their lower QY as mentioned previously. Furthermore, uneven visual fluorescence intensities of the powder were also observed. This suggested that the polymer on the C-dot surface uncontrollably affected the fluorescence emission edge states on the C-dot. A similar amount of ridge definition was achieved in both the fresh and aged fingermarks. The classification of both fingermarks was identified to follow left loop patterns.

6.7.1.1 Summary of observations for latent fingermark detection on aluminium foil substrates

The CdS/p(DMA) solution reagent, CdS/p(DMA-*co*-MMA) powder, CdS/p(DMA-*co*-Sty) powder, C-dot/p(DMA) solution reagent and C-dot/p(DMA-*co*-MMA) powder all preferentially adhered to the latent fingermark deposit over the aluminium foil substrate. The colour of fingermarks photographed under UV illumination without filters agreed with their fluorescence emission spectra previously described in Chapters 3 and 4 of this thesis for the CdS/polymer and C-dot/polymer nanocomposites, respectively. Fingermarks, in particular fresh fingermarks, developed by the solution reagents (CdS/p(DMA) and C-dot/p(DMA)) were susceptible to agitation and solubilisation by the aqueous solution, sacrificing ridge definition. It could be argued that the reagents developed aged fingermarks with better ridge detail than fresh fingermarks, however, this is too subjective to conclude as there are many other factors that could have attributed to this observation such as contaminants in the fingermark deposit and the amount of pressure applied during deposition. However, it is known that over time a fingermark can degrade or have its less stable constituents (i.e., water) evaporated [8, 16]. It was also found that the fluorescence intensity of the C-dot/polymer nanocomposites were less than the CdS/polymer nanocomposites. This was expected as the CdS/polymer nanocomposites had greater QYs than the C-dot/polymer nanocomposites.

6.7.2 Fingermark development on glass microscope slide substrates

CdS/p(DMA) and C-dot/p(DMA) nanocomposites solution reagents were not successful in developing latent fingermarks on glass microscope substrates. The nanocomposites adhered to both the fingermark and the glass microscope slides and no preferential adherence to the latent fingermark was observed. Therefore, this section will show the development of fresh and aged fingermarks deposited on glass microscope slides using of CdS/p(DMA-*co*-MMA), CdS/p(DMA-*co*-Sty) and C-dot/p(DMA-*co*-MMA) powder nanocomposites.

Figure 6.6 (a-c) shows latent fingermarks on glass microscope slides developed by the CdS QD and C-dot polymer nanocomposites and photographed under UV light (350 nm setting on the Polilight®). Rows in the figure correspond to fingermark development using (a) CdS/p(DMA-*co*-MMA) powder, (b) CdS/p(DMA-*co*-Sty) powder, and (c) C-dot/p(DMA-*co*-MMA) powder. The photographs are also sorted into columns corresponding to capture modes with no filter (Figure 1.6, left column), a green filter (555 ± 24 nm) (Figure 1.6, middle column) and red filter (640 ± 40 nm) (Figure 1.6, right column). Pairs of fingermarks are shown where the left fingermarks were developed fresh and the right are aged.

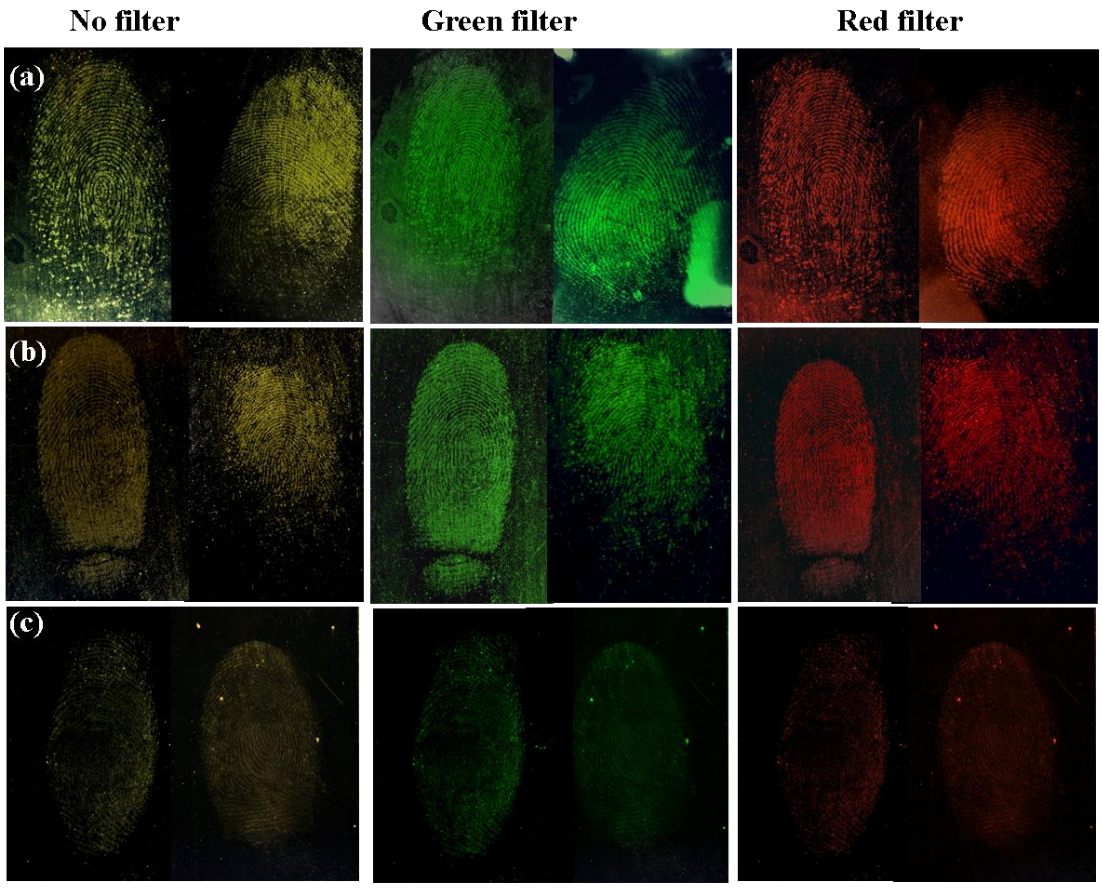

Figure 6.6. Latent fingermarks on glass microscope slides developed by row (a) CdS/p(DMA-*co*-MMA), (b) CdS/p(DMA-*co*-Sty) and (c) C-dot/p(DMA-*co*-MMA). Photographs were taken under UV illumination (350 nm) using no filter, a green filter (555 ± 24 nm) and red filter (640 ± 40 nm). Left fingermark: fresh latent fingermarks, right: aged fingermarks.

Figure 6.6 row (a) shows that there is preferential adherence of CdS/p(DMA-*co*-MMA) powder to the latent fingermark over the glass substrate. However some of the finer powder particles appear to have adhered to the glass even after attempts at removing the excess powder with gentle dusting. Analogous to Figure 6.5 (b), the CdS/p(DMA-*co*-MMA) powder appeared yellow-green under UV light with no filter and green and red with the corresponding filters used. The developed aged fingermarks (fingermarks on the right) appear to show less ridge detail on the top and bottom of the fingermark. This was most likely due to the evaporation of unstable constituents of the fingermark such as water [8, 16]. The fresh latent fingermarks fit the whorl classification whereas the aged fingermarks were classified as right loops.

Fingermarks developed by CdS/p(DMA-*co*-Sty) are shown in Figure 6.6, row (b). The powders adhered preferentially to the fingermark, but some adherence onto the glass substrate was observed. This can be clearly seen in the aged fingermarks (the fingermarks on the right, Figure 6.6). Under UV illumination, the fingermarks developed by CdS/p(DMA-*co*-Sty) powder appear yellow-orange without filters, and green and red with the corresponding filters used. Similar to CdS/p(DMA-*co*-MMA) (Figure 6.6, row (a)) the fresh fingermarks developed by the CdS/p(DMA-*co*-Sty) powder showed better ridge characteristics than the aged fingermarks. The fresh fingermarks were classified as whorls and the aged fingermarks could be classified as left loops.

Fresh and aged fingermarks on glass microscope slides developed using C-dot/p(DMA-*co*-MMA) powder is shown in Figure 6.6, row (c). Under UV illumination the developed fingermark appears lime green in colour using no filters, and the red and green fluorescence were successfully extracted using the appropriate filters. The optical intensity of these fingermarks was less when compared to the fingermarks developed by the CdS/p(DMA) solution reagent (Figure 6.6 (a)). Uneven visual fluorescence intensities of the powder were also observed similar to that previously observed in Figure 6.5, row (e). This suggests that the polymer on the C-dot surface has uncontrollably affected the fluorescence emission edge states on the C-dot. A similar amount of ridge definition was achieved in both the fresh and aged fingermarks. The classification of both fingermarks was a right loop and whorl for the fresh and aged fingermarks, respectively.

6.7.2.1 Summary of observations for latent fingermark detection on aluminium foil substrates

The CdS/p(DMA-*co*-MMA), CdS/p(DMA-*co*-Sty) and C-dot/p(DMA-*co*-MMA) powders were found to preferentially adhere to the latent fingermark deposit, however some adherence to the glass microscope substrate was observed. This was due to the hydrophilic and polar nature of the silica that makes up the glass microscope slide. Hydrophilic and polar components of the polymers (i.e., amide and ester moieties) can potentially be attracted to the silica of the glass slides. The powders developed aged fingermarks with better ridge detail than fresh fingermarks. This too could be subjective to conclude, as there are many other factors that could have attributed to this observation such as contaminants in the fingermark deposit and the amount of pressure applied during deposition. Similar to observations in Section 6.7.1 it was also found that the fluorescence intensity of the C-dot/polymer nanocomposites was less than the CdS/polymer nanocomposites. This was expected as the CdS/polymer nanocomposites had greater QYs than the C-dot/polymer nanocomposites. The colour of fluorescence emitted from the developed latent fingermarks observed when no filter was used agreed with fluorescence emission spectral analysis previously described in Chapter 3 and 4 of this thesis for the CdS/polymer and C-dot/polymer nanocomposites, respectively.

6.8 Fingermark detection using the magnetic CdS/p(DMA-*co*-MMA)* powder nanocomposites

Figure 6.7 shows photographs of latent fingermarks on aluminium foil and a glass microscope slide developed using the magnetic CdS/p(DMA-*co*-MMA)* nanocomposite. The appearance of the CdS/p(DMA-*co*-MMA)* nanocomposite under UV illumination was blue, which was expected as its fluorescence maximum was at 480 nm (described previously in Chapter 5, Section 5.3.4). In addition, the visual fluorescence intensity of the magnetic CdS/p(DMA-*co*-MMA)* powders appeared lower than the non-magnetic CdS and C-dot polymer nanocomposites previously shown, as this too correlated with fluorescence emission data discussed in Chapter 5, Section 5.3.4.

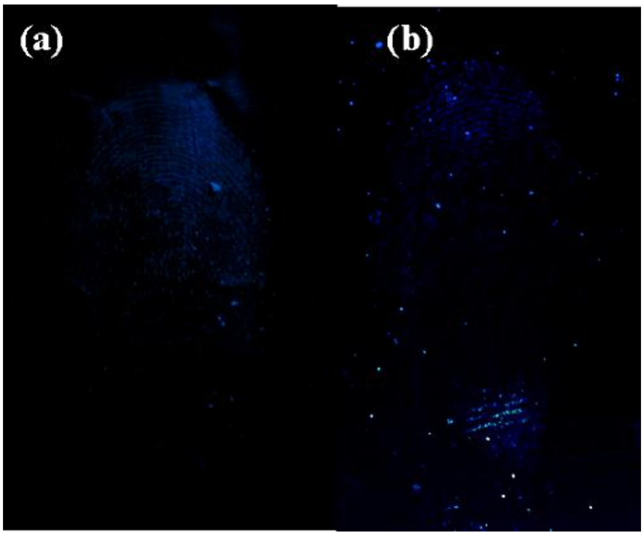

Figure 6.7. Photographs of latent fingermarks deposited on (a) aluminium foil and (b) glass microscope slide developed by the magnetic CdS/p(DMA-*co*-MMA)* powder. Photographs were taken under UV illumination (350 nm) with a blue filter (450 ± 80 nm).

In Figure 6.7 (a), preferential adherence of the CdS/p(DMA-*co*-MMA)* powder to the latent fingermark over the aluminium foil substrate was observed. The ridges are visible; however there is not a full fingermark so a classification could not be made. On the glass microscope slide (Figure 6.7 (b)) the CdS/p(DMA-*co*-MMA)* powder adhered to the fingermark deposit and slightly to the glass slide (despite attempts at gently brushing excess powder off the substrate). Similar to the CdS QD and C-dot co-polymer nanocomposites in the previous section the hydrophilic or polar constituents of the polymer backbone may have been attracted to the hydrophilic and polar silica surface of the glass. It was also found that the CdS/p(DMA-*co*-MMA)* powders were susceptible to agglomeration due to their magnetism, hence particle sizes were not homogenous which affected their ease in application.

6.8.1 Table summarising the overall performance of the QD and C-dot polymer nanocomposites application in latent fingermark detection

Table 6.3 summarises the performance of the nanocomposites (a) CdS/p(DMA), (b) CdS/p(DMA-*co*-MMA), (c) CdS/p(DMA-*co*-Sty), (d) C-dot/p(DMA), (e) C-dot/p(DMA-*co*-MMA) and (f) magnetic CdS/p(DMA-*co*-MMA)* as latent fingermark reagents. Performance is an overall score given to the nanocomposites based on fluorescence visibility (2 x), capability of developing fresh and 2 week aged fingermarks (2 x), and ridge resolution (2 x). With a maximum score of 6 x (or “ xxxxxx ”). Note that these were compared to each other, therefore, the nanocomposite that performed the best using the criteria stated, will score xxxxxx. Furthermore the magnetic CdS/p(DMA-*co*-MMA)* powder was scored based on its fluorescence visibility (2 x) and ridge resolution (2 x) as only fresh fingermarks were considered.

Table 6.3. Summary of the performance of CdS QD and C-dot polymer nanocomposites fingermark reagents.

	Nanocomposite	**Reagent type**	**Surface**		**Performance**
			Al foil	Glass	
(a)	CdS/p(DMA)	Aqueous solution	Y	N	xxxx
(b)	CdS/p(DMA-*co*-MMA)	Powder	Y	Y	xxxxxx
(c)	CdS/p(DMA-*co*-Sty)	Powder	Y	Y	xxxxxx
(d)	C-dot/p(DMA)	Aqueous solution	Y	N	xxx
(e)	C-dot/p(DMA-*co*-MMA)	Powder	Y	Y	xxxx
(f)	Magnetic CdS/p(DMA-*co*-MMA)*	Powder	Y	Y	xx

6.9 Conclusions

The powder reagents, CdS/p(DMA-*co*-MMA) and CdS/p(DMA-*co*-Sty) performed the best as fingermark developing agents compared to the other CdS and C-dot polymer nanocomposites synthesised. This was based on their ability to develop fresh and aged fingermarks with identifiable ridge definition and provide visual contrast *via* fluorescence. This was followed by the C-dot/p(DMA-*co*-MMA) powder reagent as they were capable of developing aged and fresh fingermarks with visible ridge characteristics, but their fluorescence was of lower intensity. The CdS and C-dot/p(DMA) solution based reagents scored lower than the powder reagents as they were susceptible towards solubilising and agitating the fingermark deposit (in particular the fresh latent fingermarks), resulting in indistinguishable ridge characteristics. The performance of the magnetic CdS/p(DMA-*co*-MMA)* was given the lowest score. The low fluorescence intensity of the magnetic powders showed poor visual contrast when compared to the other nanocomposites used, however, some ridge characteristics were identifiable. Furthermore, their score did not include their performance on aged fingermarks, as fresh fingermarks were only considered.

6.10 References for Chapter 6

1. Jiang, X. and Yau, W.-Y. *Fingerprint minutiae matching based on the local and global structures*. in *15th International Conference on Pattern Recognition Proceedings.* . 2000. IEEE.
2. Champod, C., Lennard, C.J., Margot, P., and Stoilovic, M., *Fingerprints and Other Ridge Skin Impressions*2004: Taylor & Francis.
3. Thomas, G.L., *The physics of fingerprints and their detection.* Journal of Physics. E, Scientific Instruments, 2001. **11** (8): p. 722.
4. Saferstein, R., *Criminalistics, an Introduction to Forensic Science*. 8th Edition (International) 2004: Pearson Education.
5. Stoilovic, M., *Detection of semen and blood stains using Polilight as a light source.* Forensic Science International, 1991. **51** (2): p. 289-296.
6. Stoilovic, M. and Lennard, C., *Fingerprint Detection and Enhancement, Australian Federal Police Workshop Manual* 2006.: Australia Federal Police Forensic Services (Canberra Australia).
7. Margot, P. and Lennard, C., *Fingerprint Detection Techniques*. Criminalistics 1994: Institut de police scientifique et de criminologie, Université de Lausanne.
8. Girod, A., Ramotowski, R., and Weyermann, C., *Composition of fingermark residue: A qualitative and quantitative review.* Forensic Science International, 2012. **223** (1–3): p. 10-24.
9. Langenburg, G., *Deposition of bloody friction ridge impressions.* Journal of Forensic Identification, 2008. **58** (3): p. 355.
10. Jain, A.K., Ross, A., and Prabhakar, S., *An introduction to biometric recognition.* IEEE Transactions on Circuits and Systems for Video Technology, 2004. **14** (1): p. 4-20.
11. Burgess, J.L. and Chandler, D., *Clandestine drug laboratories*. Occupational, industrial, and environmental toxicology (2nd ed.)2003: Mosby Publishers. 746-765.
12. Gimeno, P., Besacier, F., Bottex, M., Dujourdy, L., and Chaudron-Thozet, H., *A study of impurities in intermediates and 3, 4-methylenedioxymethamphetamine (MDMA) samples produced via reductive amination routes.* Forensic Science International, 2005. **155** (2): p. 141-157.
13. James, J., Pounds, C., and Wilshire, B., *Magnetic flake fingerprint technology.* Journal of Forensic Identification, 1991. **41** (4): p. 237-247.
14. James, J.D., Pounds, C.A., and Wilshire, B., *Flake metal powders for revealing latent fingerprints.* Journal of Forensic Sciences, 1991. **36** (5): p. 1368-1375.
15. James, J.D., Pounds, C.A., and Wilshire, B., *Magnetic flake powders for fingerprint development.* Journal of Forensic Sciences, 1993. **38**: p. 391-391.
16. Asano, K.G., Bayne, C.K., Horsman, K.M., and Buchanan, M.V., *Chemical composition of fingerprints for gender determination.* Journal of forensic sciences, 2002. **47** (4): p. 805-807.

Chapter 7. Conclusion and future research

7.1 Summary

The aim of this thesis was to synthesise new fluorescent materials for latent fingermark detection. Current advances in nano and polymer science drove this research towards manufacturing fluorescent CdS QD and C-dot polymer nanocomposites via surface initiated RAFT polymerisation. Homopolymers (p(DMA)) and random co-polymers (p(DMA-co-MMA) and p(DMA-co-Sty)) were grafted-from the CdS QD and C-dot surface modified with C_{12}*CTA and produced solution and powder reagents for latent fingermark detection, respectively. The RAFT process was further exploited with the post modification of the RAFT end group (retained on the nanocomposite) with a divinyl sulfone-magnetic bead via a one-pot aminolysis/thiol-ene click reaction to produce fluorescent magnetic CdS QD and C-dot polymer nanocomposite powders. The CdS QD and C-dot polymer nanocomposites were employed in latent fingermark detection on non-porous substrates.*

7.2 Concluding remarks

From the introduction and literature review in Chapter 1 it was found that there was a desire for incorporating nanoscience into creating one-step fluorescent latent fingermark developing reagents. QDs in particular were of interest due to their intrinsic fluorescent behaviour and stability [1-8]. Literature showed that capping agents are essential for ensuring that QDs preserve their optical capabilities [9-12]. It was found that polymeric capping agents were preferred as they are robust [12-16]. Indeed, polymers have been utilised in fingermark reagents for decades (cyanoacrylate fuming processes) due to their stability over time [17]. Current advances in controlled radical polymer science have already utilised the grafting of polymers from QD surfaces using RAFT polymerisation. RAFT polymerisation results in polymers with controlled molecular weights, and low PDIs [18-21]. The resultant RAFT polymer retains its active site whereby a plethora of post-RAFT polymer modifications can be easily performed [22-26].

Emerging literature in nanocarbons [27-38] promoted the investigation to use fluorescent C-dot nanoparticles for the first time as an alternative to QDs for latent fingermark detection. C-dots have been said to exhibit similar fluorescent capabilities to QDs (albeit *via* different electronic mechanisms) and have been shown to be non-toxic and biocompatible [28, 33-35, 37-42].

In this thesis fingermark developing reagents consisting of CdS QDs and C-dot nanoparticles with a polymer (p(DMA), p(DMA-*co*-MMA) and p(DMA-*co*-Sty) grafted from its surface *via* RAFT polymerisation were synthesised and applied to latent fingermark detection. Chapter 2 described the experimental details for the nanocomposite synthesis and characterisation, and their preparation and application to fingermark detection was described separately in Chapter 6.

Chapter 3 concentrated on the synthesis of CdS/polymer nanocomposites; CdS/p(DMA), CdS/p(DMA-*co*-MM) and CdS/p(DMA-*co*-Sty). CdS/2-mercaptoethanol was first synthesised, which allowed for DCC/DMAP coupling to carboxyl terminated C_{12}CTA (Steglich esterification). The successful synthesis of CdS QDs was monitored *via* UV-vis absorbance and fluorescence spectrophotometry, where quantum confinement was observed with respect to bulk CdS and theoretical calculations of size dependence band gaps (hyperbolic band model). The size of the CdS QDs (~ 5 nm) was determined by theoretical means, and found comparable to TEM imaging measurements. The immobilisation of C_{12}CTA to CdS/2-mercaptoethanol *via* Steglich esterification was verified using FTIR spectroscopy and TGA. The CdS/C_{12}CTA was the platform from which RAFT polymerisation of DMA, MMA and Sty was performed. FTIR and ^{1}H NMR spectroscopies were used to monitor the conversion of monomer to polymer, and kinetic studies showed first order kinetics characteristic of a controlled polymerisation. TGA was used to verify that the polymers were “grafted from” the CdS QD. The degradation temperature (T_d) of the CdS/polymer nanocomposites was greater than the polymers synthesised identically without CdS QDs, indicating that the polymers were attached to the CdS QDs. This ensured that the CdS QDs were secure in the core of the polymer nanocomposite, reducing the concerns for heavy metal leaching. The optical properties of the CdS/polymer nanocomposites were tested using UV-vis and fluorescence spectrophotometry to ensure they were visually suitable for latent fingermark detection.

Chapter 4 discussed the synthesis of C-dot nanoparticles and subsequently polymer C-dot/polymer nanocomposite; C-dot/p(DMA) and C-dot/p(DMA-*co*-MMA). C-dots were synthesised *via* treating activated charcoal with concentrated HNO_3 under reflux for 24

h. The C-dots were characterised using ^{13}C NMR, FTIR, XPS and Raman spectroscopies. From these techniques it was proposed that C-dots had a graphitic-like core (with respect to its activated charcoal precursor) with an oxidised surface. Methods previously established in Chapter 3 were applicable. C_{12}CTA was immobilised to the C-OH moieties on the oxidised surface of the C-dots *via* Steglich esterification, which was followed by the RAFT polymerisation of DMA, and DMA-*co*-MMA. RAFT polymerisation was monitored using FTIR and ^{1}H NMR spectroscopies, including kinetic studies of monomer conversions verifying a controlled polymerisation process and observed first order kinetics. The fluorescence of the C-dots was visually adequate for use as latent fingermark reagents, however, calculated QY were less than the CdS QDs synthesised. From literature the mechanism of fluorescence emission was said to have originated from quasi-fluorophore edge states of the C-dot core and C-COOH surface moieties.

CdS/p(DMA-*co*-MMA) and C-dot/p(DMA-*co*-MMA) nanocomposite powders, previously described in Chapter 3 and 4, respectively, were further subjected to RAFT end-group post modification reactions and described in Chapter 5. A one-pot aminolysis/thiol-ene click reaction with DVS-magnetic beads was devised to synthesise magnetic CdS/p(DMA-*co*-MMA)* and C-dot/p(DMA-*co*-MMA)* powder nanocomposite. A one-pot reaction ensured that the aminolysis of the trithiocarbonyl RAFT end group to produce thiols occurred simultaneously with the thiol-ene click reaction to DVS-magnetic beads, reducing the production of undesired disulfide interchain linking. The products were characterised by FTIR spectroscopy, TGA, and fluorescence and UV-vis spectrophotometry. Collectively these techniques suggested that the reaction was less successful for the C-dot/p(DMA-*co*-MMA) nanocomposite. This suggested that the mechanism of the one-pot aminolysis/thiol-ene click reaction was different for the C-dot/p(DMA-*co*-MMA) nanocomposite than the CdS/p(DMA-*co*-MMA) nanocomposite, despite their analogous synthetic origins (surface initiated RAFT polymerisation. Unfortunately, due to the nature of the magnetic beads (a dark brown powder) the fluorescence emission and intensity of the magnetic nanocomposites synthesised was compromised. There was a reduction in emission intensity and a blue-shift in emission wavelengths away from the visible spectrum range (with respect to their non-magnetic precursors).

In Chapter 6 the nanocomposites synthesised in this thesis were applied to latent fingermark detection on non-porous surfaces. CdS QD and C-dot polymer nanocomposites were prepared differently depending on the type of polymers grafted from their surface. Nanocomposites that contained the homopolymer, p(DMA), grafted from the CdS QD or C-dot surfaces were redissolved in water and used as solution-based fingermark reagents (*via* substrate immersion), whereas the p(DMA-*co*-MMA) and p(DMA-*co*-Sty) based nanocomposites were used as a dry dusting agent powder. Fresh (development within 2 h of deposition) and aged (2 weeks) fingermarks deposited on aluminium foil and glass microscope substrates were developed and photographed. It was found that aged fingermarks were developed with better ridge definition using both forms of reagents. In addition, the powder reagents performed better than the solution reagents in terms of ease of application and ridge definition. This was due to the susceptibility of the fingermark deposit to be disrupted and solubilised upon immersion into the solution reagents.

7.3 Future research

This thesis provided a new platform for fabricating fluorescent nanoparticle-polymer nanocomposites in a systematic manner. This section will briefly discuss different avenues whereby the research presented here can be directed towards.

As mentioned in Chapter 5, further investigations into the C-dot structure and surface edge states is key towards understanding their behaviour during surface modification, and post-modification reactions. It was important to remember that the fluorescence mechanism of C-dots differ to conventional QDs, as they appear to rely highly on electronic transition between the edge states of their graphitic core and oxidised moieties, carboxyl groups in particular, on the surface [43]. In literature surface modifications have been reported to improve fluorescence (and QY) of the C-dots, such as PEG surface modified C-dots. It would be interesting to modify the surface of the C-dots with different molecules or polymers differing in electron withdrawing/donating properties that can amplify the fluorescence behaviour of the C-dots.

The versatility of RAFT polymerisation offers a plethora of synthetic pathways towards different types of nanocomposites, and for different applications, such as imaging drug delivery, and not just for latent fingermark detection. Changing the RAFT agent gives opportunity to select from a wider variety of monomers, giving rise to different polymers on the surface. The function of the polymer can be customised by using different monomers chosen, or by straightforward RAFT end-group modification [21, 24, 44, 45].

Recently, research has been published on the detection of drugs and drug metabolites in latent fingermarks [46-48]. The QD or C-dot polymer nanocomposites synthesised using

RAFT polymerisation could be post-modified with an antibody or aptamers for a drug whereby a drug abuser's latent fingermark may fluoresce a different colour to one deposited by a non-drug abuser.

This project could also be directed towards synthesising QD and C-dot polymers or macro-monomers agents based on the cyanoacrylate fuming process. This method is extensively used in a forensic laboratory due to the stability of cyanoacrylate once polymerised to the fingermark deposit. Research in this area has been based on developing a one-step cyanoacrylate fuming process, whereby the fumed fingermark is simultaneously stained with a fluorescent dye as appose to post-treatments with organic dye (such as R6G) staining [49]. The problem with these new reagents is the poor photo-stability of the organic dye incorporated into the cyanoacrylate superglue reagent with a considerable amount of its visual fluorescence fading within 2 h of development [49]. Incorporating QDs or C-dots within a new polymer composite or macro-monomer (based on this fuming process) can overcome this, as both QDs and C-dots have proven to be photostable.

7.4 References for Chapter 7

1. Algarra, M., Jiménez-Jiménez, J., Moreno-Tost, R., Campos, B.B., and Esteves da Silva, J.C.G., *CdS nanocomposites assembled in porous phosphate heterostructures for fingerprint detection.* Optical Materials, 2011. **33** (6): p. 893-898.
2. Bouldin, K.K., Menzel, E.R., Takatsu, M., and Murdock, R.H., *Diimide-enhanced fingerprint detection with photoluminescent CdS/dendrimer nanocomposites.* Journal of Forensic Sciences, 2000. **45** (6): p. 1239-1242.
3. Dilag, J., Kobus, H., and Ellis, A.V., *Cadmium sulfide quantum dot/chitosan nanocomposites for latent fingermark detection.* Forensic Science International, 2009. **187** (1–3): p. 97-102.
4. Dilag, J., Kobus, H., and Ellis, A.V., *Nanotechnology as a new tool for fingermark detection: A review.* Current Nanoscience, 2011. **7** (2): p. 153-159.
5. Jin, Y., Luo, Y., Li, G., Li, J., Wang, Y., Yang, R., and Lu, W., *Application of photoluminescent CdS/PAMAM nanocomposites in fingerprint detection.* Forensic Science International, 2008. **179** (1): p. 34-38.
6. Menzel, E.R., Savoy, S. M., Ulvick, S.J., Cheng, K. H., Murdock, R. H., and Suduth, M. R, *Photoluminescent semiconductor nanocrystals for fingerprint detection.* Journal of Forensic Sciences, 2000. **45** (3): p. 545-551.
7. Sametband, M., Shweky, I., Banin, U., Mandler, D., and Almog, J. , *Application of nanoparticles for the enhancement of latent fingerprints.* Chemical Communications, 2007 (11): p. 1142 -1144
8. Wang, Y.F., Yang, R.Q., Wang, Y.J., Shi, Z.X., and Liu, J.J., *Application of CdSe nanoparticle suspension for developing latent fingermarks on the sticky side of adhesives.* Forensic Science International, 2009. **185** (1–3): p. 96-99.
9. Frantsuzov, P.A. and Marcus, R., *Explanation of quantum dot blinking without long-lived trap hypothesis.* arXiv preprint cond-mat/0505604, 2005.
10. Green, M., *Semiconductor quantum dots as biological imaging agents.* Angewandte Chemie International Edition, 2004. **43** (32): p. 4129.
11. Kairdolf, B.A., Smith, A.M., and Nie, S., *One-pot synthesis, encapsulation, and solubilization of size-tuned quantum dots with amphiphilic multidentate ligands.* Journal of the American Chemical Society, 2008. **130** (39): p. 12866.
12. Lee, J., Sundar, V.C., Heine, J.R., Bawendi, M.G., and Jensen, K.F., *Full color emission from II–VI semiconductor quantum dot–polymer composites.* Advanced Materials, 2000. **12** (15): p. 1102-1105.
13. Cao, X., Li, C.M., Bao, H., Bao, Q., and Dong, H., *Fabrication of Strongly Fluorescent Quantum Dot−Polymer Composite in Aqueous Solution.* Chemistry of Materials, 2007. **19** (15): p. 3773-3779.
14. Dabbousi, B.O., *Electroluminescence from CdSe quantum dot/polymer composites.* Applied Physics Letters, 1995. **66** (11): p. 1316.
15. Esteves, A.C.C., Bombalski, L., Trindade, T., Matyjaszewski, K., and Barros-Timmons, A., *Polymer grafting from CdS quantum dots via AGET ATRP in miniemulsion.* Small, 2007. **3** (7): p. 1230-1236.
16. Fogg, D.E., Radzilowski, L.H., Dabbousi, B.O., Schrock, R.R., Thomas, E.L., and Bawendi, M.G., *Fabrication of quantum dot-polymer composites: Semiconductor nanoclusters in dual-function polymer matrices with electron-transporting and cluster-passivating properties.* Macromolecules, 1997. **30** (26): p. 8433-8439.
17. Wargacki, S.P., Lewis, L.A., and Dadmun, M.D., *Understanding the chemistry of the development of latent fingerprints by superglue fuming.* Journal of Forensic Sciences, 2007. **52** (5): p. 1057-1062.
18. Moad, G., Chong, Y.K., Postma, A., Rizzardo, E., and Thang, S.H., *Advances in RAFT polymerization: the synthesis of polymers with defined end-groups.* Polymer, 2005. **46** (19): p. 8458-8468.

19. Moad, G., Chiefari, J., Chong, Y.K., Krstina, J., Mayadunne, R.T.A., Postma, A., Rizzardo, E., and Thang, S.H., *Living free radical polymerization with reversible addition – fragmentation chain transfer (the life of RAFT).* Polymer International, 2000. **49** (9): p. 993-1001.
20. Moad, G., *The emergence of RAFT polymerization.* Australian Journal of Chemistry, 2006. **59** (10): p. 661-662.
21. Chiefari, J., Chong, Y.K., Ercole, F., Krstina, J., Jeffery, J., Le, T.P.T., Mayadunne, R.T.A., Meijs, G.F., Moad, C.L., Moad, G., Rizzardo, E., and Thang, S.H., *Living free-radical polymerization by reversible addition-fragmentation chain transfer: The RAFT process.* Macromolecules, 1998. **31** (16): p. 5559-5562.
22. Boyer, C., Liu, J., Bulmus, V., and Davis, T.P., *RAFT polymer end-group modification and chain coupling/conjugation via disulfide bonds.* Australian Journal of Chemistry, 2009. **62** (8): p. 830-847.
23. Boyer, C., Granville, A., Davis, T.P., and Bulmus, V., *Modification of RAFT-polymers via thiol-ene reactions: A general route to functional polymers and new architectures.* Journal of Polymer Science Part A: Polymer Chemistry, 2009. **47** (15): p. 3773-3794.
24. Willcock, H. and O'Reilly, R.K., *End group removal and modification of RAFT polymers.* Polymer Chemistry, 2010. **1** (2): p. 149-157.
25. Roth, P.J., Kessler, D., Zentel, R., and Theato, P., *A method for obtaining defined end groups of polymethacrylates prepared by the RAFT process during aminolysis.* Macromolecules, 2008. **41** (22): p. 8316-8319.
26. Perrier, S., Takolpuckdee, P., and Mars, C.A., *Reversible addition−fragmentation chain transfer polymerization: End group modification for functionalized polymers and chain transfer dgent recovery.* Macromolecules, 2005. **38** (6): p. 2033-2036.
27. Zhou, L., Lin, Y., Huang, Z., Ren, J., and Qu, X., *Carbon nanodots as fluorescence probes for rapid, sensitive, and label-free detection of mercury 2+ and biothiols in complex matrices.* Chemical Communications, 2012. **48** (8): p. 1147-1149.
28. Zhao, Q.-L., Zhang, Z.-L., Huang, B.-H., Peng, J., Zhang, M., and Pang, D.-W., *Facile preparation of low cytotoxicity fluorescent carbon nanocrystals by electrooxidation of graphite.* Chemical Communications, 2008. **0** (41): p. 5116-5118.
29. Wang, F., Pang, S., Wang, L., Li, Q., Kreiter, M., and Liu, C., *One-step synthesis of highly luminescent carbon dots in noncoordinating solvents.* Chemistry of Materials, 2010. **22** (16): p. 4528-4530.
30. Tian, L., Ghosh, D., Chen, W., Pradhan, S., Chang, X., and Chen, S., *Nanosized carbon particles from natural gas soot.* Chemistry of Materials, 2009. **21** (13): p. 2803-2809.
31. Sun, Y.P., Zhou B., Lin Y., Wang W., Fernando K.A., Pathak P., Meziani M. J., Harruff B. A., Wang X., Wang H., Luo P.G., Yang H., Kose M. E., Chen B., Veca L. M., and Y., X.S., *Quantum-sized carbon dots for bright and colorful photoluminescence.* Journal of the American Chemical Society, 2006. **128** (24): p. 7756.
32. Palashuddin, S.K., Amit, J., Anumita, P., Ghosh, S.S., and Chattopadhyay, A., *Presence of amorphous carbon nanoparticles in food caramels.* Nature Scientific Reports, 2012. **2**.
33. Sahu S., Behera, B., Maitib, T.K., and Mohapatra, S., *Simple one-step synthesis of highly luminescent carbon dots from orange juice: Application as excellent bio-imaging agents.* Chemical Communications, 2012.
34. Ray, S.C., Saha, A., Jana, N.R., and Sarkar, R., *Fluorescent carbon nanoparticle: Synthesis, characterization and bio-imaging application.* arXiv preprint arXiv:0909.4622, 2009.
35. Mao, X.-J., Zheng, H.-Z., Long, Y.-J., Du, J., Hao, J.-Y., Wang, L.-L., and Zhou, D.-B., *Study on the fluorescence characteristics of carbon dots.* Spectrochimica Acta Part A: Molecular and Biomolecular Spectroscopy, 2010. **75** (2): p. 553-557.

36. Liu, H., Ye, T., and Mao, C., *Fluorescent carbon nanoparticles derived from candle soot.* Angewandte Chemie International Edition, 2007. **46** (34): p. 6473-6475.
37. Guo, Y., Wang, Z., Shao, H., and Jiang, X., *Hydrothermal synthesis of highly fluorescent carbon nanoparticles from sodium citrate and their use for the detection of mercury ions.* Carbon, 2012 (52): p. 583–589.
38. Baker, S.N. and Baker, G.A., *Luminescent Carbon Nanodots: Emergent Nanolights.* Angewandte chemie international edition, 2010. **49** (38): p. 6726-6744.
39. Liu, J.-H., Yang, S.-T., Chen, X.-X., and Wang, H., *Fluorescent carbon dots and nanodiamonds for biological Imaging: Preparation, application, pharmacokinetics and toxicity.* Current Drug Metabolism, 2012. **13** (8): p. 1046-1056.
40. Cao, L., Wang, X., Meziani, M.J., Wang, H., Luo, P.G., Lin, Y., Harruf, B.A., Veca, M., Murray, D., Xie, S.Y., and Sun, Y.P., *Carbon dots for multiphoton bioimaging.* Journal of the American Chemical Society, 2007. **129** (37): p. 11318.
41. Callan, J.F., Fowley, C.P., McCaughan, B., and Devlin, A., *Highly luminescent biocompatible carbon quantum dots by encapsulation with an amphiphilic polymer.* Chemical Communications, 2012 (48): p. 9361-9363.
42. Allam, A. and Sarkar, S., *Water soluble fluorescent quantum carbon dots*, 2010, Afreen Allam, Sabyasachi Sarkar: USA.
43. Galande, C., Mohite, A.D., Naumov, A.V., Gao, W., Ci, L., Ajayan, A., Gao, H., Srivastava, A., Weisman, R.B., and Ajayan, P.M., *Quasi-molecular fluorescence from graphene oxide.* Scientific Reports, 2011. **1**.
44. Qiu, X.-P. and Winnik, F.M., *Facile and efficient one-pot transformation of RAFT polymer end groups via a mild aminolysis/michael addition sequence.* Macromolecular Rapid Communications, 2006. **27** (19): p. 1648-1653.
45. Moad, G., Chong, Y., Postma, A., Rizzardo, E., and Thang, S.H., *Advances in RAFT polymerization: the synthesis of polymers with defined end-groups.* Polymer, 2005. **46** (19): p. 8458-8468.
46. Leggett, R., Lee-Smith, E.E., Jickells, S.M., and Russell, D.A., *"Intelligent" Fingerprinting: Simultaneous identification of drug metabolites and individuals by using antibody-functionalized nanoparticles.* Angewandte Chemie International Edition, 2007. **119** (22): p. 4178-4181.
47. Hazarika, P., Jickells, S.M., Wolff, K., and Russell, D.A., *Imaging of latent fingerprints through the detection of drugs and metabolites.* Angewandte Chemie International Edition, 2008. **47** (52): p. 10167-10170.
48. Hazarika, P., Jickells, S.M., and Russell, D.A., *Rapid detection of drug metabolites in latent fingermarks.* Analyst, 2009. **134** (1): p. 93-96.
49. Prete, C., Galmiche, L., Quenum-Possy-Berry, F.-G., Allain, C., Thiburce, N., and Colard, T., *Lumicyano™: A new fluorescent cyanoacrylate for a one-step luminescent latent fingermark development.* Forensic Science International, 2013. **233** (1): p. 104-112.

Chapter 8. Appendix

8.1 Appendix A: ^{1}H NMR spectra of CdS/p(DMA-*co*-MMA) and CdS/p(DMA-*co*-Sty)

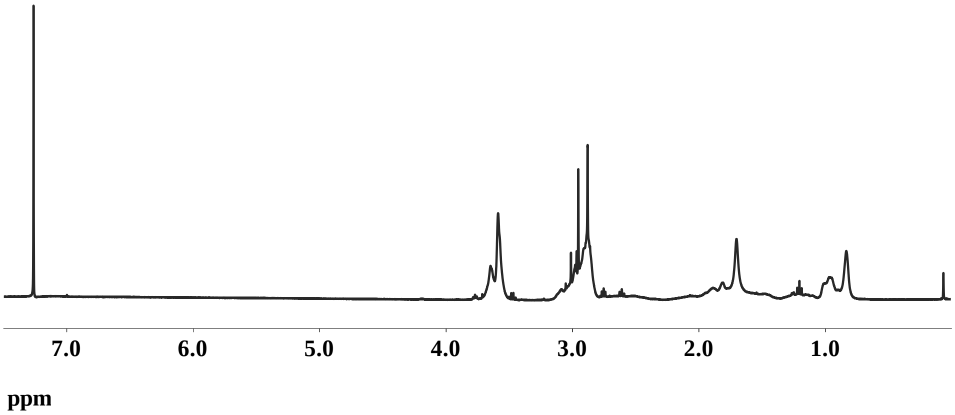

Figure 8.1.^{1}H NMR spectra of CdS/p(DMA-*co*-MMA) in $CDCl_3$

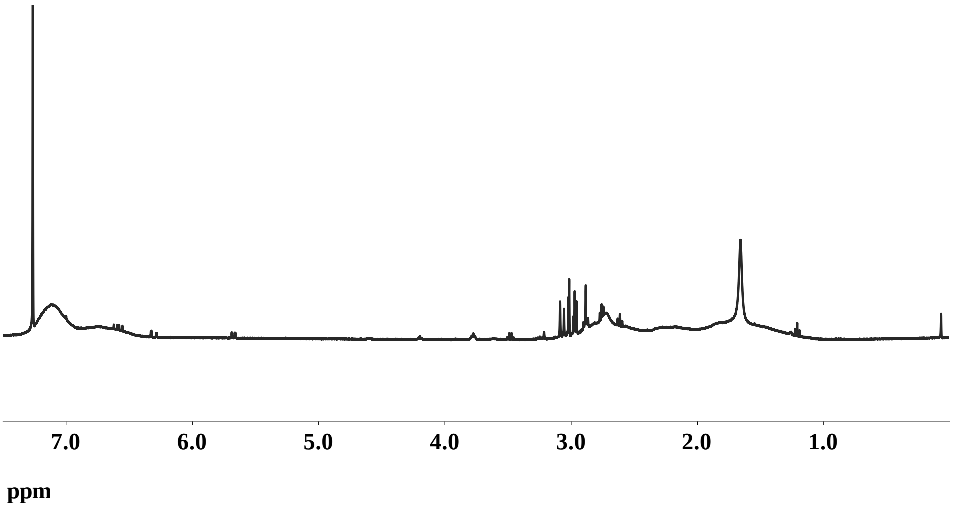

Figure 8.2.^{1}H NMR spectra of CdS/p(DMA-*co*-MMA) in $CDCl_3$

8.2 Appendix B: Photostability of CdS QDs over time (t = 2 months, 6, 12 and 18 months)

A single sample vial of CdS/p(DMA) diluted in DMF (1/25 dilution) was kept on a laboratory shelf for 18 months. The fluorescence emission spectra (average of 10 scans) were recorded after 0, 2, 6, 12 and 18 months, at an excitation wavelength of 350 nm. The fluorescence intensity was normalised against sample taken at 0 months, and the peak maxima position was noted and plotted in Figure 8.3

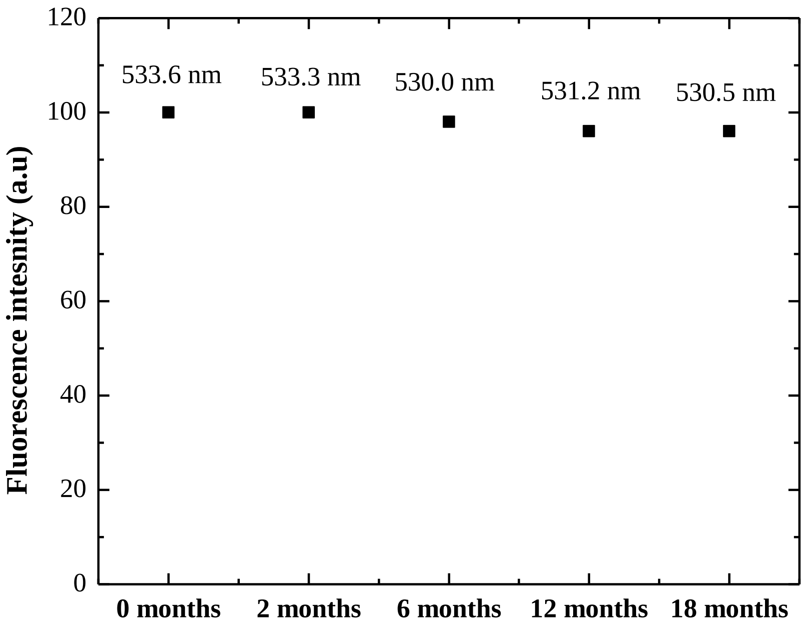

Figure 8.3. Normalised fluorescence intensity, peak maxima position of CdS/p(DMA) in DMF aged over 0, 2, 6, 12, and 18 months. (Excitation of 350 nm).